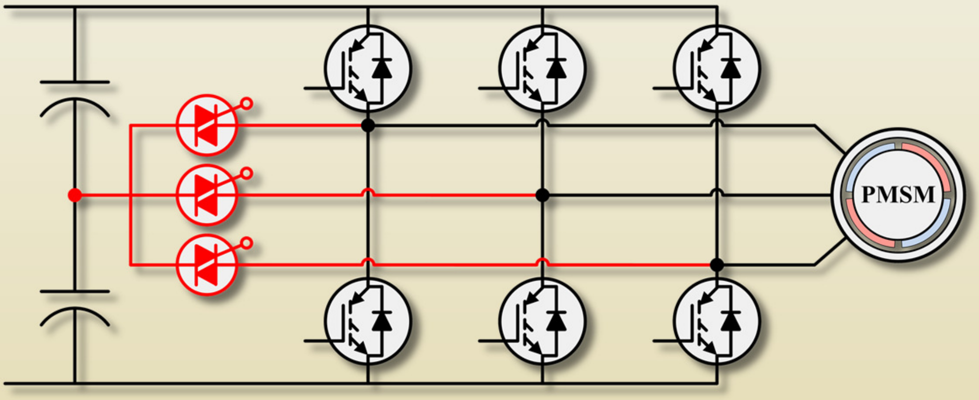

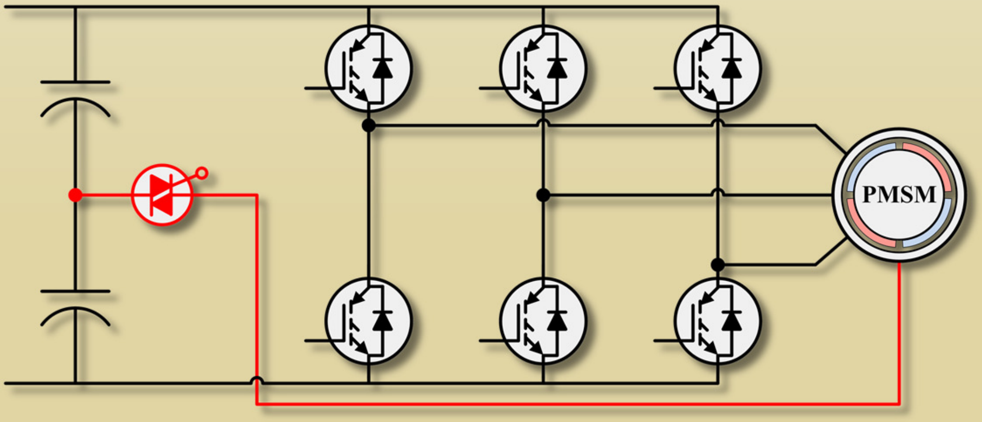

Jorge Oliveira Estima

Development and Analysis of Permanent Magnet Synchronous Motor Drives with Fully Integrated Inverter Fault-Tolerant Capabilities

Dissertation submitted to the Faculty of Sciences and Technology of the University of Coimbra for the fulfillment
of the requirements for the degree of Doctor of Philosophy in Electrical and Computer Engineering

Coimbra
2012

UNIVERSIDADE DE COIMBRA

This work was supported by the Portuguese Foundation for Science and Technology (FCT) under the project nº SFRH/BD/40286/2007.

FCT Fundação para a Ciência e a Tecnologia
MINISTÉRIO DA EDUCAÇÃO E CIÊNCIA

COMPETE
PROGRAMA OPERACIONAL FACTORES DE COMPETITIVIDADE

QUADRO
DE REFERÊNCIA
ESTRATÉGICO
NACIONAL
PORTUGAL 2007.2013

UNIÃO EUROPEIA
Fundo Europeu
de Desenvolvimento Regional

Acknowledgments

This PhD dissertation is the culmination of a long, hard, but also captivating work. It was also an exciting journey full of challenges, experiences and discoveries that would be impossible without the crucial help and support of many people. Thus, it is fair to express here my most profound and sincere gratitude to all those who helped me during these last years.

In the first place, I want to express my deepest gratitude to my supervisor, Professor António João Marques Cardoso, for his constant support, guidance and invaluable experience during the execution of this work. I also would like to thank him for all the opportunities that he gave me and that have broadened immensely my personal and professional horizons.

I am also thankful to all my colleagues and friends of the Energy Systems Laboratory. Especially, I am immeasurably grateful to Sílvia, Eunice and Nuno for their friendship, support and collaboration during these years. The great relationship with them definitely contributed to the creation of excellent working conditions and motivation levels that were extremely important to conclude this thesis.

I also want to thank all my close and old friends for being there whenever I need them. They have also been an important part during these years.

I deeply want to express my gratitude to my parents, who have always given me the strength and wisdom to be sincere in my work, for setting high moral standards and supporting me through their hard work, and for their unselfish love and care. Without them, I may never have gotten to where I am today.

A final acknowledgment to a very special person who has been always by my side, my girlfriend Joana. I would like to thank for her endless love, constant support, encouragement and patience, and for bringing me a new and special shine to my life. Her constant presence and affection were decisive in helping me to overcome all the difficulties that have arisen during these last years.

At last, I would like to acknowledge the financial support of the Portuguese Foundation for Science and Technology (FCT) under fellowship SFRH/BD/40286/2007.

Jorge Oliveira Estima

Abstract

The main goal of this work is the study, development and analysis of fully-automated fault-tolerant permanent magnet synchronous motor drives, capable of handling with voltage source inverter open-circuit faults. In order to achieve this, two distinct non-redundant power converter topologies are investigated. Additionally, in order to cover the main worldwide used control techniques applied to these variable speed drives, three control strategies are considered in this work, namely the vector control with hysteresis current controllers, vector control with space vector modulation and direct torque control.

With the aim to perform a theoretical analysis through computational simulations, the permanent magnet synchronous motor (PMSM) dynamic model equations are presented. The mathematical principles behind the three considered control methods are then exposed and validated through several results obtained under normal operating conditions.

In order to know in advance how the system reacts under abnormal operating conditions, the drive behavior is investigated when inverter open-circuit faults are introduced. Some key parameters are evaluated, allowing to obtain information that is extremely useful for the correct design of fault diagnostic algorithms and that allows to predict how the entire system will react under these conditions.

The data provided by this analysis allowed to develop two new algorithms for real-time diagnosis of inverter open-circuit faults. Comparing with the majority of the existing techniques, these two new methods present important features such as operating conditions independence, simple implementation, fast diagnosis and low computational requirements, making them especially suitable for their easy integration into the drive controller. The theoretical principles of both algorithms are presented, being then correctly validated through simulation and experimental results.

The two non-redundant fault-tolerant power converter topologies and their corresponding post-fault control modifications are presented for the three considered control strategies. Accordingly, the entire fault-tolerant control systems are proposed, allowing to automatically reconfigure the drive operation when an inverter fault occurs.

Finally, an exhaustive experimental performance analysis is presented, where the system operation is compared for normal and post-fault operating conditions. A very detailed electrical evaluation is performed, together with a thermal and acoustic analysis.

Resumo

O objectivo principal deste trabalho é o estudo, desenvolvimento e análise de accionamentos tolerantes a falhas, totalmente automatizados, baseados em motores síncronos de ímanes permanentes, capazes de lidar com avarias de circuito aberto no inversor. Com este propósito, duas topologias distintas de conversores tolerantes a falhas são investigadas. Adicionalmente, de modo a cobrir as principais técnicas de controlo globalmente utilizadas no âmbito destes accionamentos de velocidade variável, três estratégias de controlo são consideradas neste trabalho, nomeadamente o controlo vectorial com controladores de corrente por histerese, controlo vectorial com modulação do fasor espacial e controlo directo de binário.

Com o objectivo de realizar uma análise teórica através de simulações computacionais, as equações do modelo matemático do motor síncrono de ímanes permanentes são apresentadas. Os princípios matemáticos relativos às três estratégias de controlo consideradas são posteriormente expostos e validados através de vários resultados obtidos em condições normais de funcionamento.

Para saber antecipadamente como o sistema reage em condições anormais de funcionamento, o comportamento do accionamento é analisado quando falhas de circuito aberto são introduzidas no inversor. Alguns parâmetros chave são avaliados, permitindo obter informação extremamente útil para o correcto desenvolvimento de algoritmos de diagnóstico de avarias, possibilitando também prever como o sistema reagirá nestas condições.

Os dados fornecidos por esta análise permitiram desenvolver dois novos algoritmos para o diagnóstico em tempo real de avarias de circuito aberto no inversor. Comparando com a maioria das técnicas existentes, estes dois novos métodos apresentam características importantes, tais como, a independência das condições de funcionamento, simples implementação, velocidade de diagnóstico e baixos requisitos computacionais, tornando-os especialmente apropriados para a sua fácil integração no controlador do accionamento. Os princípios teóricos de ambos os algoritmos são apresentados, sendo depois correctamente validados através de resultados de simulação e experimentais.

As duas topologias não redundantes de conversores de potência tolerantes a falhas e suas correspondentes modificações de controlo pós-falha, são apresentadas para as três estratégias de controlo consideradas. Deste modo, os sistemas globais de controlo tolerante a falhas são propostos, permitindo estes a reconfiguração automática da operação do accionamento aquando da ocorrência de

uma avaria no inversor.

Finalmente, uma exaustiva análise experimental de desempenho é apresentada, onde a operação do sistema é comparada para condições de funcionamento normais e pós-falha. Uma avaliação eléctrica muito detalhada é efectuada, juntamente com uma análise térmica e acústica complementares.

Contents

Nomenclature

α	Angle between the reference voltage vector and the basic adjacent vector (rad)
Δi	Hysteresis band (A)
δ	Load angle (rad)
δ_k	Reference currents errors (A)
ω	Fundamental electrical frequency (rad/s)
ω_r	PMSM mechanical speed (rad/s)
$\overline{F}_s$	Magnetomotive force (A)
$\overline{V}_r$	Reference voltage vector (V)
ψ_d, ψ_q	Stator flux linkages in the dq synchronous reference frame (Wb)
ψ_{PM}	Rotor magnets flux linkage (Wb)
θ	Rotor flux electrical position (rad)
*	Reference value
a_k	Auxiliary variables
D	Damping coeficient (Nms/rad)
d_k	Diagnostic variables
e_k	Errors of the normalized currents average absolute values
f_c	PWM Carrier frequency (Hz)
f_s	Sampling frequency (Hz)
I_1	Current fundamental component rms value (A)

i_a, i_b, i_c	PMSM phase currents (A)
i_d, i_q	Stator phase currents in the dq synchronous reference frame (A)
I_m	Currents maximum amplitude (A)
i_n	Current through the neutral conductor (A)
i_α, i_β	Stator phase currents in the $\alpha\beta$ stationary reference frame (A)
I_{rms}	Current rms value (A)
i_{cd}, i_{cq}	Iron losses currents in the dq synchronous reference frame (A)
i_{kN}	Normalized motor phase currents
i_k	PMSM measured phase currents (A)
i_{md}, i_{mq}	Magnetizing currents in the dq synchronous reference frame (A)
J	Moment of inertia (Kgm^2)
k_d	Same phase double fault detection threshold
k_f	Detection threshold
k_l	Same phase double fault detection threshold
k_m	Multiple faults detection threshold
L_d, L_q	Stator inductances in the dq synchronous reference frame (H)
N_{ef}	Effective number of stator turns per phase
p	Pole pairs number
P_{Cu}	Stator windings copper power losses (W)
P_{Fe}	Stator iron power losses (W)
R_s	Stator winding per-phase resistance (Ω)
S_a, S_b, S_c	Inverter swiching states
T_e	Electromagnetic torque (Nm)
T_L	Load torque (Nm)

T_s	Sampling period (s)
t_x, t_y, t_0	Time values for the voltage reference vector syntetization (s)
$T_{e_{\mathrm{dc}}}$	Electromagnetic torque average value (A)
$T_{e_{\mathrm{rms}}}$	Electromagnetic torque rms value (A)
v_α, v_β	Stator phase voltages in the $\alpha\beta$ stationary reference frame (V)
v_d, v_q	Stator phase voltages in the dq synchronous reference frame (V)
v_{ab}, v_{bc}, v_{ca}	PMSM phase-to-phase voltages (V)
v_a, v_b, v_c	PMSM phase voltages (V)
V_{dc}	DC bus voltage (V)
v_d^c, v_q^c	Decoupling voltage components in the dq synchronous reference frame (V)
x	Arbitrary variable
x_{av}	Average value of the x coordinate of the vectors distribution along the real axis (V)
AC	Alternating current
DC	Direct current
DSC	Direct self control
DSP	Digital signal processor
DTC	Direct torque control
EMF	Electromotive force
FPGA	Field programmable gate array
HCC	Hysteresis current control
IGBT	Insulated gate bipolar transistor
NCM	Neutral to capacitors midpoint
PCM	Phase to capacitors midpoint
PI	Proportional-integral

PMSM	Permanent magnet synchronous motor
PWM	Pulsewidth modulation
RFOC	Rotor field oriented control
rpm	Revolutions per minute
RTD	Resistance temperature detector
SPWM	Sinusoidal pulsewidth modulation
SVM	Space vector modulation
THD	Total harmonic distortion
THIPWM	Third harmonic injection pulsewidth modulation
TWD	Total waveform distortion
TWO	Total waveform oscillation
VSI	Voltage source inverter

Chapter 1

Introduction

With the advent of new magnetic materials such as the neodymium-iron-boron, the development of permanent magnet synchronous motors (PMSMs) has accelerated during the last decades. The improvement of these magnetic materials with a high energy product allows the PMSMs to achieve high power density levels and high efficiency values, being these characteristics extremely desired for a wide range of applications [1].

Hence, PMSM drives have become serious competitors against induction motor drives. In fact, and thanks to their characteristics, presently these motors are preferred and widely used in a great variety of applications such the ones related to the aerospace and automotive industry.

On the other hand, the invention and development of digital controllers such as digital signal processors (DSPs), microprocessors, field programmable gate arrays (FPGAs), microcontrollers, etc, together with the advent of semiconductor technology, drastically changed the industrial and commercial applications. Beyond the impact that this had on the industrial automation and commercial equipment control with reduced human intervention, a great number of applications, pneumatic and mechanical systems were replaced by variable speed AC drives due to the improved efficiency, ease of control and reduced maintenance.

The invention of new semiconductor power devices also triggered the development of new drive control strategies that, together with the advancement in the sensor technology, provided efficient and robust control solutions for electric drive applications.

However, for some specific applications, the availability and safe operation of electric drives is a mandatory feature. For instance, taking into account the interlinked production processes that characterizes modern industrial processing plants, a fault in a single drive can result in tremendous repairing and production costs.

Furthermore, there are some critical applications like power plants, aerospace, railway locomotives, automobiles, etc, where a failure in a drive can be dangerous or can result in even more catastrophic human consequences. In order to improve the availability and safety of the industrial drives, fault-tolerant solutions can be implemented. From a different perspective, fault tolerance is a need in many applications because the consequences of fault or malfunction are more expensive than the cost of avoiding the faults. Accordingly, fault-tolerant drives will entail the reduction in maintenance costs, downtimes, and more importantly the avoidance of unnecessary failures, with their potential costly or even perhaps catastrophic consequences [2].

A typical modern variable speed AC drive is a relatively complex system that comprises several devices. In general, it consists of a power electronic converter with a diode bridge rectifier, a DC link with smoothing capacitors, and an inverter that supplies the AC machine. A digital controller is also required for the drive control implementation, using feedback sensors for signals input. Due to the complexity of these energy conversion systems, they are therefore very susceptible to suffer several kinds of failures that can lead to unplanned stoppages or at least, affect the drive's performance.

In order to achieve continuous operation, typically fully redundant systems or conservative designs are the most obvious solutions. The redundancy concept consists of disposing of two or more independent units, where some are used as active parts and the others are considered as spare units. In case of a fault, the additional units are used to replace the faulty ones. On the other side, conservative designs are obtained by oversizing the drive in order to minimize the likelihood of fault occurrences since a lower stress on the drive components under normal operating conditions increases the expected lifetime [3]. Nevertheless, and as main drawback, both solutions highly increase the overall system costs.

In some cases, continuous drive operation can be ensured when the reduced post-fault performance levels are acceptable. Typically, this is accomplished through minor changes at a hardware/software level, avoiding the use of extra redundant units and the subsequent increase of the system costs.

Some innovation has been brought by the development of diagnostic methods and condition monitoring techniques since the detection of incipient faults allows taking measures that prevent unplanned stoppages. However, this implies that the fault must be detected at an incipient stage of development. In case of sudden faults such the ones related to power converter faults, typically this is not possible and therefore, the standard protection mechanisms act in order to immediately shutdown the drive.

In fact, considering the modern variable speed drives, the voltage source inverter (VSI), because of its complexity, is a device very susceptible to suffer critical failures. In general, these can be classified as short-circuit faults and open-circuit faults. The first ones, typically, can be very destructive and therefore, today's drives include standard protection strategies intended to shutdown the drive and avoid more catastrophic consequences. On the contrary, open-circuit faults can remain undetected for long time periods, which may lead to secondary faults and high repairing costs.

Accordingly, further than the basic control routines, there is a growing trend to integrate into the drive digital controller, condition monitoring techniques/algorithms, as well as fault-tolerant remedial strategies, resulting in more advanced and intelligent drive systems [4].

Taking all this into account, the main objective of this work is the study, development and analysis of fully-integrated fault-tolerant variable speed PMSM drives, capable of handling with inverter open-circuit faults. In order to achieve this, two real-time inverter diagnostic algorithms were especially developed for their implementation into the drive controller. Dedicated fault-tolerant control strategies are proposed with the aim to enable the drive automatic reconfiguration under the presence of an inverter malfunction. For the post-fault drive operation, two non-redundant inverter topologies are considered. In order to cover the main control techniques used worldwide, the vector control using hysteresis currente controllers (HCC vector control), vector control using space vector modulation (SVM vector control) and direct torque control (DTC) are considered in this work. Finally, a detailed drive system performance evaluation is presented, allowing to compare the three considered control strategies for the two power converter fault-tolerant topologies.

1.1 Main Contributions

Despite the existing research work applied to variable speed induction motor drives, the literature review shows that the study and development of fault-tolerant strategies applied to variable speed permanent magnet synchronous motor drives still presents some limitations.

In this context, a detailed study is presented in this thesis by analyzing three main topics, namely the drive faulty operation, inverter fault diagnosis and fault-tolerant remedial strategies.

Regarding the first topic and in order to develop a fault-tolerant drive, it is very important to know in advance how the system behaves under the presence of a failure. Therefore, from the drive faulty operation analysis it is possible to extract valuable information that can be extremely useful for the correct design of fault diagnostic algorithms, for the development of special hardware protection devices and that allows to predict how the entire system will react under unexpected operating conditions. As a result, it was evaluated how an inverter fault influences the drive performance through the analysis of some key parameters such as the PMSM phase currents and electromagnetic torque.

With respect to the inverter fault diagnosis, the literature shows a great lack of research on simple and effective diagnostic algorithms for open-circuit faults in two-level VSIs, presenting mandatory features such as motor operating conditions independence, simple implementation, fast diagnosis and low computational requirements. Therefore, two new real-time algorithms were developed that take into account all these important requirements, making them especially suitable for their integration into the drive controller, providing simultaneously the required information to trigger fault-tolerant remedial strategies.

Two non-redundant power converter fault-tolerant topologies are considered and evaluated in this work. Despite these two reconfigurations are not new in the literature, the drive operating limits for both cases were not clearly defined yet. Moreover, the literature review shows that inverter fault diagnosis and fault-tolerant strategies are typically discussed and implemented separately. As an added value, in this work these two major subjects are addressed and implemented together in order to obtain a complete fault-tolerant drive system. Additionally, the operating limits for the two considered fault-tolerant topologies are also investigated and defined.

Apart from these three main topics, an exhaustive experimental performance evaluation was performed, with special focus on the PMSM. This was accomplished through a very detailed electrical analysis as well as complementary thermal and acoustic tests. For the first one, an enormous amount of data were acquired in order to build three-dimension plots that fully characterize several key parameters in all possible operating points. This kind of deep analysis applied to fault-tolerant variable speed PMSM drives, together with the thermal and acoustic evaluations, is new in the literature, being another important contribution of this thesis.

Finally, it is worth noting that for all the previous topics, three commonly used control strategies for PMSM variable speed drives were considered with the aim to cover the main control techniques used worldwide in modern variable speed drives.

1.2 Structure of the Thesis

All the content in this thesis is organized into eight chapters. Chapter 1 corresponds to this thesis introduction, where the principal motivation interests behind this research work are presented, highlighting the importance of fault-tolerant variable speed PMSM drives. Additionally, the main contributions resulting from the work developed in this thesis are also exposed.

Chapter 2 is fully dedicated to the study and presentation of the PMSM dynamic model, mandatory for the theoretical analysis of this work. A literature review regarding the different ways for modeling this machine is firstly presented. Then, the equations referred to a synchronous reference frame that were used for the PMSM modeling are enumerated.

The main control strategies applied to variable speed PMSM drives are discussed in Chapter 3. Initially, a literature review is performed, covering the main aspects and variants related to the control of PMSM drives. Then, the theoretical principles behind the HCC vector control, SVM vector control and DTC are presented. Finally, simulation and experimental results are presented for the drive normal operation.

Chapter 4 deals with the PMSM drive faulty operation analysis. In analogy to the previous cases, a literature review on this topic is primarily done. Then, simulation results regarding the PMSM drive system operation under inverter open-circuit faults are presented and analyzed. Finally, these results are validated through the analysis of equivalent experimental tests.

The research work on inverter fault diagnosis is discussed in Chapter 5. Firstly, a detailed literature survey on diagnostic methods for inverter open-circuit fault diagnosis is presented, providing a good state-of-the-art on this subject. Then, the theoretical principles of two new algorithms that were developed for real-time inverter fault diagnostics are presented. These two methods are properly tested and validated through several simulation and experimental results.

The developed work on the fault-tolerant strategies that can be applied to variable speed PMSM drive systems is exposed in Chapter 6. In a similar way to previous cases, a related literature review is provided at the beginning of the chapter. Then, the post-fault control theoretical fundamentals for each of the three considered control techniques are presented, taking into account the specificities of the two non-redundant power converter topologies. The global fault-tolerant control, which allows to obtain a fully-automated fault-tolerant PMSM drive is discussed. At last, various simulation and experimental results are presented with the aim to validate all the developed work.

Chapter 7 is entirely dedicated to the drive performance analysis. A very detailed electrical evaluation is performed through the analysis of several key parameters, with special focus on the PMSM. Additionally, a complementary thermal and acoustic analysis are also performed.

At last, in Chapter 8 the main conclusions of this thesis are presented, including also some topics for potential future research work.

Chapter 2

PMSM Mathematical Model

With the aim to perform a detailed theoretical study of the PMSM drive, it is necessary to develop and implement a suitable mathematical model of the machine that allows to characterize its behavior and quantities with an acceptable accuracy.

From a construction point of view, the PMSM is very similar to the conventional synchronous motor and as a result, its dynamic model can be derived from the well-known equations of the classical synchronous machine [5]. This model can describe the machine in a real abc frame or in a dq rotating frame. Typically, by using the first one, the obtained equations are non-linear, meaning that they are relatively complex, and the variables are time-variant. If the machine is described using a dq rotor reference frame, the obtained equations are much more simple, allowing to accelerate the numerical calculations involved in the computational simulations. Furthermore, under steady-state operation the obtained variables do not vary in time, making easier additional calculations and simplifying the control system implementation.

According to this, the dq model in the rotor reference frame is the most common and widely used model in the literature [6]-[15]. This model assumes that the saturation is neglected, the back-EMF is sinusoidal, that there is no cage in the rotor and that the eddy currents and hysteresis losses are negligible. Taking into account these restrictions, the resulting equations become very simple, allowing to predict the machine behavior with a reasonable accuracy. For the study of line-start PMSMs, typically the rotor includes a cage in a similar way to induction motors. In this case, the machine equations can be described in order to include a rotor cage [16]-[18]. The PMSM dynamic model can also be defined with the aim to take into account the iron losses in the stator stack, namely the eddy currents losses [19]-[25]. This model allows to achieve a more detailed power losses characterization, being therefore suitable for a more accurate efficiency evaluation. Much more complex simulation models can be defined using finite element analysis [26]-[30]. By using these software-based tools, a very accurate model can be defined, allowing to obtain a good agreement between the simulated results and the experimental ones. Moreover, beyond the electrical modeling, these software tools also allow to perform other important analysis such as magnetic flux distribution and temperature analysis. However, due to their complexity, the definition of these models can be relatively difficult and since they are typically very computationally demanding, the simulation times can be very long.

2.1 Dynamic Model

As said before, for describing and analyzing a PMSM, the most convenient way is to consider a synchronous rotating reference frame fixed to the rotor. The transformation of the state variables (voltages, currents and fluxes) from the abc stationary frame into the rotating $dq0$ coordinates, is accomplished by using the amplitude-invariant transformation matrix defined as:

$$\begin{bmatrix} x_d \\ x_q \\ x_0 \end{bmatrix} = \frac{2}{3} \begin{bmatrix} \cos(\theta) & \cos\left(\theta - \frac{2\pi}{3}\right) & \cos\left(\theta + \frac{2\pi}{3}\right) \\ -\sin(\theta) & -\sin\left(\theta - \frac{2\pi}{3}\right) & -\sin\left(\theta + \frac{2\pi}{3}\right) \\ 1/2 & 1/2 & 1/2 \end{bmatrix} \begin{bmatrix} x_a \\ x_b \\ x_c \end{bmatrix} \tag{2.1}$$

where θ is the angle between the stator phase a and the rotor flux. On the contrary, the state variables in the abc stationary frame can be obtained from the rotating $dq0$ components using the inverse amplitude-invariant transformation matrix:

$$\begin{bmatrix} x_a \\ x_b \\ x_c \end{bmatrix} = \begin{bmatrix} \cos(\theta) & -\sin(\theta) & 1 \\ \cos\left(\theta - \frac{2\pi}{3}\right) & -\sin\left(\theta - \frac{2\pi}{3}\right) & 1 \\ \cos\left(\theta + \frac{2\pi}{3}\right) & -\sin\left(\theta + \frac{2\pi}{3}\right) & 1 \end{bmatrix} \begin{bmatrix} x_d \\ x_q \\ x_0 \end{bmatrix} \tag{2.2}$$

For a more accurate modeling, the implemented PMSM dynamic model takes into account the iron losses, specifically the eddy current losses. These are modeled by a resistor R_c which is inserted in parallel with the magnetizing branch of the equivalent circuit, so that the power losses depend on the air-gap flux linkage [25]-[30]. Thus, the dq axes currents (i_d, i_q) are divided into the iron loss currents (i_{cd}, i_{cq}) and the magnetizing currents (i_{md}, i_{mq}), as shown in Fig. 2.1.

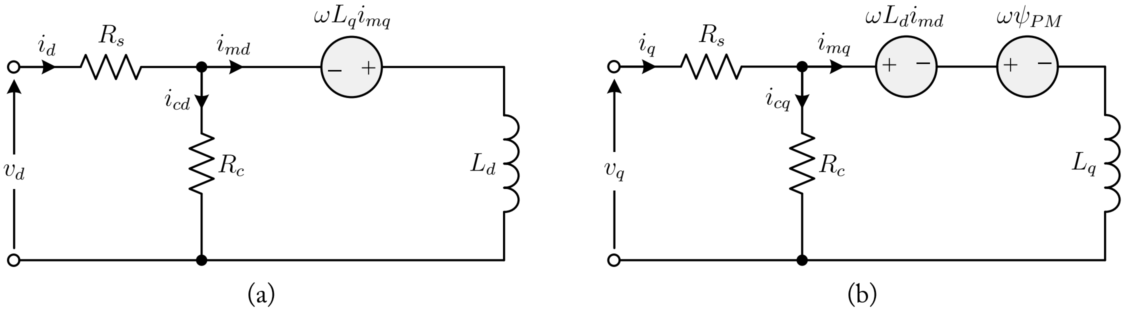

Figure 2.1: dq axes equivalent circuits for the PMSM model taking iron losses into account: (a) d-axis; (b) q-axis.

Considering this, and assuming that the saturation is neglected, the electromotive force is sinusoidal, and a cageless rotor, the voltage equations of the PMSM dynamic model in the synchronous reference frame, are given by:

$$v_d = R_s i_d + L_d \frac{di_{md}}{dt} - \omega L_q i_{mq} \tag{2.3}$$

$$v_q = R_s i_q + L_q \frac{di_{mq}}{dt} + \omega L_d i_{md} + \omega \psi_{PM} \tag{2.4}$$

From 2.3 and 2.4 it is possible to derive the state equations that allow to build the complete PMSM dynamic model:

$$\frac{di_{md}}{dt} = \frac{1}{L_d} \left(v_d - R_s i_d + \omega L_q i_{mq}\right) \tag{2.5}$$

$$\frac{di_{mq}}{dt} = \frac{1}{L_q} \left(v_q - R_s i_q - \omega L_d i_{md} - \omega \psi_{PM}\right) \tag{2.6}$$

$$\frac{d\omega_r}{dt} = \frac{1}{J} \left(T_e - D\omega_r - T_L\right) \tag{2.7}$$

$$\frac{d\theta}{dt} = \omega = \omega_r p \tag{2.8}$$

where

$$i_d = \frac{1}{R_c} \left(L_d \frac{di_{md}}{dt} - \omega L_q i_{mq} + R_c i_{md}\right) \tag{2.9}$$

$$i_q = \frac{1}{R_c} \left(L_q \frac{di_{mq}}{dt} + \omega L_d i_{md} + \omega \psi_{PM} + R_c i_{mq}\right) \tag{2.10}$$

$$i_{cd} = i_d - i_{md}; \; i_{cq} = i_q - i_{mq} \tag{2.11}$$

$$T_e = \frac{3}{2} p \left[\psi_{PM} i_{mq} + \left(L_d - L_q\right) i_{md} i_{mq}\right] \tag{2.12}$$

By referring equations 2.5, 2.6, 2.9 and 2.10 to a steady-state condition, it is possible to define a mathematical expression for the power losses in the stator windings. These can be calculated according to following expression:

$$P_{Cu} = \frac{3}{2} R_s \left(i_d^2 + i_q^2\right) \tag{2.13}$$

In a similar way, the power losses that are caused by the fundamental component of the total flux linkage in the iron stack can be calculated as:

$$\begin{aligned} P_{Fe} &= \frac{3}{2} R_c \left(i_{cd}^2 + i_{cq}^2 \right) \\ &= \frac{3}{2} \frac{\omega^2}{R_c} \left[\left(L_q i_{mq} \right)^2 + \left(\psi_{PM} + L_d i_{md} \right)^2 \right] \end{aligned} \tag{2.14}$$

Although not considered in this work, hysteresis losses can also be taken into account. These losses are proportional to the machine phase currents frequency. Therefore, in order to include them into the machine model, the iron losses resistance is usually treated as a function of ω.

Chapter 3

Control Strategies

Comparing with DC drives, the control of AC machines is much more complex since typically it requires computationally intensive algorithms. For this reason, variable speed drives based on DC motors have dominated the industry in the past. However, due the advent of low cost, high performance microcontrollers and DSPs especially designed for motor control applications, the control of AC motor drives is today very common and widely spread in industry.

Regarding the PMSM control, all the developed theory firstly done for induction motor drives can be extended to these specific AC machines. Consequently, the control strategies applied to PMSM motor drives can be broadly divided into three major groups: scalar control, vector control and direct torque control.

In scalar control, also called open-loop volt/Hz control, only the rms value of the inverter output voltage and frequency are controlled. These variables are controlled in such a way that the machine airgap flux is kept practically constant for the operating range. This is easily accomplished since the relation between these two quantities is linear, with the exception for low speeds. In this case, a boost voltage is added so that the flux does not decrease at low frequency. Considering this, the frequency (command signal) controls the machine speed whereas the flux is regulated by varying the voltage rms value. As a result, this control technique is relatively simple and does not require complex calculations. Furthermore, there is no need for feedback sensors which in practice strongly contributes to decrease the system cost and increase its reliability. On the other hand, the performance of this technique is very sluggish because of the inherent coupling effect due to torque and flux being functions of current and frequency. Scalar control is extensively used in a wide range of industry applications such as the speed control of pumps and fans. However, its importance has recently diminished as a result of the superior performance provided by vector-controlled drives, which is demanded in many applications [31]. Further research work was done in this field with the aim to develop new scalar control schemes applied to PMSM drives that allow, for example, to improve the dynamic response, stability and machine efficiency [32]-[35].

In the past, high-performance applications were dominated by separately excited DC motor drives since they allowed to obtain a decoupling between the torque and flux. In DC machines, the armature current and the field flux are orthogonal in space by nature. As a consequence, by controlling the torque adjusting the armature current, the field flux is not affected, which allows to achieve a fast transient response and a high torque per ampere ratio. Due to this inherent coupling in AC machines, they typically cannot give such fast response. These problems were solved by the invention of the vector control in the beginning of 1970s by Blaschke [36], where the demonstration that an induction motor can be controlled in a similar way to a separately excited DC motor has brought a renaissance in the high-performance control of AC drives. Therefore, vector control seeks to recreate these orthogonal components in the AC machine in order to control the torque producing current separately from the magnetic flux producing current. Due to the need of powerful hardware requirements, its initial acceptance was not good since its implementation was very difficult. However, with the arrival of dedicated low cost high-performance DSPs, vector control of AC motors is now applied cost effectively to a wide range of applications from machine tools to washing machines. Comparing with scalar control, one big disadvantage of vector control is the need for a feedback sensor. Nevertheless, a lot of research in sensorless vector control was conducted over the last decades in order to develop estimation techniques that allow to eliminate the need for extra hardware [37]. Several estimators based on back-EMF [38]-[42], machine physical properties [43]-[51], artificial intelligence [52]-[56] and observers [57]-[64] can be applied to the development of sensorless vector control techniques. Indeed, some of these techniques were already incorporated into industrial drives with the capability to operate with scalar control, closed-loop vector control (with feedback sensor) and open-loop sensorless vector control [65]-[66].

In order to implement vector control, the power converter must be properly controlled. This is typically accomplished by using pulsewidth modulation (PWM), which can be divided into current and voltage control techniques [31], [67]-[69].

With respect to the first ones, also classified as nonlinear controllers, the motor phase currents are directly controlled in order to follow a reference signal. Typically, they can be classified as ramp comparators, hysteresis controllers, and predictive controllers [70]. With the ramp comparators, the current errors are compared with a triangular carrier to generate the firing signals. As a result, the switching frequency is limited to the triangular waveform frequency and the produced harmonics are defined at a fixed frequency. As major drawbacks, it is pointed out the inherent phase and amplitude errors that affect the system response. With hysteresis controllers, the motor phase currents are adjusted in order to maintain them within a defined range. They are characterized by their simplicity and great dynamic response. The operating principle of the predictive controllers is based on the calculation of the inverter voltage required to force the currents to follow their respective reference signals.

Regarding the voltage modulation techniques, also known as linear strategies, the most used ones are classified as carrier-based PWM and space vector PWM (SVM) [68], [71]. The principle behind carrier-based PWM methods is based on the comparison of a modulation signal with a high-frequency carrier waveform to generate the gate firing signals. The switching signals are determined by the intersection of these two signals in such a way that when the modulation signal is higher than the carrirer, the phase terminal is connected to the DC bus positive point. On the contrary, the phase terminal is connected to the DC bus negative point. According to shape of the modulation signal, several carrier-based PWM variants can be obtained [72]. The most common ones are the sinusoidal PWM (SPWM) and the third harmonic injection PWM (THIPWM). As the name suggests, SPWM uses a sinusoidal waveform as the modulation signal and it is the simplest to implement. However, with this technique the utilization of the DC bus is relatively poor. This can be improved by using a THIPWM technique, where a third harmonic component is added to the sinusoidal modulation signals. The ratio between the amplitude of the modulation signal and the carrier (modulation index) allows to adjust the output voltage fundamental component while its frequency is the same as the modulation signal.

The SVM is probably the best among all the PWM techniques for variable speed AC drives and thanks to its superior performance, it has been finding a great widespread application during the last decades. With this advanced modulation strategy, instead of using a separate modulator for each phase, the complex reference voltage vector is processed as a whole. In a three-phase two level inverter, six active and two zero vectors are available. Accordingly, the desired reference voltage vector is synthetized using the two nearest active vectors and zero vectors on a time-sharing basis so that the average value matches with the reference vector [73]. Therefore, the interaction between the three motor phases is exploited. It has been proven that SVM generates less harmonic distortion in both output voltage and current applied to the phases of an AC motor and provides a more efficient use of the supply voltage in comparison with direct sinusoidal modulation techniques. Furthermore, the SVM technique is very interesting because the switching sequence can be adapted by taking into account specific control targets such as common-mode voltage elimination, current ripple reduction, and switching losses minimization [74].

Finally, the last group of control techniques that can be applied to PMSMs is the direct torque control (DTC). This method was introduced by Takahashi and Noguchi [75] and by Depenbrock with the designation of Direct Self Control (DSC) [76]. Comparing with the other control strategies, DTC does not rely on the magnitude adjustment of the output inverter voltage and frequency as for scalar control neither on coordinate transformation for components decoupling, required for vector control. Instead, both torque and flux are directly controlled through control loops, where the feedback signals are estimated from the machine terminal voltages and currents. The loop errors are processed by hysteresis controllers and fed to a voltage vector look-up table, together with the location of the stator flux. Taking into account the information of these three inputs, the voltage vector table selects the optimum voltage vector to control the inverter power switches [77]-[82]. This technique also became very popular and was adopted by a major industry company [83].

With the invention of this control technique, the arising of comparison studies between DTC and vector control was inevitable [84]-[86]. From these, it was possible to demonstrate that both have similar performances but in general, DTC has a faster dynamic torque response, simpler implementation and low machine parameters dependence. Conversely, vector control allows to achieve better steady state performance with lower current and torque ripple content and the current control allows to avoid uncontrolled current transients.

Several research work has been done in order to improve the classical DTC scheme applied to variable speed AC drives in general and to PMSM drives specifically. The research cover some areas such the development of sensorless DTC techniques [37], [87]-[92] and algorithms focused on the machine efficiency [93]-[97]. Some interest is also given to the combination of the DTC principles with fixed switching frequency PWM techniques. The majority of these schemes are based on the SVM [98]-[104], which guarantees a constant switching frequency and the resulting advantages of this modulation strategy. Nevertheless, they usually require additional controllers, which increase the implementation complexity. Different approaches were also proposed that allow a simpler implementation of fixed switching frequency DTC [105]-[108].

Regarding the implementation of DTC in PMSM drives, several problems were identified [109]. Consequently, some research has been done in order to overcome the issues associated to erroneous flux estimation [110]-[116], the effect and compensation of the stator resistance variation [117]-[118] and the correct initial detection of the rotor position without sensors [119]-[122].

The work developed in this thesis is intended to be applied to high-performance PMSM drives and therefore, scalar control is disregarded. In order to cover the most common control strategies used worldwide, vector control with hysteresis current controllers (HCC Vector Control), vector control with SVM (SVM Vector Control) and the classical DTC are considered. A more detailed analysis and description of these three techniques is presented in the following sections.

3.1 HCC Vector Control

As said before, the aim of the vector control applied to AC machines is to achieve high-performance levels by decoupling and separately adjusting the torque producing current component from the flux current component, in a similar way to the separately excited DC motor drives. To accomplish this, the rotor instantaneous position must be known in order to force the motor phase currents to maintain the required angle. The three motor phase currents are calculated taking into account the motor operating zones, namely the constant torque zone and the flux weakening zone. These are based on the drive physical limitations and are defined by the motor rated speed value[1].

Vector control can be accomplished by aligning the reference frame with the spacial phasor of

---

[1] In this work, it is only considered the drive operation at speed values equal or below the PMSM rated speed, thus operating in the constant torque zone.

the stator flux linkage, the rotor flux linkage or the synchronous reference frame. The most used one for variable speed AC drives and also considered in this work is based on the rotor field oriented control (RFOC). In this specific case, the reference frame is controlled in such a way that the rotor flux space vector is always aligned with the d axis. Considering this, Figure 3.1 presents the block diagram of this vector control strategy applied to a PMSM, using current controllers to generate the inverter gate command signals.

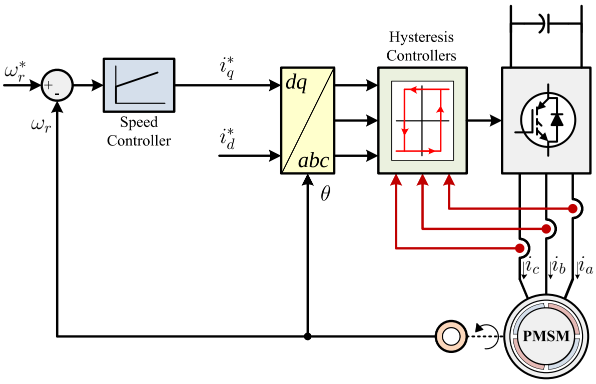

Figure 3.1: Block diagram of the HCC vector control.

The rotating reference frame d axis can be aligned with the rotor flux by taking into account the machine flux linkage equations, derived from the model of the PMSM presented in Section 2.1:

$$\psi_d = L_d i_{md} + \psi_{PM} \tag{3.1}$$

$$\psi_q = L_q i_{mq} \tag{3.2}$$

As a result and according to 3.1 this can be accomplished by forcing $i_{md} = 0$[2]. As a consequence, the torque equation (2.12) can be rewritten as:

$$T_e = \frac{3}{2} p \psi_{PM} i_{mq} \tag{3.3}$$

Since the magnets flux linkage is constant, from this last equation it can be proved that the PMSM electromagnetic torque is controlled in a similar way to the separately excited DC motor, where it will just depend on the q-axis current component.

Finally, the three motor phase currents reference signals are obtained from the corresponding dq components using the transformation defined in (2.2). These are then used by the hysteresis current controllers in order to generate the inverter gate command signals.

---

[2] In practice, and for the sake of simplicity, the iron losses are ignored. This means that $i_{md} = i_d$ and as a result, the d axis is aligned with the rotor flux by forcing $i_d = 0$.

3.1.1 Hysteresis Current Controllers

As said before, an effective way to generate PWM control signals to the inverter is to use hysteresis current controllers (HCCs). This control type, also known as bang-bang control, is intended for the direct control of the motor phase currents, being very simple from a conceptual point of view and quite straightforward to implement. The switching strategy is done by using three hysteresis comparators, each being responsible to control separately the current in its corresponding phase, as shown in Figure 3.2.

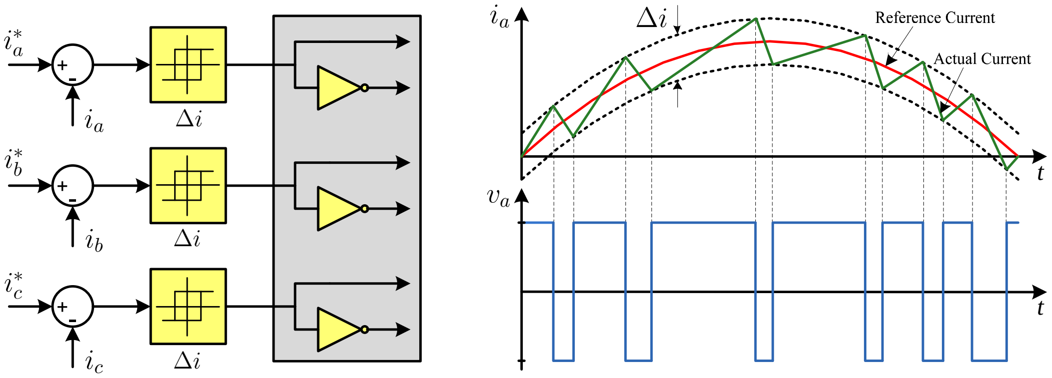

Figure 3.2: Hysteresis current control operating principles.

Each controller determines the semiconductors switching states in each inverter arm in such a way that the corresponding phase current is kept within a defined hysteresis band Δi. The measured motor phase currents are subtracted to their reference signals and the resulting error is fed to the hysteresis comparators. If this error tends to pass the hysteresis band lower limit, the top power switch of the corresponding phase is turned off, turning on the lower one. On the contrary, if the error tends to be greater than the higher limit, the top power switch is turned on and the bottom one is deactivated. In this way, the motor phase currents will be as much sinusoidal as smaller is the hysteresis band. However, this leads to the increasing of the semiconductors switching frequency and consequently, the inverter power losses.

The dynamic performance of this approach is considered to be excellent since maximum voltage values are applied to minimize the errors and it is only limited by the switching speed and load time constant. Furthermore, this technique is also very simple, presents an outstanding robustness, lack of tracking errors and it is very independent of the load parameters. As main disadvantages it can be pointed out its variable switching frequency, the fact that its discrete implementation does not guarantee that the error is strictly limited within the hysteresis band, the lack of interaction between the three phases which limits the generation of zero-voltage vectors and the increased switching losses at lower modulation or motor speed values.

3.2 SVM Vector Control

Figure 3.3 shows the typical block diagram of a RFOC strategy applied to a PMSM using SVM to control the machine phase currents. As it can be seen, the principle of coordinate transformation seen for the HCC vector control scheme is also applied. As a result, the RFOC description previously done is also applied in this case.

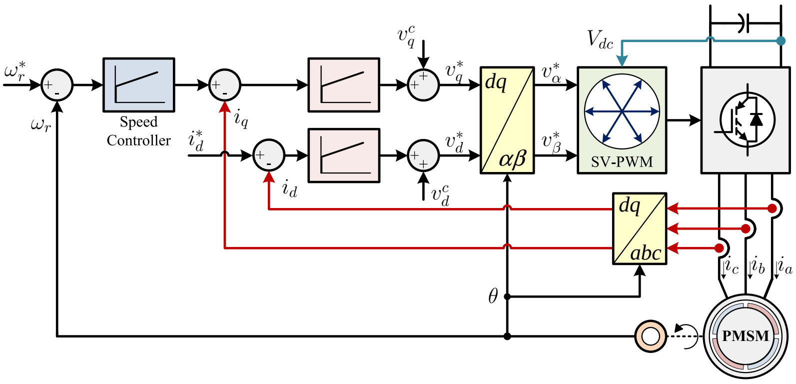

Figure 3.3: Block diagram of the SVM vector control.

The most important difference is that instead of the three motor phase currents are directly controlled, with this technique the current components i_d and i_q are indirectly controlled by controlling the machine voltages. To accomplish this, the errors between the reference and measured dq motor phase currents are fed into PI current controllers, where their outputs correspond to the dq reference voltages. However, according to the voltage equations 2.3 and 2.4, these components are not decoupled from each other since v_d depends on the i_q and the quadrature axis component v_q depends on i_d[3]. This problem can be solved by adding decoupling components to the PI controller outputs:

$$v_d^c = -\omega L_q i_q \tag{3.4}$$

$$v_q^c = \omega L_d i_d + \omega \psi_{PM} \tag{3.5}$$

By doing this feedforward decoupling, it is possible to transform the nonlinear motor voltage model into linear equations which can be controlled by general PI controllers, assuring the decoupling between the dq components required for the vector control.

The $\alpha\beta$ voltage components in the stationary reference frame are obtained from the dq components using the inverse Park transformation defined as:

$$\begin{bmatrix} x_\alpha \\ x_\beta \end{bmatrix} = \begin{bmatrix} \cos(\theta) & -\sin(\theta) \\ \sin(\theta) & \cos(\theta) \end{bmatrix} \begin{bmatrix} x_d \\ x_q \end{bmatrix} \tag{3.6}$$

---

[3] For the sake of simplicity, the iron losses are ignored. As a consequence, $i_d = i_{md}$ and $i_q = i_{mq}$.

At last, the obtained $\alpha\beta$ reference voltages are fed to the space vector modulator that will generate the inverter gate command signals that synthetize voltage waveforms with the required fundamental component.

3.2.1 Space Vector Modulation

Space vector modulation is one of the most widely used techniques for PWM control of power converters in variable speed AC drives. The principle of this PWM strategy is to approximate the required voltage vector by a combination of eight basic switching patterns on a time-sharing basis so that the average value matches with this reference vector.

As said before, this is an advanced technique that comparing with other modulation strategies generates less harmonic content, allows to decrease the inverter switching losses, presents a wide linear modulation range and enables the analysis of three-phase systems as a whole instead of looking at each phase. Comparing with other popular fixed switching frequency techniques, namely SPWM, it increases the output capability without distorting the line-to-line output voltage waveform, which means that it has a more efficient use of the DC link supplying voltage.

Considering the structure of a typical three-phase six switch VSI reproduced in Figure 3.4, the switching states of all IGBTs from T1 to T6 can be defined by the combination of the switching signals S_a, S_b and S_c.

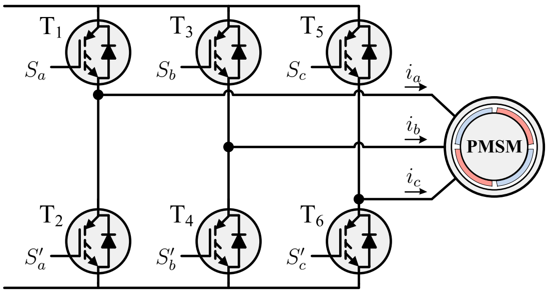

Figure 3.4: Scheme of a typical voltage source inverter feding a PMSM.

As an example, if the upper switch in phase a (T1) is on, the bottom one is off (T2), and the corresponding state is defined as $S_a = 1$. Conversely, $S_a = 0$ means that power switch T1 is off and T2 is on. This assumption is also extended to the remaining cases. Therefore, the relationship between the switching variable vector and the phase-to-phase output voltage vector and the phase (line-to-neutral) output voltage vector is given by:

$$\begin{bmatrix} v_{ab} \\ v_{bc} \\ v_{ca} \end{bmatrix} = V_{dc} \begin{bmatrix} 1 & -1 & 0 \\ 0 & 1 & -1 \\ -1 & 0 & 1 \end{bmatrix} \begin{bmatrix} S_1 \\ S_2 \\ S_3 \end{bmatrix} \tag{3.7}$$

$$\begin{bmatrix} v_a \\ v_b \\ v_c \end{bmatrix} = \frac{V_{dc}}{3} \begin{bmatrix} 2 & -1 & -1 \\ -1 & 2 & -1 \\ -1 & -1 & 2 \end{bmatrix} \begin{bmatrix} S_1 \\ S_2 \\ S_3 \end{bmatrix} \tag{3.8}$$

The vector representations of the motor phase voltages corresponding to the eight switching combinations can be obtained by using the space vector definition. The generated voltage space vector $\overline{v}_s$ is calculated using the machine phase voltages as:

$$\overline{v}_s = \frac{2}{3}\left(v_a + a v_b + a^2 v_c\right) \tag{3.9}$$

where $a = e^{j2\pi/3}$ is the space rotation factor. In practice, this is equivalent to refer abc quantities in a $\alpha\beta$ stationary reference frame. This can be accomplished by using the transform defined as:

$$\begin{bmatrix} x_\alpha \\ x_\beta \end{bmatrix} = \frac{2}{3} \begin{bmatrix} 1 & -\frac{1}{2} & -\frac{1}{2} \\ 0 & \frac{\sqrt{3}}{2} & -\frac{\sqrt{3}}{2} \end{bmatrix} \begin{bmatrix} x_a \\ x_b \\ x_c \end{bmatrix} \tag{3.10}$$

By substituting (3.8) in (3.10), the voltage space vector components can be obtained:

$$\begin{cases} v_\alpha = \frac{2}{3} V_{dc} \left(S_a - \frac{S_b + S_c}{2}\right) \\ v_\beta = \frac{1}{\sqrt{3}} V_{dc} \left(S_b - S_c\right) \end{cases} \tag{3.11}$$

From (3.11) it can be verified that a total of eight voltage vectors are generated (Table 3.1), which can be divided into six active vectors ($\overline{V}_1$ to $\overline{V}_6$) and two zero vectors ($\overline{V}_7$ and $\overline{V}_8$). The nonzero vectors form the axes of a hexagon. The angle between any adjacent two active vectors is 60 degrees and the area between them defines a sector. The zero vectors are at the origin and apply zero voltage to a three phase load (Figure 3.5).

Table 3.1: Basic voltage vectors generated by a normal two-level VSI.

$\overline{V}_x(S_a, S_b, S_c)$	v_a	v_b	v_c	$\overline{v}_s$
$\overline{V}_1(100)$	$\frac{2}{3}V_{dc}$	$-\frac{1}{3}V_{dc}$	$-\frac{1}{3}V_{dc}$	$\frac{2}{3}V_{dc}\angle 0^\circ$
$\overline{V}_2(110)$	$\frac{1}{3}V_{dc}$	$\frac{1}{3}V_{dc}$	$-\frac{2}{3}V_{dc}$	$\frac{2}{3}V_{dc}\angle 60^\circ$
$\overline{V}_3(010)$	$-\frac{1}{3}V_{dc}$	$\frac{2}{3}V_{dc}$	$-\frac{1}{3}V_{dc}$	$\frac{2}{3}V_{dc}\angle 120^\circ$
$\overline{V}_4(011)$	$-\frac{2}{3}V_{dc}$	$\frac{1}{3}V_{dc}$	$\frac{1}{3}V_{dc}$	$\frac{2}{3}V_{dc}\angle 180^\circ$
$\overline{V}_5(001)$	$-\frac{1}{3}V_{dc}$	$-\frac{1}{3}V_{dc}$	$\frac{2}{3}V_{dc}$	$\frac{2}{3}V_{dc}\angle 240^\circ$
$\overline{V}_6(101)$	$\frac{1}{3}V_{dc}$	$-\frac{2}{3}V_{dc}$	$\frac{1}{3}V_{dc}$	$\frac{2}{3}V_{dc}\angle 300^\circ$
$\overline{V}_7(000)$	0	0	0	0
$\overline{V}_8(111)$	0	0	0	0

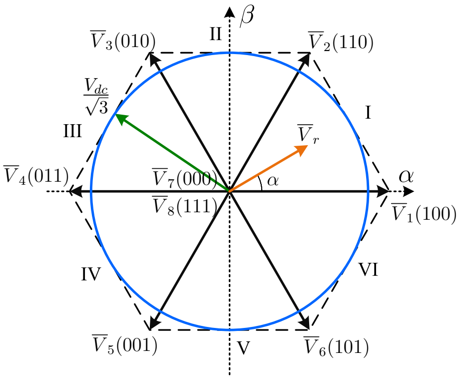

Figure 3.5: Representation of the basic voltage vectors and the rotating reference vector in the complex plane.

The reference voltage vector $\overline{V}_r$, defined by the reference voltage components (v^*_α, v^*_β) calculated by the vector control, can be synthetized through an average relationship between two neighboring active vectors. Zero vectors are used to fill-up the gap to a constant sampling interval. Taking as an example a reference vector in Sector 1, this can be expressed by:

$$T_s\overline{V}_r = t_x\overline{V}_1 + t_y\overline{V}_2 + t_0\overline{V}_0 \tag{3.12}$$

The switching time duration of each vector t_x and t_y and the equivalent zero vector t_0 are given by:

$$\begin{cases} t_x = & \frac{\sqrt{3}\left|\overline{V}_r\right|}{V_{dc}} T_s \sin\left(\frac{\pi}{3} - \alpha\right) \\ t_y = & \frac{\sqrt{3}\left|\overline{V}_r\right|}{V_{dc}} T_s \sin\left(\alpha\right) \\ t_0 = & T_s - t_x - t_y \end{cases} \tag{3.13}$$

The previous equations are also valid for the remaining sectors by knowing in which sector the reference vector is located and by making α corresponding to the angle between the immediately previous basic vector and the reference vector.

Several switching patterns can be generated according to the choice of the zero vectors and the sequence in which the vectors are applied within the switching cycle. The most commonly used are based on a symmetrical distribution of the basic switching vectors since they generate less harmonic distortion. A switching pattern can be considered where every PWM period starts and ends with zero vectors and the amount of $\overline{V}_7$ inserted is the same as that of $\overline{V}_8$. In this case, there will be two zero vectors per T_s so that the zero interval is divided into two equal halves of length $t_0/2$. These half intervals are placed at the beginning and end of every sampling interval. If the half at the beginning is realised as $\overline{V}_7$, that at the end is realised as $\overline{V}_8$, and vice versa. According to this, the SVM voltage vectors sequence and timing plans can be defined, as shown in Table 3.2.

The construction of this symmetrical pulse pattern is accomplished for two consecutive T_s in-

Table 3.2: SVM voltage vectors sequence and timing plan.

Sector	Voltage Vector Sequence	Voltage Vector Timing
I	$\overline{V}_7 \rightarrow \overline{V}_1 \rightarrow \overline{V}_2 \rightarrow \overline{V}_8 \rightarrow \overline{V}_2 \rightarrow \overline{V}_1 \rightarrow \overline{V}_7$	$(t_0/2) \rightarrow (t_x) \rightarrow (t_y) \rightarrow (t_0) \rightarrow (t_y) \rightarrow (t_x) \rightarrow (t_0/2)$
II	$\overline{V}_7 \rightarrow \overline{V}_3 \rightarrow \overline{V}_2 \rightarrow \overline{V}_8 \rightarrow \overline{V}_2 \rightarrow \overline{V}_3 \rightarrow \overline{V}_7$	$(t_0/2) \rightarrow (t_y) \rightarrow (t_x) \rightarrow (t_0) \rightarrow (t_x) \rightarrow (t_y) \rightarrow (t_0/2)$
III	$\overline{V}_7 \rightarrow \overline{V}_3 \rightarrow \overline{V}_4 \rightarrow \overline{V}_8 \rightarrow \overline{V}_4 \rightarrow \overline{V}_3 \rightarrow \overline{V}_7$	$(t_0/2) \rightarrow (t_x) \rightarrow (t_y) \rightarrow (t_0) \rightarrow (t_y) \rightarrow (t_x) \rightarrow (t_0/2)$
IV	$\overline{V}_7 \rightarrow \overline{V}_5 \rightarrow \overline{V}_4 \rightarrow \overline{V}_8 \rightarrow \overline{V}_4 \rightarrow \overline{V}_5 \rightarrow \overline{V}_7$	$(t_0/2) \rightarrow (t_y) \rightarrow (t_x) \rightarrow (t_0) \rightarrow (t_x) \rightarrow (t_y) \rightarrow (t_0/2)$
V	$\overline{V}_7 \rightarrow \overline{V}_5 \rightarrow \overline{V}_6 \rightarrow \overline{V}_8 \rightarrow \overline{V}_6 \rightarrow \overline{V}_5 \rightarrow \overline{V}_7$	$(t_0/2) \rightarrow (t_x) \rightarrow (t_y) \rightarrow (t_0) \rightarrow (t_y) \rightarrow (t_x) \rightarrow (t_0/2)$
VI	$\overline{V}_7 \rightarrow \overline{V}_1 \rightarrow \overline{V}_6 \rightarrow \overline{V}_8 \rightarrow \overline{V}_6 \rightarrow \overline{V}_1 \rightarrow \overline{V}_7$	$(t_0/2) \rightarrow (t_y) \rightarrow (t_x) \rightarrow (t_0) \rightarrow (t_x) \rightarrow (t_y) \rightarrow (t_0/2)$

tervals, being the PWM carrier switching frequency defined as $f_c = f_s/2$.

Analyzing Figure 3.5, it can be also seen that the boundary between linear modulation and over modulation, illustrated by the blue circle, occurs when the amplitude of the reference vector reaches a value equivalent to $0.577V_{dc}$.

Finally, it is worth noting that during the sampling interval, the desired reference vector is approximated in the average sense. However, instantaneously, the actual vectors produced by the inverter are different from the reference vector which means that current harmonics are always present.

3.3 Direct Torque Control

As mentioned before, DTC is also a control strategy that can be applied to PMSMs, presenting a performance level similar to the one obtained by vector control. The basic principle of DTC is to control the motor torque by controlling the angle between the stator flux linkage and the rotor flux linkage. This can be demonstrated by the PMSM electromagnetic torque expression in the stator reference frame:

$$T_e = \frac{3p\left|\overline{\psi}_s\right|}{4L_dL_q}\left(2\left|\overline{\psi}_{PM}\right|L_q\sin\delta - \left|\psi_s\right|\left(L_q - L_d\right)\sin 2\delta\right) \tag{3.14}$$

In the DTC system, both electromagnetic torque and stator flux are directly and separately controlled. The control scheme of this technique applied to a PMSM is shown in Figure 3.6.

Since the PMSM rotor flux linkage is constant due to the magnets, the electromagnetic torque is controlled by varying the stator flux amplitude and the load angle δ. This is accomplished through the correct selection of voltage space vectors which allows to control the stator magnetic flux amplitude and direction.

Considering the typical three-phase VSI, the generated voltage space vectors can be calculated

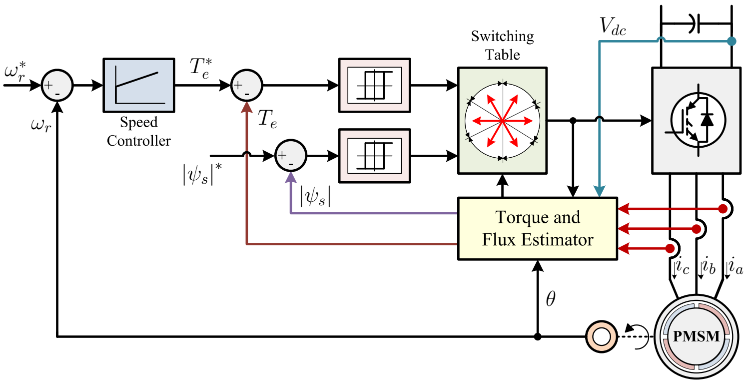

Figure 3.6: Block diagram of the direct torque control.

using equation (3.11). From this, six active vectors and two null vectors are generated, as described in Table 3.1 and Figure 3.5. Accordingly, it is possible to control the amplitude, moving direction and moving speed of the stator flux linkage by selecting the proper voltage space vector.

For the convenience of selecting these vectors, it is desired to divide the space vector plane into six sectors, as shown in Figure 3.7.

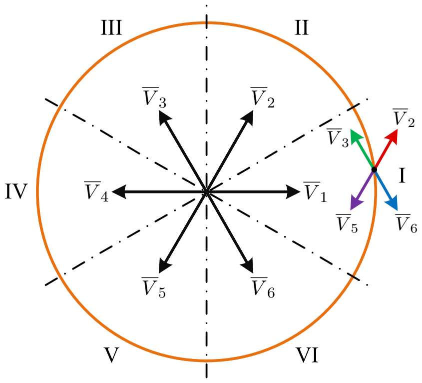

Figure 3.7: Voltage vectors selection for DTC.

For instance, if the stator flux is located in sector I, and it is required to increase the torque in order to achieve a counter clockwise rotation, $\overline{V}_2$ should be used to increase the stator flux linkage amplitude and, otherwise, $\overline{V}_3$ to decrease its amplitude. On the contrary, if the stator flux is moving in a clockwise direction (negative torque) also in the same region, $\overline{V}_6$ should be used to increase the amplitude and $\overline{V}_5$ to decrease it.

As far as induction machines are concerned, the stator flux is determined uniquely by the stator voltage. Consequently, the selection of zero vectors makes the stator flux linkage vector to stand still in the same position where it was in without producing torque, so the motor is controlled in order to run and stop alternately. However, for PMSMs the interaction between the stator voltage and the rotor magnets must be taken into account. Since the permanent magnets are always rotating, the stator flux linkage still exists even if null vectors are used. Consequently, torque will be produced which makes the motor still running. As a result, zero voltage space vectors are normally not used in the DTC of PMSMs [77]-[82].

Considering all this, the optimum switching table for the DTC applied to a PMSM is presented in Table 3.3. ‘Flux’ and ‘Torque’ are the logic variables denoting the need of flux linkage and torque, respectively, in which the superscript ‘-’ means the need to decrease and ‘+’ means the need to increase.

Table 3.3: DTC voltage vectors switching table.

Flux	Torque	Section					
		I	II	III	IV	V	VI
F^-	T^-	$\overline{V}_5$	$\overline{V}_6$	$\overline{V}_1$	$\overline{V}_2$	$\overline{V}_3$	$\overline{V}_4$
	T^+	$\overline{V}_3$	$\overline{V}_4$	$\overline{V}_5$	$\overline{V}_6$	$\overline{V}_1$	$\overline{V}_2$
F^+	T^-	$\overline{V}_6$	$\overline{V}_1$	$\overline{V}_2$	$\overline{V}_3$	$\overline{V}_4$	$\overline{V}_5$
	T^+	$\overline{V}_2$	$\overline{V}_3$	$\overline{V}_4$	$\overline{V}_5$	$\overline{V}_6$	$\overline{V}_1$

This table takes into account that when the torque is lower than its reference value, a voltage vector is applied in order to make the stator flux linkage vector rotate in its original direction. Due to the rotor mechanical inertia, the rotor flux instantaneous velocity could be much slower than the stator flux, which obviously causes the angle δ to increase instantaneously, achieving this way a very fast torque dynamic control.

After defining the algorithm for the torque and flux estimation, these values are used in a double closed-loop topology, providing the feedback signals that are compared with their respective reference values. The errors are then fed into hysteresis comparators that give the output control signals corresponding to the need of decreasing and increasing the torque. Combining this information with the stator flux vector position, the optimum voltage space vector is selected, allowing this way to control the amplitude, rotating speed and direction of the stator flux linkage vector, leading to a fast torque response.

3.3.1 Torque and Flux Estimation

The torque and flux estimation algorithm assumes a critical role in a DTC strategy and it is important for the drive correct operation. Several research work has been done in this field and the majority of the existing methods can be broadly classified as voltage model based methods and current model based methods. A brief description of these methods is presented in the next subsections.

3.3.1.1 Voltage Model Based Methods

The flux estimation using the PMSM voltage model equations is widely used and it is very simple to implement. This can be simply accomplished by integrating the motor back-EMF, using the motor voltages and currents:

$$\psi_\alpha = \int_0^t (v_\alpha - R_s i_\alpha)\, dt + \psi_{\alpha|t=0} \tag{3.15}$$

$$\psi_\beta = \int_0^t (v_\beta - R_s i_\beta)\, dt + \psi_{\beta|t=0} \tag{3.16}$$

The voltage and current space vector components can be directly obtained by measuring the PMSM voltages and phase currents and applying the transformation given by (3.10). Regarding the voltage space vector, a different way can be applied by using the inverter switching states (S_a, S_b and S_c). In this case, the voltage components can be directly calculated using (3.11).

One advantage of this technique is the low independence on the machine parameters since only the stator resistance is used. Since its value also varies with the machine temperature, online correction methods can also be implemented to improve the flux estimation accuracy [117]-[118]. Another advantage is the independence of the rotor position, which makes DTC an inherent sensorless control technique. Nevertheless it must be noticed that unlike induction motors, the initial value of the stator flux vector is not zero in PMSMs. As a result it has to be measured or estimated, preferably in a sensorless way [119]-[122].

In practice, other problems arise from this flux estimation method since a pure integrator has DC drift problems. These issues can be strongly attenuated by using low-pass filters and more advanced closed-loop compensation schemes [110]-[116].

3.3.1.2 Current Model Based Methods

In order to avoid the problems associated with the integration of the back-EMF, the stator flux linkage can be calculated by using the current model. This method takes into account the PMSM dynamic equations that express the relation between the stator flux linkage and the motor phase currents, referred to the $\alpha\beta$ reference frame:

$$\psi_\alpha = L_d i_\alpha + \psi_{PM} \cos\theta \tag{3.17}$$

$$\psi_\beta = L_q i_\beta + \psi_{PM} \cos\theta \tag{3.18}$$

It can be verified that the open-loop current model defined by these equations is independent from the stator resistance and an offset will not lead to drift in the flux estimation. However it is dependent on the stator inductances and the rotor position. The resulting need for a position sensor is considered as a major disadvantage, especially in DTC which is an inherently position sensorless method. The stator inductances and rotor flux are also variable as they depend on the magnetic saturation in the machine. Nevertheless, if a position feedback sensor is already required for closed-loop speed control, this method is preferable. This means that it will also be very stable and have smooth low-speed operation, compared to the voltage model based method.

3.4 Simulation Results

In order to theoretically validate the three considered control strategies applied to variable speed PMSM drives, they were implemented using the Matlab/Simulink environment, in association with the SimPowerSystems blockset software toolbox.

The modeling of the PMSM was carried out taking into account the developed dynamic model previously described in Section 2.1. The used PMSM is a 2.2 kW 1500 rpm 50 Hz connected in a star configuration. The detailed machine parameters as well as other relevant simulation aspects are presented in Appendix A.

For all the considered cases, the DC bus is fed by a three-phase full-bridge diode rectifier, connected to a typical 400 V/50 Hz mains supply. All the results are obtained for a reference mechanical speed and load torque equivalent to 50% of the PMSM corresponding rated values (750 rpm and 7 Nm).

3.4.1 HCC Vector Control

The PMSM closed-loop speed control based on the HCC vector control formerly discussed was implemented using the Matlab/Simulink software. As sensor feedback signals, the control system requires the three motor phase currents and the actual mechanical speed/position, generating the six gate command signals for each inverter IGBT.

Regarding the hysteresis controllers, they were configured in order to achieve a hysteresis band Δi equivalent to 6% of the PMSM rated current[4].

Figure 3.8 presents the time-domain waveforms of the PMSM phase currents and one phase voltage for steady-state operation at 750 rpm and 7 Nm under normal operating conditions.

From Figure 3.8a it can be verified that the PMSM is supplied by a balanced three-phase current system, where the phase currents are sinusoidal with a phase shift of 120°. They also present the high frequency noise imposed by the HCC, leading to a well-defined ripple band.

The time-domain waveform of the phase b voltage presented in Figure 3.8b shows the typical characteristics when a three-phase load is fed by a VSI. As expected, it can be seen the high-frequency switching content within two distinct voltage levels that correspond to ±1/3 and ±2/3 of the DC link voltage V_{dc}.

---

[4] Please see the PMSM nameplate parameters in Appendix B.

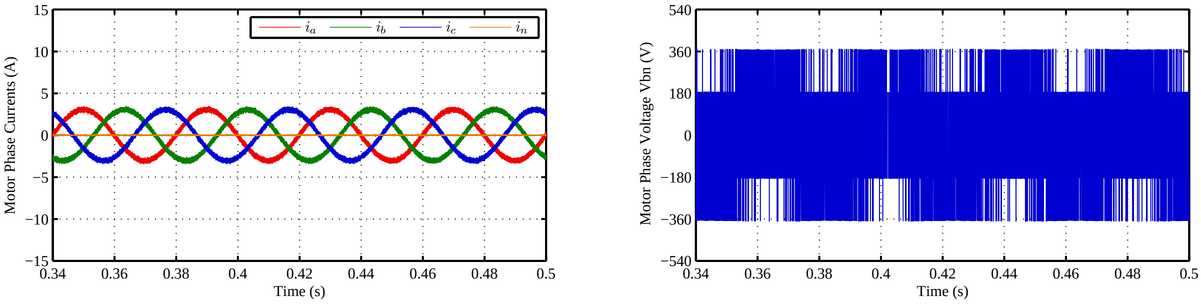

(a) (b)

Figure 3.8: Simulation results of the time-domain waveforms for a HCC vector control strategy: (a) motor phase currents; (b) phase *b* voltage.

3.4.2 SVM Vector Control

For the SVM vector control, the implemented control system needs the feedback of the three motor phase currents, the actual mechanical speed/position and the DC bus voltage in order to correctly generate the six IGBT gate signals.

Considering the SVM technique, a switching frequency of 5.5 kHz was assumed.

Figure 3.9 presents the time-domain waveforms of the motor phase currents and one phase voltage for steady-state operation at 750 rpm and 7 Nm under normal operating conditions.

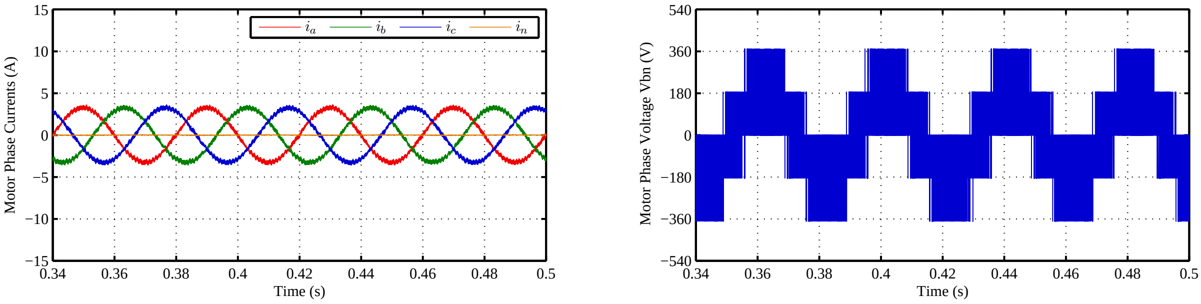

(a) (b)

Figure 3.9: Simulation results of the time-domain waveforms for a SVM vector control strategy: (a) motor phase currents; (b) phase *b* voltage.

Regarding the motor phase currents, in a similar way to the previous case, they also present a sinusoidal shape with a phase shift of 120º between them. However, comparing to the HCC vector control, it can be verified that the high-frequency noise introduced is less because of the superior modulation strategy.

From Figure 3.9b it can be also concluded that because of the fixed switching frequency, the harmonic content of the PMSM phase voltages is greatly reduced, contributing to a more sinusoidal waveform. As a result, the same voltage levels equivalent to ±1/3 and ±2/3 of the DC link voltage are clearly defined.

3.4.3 Direct Torque Control

The DTC strategy applied to PMSMs was implemented and analyzed. For the torque and flux estimators, two options are available according to the use of the voltage model based methods or current model based methods. Since a position feedback device is already available, the current model based method was chosen in this work.

Considering this, the implemented DTC control system feedback signals are the three motor phase currents and the actual mechanical speed/position.

The torque and flux hysteresis controllers were configured with a hysteresis band equivalent to 2% of their corresponding rated values.

Figure 3.10 presents the time-domain waveforms of the PMSM phase currents and one phase voltage for DTC under normal operating conditions.

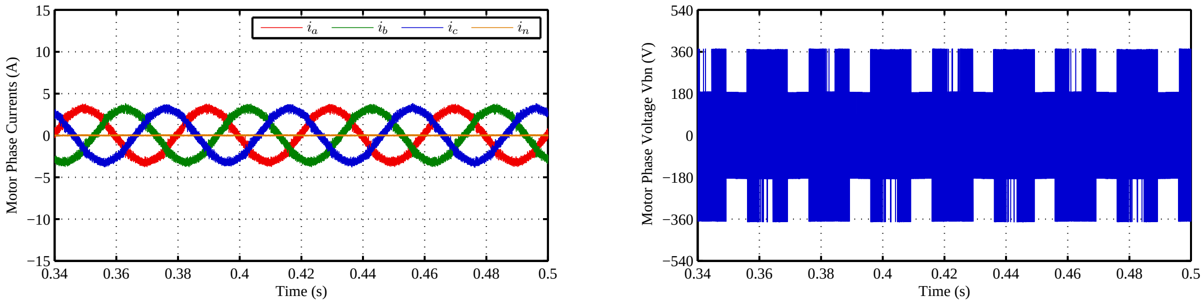

(a) (b)

Figure 3.10: Simulation results of the time-domain waveforms for a DTC control strategy: (a) motor phase currents; (b) phase b voltage.

As expected and in a similar way to the other cases, the three motor phase currents are also sinusoidal, presenting high-frequency noise. Nevertheless, due to the inherent large torque ripple that characterizes the DTC, it can be seen that motor phase currents present a higher harmonic distortion.

Regarding the motor phase voltage shown in Figure 3.10b, it is similar to the one obtained for the HCC vector control since these techniques do not have a fixed switching frequency, generating a waveform with a larger harmonic distortion.

3.5 Experimental Validation

The considered control strategies for variable speed PMSM drives described in this chapter were also experimentally validated through their implementation in a laboratory prototype. The experimental setup basically comprises a PMSM coupled to a four-quadrant test system, a Semikron SKiiP three-phase diode bridge rectifier and three-phase VSI, a dSPACE DS1103 digital controller and two precision digital power analysers. The voltage and current signals as well as all the IGBTs gate commands are connected to the dSPACE controller trough interface and isolation boards. Two digital power analyzers Yokogawa WT3000 were connected in series in the power circuit in order to measure important variables. A shematic block diagram of the experimental setup is depicted in Figure 3.11.

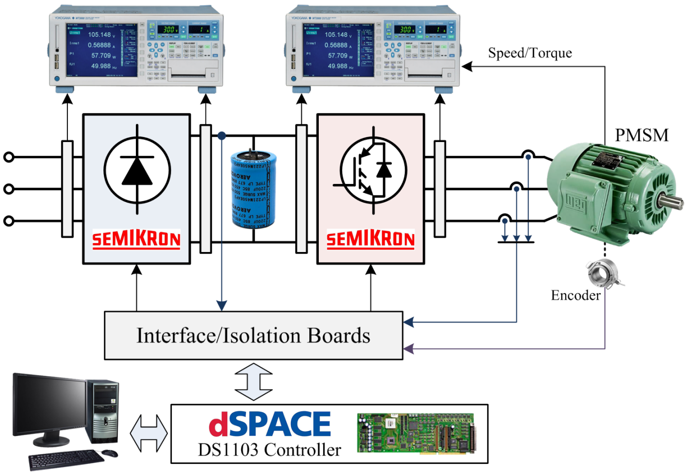

Figure 3.11: Block diagram with the main components of the experimental setup.

The used PMSM is a 2.2 kW 1500 rpm 50 Hz machine, with the same parameters used for the simulation results. Its nameplate parameters are presented in Appendix B.

The real-time interface board library for the DS1103 controller is designed as a common Matlab/Simulink Blockset that provides blocks to implement the I/O capabilities in Simulink models.

All the control strategies were implemented in the DS1103 digital controller board, using a sampling time of 25 μs. The rotor position is obtained by an incremental encoder with 1024 pulses per revolution. Further details about the experimental setup are presented in Appendix B.

The drive is fed by a mains supply with a typical 400 V/50 Hz. In a similar way to the simulation results, all tests were performed for a reference mechanical speed of 750 rpm and 7 Nm of load torque. The same simulation parameters used for the hysteresis controllers in HCC vector control and DTC and the same switching frequency of SVM are also assumed for the experimental tests.

For the electromagnetic torque analysis, a parameter called Total Waveform Oscillation (TWO) is defined in order to quantify its ripple/oscillation:

$$\mathrm{TWO} = \frac{\sqrt{T_{e_{\mathrm{rms}}}^2 - T_{e_{\mathrm{dc}}}^2}}{|T_{e_{\mathrm{dc}}}|} \times 100\% \tag{3.19}$$

where $T_{e_{\mathrm{rms}}}$ and $T_{e_{\mathrm{dc}}}$ stand for the electromagnetic torque rms and average values, respectively.

3.5.1 HCC Vector Control

Figure 3.12 presents the experimental results of the time-domain waveforms of the PMSM phase currents and one phase voltage for HCC vector control under normal operating conditions.

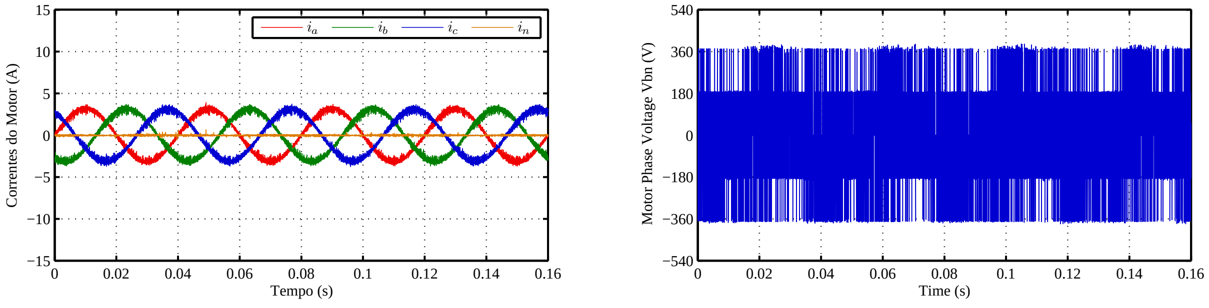

(a) (b)

Figure 3.12: Experimental results of the time-domain waveforms for a HCC vector control strategy: (a) motor phase currents; (b) phase b voltage.

Comparing these results with the ones obtained from the computational simulations shown in Figure 3.8, it can be seen that they are very similar to each other, proving that there is a very good agreement between the theoretical and practical results.

Regarding the electromagnetic torque developed by the machine under these circumstances, Figure 3.13 presents its time-domain waveform.

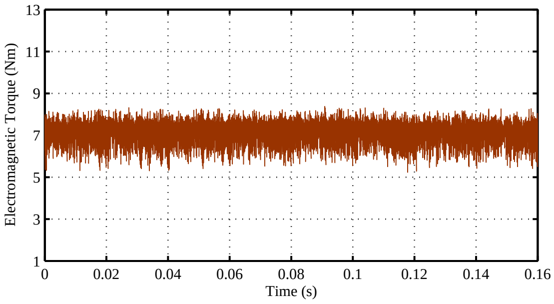

Figure 3.13: Experimental results of the time-domain waveform of the PMSM electromagnetic torque for a HCC vector control.

As expected, it can be verified that the average value is approximately equal to the imposed load torque. Since the electromagnetic torque is directly related to the motor phase currents, it also presents high-frequency ripple that is proportional to the phase currents ripple. As a result, a TWO value of 8.66% is obtained for this case.

Finally, it is also possible to analyze the complex representation of the inverter generated voltage space vectors, as shown in Figure 3.14.

From this figure it can be clearly identified the six active vectors and the null ones, in accordance to the theoretical predictions shown in Figure 3.5. It must be noticed that in practice, the motor

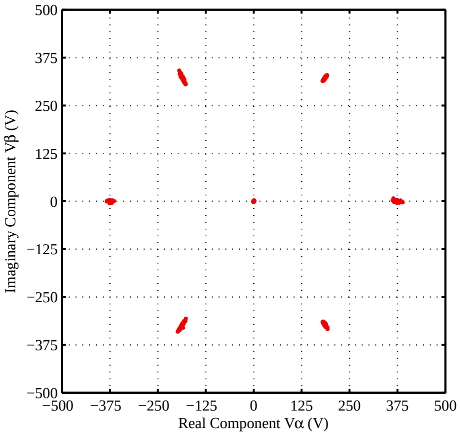

Figure 3.14: Experimental results of the PMSM phase voltages representation in the complex plane for a HCC vector control strategy.

phase voltages present some voltage spikes due to the inverter switching transients and the inherent noise introduced by the working system. As a consequence, other points appear around the principal voltage vector coordinates.

3.5.2 SVM Vector Control

The experimental results regarding the time-domain waveforms of the motor phase currents and phase voltage for a SVM control strategy are presented in Figure 3.15.

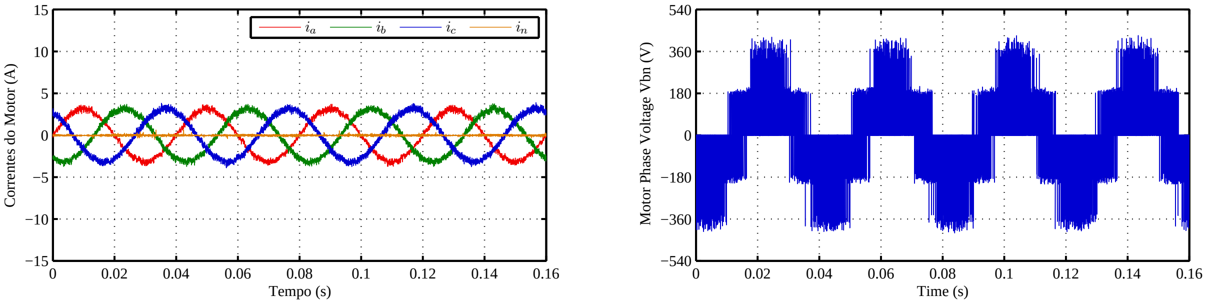

(a) (b)

Figure 3.15: Experimental results of the time-domain waveforms for a SVM vector control strategy: (a) motor phase currents; (b) phase b voltage.

By analyzing these results and comparing them with the equivalent ones obtained from the computational simulations, it is also clear that they are very similar, demonstrating that the theoretical results are in accordance with the experimental ones.

Figure 3.16 presents the time-domain waveform of PMSM electromagnetic torque for the SVM vector control under steady-state operation.

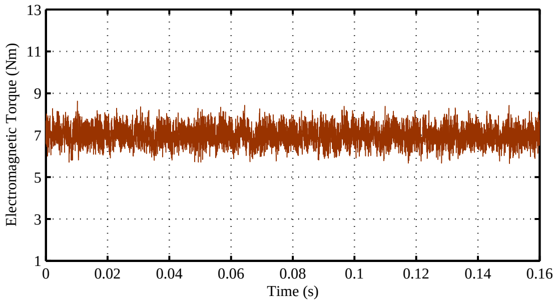

Figure 3.16: Experimental results of the time-domain waveform of the PMSM electromagnetic torque for a SVM vector control.

Once more, the generated electromagnetic torque presents an average value approximately equal to the load torque, including the high-frequency noise due to the harmonic content present in the motor phase currents. The oscillating content can be represented by the TWO factor, achieving a value of 6.84%.

Regarding the complex representation of the PMSM phase voltages, Figure 3.17 presents the corresponding coordinates of the generated voltage vectors.

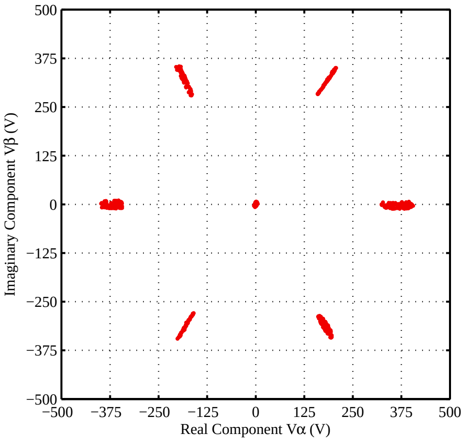

Figure 3.17: Experimental results of the PMSM phase voltages representation in the complex plane for a SVM vector control strategy.

The six active voltage vectors and the null vectors are also clearly recognizable in this figure. In this case, the voltage spikes presented in the motor phase voltages are more noticeable, leading to a more dispersion of voltage vectors around the expected main vectors theoretical coordinates.

3.5.3 Direct Torque Control

Figure 3.18 presents the time-domain waveforms of the PMSM phase currents and one phase voltage for the DTC under normal operating conditions.

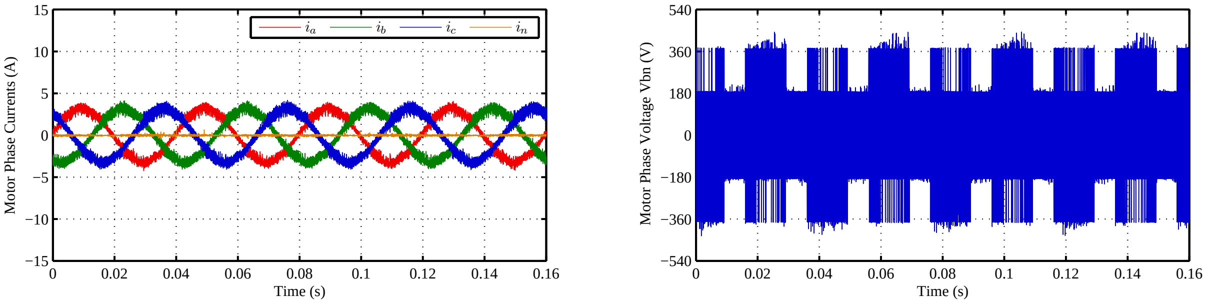

(a) (b)

Figure 3.18: Experimental results of the time-domain waveforms for a DTC control strategy: (a) motor phase currents; (b) phase *b* voltage.

Once more, the obtained experimental results for this control strategy are also in a very good agreement with the simulation results show in Figure 3.10.

Considering the electromagnet torque analysis, Figure 3.19 presents its time-domain waveform for steady-state operation at 750 rpm and 7 Nm.

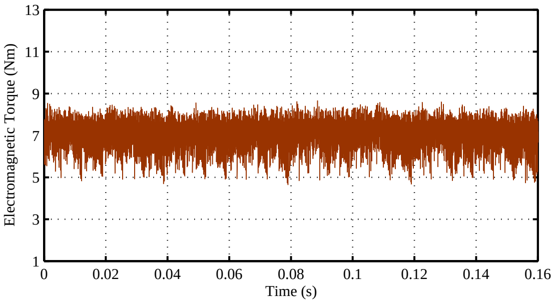

Figure 3.19: Experimental results of the time-domain waveform of the PMSM electromagnetic torque for a DTC control strategy.

In a similar way to the previous cases, the average value corresponds to approximately the load torque level. However, comparing with the other control strategies, it can be seen that the high-frequency noise is larger, leading to a TWO value of 10.89%.

The complex representation of the motor phase voltages is illustrated in Figure 3.20.

The same theoretically predicted active vectors are also clearly defined in the complex plane. Once more, the voltage spikes lead to the arising of voltage vectors spread around the coordinates of the main vectors. It is worth noticing the absence of null vectors since the implemented DTC strategy uses a two level hysteresis controller for the electromagnetic torque. Consequently, only the six active voltage vectors are applied to the PMSM.

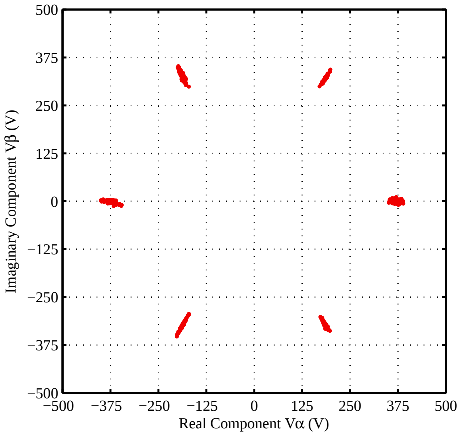

Figure 3.20: Experimental results of the PMSM phase voltages representation in the complex plane for a DTC control strategy.

3.6 Final Remarks

The most commonly used control strategies applied to PMSM drives were presented and briefly described in this paper through an extensive literature survey, showing their main advantages and drawbacks, as well as main features.

Then, the three most used control strategies for closed-loop high-performance PMSM drives were presented and described in a more detailed way. Their implementation philosophy was explained and their main technical and mathematical fundamentals were addressed.

Simulation and experimental results were presented regarding the drive system analysis under normal operating conditions for the three considered control techniques. The obtained results allow to demonstrate an excellent agreement between the theoretical results obtained from the computational simulations and the experimental ones, obtained from the laboratory tests.

As a global evaluation, for the considered operating conditions, the implemented SVM vector control allows to achieve lower currents distortion and electromagnetic torque ripple, whereas DTC presents the worst steady-state performance. A more complete and detailed analysis is later performed in Chapter 7.

Chapter 4

Faulty Operation Analysis

In order to develop a fault-tolerant drive, it is very important to know in advance how the system behaves under the presence of a failure. Therefore, from the drive faulty operation analysis it is possible to obtain relevant information such as on how the main control variables behave, the maximum values that they reach, how the fault affects the available output power and if it is necessary to apply special protection measures. This information is extremely useful for the correct design of fault diagnostic methods and algorithms, to the development of special hardware protection devices and allows to predict how the entire system will react under unexpected operating conditions.

Some research work on this field can be found in the literature regarding the fault analysis of several failures that can affect PMSM variable speed drives. In [123] it was considered the faulty operation analysis of PMSM drives during flux weakening operation. Under this specific conditions, the resulting phase EMF can be extremely high. As a consequence, the effects on currents, voltages and torque of different drive failures are investigated, being this information used as a starting point for a successful design of an effective protection system and a fault-tolerant control.

The analysis of a PMSM drive response to a single phase open-circuit fault was addressed in [124]-[125]. This fault results in rotational electromagnetic asymmetry on both the stator and rotor, which makes it difficult to analyze using classical dq transformation techniques. As a consequence, a new synchronous-frame machine model that is capable of handling this highly asymmetrical fault condition, including the effects of magnetic saturation, is presented.

The steady-state response of a PMSM drive to symmetrical and asymmetrical short-circuit faults, including the effects analysis of the magnetic saturation was presented in [126]. The simulation and experimental results proved that single-phase asymmetrical short-circuit faults produce more severe fault responses with high pulsating torque and a significant threat of rotor demagnetization.

Using the finite element analysis, a detailed fault analysis was performed for a brushless PM motor [127]. The transient behavior of voltages, currents, electromagnetic torque and mechanical speed was considered for three types of fault conditions, namely for a single phase open-circuit fault, phase-to-phase terminal short-circuit, and internal turn-to-turn short-circuit.

Simulation models were developed in order to allow the fault analysis in PMSM drives [128]. Several fault types such as single-phase open-circuit, single-phase and three-phase short-circuit, uncontrolled generation, and switch-on failure of one transistor were considered.

In [129] a simple dynamic model for a PMSM with inter-turn winding fault is derived. The comparison of the results obtained by the simulation model and experimental results allowed to verify the precision of the proposed dynamic model. Beyond this fault type, in [130] it was also considered the behavior analysis for a power switch open-circuit fault. For both cases, a fault model of an inverter-fed PMSM is derived using the line voltage.

The analysis of power switch open-circuit faults and single phase open-circuit faults in a vector controlled inverter-fed PMSM drive was discussed in [131]. Through the evaluation of some key parameters such as motor efficiency, electromagnetic torque oscillation, power factor and currents harmonic distortion, it was concluded that a single phase open-circuit fault has a greater negative impact on the PMSM performance than a single power switch open-circuit failure. The same conclusion was obtained for the faulty operation analysis of a PMSM drive with a DTC control strategy [132].

The real-time simulation and analysis of a PMSM drive in different faulty modes was also addressed in [133]. A validation of the developed model against an actual drive in free-running, dynamic braking and open-phase modes was performed.

The impact of inverter single power switch open-circuit faults and single phase open-circuit faults in the overall performance of a PMSM drive was addressed in [134]. The obtained results allowed to prove that a single phase open-circuit fault contributes to worst drive performance, justified by the lowest overall efficiency, rather than a single IGBT open-circuit failure. With respect to the mains supply side, both the considered faulty operating conditions cause the arising of interharmonics components on the mains supply phase currents and voltages and the decrease of the drive power factor [135].

In order to diagnose faults in PMSMs for electric traction applications, a finite-element model of PMSM with capability for partial demagnetization faults simulation and stator interturn faults was considered in [136].

4.1 Simulation Results

The drive faulty behavior analysis was firstly performed through several computational simulations. The Matlab/Simulink programming environment together with the SimPowerSystems blockset was again used to implement the PMSM drive system mathematical models. The same conditions and parameters defined for the normal operation analysis described in the previous chapter were also used.

In order to simulate an open-circuit fault in an inverter IGBT, the corresponding gate command signal was removed, making impossible to that semiconductor to switch on. Nevertheless, it must be noticed that the antiparallel diode still remains connected.

All the results are obtained for an open circuit-fault in IGBT T1 and for a PMSM reference mechanical speed of 750 rpm and for a load torque equal to 7 Nm.

4.1.1 HCC Vector Control

Figure 4.1 presents the simulation results regarding the time-domain waveforms of the PMSM phase currents and electromagnetic torque for an open-circuit fault in IGBT T1.

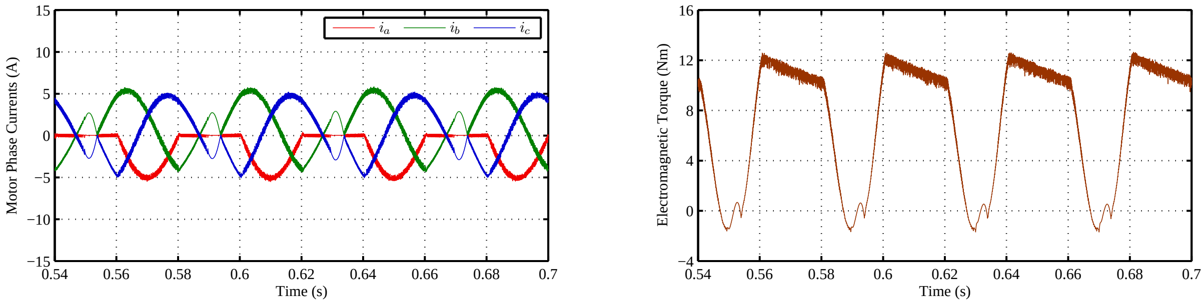

(a) (b)

Figure 4.1: Simulation results of the time-domain waveforms for a HCC vector control strategy with an open-circuit fault in IGBT T1: (a) motor phase currents; (b) electromagnetic torque.

Comparing all the motor phase currents, it is possible to verify that due to this fault type, the PMSM phase currents do not have a sinusoidal shape anymore (Figure 4.1a). As the opened power switch T1 corresponds to the upper IGBT in the inverter phase a, the current in this phase will only take negative values. In addition, DC components are introduced, which contribute to an increase of the copper losses. This fault also has a negative impact on the currents of the healthy phases, leading to a more distorted waveform.

The results presented in Figure 4.1b show that the PMSM electromagnetic torque waveform is no longer constant. Beyond the DC component, it presents now a noticeable pulsating nature. As the developed electromagnetic torque is directly related to the motor phase currents, their distorted nature contributes to an oscillating electromagnetic torque, with the same fundamental frequency.

4.1.2 SVM Vector Control

Considering now the behavior analysis for a SVM vector control strategy, Figure 4.2 presents the time-domain waveforms of the motor phase currents and electromagnetic torque for an open-circuit fault in IGBT T1.

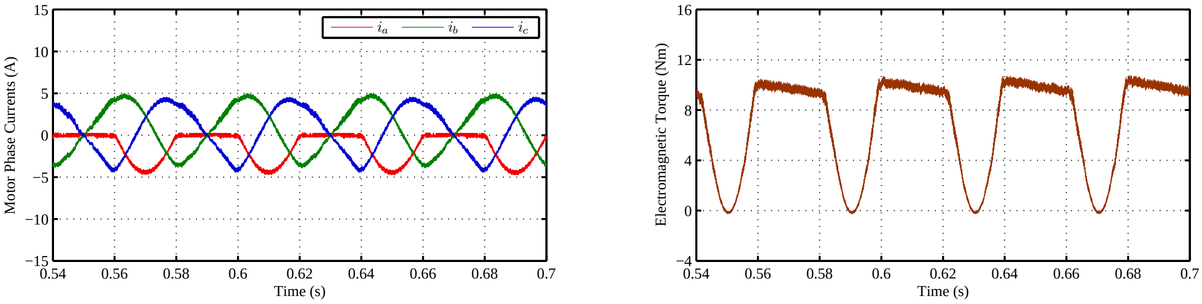

(a) (b)

Figure 4.2: Simulation results of the time-domain waveforms for a SVM vector control strategy with an open-circuit fault in IGBT T1: (a) motor phase currents; (b) electromagnetic torque.

In this case, it can be also seen that there is current flowing in phase a only during each negative half-cycle since the faulty IGBT does not allow a positive current flow. The fault in the inverter phase a also influences the remaining phases, contributing to the increase of their harmonic distortion.

The currents distortion also directly affects the PMSM electromagnetic torque, leading to the generation of undesired oscillations at the same frequency.

4.1.3 Direct Torque Control

The simulation results obtained for the faulty operation with DTC are also very similar to the previous ones. The time-domain waveforms of the PMSM phase currents and electromagnetic torque for an open-circuit fault in IGBT T1 are shown in Figure 4.3.

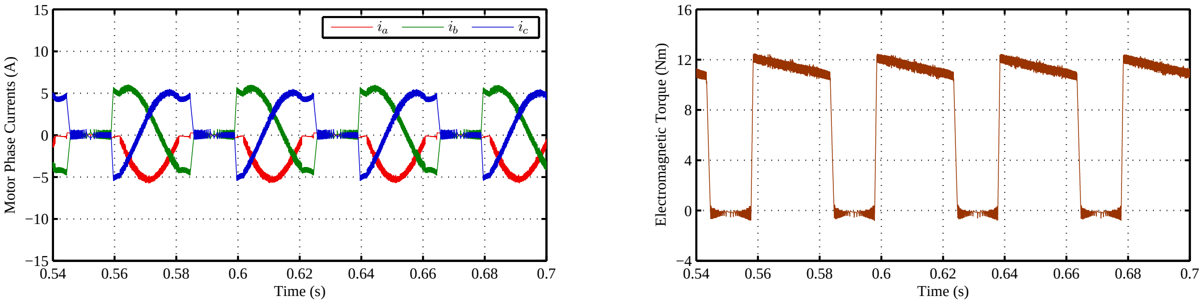

(a) (b)

Figure 4.3: Simulation results of the time-domain waveforms for a DTC control strategy with an open-circuit fault in IGBT T1: (a) motor phase currents; (b) electromagnetic torque.

The introduced fault also has a similar effect on the PMSM phase currents, inhibiting the phase a current flow during the positive half-cycle, and distorting the currents on the remaining healthy ones.

As far as the electromagnetic torque is concerned, it can be verified that the fault leads to the generation of a pulsating waveform, at the same frequency of the motor phase currents. Furthermore, due to the specific characteristics of the DTC, the waveform is similar to a square wave, presenting zero torque values during noticeable time intervals.

4.2 Experimental Validation

For the experimental validation of the PMSM drive behavior under inverter single power switch open-circuit faults, the same laboratory setup and conditions previously described in Section 3.5 were also considered.

In a similar way to the simulation results, open-circuit faults were introduced by removing the IGBT gate command signals for the desired power switch. Once more, it must be noticed that the corresponding antiparallel diode still remains connected.

All the laboratory results were also obtained considering a fault in IGBT T1 and assuming a reference mechanical speed of 750 rpm and a load torque equal to 7 Nm.

In order to evaluate the currents harmonic content, a Total Waveform Distortion (TWD) factor is defined:

$$\mathrm{TWD} = \frac{\sqrt{I_{\mathrm{rms}}^2 - I_1^2}}{I_1} \times 100\% \tag{4.1}$$

being I_{rms} the current total rms value and I_1 its corresponding rms value of the fundamental component. This parameter is more advantageous than the Total Harmonic Distortion (THD) since it takes into account all the interharmonic components as well as the undesired DC component.

4.2.1 HCC Vector Control

Considering first the HCC vector control strategy, Figure 4.4 presents the time-domain waveforms of the PMSM phase currents and their corresponding spectrograms for an inverter open-circuit fault in IGBT T1.

By analyzing the time-domain waveforms, it can be seen that the experimental results are virtually equal to the ones obtained from the computational simulations. As the IGBT T1 is in open-circuit, current flow in phase a is only possible during the negative half-cycle. From its corresponding spectrogram, a large DC component is clearly observed, contributing to a relatively high waveform distortion, represented by the large TWD of 100.48%.

Regarding the currents on the healthy phases, they are also negatively affected by the fault, leading to the appearance of a DC component and harmonics multiple of the fundamental component at 25 Hz. Nevertheless, lower TWD values are obtained since their fundamental component is much more significant comparing to the one of phase a current.

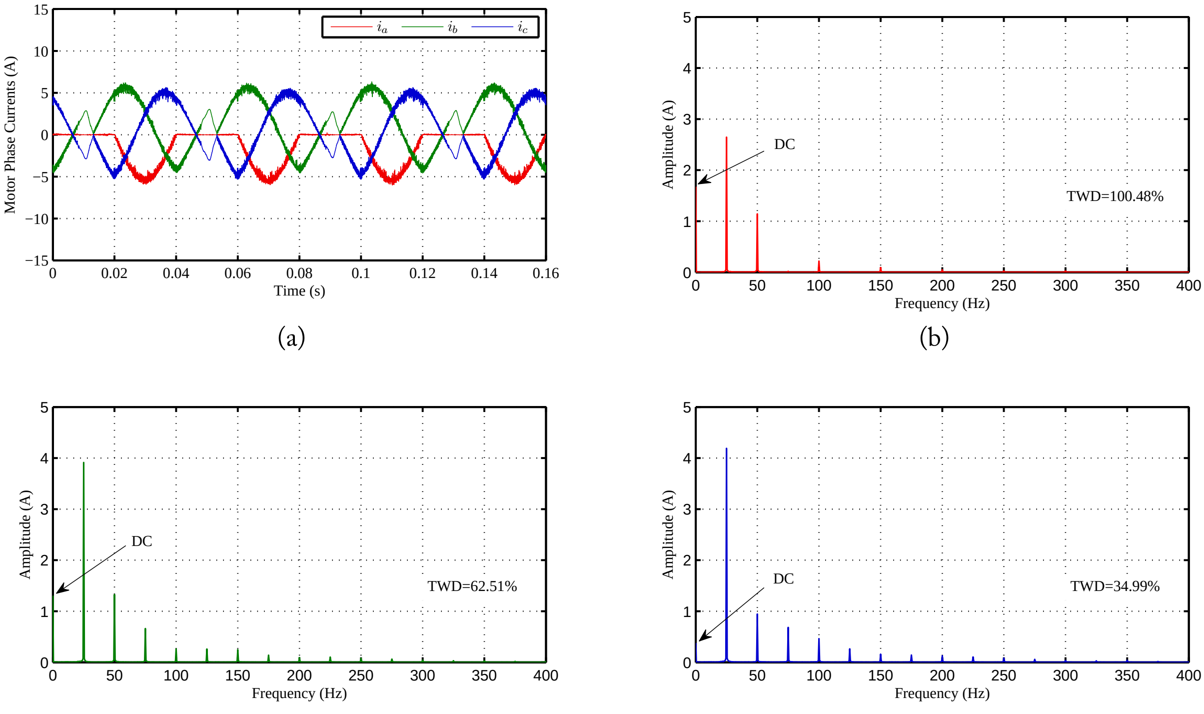

(a) (b)

(c) (d)

Figure 4.4: Experimental results of the PMSM phase currents for a HCC vector control strategy with an open-circuit fault in IGBT T1: (a) time-domain waveforms; (b) phase a current spectrogram; (c) phase b current spectrogram; (d) phase c current spectrogram.

Regarding the electromagnetic torque analysis, Figure 4.5 presents its time-domain waveform as well as its corresponding spectrogram.

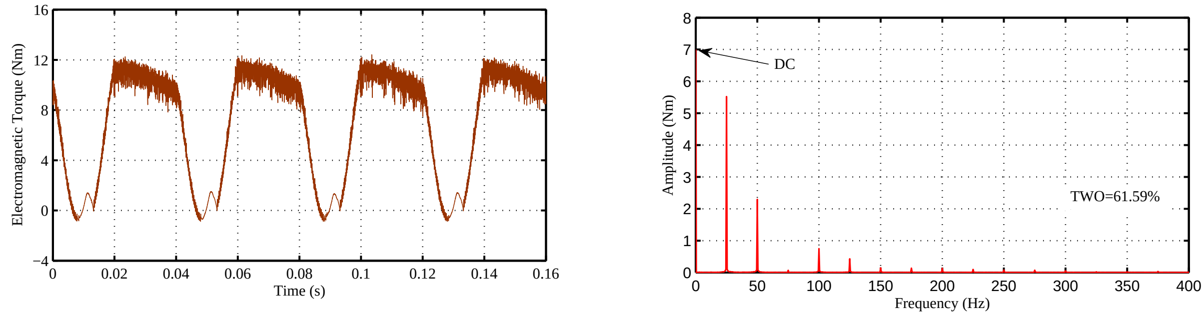

(a) (b)

Figure 4.5: Experimental results of the PMSM electromagnetic torque for a HCC vector control strategy with an open-circuit fault in IGBT T1: (a) time-domain waveform; (b) spectrogram.

Once more, comparing with the equivalent simulations results, it can be verified a great agreement between the theoretical and experimental results. The spectral analysis also shows the pulsating nature of the generated electromagnetic torque at a fundamental frequency equal to the PMSM phase currents (25 Hz), and the introduced harmonics. Despite this, under faulty operating conditions the same average torque equivalent to the load torque of 7 Nm is also generated.

4.2.2 SVM Vector Control

With respect to the SVM vector control strategy, the time-domain waveforms of the PMSM phase currents and their corresponding spectrograms for an open-circuit fault in IGBT T1 are shown in Figure 4.6.

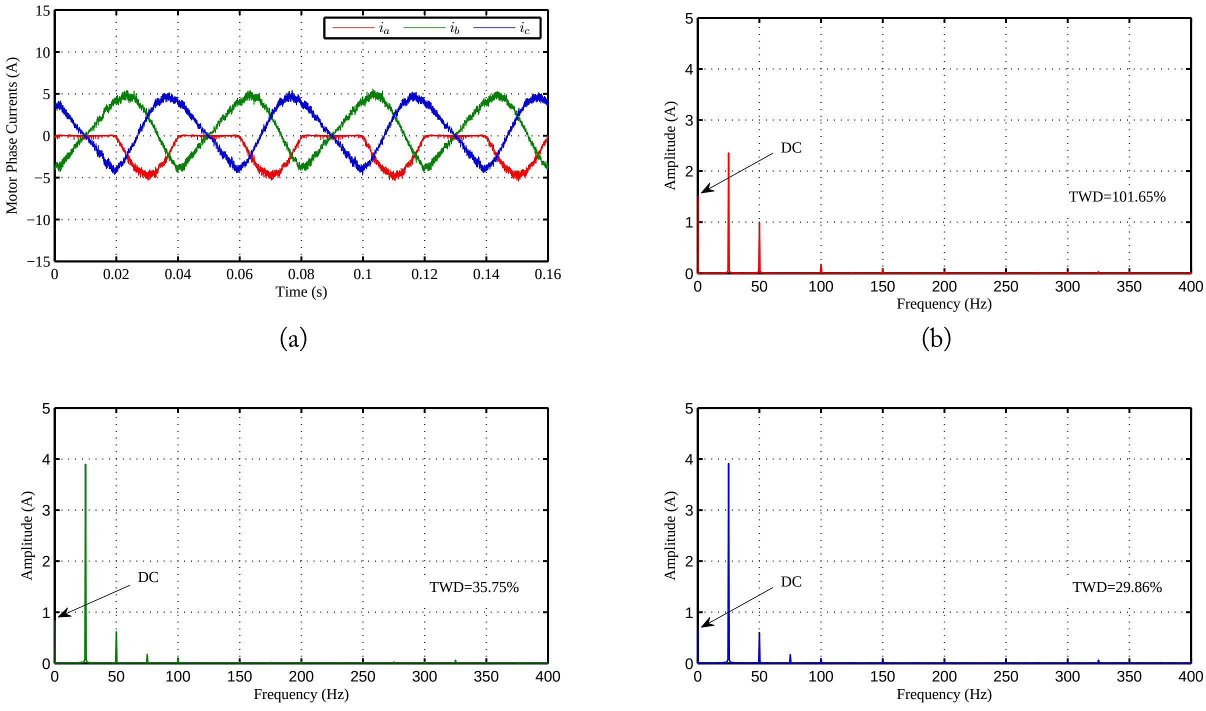

(a) (b)

(c) (d)

Figure 4.6: Experimental results of the PMSM phase currents for a SVM vector control strategy with an open-circuit fault in IGBT T1: (a) time-domain waveforms; (b) phase a current spectrogram; (c) phase b current spectrogram; (d) phase c current spectrogram.

Comparing with the simulation results presented in Figure 4.2a, it is also possible to conclude that the experimental ones are practically equal. Regarding the spectral analysis of the currents, it is also visible that phase a current presents a noticeable DC component and a second order harmonic, which results in a larger TWD value. From a spectral point of view, motor phase b and phase c currents are very similar, resulting in equivalent distortion values.

Figure 4.7 presents the time-domain waveform of the PMSM electromagnetic torque and its corresponding spectrogram.

In a similar way, the experimental time-domain waveform is very similar to the one obtained from the computational simulations, shown in Figure 4.2. Regarding its spectral analysis, it presents the fundamental oscillating component at 25 Hz and their multiple harmonics. The DC component remains unchanged with a value equivalent to the load torque.

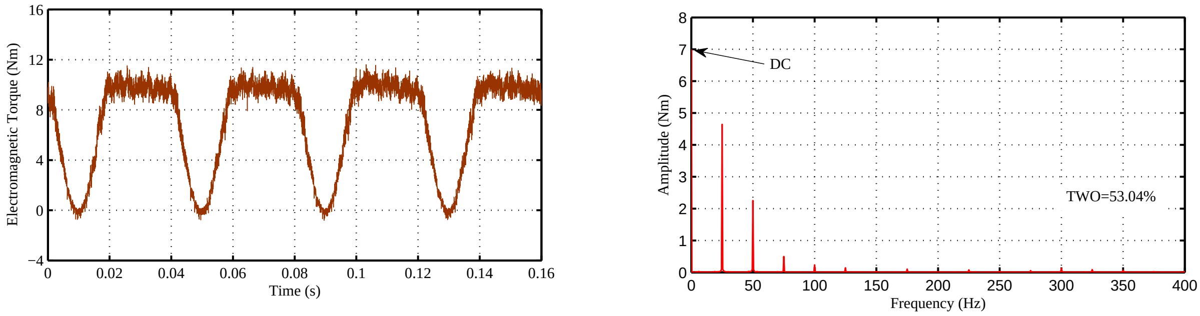

(a) (b)

Figure 4.7: Experimental results of the PMSM electromagnetic torque for a SVM vector control strategy with an open-circuit fault in IGBT T1: (a) time-domain waveform; (b) spectrogram.

4.2.3 Direct Torque Control

Finally, regarding the faulty behavior analysis for a DTC control strategy, Figure 4.8 presents the time-domain waveforms of the PMSM phase currents and their corresponding spectrograms for an open-circuit fault in IGBT T1.

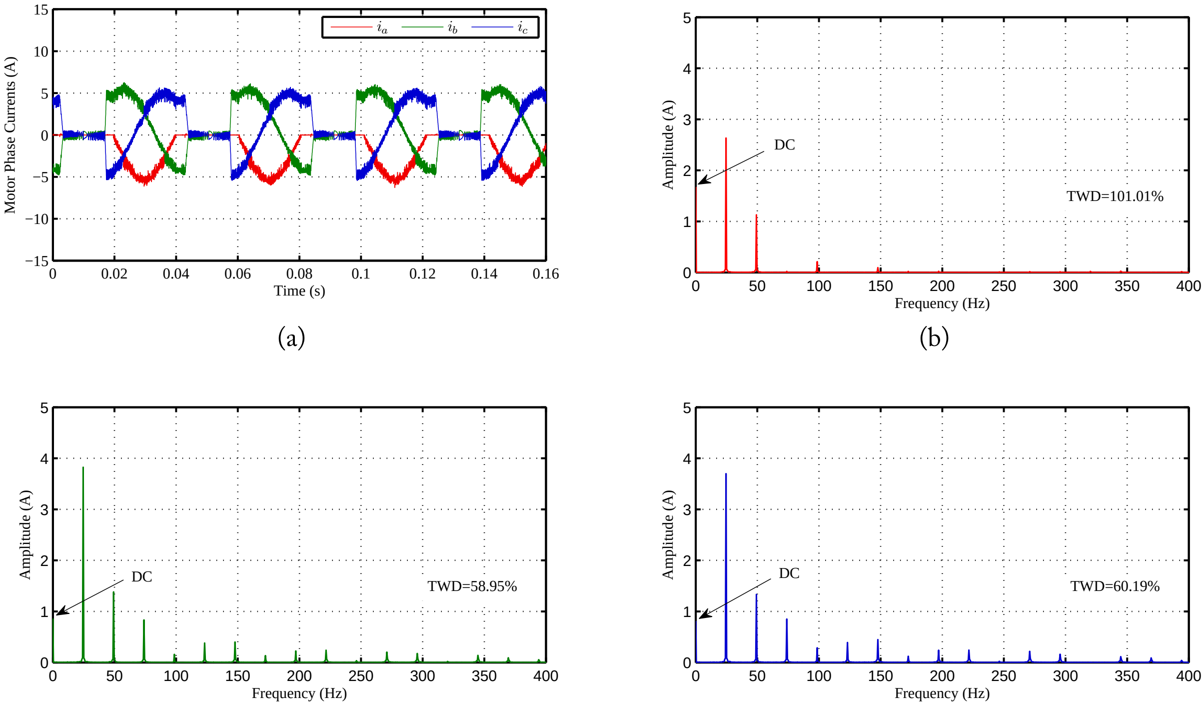

(c) (d)

Figure 4.8: Experimental results of the PMSM phase currents for a DTC control strategy with an open-circuit fault in IGBT T1: (a) time-domain waveforms; (b) phase a current spectrogram; (c) phase b current spectrogram; (d) phase c current spectrogram

Once more, the simulation and experimental results are very similar, demonstrating the excellent agreement between the theoretical predicted behavior and the experimentally obtained one. Regarding the motor phase currents spectral analysis, similar results are also obtained when comparing to the previous cases.

The PMSM electromagnetic torque experimental time-domain waveform is also very similar to the theoretical one, as shown in Figure 4.9.

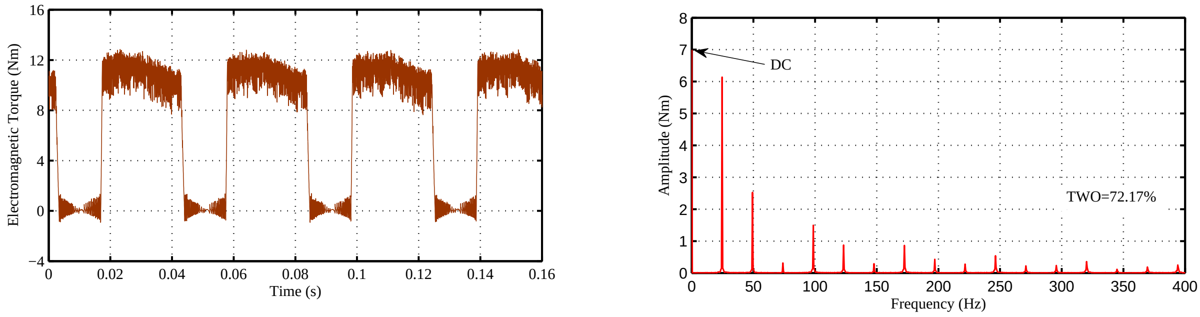

(a) (b)

Figure 4.9: Experimental results of the PMSM electromagnetic torque for a DTC control strategy with an open-circuit fault in IGBT T1: (a) time-domain waveform; (b) spectrogram.

From its corresponding spectrogram, it is also evident the fundamental oscillating component at the motor phase currents frequency and their multiple harmonics. The electromagnetic torque average value is also equivalent to the load torque.

4.3 Final Remarks

In this chapter the PMSM drive faulty operation analysis was discussed. A literature survey was presented, covering the research work in this specific subject.

Several simulation and experimental results were presented for the PMSM drive faulty operation under an inverter single IGBT open-circuit fault. The three main control strategies considered in this work were taken into account and the faulty behavior was evaluated for each one.

The obtained results allow to demonstrate an excellent agreement between the theoretical results obtained from the computational simulations and the experimental ones, obtained from the laboratory tests.

A well-defined pattern common to the three control techniques can be observed. Under a VSI power switch open-circuit fault, the faulty phase will be the most affected one, presenting a more distorted waveform. If a fault occurs in the top IGBT of one phase, current flow in that phase is only possible during the negative half-cycle. On the contrary, a fault in the bottom IGBT only allows current flow in that phase during the positive half-cycle. A single power switch open-circuit fault also has a negative impact on the other two healthy phases, contributing to the increase of their waveform distortion.

Regarding the electromagnetic torque, under these faulty operating conditions its waveform cannot be constant any longer. A defined oscillating component is introduced at the same frequency of the motor phase currents, maintaining the same average value equivalent to the load torque.

Analyzing the three considered control strategies, the obtained results prove that the DTC has the lowest performance by presenting the highest TWD and TWO values, while the SVM vector control shows the best performance under inverter faulty operating conditions.

Despite of only a fault in the IGBT T1 of phase a was considered, further simulation and experimental results have demonstrated that an equivalent behavior is also observed for the other five remaining cases, being therefore applied the same analysis.

Chapter 5

Inverter Fault Diagnosis

Due to their complexity and considering that they are often exposed to high stresses [137], VSIs are very prone to suffer critical failures that may negatively affect the entire variable speed drive. The great susceptibility of these power converters is confirmed by several statistical studies that show that semiconductor power switches and their corresponding gate drivers electronic circuits are among the main responsible for critical failures [138]-[142].

Therefore, in order to preclude this harmful influence as well as to improve the system reliability, the development of fault diagnostic methods for these devices has gain a lot of interest during the last years. This can be especially important for the development of fault-tolerant variable speed drives, which allow the system to continue operating under faulty conditions.

In general, inverter power device failures can be broadly classified as open-circuit faults and short-circuit faults. Typically, short-circuit faults are very destructive, requiring special measures to shutdown the drive immediately. On the other hand, open-circuit faults do not necessarily cause the system shutdown and can remain undetected for an extended period of time. This may lead to secondary faults in the converter or in the remaining drive components, resulting in the total system shutdown and high repairing costs.

The use of the Park's Vector Approach as a fault diagnostic tool for power converter faults was successfully firstly applied in [143]. Based on the same principle, other scientific works were then developed and published by other authors [144]-[149]. Basically, with this technique the damaged power switches can be detected and localized through the analysis of patterns. However, this approach requires very complex pattern recognition algorithms which are not suitable for integration into the drive controller.

The localization of the faulty switch can also be performed by the analysis of the current space vector trajectory diameter [150]. Its slope is used to identify the faulty leg and the missing half-cycle of the current waveform is used to locate the faulty switch. An improved version of this technique was presented in [151] with the capability to detect multiple faults. Nevertheless, this technique has serious drawbacks related to slow detection, tuning and problems under low current values.

A different technique, based on the average current Park's Vector approach was introduced in [152]. Instead of using the instantaneous current values, this method uses the currents average values in order to determine the Park's Vector. The operating philosophy is based on the vector absolute value to detect the fault and its corresponding phase to identify the faulty semiconductor. In spite of the further developments reported in [153]-[154] in order to improve its robustness, the tuning effort related to the fact that it is load dependent, together with some false alarm issues, remain the principal disadvantages of this diagnostic method.

Through the voltages analysis, on the inverter AC side or on the machine side, it is possible to conceive special methods that minimize the time between the fault occurrence and detection [155]-[158]. Under open-circuit faults, these voltages show some characteristic irregularities that can be detected, which give a direct localization of the faulty device. Although lower detection times can be achieved with these methods, additional voltage sensors are required, which in many cases is not desirable since it increases the drive costs and complexity.

The indirect measurement of inverter terminal voltages can also be used to implement fault diagnostic methods [159]-[162]. In this case, instead of using voltage sensors, the inverter output voltages are obtained through simple analogue circuits comprising optocouplers and basic components. The diagnostic strategy is also implemented by using this hardware approach and using the inverter gate command signals. As main advantage of this method it is pointed out the fast detection times that can be achieved. However, despite of the additional hardware, in order to avoid false alarms, some time-delay values must be correctly defined which can be very difficult since they depend on several variables such as the semiconductors switching characteristics, temperature and the operating current and voltage values.

A voltage-based approach without using voltage sensors or any other additional hardware was presented in [163]. This method is based on the comparison of the reference voltages, provided by the vector control, and the real voltages, estimated using the machine parameters. Due to this motor parameters dependence that may change according due to several reasons, the method robustness and tuning can be negatively affected.

A different voltage-based approach for open-circuit fault diagnosis in voltage-fed PWM motor drives without requiring extra hardware was presented in [164]. This technique uses a flux observer based on the machine current model, which allows to estimate the motor terminal voltages. The diagnostic method uses the average values of the errors between the reference and the estimated voltages.

The tendency to issue false alarms resulting from misinterpreting large transient variations of the currents average values, was reduced by the normalization of the diagnostic variables, as shown in [165]. This was accomplished by dividing the average value of each motor phase by its respective fundamental component value. This fault diagnostic method was later enhanced by the use of the currents average absolute values as normalization quantities [166]-[167]. Furthermore, by the calculation of additional diagnostic signals, the technique robustness was improved, having simultaneously the capability to detect multiple power switches open-circuit failures. Despite of these advantages, these enhancements bring some drawbacks such as a higher complexity and larger detection times.

Some reviews and surveys can also be found in the literature regarding fault diagnostic methods for VSIs single power switch open-circuit faults [142], [168]-[171].

A novel approach for real-time open-circuit fault diagnostics in inverter-fed PWM motor drives was proposed in [172] and later improved with multiple faults diagnosis in [173]-[174]. This algorithm presents a very high immunity against the issue of false alarms, it does not depend on the motor load level neither on its mechanical speed and it can achieve a detection speed equivalent to 1/9 of the currents period. In addition, it is quite simple and can be easily integrated into the main control system without great effort. This technique was recently used to effectively diagnose current sensor faults in wind energy conversion systems [175].

An observer-based diagnosis scheme for single and simultaneous open-switch faults in induction motor drives was addressed in [176]. The algorithm proves to be load independent and does not require additional sensors. However, as main drawbacks, the method implementation is not straightforward, being computationally demanding and requiring the knowledge of the machine parameters.

Fault diagnostic methods based on the operating characteristics of brushless direct current motor drives were presented in [177]-[179], where the diagnosis is accomplished without using additional sensors or electrical devices. This allows to embed them into the existing drive software as a subroutine without excessive computational effort.

Fast detection of open-circuit faults and short-circuit faults in IGBTs was addressed in [180]. A novel failure-detection technique and its analog circuit was proposed and applied to a three-phase induction motor drive. The obtained results prove that a fast detection time lower than 10 μs can be achieved. Nevertheless, the analog circuit requires some voltage measurements, which increases the system complexity, and the technique cannot be applied to all power devices since it strongly depends on the power device characteristics.

VSI open-circuit faults can also be effectively detected and localized by the analysis of the second-order harmonic component in the q-axis or by using the discrete wavelet transform [181]-[184].

An on-line fault detection and isolation method for sensor and open-phase faults in three-phase AC drives was presented in [185].The method is based on the detection of the stator current positive- and negative-sequence fundamental components expressed in the stationary $\alpha\beta$ reference frame. These components allow calculating two fault indices used for the detection and isolation of an open-phase fault and a sensor fault, using the cumulative sum algorithm.

The use of artificial neural network techniques to the diagnostic of inverter faults was also discussed in [186]-[188]. These more advanced techniques allow an intelligent diagnostic, being capable to detect both open- and short-circuit faults, without detailed background knowledge of the drive system. As main drawbacks, it is pointed out the relative complexity and tuning effort required to implement and train the neural networks.

Power converter open-circuit fault diagnosis can also be accomplished by using the currents Park's Vector phase and their corresponding polarity, as demonstrated in [189]-[190]. Despite this technique was firstly developed for fault diagnosis of back-to-back power converters used in wind turbine applications, it was also extended to VSI faults detection and localization in variable speed AC drives [191]. This method combines a detection algorithm based on the derivative of the current Park's Vector phase, with a localization method based on the currents polarity. This technique shows a very robust behavior regarding the issue of false alarms, having also the capability to diagnose multiple faults.

The information provided by an extra DC link current sensor together with the inverter switching states can also be used for inverter fault detection and localization [192]. A fast diagnosis can be achieved with this technique at a cost of an additional sensor with a fast sampling frequency.

A new approach for single power switch open-circuit fault diagnosis based on the reference current errors was presented in [193]. This method was later improved by adding multiple faults diagnostic capability [194]. The presented simulation and experimental results prove that the algorithm behavior does not depend on the motor operating conditions such as the mechanical speed and load level, showing simultaneously a great robustness against the emission of false alarms and a fast detection time equivalent to 5% of the motor phase currents fundamental period.

5.1 Developed Algorithms

For the real-time diagnosis of inverter power switch open-circuit faults, it is mandatory that the developed algorithms present some critical features such as independence of the machine operating conditions and rated power, robustness against the issue of false alarms, no need for extra sensors, low computational requirements, simple implementation and multiple faults diagnostic capability.

The literature review shows that, despite of all the existing work done by several authors concerning the diagnostic methods for VSI open-circuit faults, there is a great lack of research regarding the development of algorithms that fulfill the previously mentioned requirements.

Therefore, two novel real-time diagnostic algorithms were developed taking into account these requirements, making them very suitable for integration into the drive controller.

5.1.1 Errors of the Normalized Currents Average Absolute Values

This fault diagnostic algorithm for real-time detection and localization of inverter open-circuit faults was firstly presented in [172] and improved in [173]-[174]. A block diagram of the algorithm is presented in Figure 5.1.

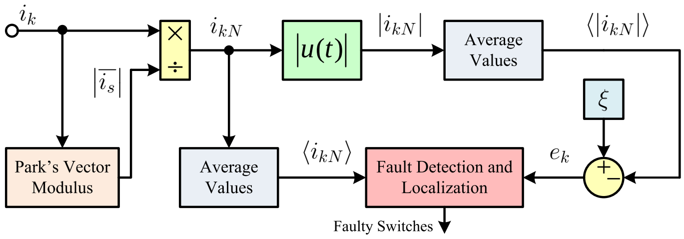

Figure 5.1: Block diagram of the algorithm based on the errors of the normalized currents average absolute values.

The three motor phase currents are the unique inputs required by this technique since it is desirable that the fault diagnostic method utilizes variables already used by the main control, avoiding the use of extra sensors and the inherent increase of the system complexity.

In order to overcome the problems associated with the machine mechanical operating conditions dependency and the issue of false diagnostics, the measured motor phase currents are normalized using the modulus of the Park's Vector, defined as:

$$i_d = \sqrt{\frac{2}{3}} i_a - \frac{1}{\sqrt{6}} i_b - \frac{1}{\sqrt{6}} i_c \tag{5.1}$$

$$i_q = \frac{1}{\sqrt{2}} i_b - \frac{1}{\sqrt{2}} i_c \tag{5.2}$$

being i_d and i_q the Park's Vector components and i_a, i_b and i_c the motor phase currents. The Park's Vector modulus$|\bar{i_s}|$ is given by:

$$|\bar{i_s}| = \sqrt{i_d^2 + i_q^2} \tag{5.3}$$

The normalization is performed by dividing the motor phase currents by the Park's Vector modulus. The obtained normalized motor phase currents i_{kN} are given by:

$$i_{kN} = \frac{i_k}{|\bar{i_s}|} \tag{5.4}$$

where $k = a,\, b,\, c$. Therefore, assuming that the motor is fed by a healthy inverter generating a perfectly balanced three phase sinusoidal current system:

$$i_k = \begin{cases} i_a = I_m \sin\left(\omega t + \phi\right) \\ i_b = I_m \sin\left(\omega t - \frac{2\pi}{3} + \phi\right) \\ i_c = I_m \sin\left(\omega t + \frac{2\pi}{3} + \phi\right) \end{cases} \tag{5.5}$$

where I_m is the currents maximum amplitude, ω is the motor currents frequency and ϕ is the initial phase angle, it can be proven that the Park's Vector modulus can be given by:

$$|\overline{i_s}| = I_m\sqrt{\frac{3}{2}} \tag{5.6}$$

As a consequence of this normalization process, the normalized motor phase currents will always take values within the range of $\pm\sqrt{2/3}$, independently of the measured motor phase currents amplitude, since:

$$i_{kN} = \begin{cases} i_{aN} = \sqrt{\frac{2}{3}}\sin\left(\omega_s t + \phi\right) \\ i_{bN} = \sqrt{\frac{2}{3}}\sin\left(\omega_s t - \frac{2\pi}{3} + \phi\right) \\ i_{cN} = \sqrt{\frac{2}{3}}\sin\left(\omega_s t + \frac{2\pi}{3} + \phi\right) \end{cases} \tag{5.7}$$

Under these conditions, the average absolute values of the three normalized motor phase currents $\langle|i_{kN}|\rangle$ are given by:

$$\frac{\omega_s}{2\pi}\int_0^{\frac{2\pi}{\omega_s}} |i_{kN}|\ dt = \frac{1}{\pi}\sqrt{\frac{8}{3}} \tag{5.8}$$

Finally, the three diagnostic variables e_k, are obtained from the errors , given by:

$$e_k = \xi - \langle|i_{kN}|\rangle \tag{5.9}$$

being ξ a constant value equivalent to the average absolute value of the normalized motor phase currents under normal operating conditions given by equation (5.8), that is:

$$\xi = \frac{1}{\pi}\sqrt{\frac{8}{3}} \approx 0.5198 \tag{5.10}$$

The three diagnostic variables defined in (5.9) have specific characteristics which allow for the inverter fault diagnosis. When the drive is operating under normal operating conditions, all the diagnostic variables will take values near to zero. However, if an inverter open-circuit fault is introduced, at least one of the diagnostic variables will assume a distinct positive value. Consequently, the errors e_k can be effectively used to detect an anomalous inverter behavior.

On the other side, these variables are not capable to perform a complete inverter diagnostic since that they just carry information about the affected phases. So, this information together with the currents average values $\langle i_{kN}\rangle$, can be used to identify the faulty power switches. To achieve this, fault symptom variables can be formulated according to the following expressions:

$$E_k = \begin{cases} \text{N} & \text{if } e_k < 0 \\ 0 & \text{if } 0 \leq e_k < k_f \\ \text{P} & \text{if } k_f \leq e_k < k_d \\ \text{D} & \text{if } e_k \geq k_d \end{cases} \tag{5.11}$$

$$M_k = \begin{cases} \text{L} & \text{if } \langle i_{kN} \rangle < 0 \\ \text{H} & \text{if } \langle i_{kN} \rangle > 0 \end{cases} \tag{5.12}$$

The values taken by E_k and M_k allow to generate a distinct fault signature which corresponds to a specific faulty operating condition. The threshold value k_f is directly related to any fault detection while k_d performs an important role in case of a double failure in the same inverter phase. Since the method is normalized, it is not required to adjust these values for each load and speed conditions. They can be empirically established by simply analyzing the variables behavior for different faulty operating conditions. Taking this into account, 15 distinct fault signatures can be generated, which enable the effective fault detection and localization of an equal number of different VSI failure combinations. As a result, considering a typical motor drive system with a VSI supplying an AC motor (Figure 3.4), the 15 fault combinations can be detected and identified using Table 5.1.

Table 5.1: Diagnostic signatures for the faulty switches identification.

Faulty Switches	E_a	E_b	E_c	M_a	M_b	M_c
T1	P	N	N	L	−	−
T2	P	N	N	H	−	−
T3	N	P	N	−	L	−
T4	N	P	N	−	H	−
T5	N	N	P	−	−	L
T6	N	N	P	−	−	H
T1, T2	D	−	−	−	−	−
T3, T4	−	D	−	−	−	−
T5, T6	−	−	D	−	−	−
T1, T3	P	P	N	L	L	H
T2, T4	P	P	N	H	H	L
T3, T5	P	N	P	L	H	L
T4, T6	P	N	P	H	L	H
T1, T5	N	P	P	H	L	L
T2, T6	N	P	P	L	H	H

5.1.2 Normalized Reference Current Errors

This algorithm was firstly presented in [193] and later enhanced by adding multiple faults diagnostic capability [194]. A block diagram of its structure is depicted in Figure 5.2.

Once more, this fault diagnostic method utilizes variables already used by the main control, avoiding the use of extra sensors and the subsequent increase of the system complexity and costs.

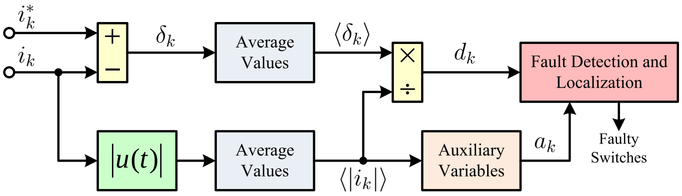

Figure 5.2: Block diagram of the algorithm based on the normalized reference current errors.

Hence, this method has as inputs the motor phase currents and their corresponding reference signals, which can be obtained from the main control system. Considering a vector controlled drive with hysteresis current controllers in the *abc* reference frame, the motor reference currents are directly available from the control strategy. For the case where PI current controllers are used together with a SVM or other modulation techniques, if the reference currents are not directly available, they can be easily obtained from the *dq* current components using the inverse Park transformation.

The three reference current errors δ_k are calculated from the measured motor phase currents i_k and from their corresponding reference signals i_k^* by:

$$\delta_k = i_k^* - i_k \tag{5.13}$$

The properties of the final diagnostic variables result from the average values of the three reference current errors $\langle \delta_k \rangle$:

$$\langle \delta_k \rangle = \frac{\omega}{2\pi} \int_0^{\frac{2\pi}{\omega}} \delta_k \, dt \tag{5.14}$$

In order to overcome the problems related to the drive rated power and machine mechanical operating conditions dependency such as the speed and load levels, the average reference current errors are normalized using the average absolute values of the motor phase currents $\langle |i_{kN}| \rangle$. Therefore, the final diagnostic variables d_k are given by:

$$d_k = \frac{\langle \delta_k \rangle}{\langle |i_k| \rangle} \tag{5.15}$$

Under healthy operating conditions, and neglecting the low amplitude high frequency noise, the motor is supplied by a perfectly balanced three-phase sinusoidal current system that can be given by (5.5).

As the inverter is operating normally, the three motor phase currents follow their corresponding reference signals i_k^*, which can be also given by (5.5). As a result, the diagnostic variables d_k will be zero since $\langle \delta_k \rangle$ are also zero. In practice δ_k are not exactly zero since they present the currents low amplitude high frequency ripple. Nevertheless, as their average values are calculated, $\langle \delta_k \rangle$ are zero under these conditions.

When a fault is introduced, the motor currents cannot perfectly follow their reference signals.

Taking as an example a fault in the inverter phase a upper switch (T1), the current in this phase is strongly affected since during its positive half-cycle the current is zero. Under these conditions and assuming $\phi = 0$, during one fundamental period i_a can be given by:

$$i_a = \begin{cases} 0 & , 0 < t \leq \frac{\pi}{\omega} \\ I_m \sin(\omega t) & , \frac{\pi}{\omega} < t \leq \frac{2\pi}{\omega} \end{cases} \tag{5.16}$$

Regarding the variable $|i_a|$ and taking into account that under these faulty operating conditions i_a just assumes negative values, it can be verified that $|i_a| = -i_a$. The reference current signals are always sinusoidal, in accordance to (5.5). Following this and using (5.15), the phase a diagnostic variable can be calculated as:

$$d_a = \frac{\frac{\omega}{2\pi}\int_0^{\frac{2\pi}{\omega}} I_m \sin(\omega t)\,dt - \frac{\omega}{2\pi}\int_{\frac{\pi}{\omega}}^{\frac{2\pi}{\omega}} I_m \sin(\omega t)\,dt}{\frac{\omega}{2\pi}\int_{\frac{\pi}{\omega}}^{\frac{2\pi}{\omega}} -I_m \sin(\omega t)\,dt} \tag{5.17}$$

Solving this equation by calculating the average values of the three signals, the value of the diagnostic variable d_a can be obtained by the expression:

$$d_a = \frac{0 - \left(-\frac{I_m}{\pi}\right)}{\frac{I_m}{\pi}} = 1 \tag{5.18}$$

According to this last equation and taking into account that this theory is also extended to the remaining cases, it can be proved that after the fault occurrence, the diagnostic variable corresponding to the inverter faulty leg will converge to a value of approximately +1 or -1, if the damaged switch is the top or the bottom one, respectively.

Furthermore, the diagnostic variable associated with the affected phase will converge more rapidly to its final value. Therefore, a single open-circuit fault is detected by observing which is the first variable d_k that crosses a defined threshold value k_f, whereas its signal gives information about the fault localization. This diagnostic can be easily accomplished using Table 5.2.

Table 5.2: Single power switch open-circuit fault detection and localization.

d_a	d_b	d_c	Faulty IGBT
$> k_f$			T1
$< -k_f$			T2
	$> k_f$		T3
	$< -k_f$		T4
		$> k_f$	T5
		$< -k_f$	T6

Regarding the multiple open-circuit fault diagnosis, the formulated variables carry also information that allows to achieve this goal. However, in case of a double fault in the same inverter leg, the diagnostic variables defined by (5.15) become ill-conditioned since the corresponding value of

$\langle|i_k|\rangle$ is close to zero. With the aim to handle with these specific faults, three additional auxiliary variables can be defined as:

$$a_k = \frac{2\,\langle|i_k|\rangle}{\langle|i_l|\rangle + \langle|i_m|\rangle} \tag{5.19}$$

where $k, l, m \in \{a, b, c\}$, and $k \neq l \neq m$. Therefore, for a double fault in phase k, the variable a_k will decrease considerably to a value near to zero, indicating a lack of current flow in that phase.

To accomplish multiple fault diagnosis, two more threshold values k_m and k_l can be used and fault symptom variables can be formulated according to the following expressions:

$$D_k = \begin{cases} \mathrm{N} & \text{if } d_k \leq -k_m \\ 0 & \text{if } |d_k| < k_m \\ \mathrm{P} & \text{if } d_k \geq k_m \end{cases} \tag{5.20}$$

$$A_k = \begin{cases} \mathrm{L} & \text{if } a_k \leq k_l \\ \mathrm{H} & \text{if } a_k > k_l \end{cases} \tag{5.21}$$

Taking this into account and considering a typical motor drive system with a voltage source inverter supplying an AC motor (Figure 3.4), the generated fault signatures allow to detect and localize 27 possible combinations of faulty IGBTs, as shown in Table 5.3. All these combinations correspond exactly to the maximum number of faulty modes that can be distinguished from one another based on just the current analysis. In this table, "[ ]" means that the switch may or may not be in open-circuit and "(|)" means that both or at least one switch is in open-circuit.

According to Table 5.3, all these open-circuit fault combinations can be separated into five groups as follows: single switch faults; single phase faults; crossed double faults in different legs, i.e., an upper and a bottom switch in different legs are damaged; double faults in upper (lower) switches, which are indistinguishable from triple faults that includes two upper (lower) switches and the bottom (upper) switch of the remaining leg; and triple faults involving a single phase fault, which are also indistinguishable from quadruple faults combining a single phase fault with an upper and a bottom faulty switch in each remaining leg.

The threshold values k_f, k_m and k_l can be empirically established by simply analyzing the variables behavior for different faulty operating conditions and taking into account a tradeoff between fast detection and robustness against false alarms. A more detailed explanation regarding the selection of these thresholds is presented in [194].

Table 5.3: Diagnostic signatures for the faulty switches identification.

Faulty Switches	D_a	D_b	D_c	A_a	A_b	A_c
T1	P	0	0	H	H	H
T2	N	0	0	H	H	H
T3	0	P	0	H	H	H
T4	0	N	0	H	H	H
T5	0	0	P	H	H	H
T6	0	0	N	H	H	H
T1, T2	−	0	0	L	H	H
T3, T4	0	−	0	H	L	H
T5, T6	0	0	−	H	H	L
T1, T4	P	N	0	H	H	H
T2, T3	N	P	0	H	H	H
T1, T6	P	0	N	H	H	H
T2, T5	N	0	P	H	H	H
T3, T6	0	P	N	H	H	H
T4, T5	0	N	P	H	H	H
T1, T3, [T6]	P	P	N	H	H	H
T2, T4, [T5]	N	N	P	H	H	H
T3, T5, [T2]	N	P	P	H	H	H
T4, T6, [T1]	P	N	N	H	H	H
T1, T5, [T4]	P	N	P	H	H	H
T2, T6, [T3]	N	P	N	H	H	H
T1, T2, (T3|T6)	−	P	N	L	H	H
T1, T2, (T4|T5)	−	N	P	L	H	H
T3, T4, (T1|T6)	P	−	N	H	L	H
T3, T4, (T2|T5)	N	−	P	H	L	H
T5, T6, (T1|T4)	P	N	−	H	H	L
T5, T6, (T2|T3)	N	P	−	H	H	L

5.2 Simulation Results

The developed real-time inverter fault diagnostic algorithms were firstly tested and validated through various simulation results. In order to accomplish this and for the sake of simplicity, both techniques were implemented and tested for a HCC vector control strategy. The same parameters already defined for this specific control technique were also used to obtain these simulation results.

With the aim to evaluate the diagnostic algorithms performance under different operating conditions, they were tested for two distinct mechanical speed values corresponding to 750 rpm and 1200 rpm. In addition, for each reference speed value, two different load levels equivalent to 10% and 50% of the PMSM rated load torque were considered. For all cases, only single power switch open-circuit faults in IGBT T1 were considered.

5.2.1 Errors of the Normalized Currents Average Absolute Values

Considering first the diagnostic algorithm based on the errors of the normalized currents average absolute values, the threshold values for k_f and k_d were chosen to be equal to 0.08 and 0.32, respectively. A detailed explanation regarding the selection of these threshold values is presented in Subsection ??.

5.2.1.1 750 rpm Operation

Figure 5.3 presents the simulation results regarding the time-domain waveforms of the PMSM phase currents, the main diagnostic variables and the auxiliary variables for a mechanical speed of 750 rpm and for a fault in IGBT T1.

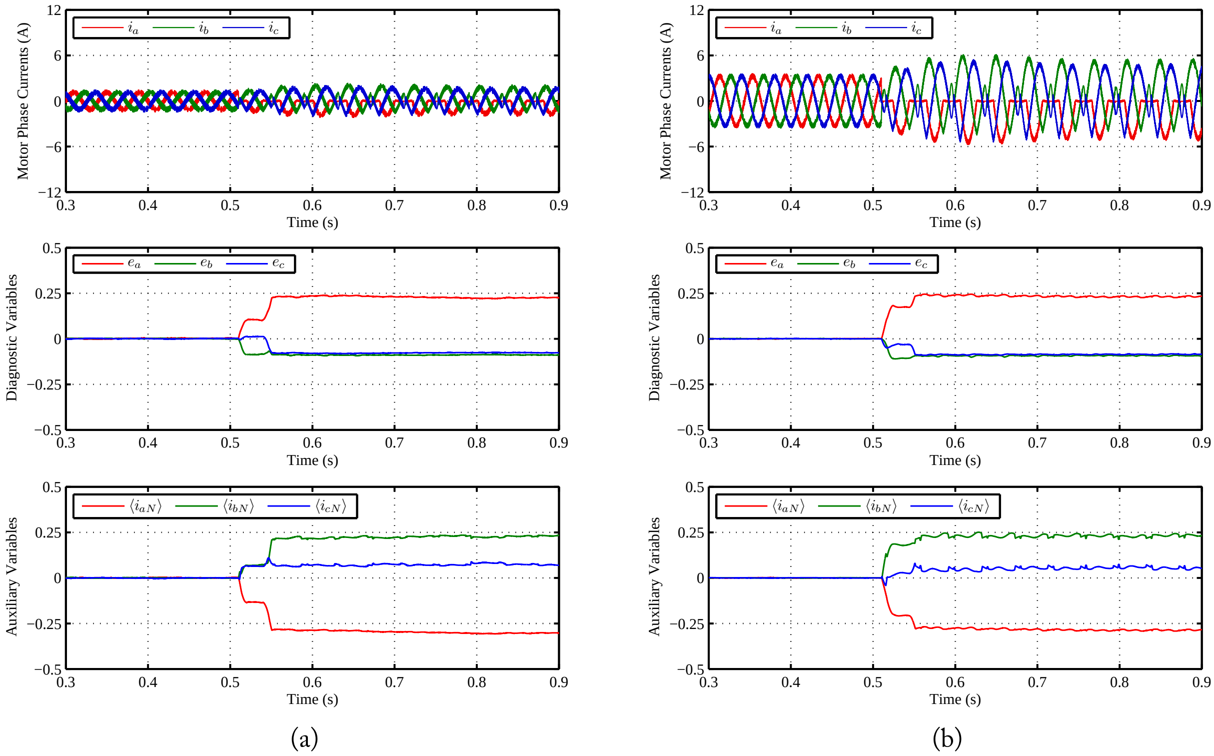

Figure 5.3: Simulation results regarding the time-domain waveforms of the PMSM phase currents, the main diagnostic variables and the auxiliary variables for a mechanical speed of 750 rpm and for a fault in IGBT T1; (a) 10% of load torque; (b) 50% of load torque.

Considering first the operation under low load level shown in Figure 5.3a, as expected, under normal operating conditions all the three diagnostic variables are zero. At the instant $t = 0.5101\,s$, a fault in IGBT T1 is introduced, leading to a different behavior of the diagnostic and auxiliary variables. The diagnostic variables related to the healthy inverter phases e_b and e_c decrease and converge to a final value of about -0.08. On the other side, the faulty phase diagnostic variable e_a rapidly increases after the fault occurrence, converging to a final value of approximately 0.23.

Regarding the normalized currents average values that are used as auxiliary variables, the one associated with the faulty phase becomes negative will the remaining two assume positive values. Combining all this information and according to equations (5.11) and (5.12) and Table 5.1, a specific fault signature is generated, correctly identifying the IGBT T1 as the faulty one.

The fault detection is performed when the e_a crosses the threshold k_f at the instant $t = 0.5156s$. Consequently, this fault is detected and localized in a time interval equivalent to 13.7% of the motor phase currents fundamental period.

For the drive operation at the same mechanical speed but under a load torque equivalent 50% of the PMSM rated value, the results depicted in Figure 5.3b allow to demonstrate that a similar behavior to the previous case is obtained. After the fault occurrence, the diagnostic variables converge to approximately the same final values as the ones obtained for the low load operating conditions. The generated fault signature by the auxiliary variables is also the same, which means that combining all the information, the same faulty IGBT is correctly identified. In this case, the detection speed is equivalent to 12.2% of the current fundamental period.

Due to the same algorithm behavior for both operating conditions, it can be clearly verified that it does not depend on the motor load level.

5.2.1.2 1200 rpm Operation

Considering now the PMSM operation at a reference speed of 1200 rpm, Figure 5.4 presents the simulation results regarding the time-domain waveforms of the motor phase currents, the main diagnostic variables and the auxiliary variables for a fault in IGBT T1.

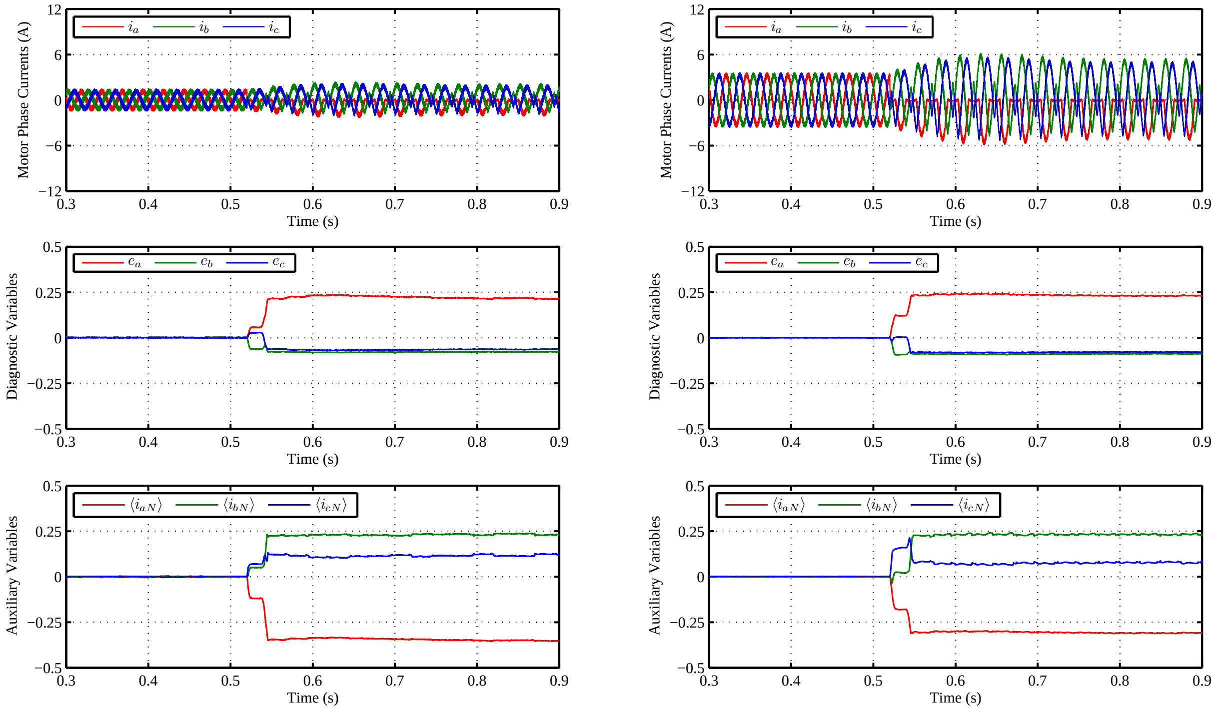

(a) (b)

Figure 5.4: Simulation results regarding the time-domain waveforms of the PMSM phase currents, the main diagnostic variables and the auxiliary variables for a mechanical speed of 1200 rpm and for a fault in IGBT T1; (a) 10% of load torque; (b) 50% of load torque.

Analyzing the results obtained for a low load torque value (Figure 5.4a), it is possible to verify that despite the higher PMSM operating speed, the behavior of the diagnostic and auxiliary variables is very similar to the one observed for the previous case (Figure 5.3). Therefore, the combination of these variables generates the same diagnostic signature that corresponds to a fault in power switch T1. For this specific case, a diagnostic speed equivalent to 77.2% of the motor phase currents fundamental period is achieved.

Under a higher load level, the results depicted in Figure 5.4b also allow to demonstrate that the real-time algorithm behavior is virtually equal to the one obtained for the previous situations. All variables converge to approximately the same final values observed for the previous cases, leading to the generation of the same fault signature. As far as the detection speed is concerned, in this case a value equivalent to 15.6% of the currents fundamental period is achieved.

Comparing all the simulation results obtained for the different speed and load torque values, it becomes clear that the developed algorithm does not depend on the motor operating conditions.

5.2.2 Normalized Reference Current Errors

Considering now the second diagnostic algorithm based on the normalized reference currents errors, the threshold values for k_f, k_m and k_l were chosen to be equal to 0.08, 0.5 and 0.2, respectively. A detailed explanation regarding the selection of these threshold values is presented in Subsection 5.3.2.4.

5.2.2.1 750 rpm Operation

Figure 5.5 presents the simulation results regarding the time-domain waveforms of the PMSM phase currents, the main diagnostic variables and the auxiliary variables for a mechanical speed of 750 rpm and for a fault in IGBT T1.

According to the results shown in Figure 5.5a, under low load operating conditions, the diagnostic variables are zero for normal operating conditions, while the auxiliary variables assume a value of 1. At the instant $t = 0.5099\,s$, a fault in IGBT T1 is introduced, leading to the increase of the variable d_a, converging to a final value of approximately 1. The diagnostic variables associated to the inverter healthy phases converge to negative values. After the fault occurrence, d_b and d_c assume the values of about -0.357 and -0.262, respectively.

Regarding the auxiliary variables, their behavior modifies for the inverter abnormal operation. Nevertheless, all of them stay above the threshold associated to an inverter leg double fault (k_l). As a result, the specific inverter fault in IGBT T1 is correctly detected and localized.

In this case, this inverter fault is detected when any of the three diagnostic variables is the first to verify the conditions in Table 5.2. This is accomplished for d_a at the instant $t = 0.5119\ s$, corresponding to a detection time equivalent to 5% of the currents fundamental period.

For the PMSM operation at a load torque equivalent to one-half of its rated value, the results in Figure 5.5b allow to verify that the behavior of the main diagnostic variables and the auxiliary ones is virtually the same. Therefore, the same fault signature is generated, correctly identifying the

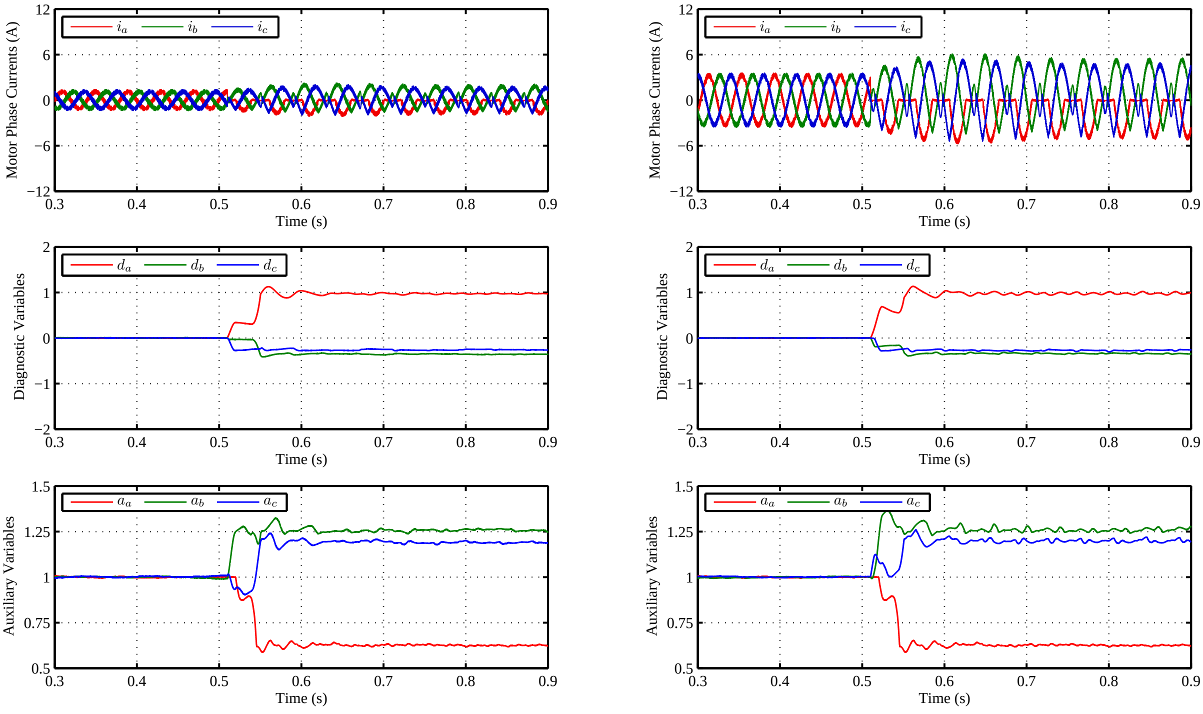

(a) (b)

Figure 5.5: Simulation results regarding the time-domain waveforms of the PMSM phase currents, the main diagnostic variables and the auxiliary variables for a mechanical speed of 750 rpm and for a fault in IGBT T1; (a) 10% of load torque; (b) 50% of load torque.

IGBT T1 as the faulty device. For this specific situation, the diagnostic process is accomplished in a time interval equivalent to 6.1% of the currents fundamental period.

5.2.2.2 1200 rpm Operation

For the PMSM operation at a reference speed of 1200 rpm, Figure 5.6 presents the simulation results regarding the time-domain waveforms of the motor phase currents, the main diagnostic variables and the auxiliary variables for a fault in IGBT T1.

Comparing with the previous case, despite the motor higher speed operation, it can be seen that for both 10% and 50% of load torque, all the main diagnostic variables as well as the auxiliary variables, converge to approximately the same steady-state values. Therefore, the same fault signature is generated, effectively diagnosing the inverter IGBT T1 as the faulty element.

With respect to the algorithm detection speed, a value equivalent to 5.2% and 5.6% of the currents period is obtained for the cases in Figure 5.6a and Figure 5.6b, respectively.

In analogy to the algorithm based on the errors of the normalized currents average absolute values, from the comparison of the simulation results obtained for the different speed and load torque values, it is confirmed that this algorithm also does not depend on the machine operating conditions.

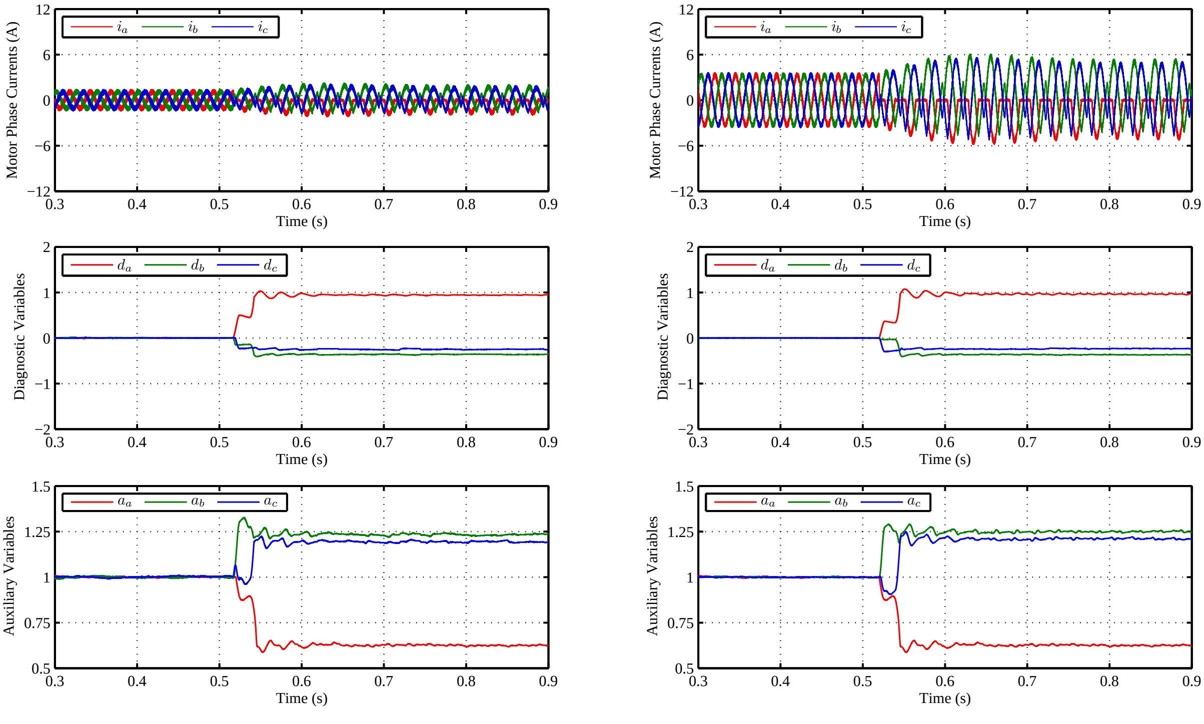

(a) (b)

Figure 5.6: Simulation results regarding the time-domain waveforms of the PMSM phase currents, the main diagnostic variables and the auxiliary variables for a mechanical speed of 1200 rpm and for a fault in IGBT T1; (a) 10% of load torque; (b) 50% of load torque.

5.3 Experimental Validation

The two developed real-time algorithms for open-circuit fault diagnosis in voltage-fed PWM AC motor drives were also experimental validated in the laboratory. To accomplished this, both techniques were implemented and tested for a HCC vector control strategy. The same laboratory setup and conditions previously described in Section 3.5 for this specific control strategy were also considered.

In a similar way to the simulation results, only open-circuit faults in the inverter IGBT T1 were considered by removing its gate command signal. Once more, it must be noticed that the corresponding antiparallel diode still remains connected.

Both the developed techniques were evaluated for the same mechanical operating conditions used to obtain the simulation results. Therefore, experimental tests were performed for a PMSM reference mechanical speed of 750 rpm and 1200 rpm. For each operating speed, the algorithms behavior is analyzed for a load torque equivalent to 10% and 50% of the PMSM rated load torque. The same threshold values used for the simulation results were also used for the experimental validation.

Finally, with the aim to verify the algorithms robustness against the issue of false diagnostics, their behavior is investigated when strong load steps are introduced.

5.3.1 Errors of the Normalized Currents Average Absolute Values

5.3.1.1 750 rpm Operation

Figure 5.7 presents the experimental results regarding the time-domain waveforms of the PMSM phase currents, the main diagnostic variables and the auxiliary variables for a mechanical speed of 750 rpm and for a fault in IGBT T1.

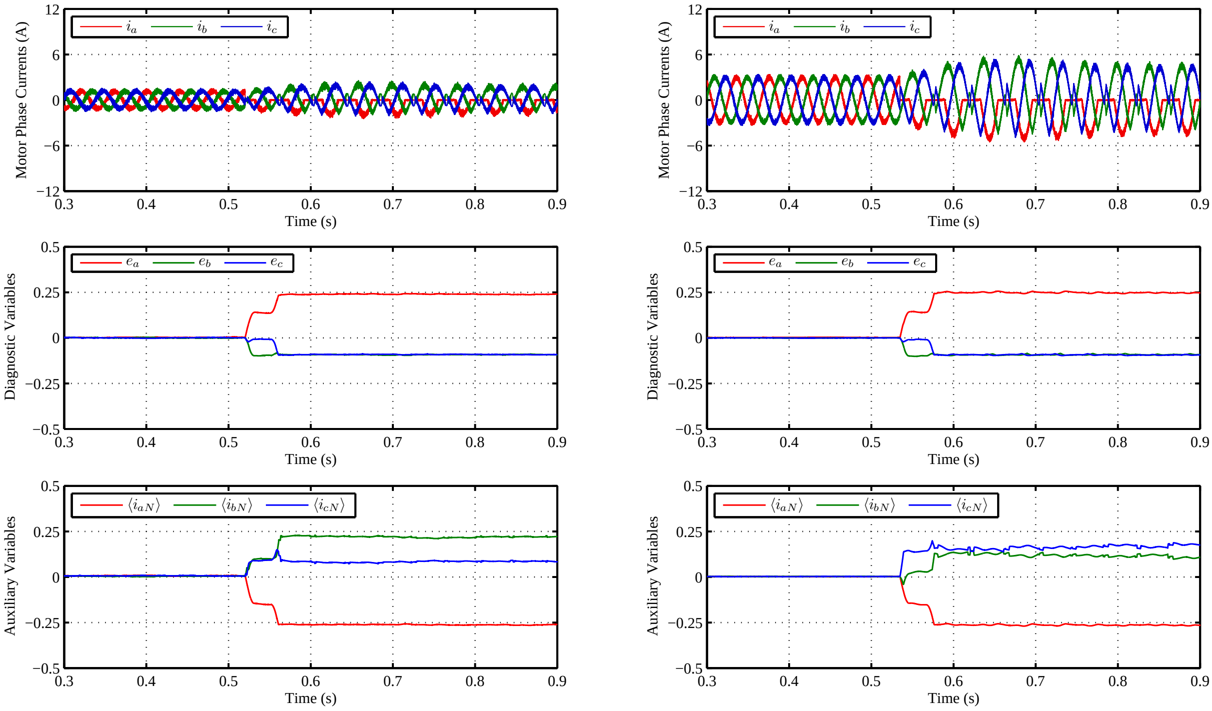

(a) (b)

Figure 5.7: Experimental results regarding the time-domain waveforms of the PMSM phase currents, the main diagnostic variables and the auxiliary variables for a mechanical speed of 750 rpm and for a fault in IGBT T1; (a) 10% of load torque; (b) 50% of load torque.

Comparing these results with the ones presented in Figure 5.3, it can be observed that there is an excellent agreement between the simulation and experimental results. Under normal operating conditions, all the main diagnostic variables and the auxiliary variables are zero. After the fault occurrence, the behavior of all variables is very similar to the theoretical results, converging to approximately the same steady-state value. As a result, the same fault signature is also generated, leading to the effective diagnosis of the inverter faulty device.

As far as the detection speed is concerned, a value equivalent to 11.2% and 11.5% of the currents fundamental period is obtained for the cases shown in Figure 5.7a and Figure 5.7b, respectively.

5.3.1.2 1200 rpm Operation

Considering now the PMSM operation at a reference speed of 1200 rpm, Figure 5.8 presents the experimental results regarding the time-domain waveforms of the motor phase currents, the main diagnostic variables and the auxiliary variables for a fault in IGBT T1.

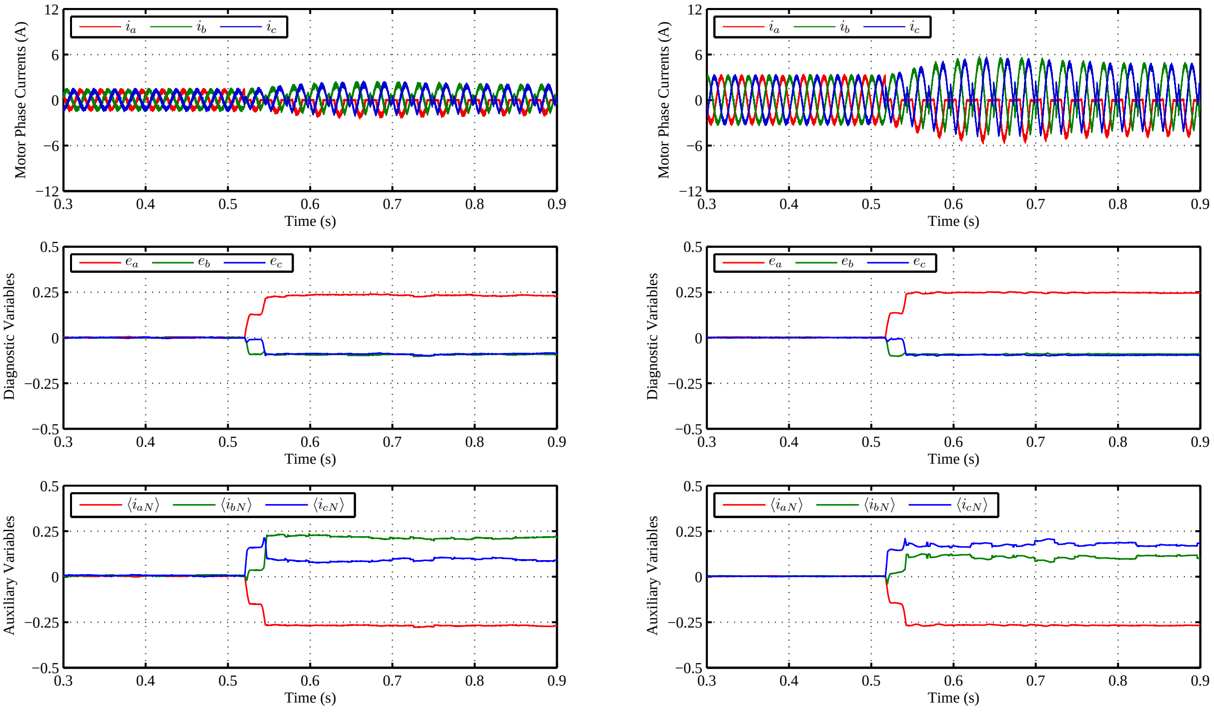

(a) (b)

Figure 5.8: Experimental results regarding the time-domain waveforms of the PMSM phase currents, the main diagnostic variables and the auxiliary variables for a mechanical speed of 1200 rpm and for a fault in IGBT T1; (a) 10% of load torque; (b) 50% of load torque.

In analogy to the previous case, by comparing these results with the equivalent simulation ones (Figure 5.4), it is also evident the great agreement between the theoretical and experimental results. When a fault occurs, the variables behavior is very similar, converging to approximately the same final values. The detection speed for these two cases is equivalent to 13.2% and 11.9% of the currents fundamental period, respectively.

Comparing all the experimental results obtained for the different combinations of motor operating speed and load torque levels, it can be concluded that the developed algorithm does not depend on the machine operating conditions.

5.3.1.3 Load Transients Analysis

Figure 5.9 presents the experimental results regarding the time-domain waveforms of the motor phase currents, the main diagnostic variables and the auxiliary variables for load torque transients at a reference speed of 1200 rpm.

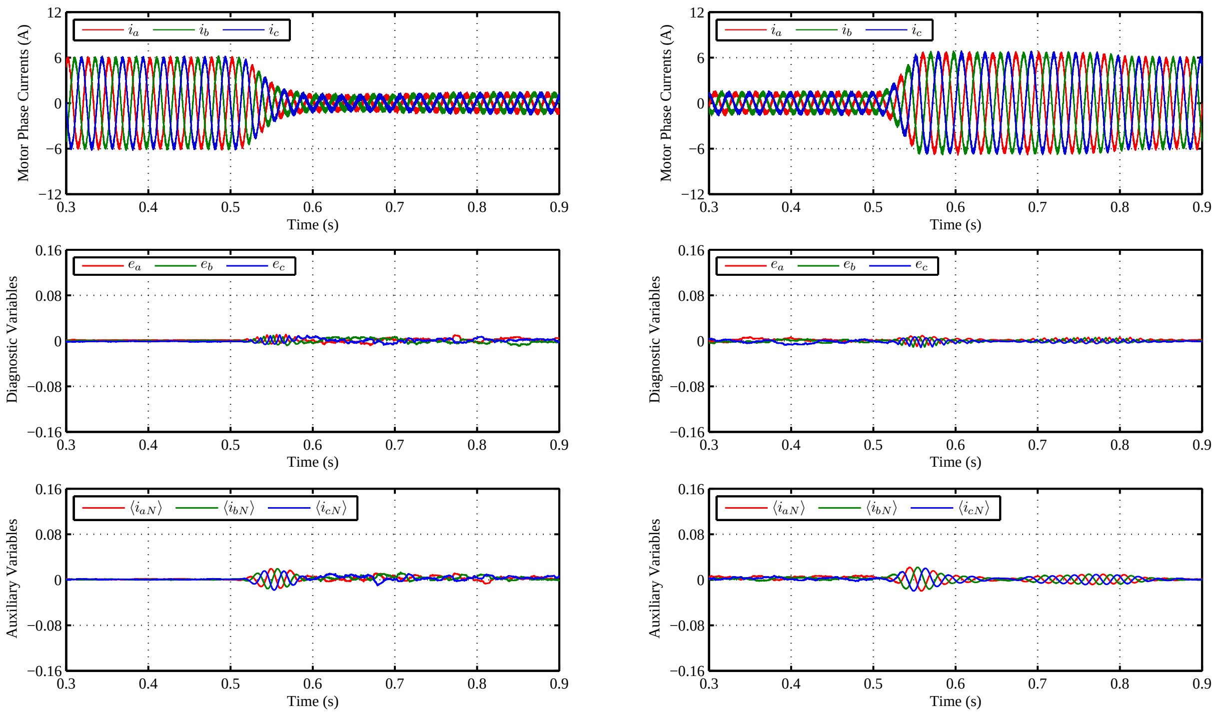

(a) (b)

Figure 5.9: Experimental results regarding the time-domain waveforms of the PMSM phase currents, the main diagnostic variables and the auxiliary variables for load transients; (a) rated load to no-load; (b) no-load to rated load.

Under full load torque operation, the motor phase currents present less distortion, resulting in more stable values around zero. For no-load operating conditions, the motor phase currents are much smaller, presenting a more noticeable harmonic distortion. As a consequence, the calculation of the diagnostic and auxiliary variables is less precise, resulting in more visible oscillations around zero. Nevertheless, despite this fact and taking into account these strong and fast load variations, all the diagnostic variables remain far from the defined threshold value $k_f = 0.08$ in both cases. This means that the defined diagnostic variables present an inherent immunity against strong transients, making the developed algorithm very robust against the issue of false alarms.

5.3.1.4 Threshold Values Selection

The correct selection of the used threshold values is critically important for the correct algorithm diagnostic performance. In a similar way to the majority of the existing open-circuit fault diagnostic techniques, the definition of the threshold values is accomplished by analyzing the diagnostic variables behavior for the healthy case and all faulty modes. Then, the values are set taking into account a tradeoff between a fast diagnosis and the robustness against the issue false alarms.

According to this, the selection of the threshold value for k_f is based on the behavior analysis of the diagnostic variables e_k under normal operating conditions and for a single open-circuit fault.

The obtained results show that the diagnostic variable related to the faulty phase assumes a value within the range of 0 and 0.25. This means that, theoretically, k_f can have a value within this range, where a low value means fast detection speed but worse robustness against false diagnostics. On the contrary, a large value greatly increases the algorithm robustness but decreases its diagnostic speed. However, the recommended procedure consists of analyzing first the diagnostic variables behavior for the worst case scenario. It is known that the majority of the existing methods fail (by generating false alarms) for these extreme situations since there are very fast variations and the currents become very small, which lead to incorrect average values calculation. All these problematic issues are presented for the transient shown in Figure 5.9a. From these results it can be verified that after the transient, the e_k oscillations increase but their amplitude are always below 0.012. This means that this value could be used for k_f, assuring a good diagnostic behavior for the other less extreme operating conditions. However, it is always better to consider a safety margin and therefore, the considered value of 0.08 can guarantee a much more robust diagnostic. On the other hand, the maximum value of k_f should be lower than 0.25, since in practice the diagnostic variables may not reach this value. Considering all this and according to the obtained results, k_f can be chosen within the range between 0.012 and 0.2. It must be pointed out that, in case of a double power switch fault, for example in T1 and T3, the diagnostic variables related to the faulty phases converge to a value of approximately 0.14. Therefore, if multiple power switch open-circuit fault diagnosis is considered, the selection range for k_f must be limited between 0.012 and 0.12.

The selection of k_d is done by analyzing the behavior of the diagnostic variables e_k for a single power switch open-circuit fault and for a same phase double fault. In this case, additional results show that the diagnostic variable associated to the faulty phase converges to a value of approximately 0.5 in case of a same leg double power switch failure. This means that the theoretical value for k_d can be chosen within the range between 0.25 and 0.5. In order to guarantee a safety margin, in practice this range must be adjusted between 0.28 and 0.47.

It must be noticed that as the diagnostic variables are normalized, these thresholds can be considered universal since they do not depend on the motor rated power, its operating load level and mechanical speed.

5.3.2 Normalized Reference Current Errors

5.3.2.1 750 rpm Operation

Figure 5.10 presents the experimental results regarding the time-domain waveforms of the PMSM phase currents, the main diagnostic variables and auxiliary variables for a mechanical speed of 750 rpm and for a fault in IGBT T1.

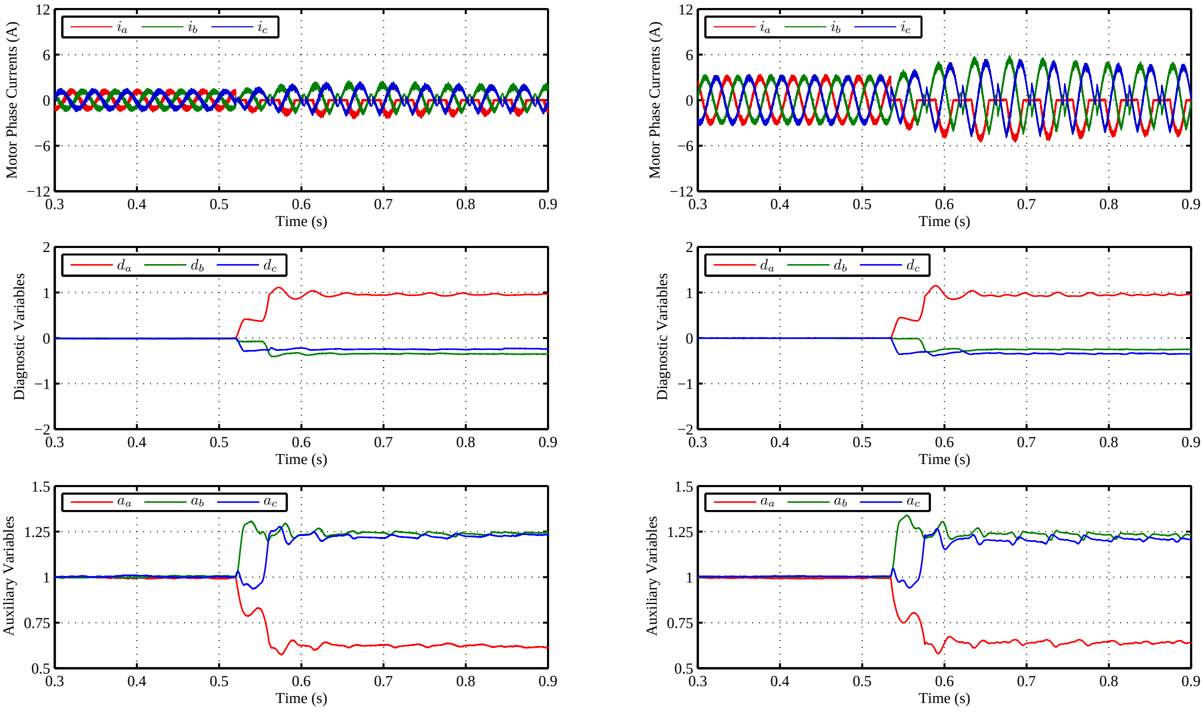

(a) (b)

Figure 5.10: Experimental results regarding the time-domain waveforms of the PMSM phase currents, the main diagnostic variables and the auxiliary variables for a mechanical speed of 750 rpm and for a fault in IGBT T1; (a) 10% of load torque; (b) 50% of load torque.

Once more, comparing with the equivalent simulation results presented in Figure 5.5, it is also observed an excellent agreement between the results obtained from the simulation models and the experimental tests. Under normal operating conditions, the three motor phase currents follow their corresponding reference signals and, therefore, the diagnostic variables are zero. After the fault occurrence, the d_a diagnostic variable increases and converges to a final value of approximately 1. The two remaining variables decrease and converge to steady-state values equal to the ones obtained for the simulation results.

Regarding the auxiliary variables, their behavior is also very similar to the equivalent one observed for the simulation results. Consequently, considering all this, the same fault signature is also generated, correctly identifying the faulty IGBT T1.

For the case shown in Figura 5.10a, a detection speed equivalent to 5.7% of the motor phase currents fundamental period is achieved, while a value of 5.5% is obtained for the case in depicted in Figure 5.10b.

5.3.2.2 1200 rpm Operation

For the PMSM operation at a reference speed of 1200 rpm, Figure 5.11 presents the experimental results regarding the time-domain waveforms of the motor phase currents, the main diagnostic variables and auxiliary variables for a fault in IGBT T1.

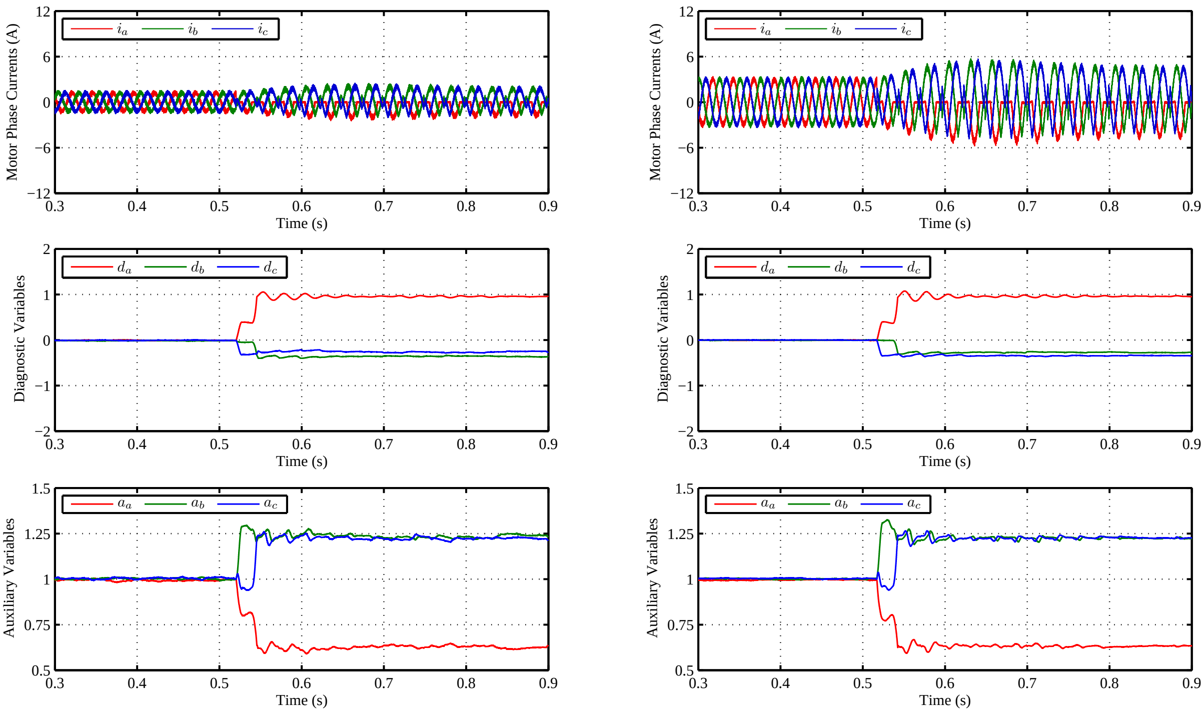

(a)

(b)

Figure 5.11: Experimental results regarding the time-domain waveforms of the PMSM phase currents, the main diagnostic variables and the auxiliary variables for a mechanical speed of 1200 rpm and for a fault in IGBT T1; (a) 10% of load torque; (b) 50% of load torque.

Comparing with the previous case, despite the motor higher speed operation, it can be seen that for both load torque situations, all the main diagnostic variables as well as the auxiliary variables, converge to approximately the same steady-state values. Furthermore, these results are also virtually equal to the ones obtained from the computational simulations. Therefore, the same fault signature is generated, effectively diagnosing the inverter IGBT T1 as the faulty semiconductor.

With respect to the algorithm detection speed, a value equivalent to 5.6% and 5.9% of the currents period is obtained for the cases in Figure 5.11a and Figure 5.11b, respectively.

The analysis of the experimental results obtained for the different speed and load torque values, also confirms that this algorithm behavior also does not depend on the machine operating conditions.

5.3.2.3 Load Transients Analysis

Figure 5.12 presents the experimental results regarding the time-domain waveforms of the motor phase currents, the main diagnostic variables and the auxiliary variables for load torque transients at a reference speed of 1200 rpm.

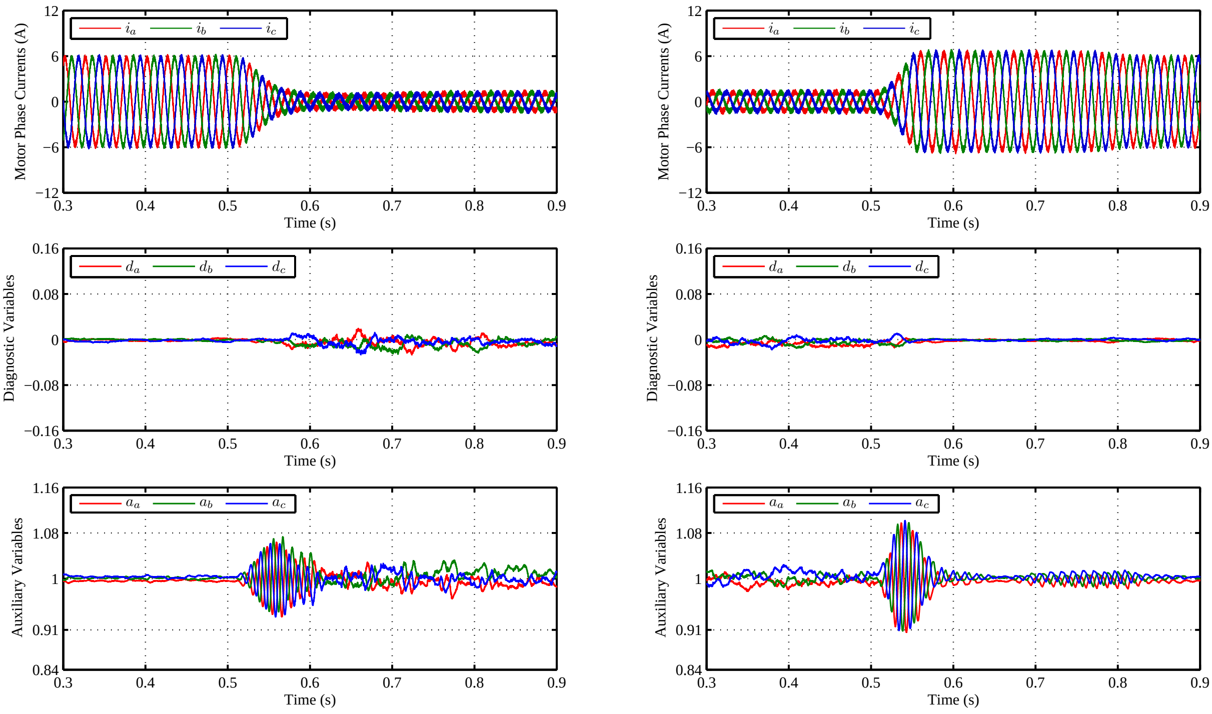

(a) (b)

Figure 5.12: Experimental results regarding the time-domain waveforms of the PMSM phase currents, the main diagnostic variables and the auxiliary variables for load transients; (a) rated load to no-load; (b) no-load to rated load.

In analogy to the load transient analysis performed for the first developed algorithm, the same behavior is also seen. For the PMSM full load torque operation, the motor phase currents present less distortion, resulting in more exact calculation of the average quantities, leading to more stable values around zero. For no-load operating conditions, the motor phase currents waveforms present a more noticeable distortion. This results in a less precise calculation of the average values, observed by the arising of more visible oscillations around zero.

In spite of this fact and considering these strong and fast load variations, all the diagnostic variables remain far from the defined threshold value $k_f = 0.08$ in both cases. Hence, it is also demonstrated the great robustness of the developed technique against the issue of false diagnostics.

5.3.2.4 Threshold Values Selection

As said before, the correct selection of the threshold values is accomplished by analyzing the diagnostic variables behavior for the healthy and all faulty scenarios, resulting in final tradeoff between a fast diagnosis and the robustness against the issue false alarms.

For this algorithm, the choice of k_f is based on the fact that if more than two power switches fail at exactly the same instant, the initial behavior is always equivalent to a single fault in one of them. Therefore, Table 5.2 can be used to rapidly diagnose one of the faulty devices using k_f. Hence, for the selection of its value, the behavior of d_k under normal operating conditions and for a single fault is considered. For these two cases, the absolute values of these variables are between 0 and 1. However, by analyzing the behavior for an extreme scenario shown in Figure 5.12a, it can be verified that the absolute values of d_k are always below 0.025, meaning that a value higher than this must be used to avoid false alarms. Therefore, considering a safety margin, the chosen value of 0.08 can guarantee a much more robust diagnostic. On the other hand, the maximum value of k_f should be lower than 1, since in practice the diagnostic variables may not reach this value. Considering all this and according to the obtained results, k_f can be chosen within the range between 0.025 and 0.9.

The selection of k_m is done by analyzing the behavior of the variables d_k for single faults and multiple faults (excluding double faults in the same inverter leg). For a single fault, the values of $|d_k|$ (corresponding to the faulty leg) will converge to almost 1 while the other two converge to values below 0.36. Further results show that for multiple faults, they will converge to about 1 and 0. Therefore, and taking also into account a safety margin, k_m can be chosen to be between 0.4 and 0.9. It must be noticed that in order to maintain the diagnostic coherence, the condition $k_f \leq k_m$ must be verified.

The threshold k_d is the less important one since it is only used for same inverter leg double faults. Excluding these specific faults, the values taken by a_n are always greater than 0.5. When this fault type occurs, one of the variables will fall to practically zero. Hence, and assuring also a safety margin, k_d can assume a value between 0.4 and 0.05.

It is worth noting that if a fast diagnosis is not a major requirement (since the lower limit of k_m is higher than for k_f), the threshold k_f and Table 5.2 can be neglected and only Table 5.3 can be used.

In a similar way to the previous algorithm, as the diagnostic variables are normalized, these thresholds can be considered universal since they do not depend on the motor rated power, its operating load level and mechanical speed.

5.4 Final Remarks

An extensive literature survey on inverter fault diagnostic methods for two-level inverters has been presented in this chapter. Moreover, two new real-time algorithms for open-circuit fault diagnosis in voltage fed-PWM motor drives were developed and presented.

Both methods were exhaustively tested and validated through various simulation and experimental results. The obtained data allow to demonstrate the excellent agreement between the theoretically predicted results and the experimental ones. It is worth noting that despite of only a fault in the IGBT T1 of phase a was considered, further simulation and experimental results have demonstrated that an equivalent behavior is also observed for the other five remaining cases, being therefore applied the same analysis.

The developed algorithms just use, as inputs, variables that are already available from the main control system. This means that comparing with other techniques, they avoid the use of extra sensors or electric devices and the subsequent increase of the system complexity and costs. They can also handle with extreme and fast transients, without emitting false diagnostics. Furthermore, thanks to the use of normalized quantities, their behavior does not depend neither on the motor rated power, and its load level, nor on its mechanical speed. Accordingly, universal threshold values can be defined, independently of these issues.

The thresholds values are empirically established through the analysis of the diagnostic and auxiliary variables behavior under faulty conditions and for the occurrence of extreme transients. Therefore, the values must be selected in order to handle extreme transients, avoiding the issue of a false diagnostic, and guarantee that they are reached in case of a fault. This results in a trade-off between the algorithms robustness against false diagnostics and their corresponding detection speed.

Beyond the threshold values, the algorithms detection speed also depends on the time instant of the fault occurrence. If a fault occurs during a positive current half-cycle and in the top IGBT of that phase, the effect can be clearly seen since the current tends immediately to zero. An equivalent result is also verified during a negative current half-cycle for a fault in the respective bottom transistor of that phase. For these cases, the detection and localization is, typically, relatively fast. However, if the fault occurs during a current half-cycle where the faulty IGBT does not immediately affect it, the fault effects will just be noticed at the next current half-cycle. Under these conditions, the fault can remain undetected for a period of time that can reach more than one-half of the motor phase currents fundamental period.

Considering all this, additional experimental tests allow to verify that the diagnostic detection speed for the algorithm based on the errors of the normalized currents average absolute values, can be as fast as 11% and as slow as 77% of the motor phase currents fundamental period. For the method based on the normalized reference currents errors, the detection speed oscillates within 5% and 67%. This can be considered quite fast since, comparing with the majority of the existing methods, the diagnostic is typically accomplished in practically one fundamental period.

The developed diagnostic algorithms are also much more simple since they just require a few and basic mathematical operations. This make them not computationally demanding and therefore, they can be easily integrated into the main control system without great effort.

Chapter 6

Fault-Tolerant Strategies

The fault-tolerant remedial strategies that can be applied to variable speed AC drives based on two-level inverters, can be broadly classified into two fundamental fault-tolerant converter topologies: the non-redundant topologies and the redundant ones. For the redundant converters, typically extra inverter legs are added (at least one) and used as back-up units, as an alternative to the faulted ones. Regarding the non-redundant configurations, in general they only use supplementary and cheaper devices that create a different path for load current flow without any additional redundant devices. As a result, the non-redundant topologies are cheaper than the redundant ones, and may be considered acceptable in some applications, requiring also a slightly modification of the control strategy. On the other hand, redundant topologies are more expensive but present the advantage of integrally saving the drive system operation.

Considering first the non-redundant fault-tolerant strategies group, there are two basic configurations that can be applied to variable speed AC drives. The first one comprises the connection of the faulty inverter phase to the DC link capacitors midpoint through triacs (Figure 6.1a) and the second one consists of the machine neutral point connection to the DC link capacitors midpoint (Figure 6.1b).

Several research work can be found in the literature regarding the faulty phase connection to the capacitors midpoint topology [195]-[206]. For this situation and assuming a three-phase machine, the fault-tolerant converter is based on the typical three-phase six switch inverter with three additional triacs that connect each motor phase to the DC bus capacitors midpoint (Figure 6.1a). Under normal operating conditions all triacs are off. For the post-fault operating conditions, the motor is supplied by the two healthy phases, being the faulty phase connected to the DC link through the corresponding triac. Under these circumstances, the machine is fed by a four-switch three-phase power converter that still allows the machine rated torque operation. However, this converter will generate non-balanced voltage space vectors that limit the voltage phasor amplitude to a value equivalent to one-half of the one obtained under normal operating conditions. As a consequence, for the post-fault operating mode, the motor mechanical speed must be limited to

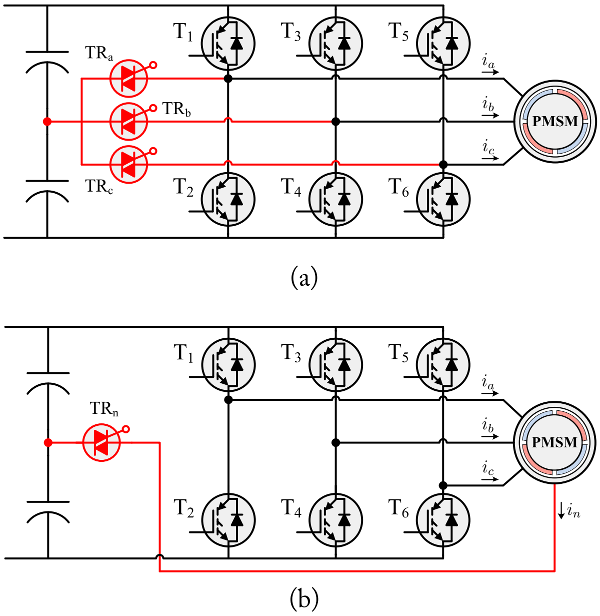

Figure 6.1: Non-redundant two-level power converter topologies: (a) phase connection to capacitors midpoint; (b) neutral connection to capacitors midpoint.

one-half of its rated value in order to allow rated torque production with minimum torque ripple.

Further than this mechanical speed limitation under post-fault operating conditions, other software modifications may be required. If a vector control strategy with hysteresis current controllers is used, no additional software changes are required. On the other hand, if a different modulation strategy such as SVM is used, due to the incapability of generating zero voltage vectors after the inverter reconfiguration, the modulation technique must be changed and adapted to a three-phase four-switch inverter topology [207]-[222]. Another important issue that must be taken into account when this modulation technique is used is the voltage unbalance across the two DC link capacitors, that may lead to a large DC link voltage ripple. With the aim to compensate for this problem, dedicated modulation strategies can be used [223]-[227].

For the case of DTC variable speed PMSM drives, the control strategy must be also changed in order to optimize the drive overall performance. Basically, this is accomplished by changing the voltage vectors selection for each sector [228]-[234].

For the second non-redundant topology shown in Figure 6.1b, the fault-tolerant converter is based on the typical three-phase six switch inverter with one additional triac that connects the motor neutral point to the DC bus capacitors midpoint [201]-[206], [235]-[239]. Comparing with the first topology and taking into account the number of supplementary power devices and connections, this one is simpler and less expensive. However, some disadvantages can be pointed out to this configuration. Beyond the PMSM neutral point availability, the motor mechanical speed must be limited to about 75% of its rated value in order to avoid electromagnetic torque pulsation. With the aim to reach the same magnetomotive force obtained under normal operating conditions, for the post-fault operation, the motor phase currents must increase by a factor of $\sqrt{3}$ with an imposed phase-shift of 60º. As a consequence, either the inverter and the motor must be overdimensioned, increasing the overall system cost, or the post-fault available torque must be limited to $1/\sqrt{3}$ of the machine rated torque. Additionally, more power losses are generated due to the larger current values. In a similar way to the previous topology, this reconfiguration does not allow the inverter to generate zero voltage vectors. As a result, the same post-fault control strategies are also applied to SVM or DTC.

Considering now the redundant fault-tolerant topologies, there are also two basic configurations that can be applied to two-level inverters in variable speed AC drives. The first one consists of the connection of the faulty inverter phase to an extra inverter leg through triacs (Figure 6.2a) and the second one comprises the machine neutral point connection to an inverter additional leg (Figure 6.2b).

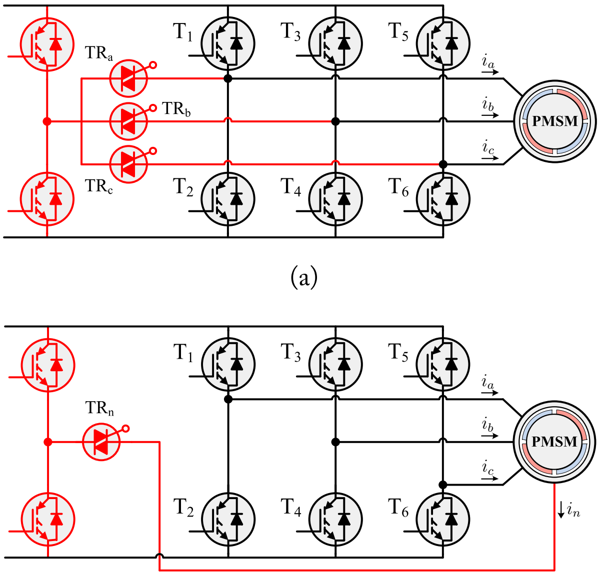

(a)

(b)

Figure 6.2: Redundant two-level power converter topologies: (a) phase connection to an extra inverter leg; (b) neutral connection to an extra inverter leg.

Regarding the first reconfiguration, after detected and localized the inverter faulty phase, the affected motor phase is connected to an extra inverter leg through a triac. As a result and considering a three-phase machine, the fault-tolerant power converter comprises a four-phase VSI with three additional triacs that connect each motor phase to the inverter extra phase [240]-[245]. As expected, this topology presents the great advantage of allowing the post-fault operating conditions to be the same as the normal ones, requiring just a hardware reconfiguration and the redirection of the gate signals from the faulty inverter phase to the extra one. However, this is accomplished at a larger cost since this topology requires more power semiconductors, including two more extra power switches for the fourth leg with the same specifications of the conventional inverter.

Finally, for the topology shown in Figure 6.2b, the motor neutral point is connected through a triac to an inverter extra leg [246]-[255]. Comparing to the previous redundant fault-tolerant converter, beyond the same requirement of an inverter additional phase, this one just needs one triac instead of three, contributing to the decrease of the global system complexity and cost. Nevertheless, under post-fault operating conditions, this power converter does not allow the drive to maintain the same performance level as for the healthy case. In similar way to the converter depicted in Figure 6.1b, in order to produce the same magnetomotive force obtained for normal operating conditions, the motor phase currents must increase by a factor of $\sqrt{3}$ with a phase-shift of 60º. Consequently, either the inverter and the motor must be oversized or the post-fault available torque must be limited to $1/\sqrt{3}$ of the machine rated torque. Regarding the post-fault control strategies, no additional changes are required beyond the redirection of the gate signals from the faulty inverter phase to the extra one.

A different group of two-level fault-tolerant power converters comprises the use of VSIs in series architecture [256]-[258], as depicted in Figure 6.3.

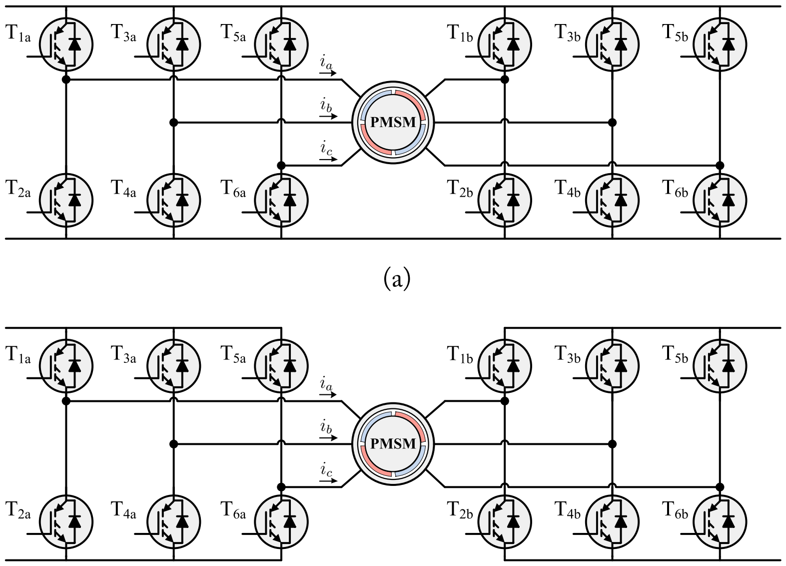

(a)

(b)

Figure 6.3: Series fault-tolerant converter topologies: (a) same DC supply; (b) two independent DC sources.

There are two variants for this configuration: in the first one, both VSIs are supplied by the same DC voltage, which is the same of supplying the motor by a three-phase H-bridge converter (Figure 6.3a), and the other one consists of supplying each inverter by independent DC electrical sources (Figure 6.3b).

Due to the higher number of power switches (twice in comparison with the typical two-level inverter), these power converters present an inherent fault-tolerant capability.

Under a single power switch open-circuit fault, it is possible to create a neutral point with the remaining healthy devices, allowing the machine operation. However, this also reduces the voltage vectors applied to the machine, and consequently, the maximum mechanical speed achievable. Another way is to simply force the current in the faulty phase to zero and generate new reference currents for the two healthy phases in order to compensate for the electromagnetic torque ripple or power losses.

In case of a power device short-circuit in any of the two converters, after guarantee the pulse inhibition to the complementary device, a neutral point can be created using the healthy power switches. Although there is a mechanical speed limitation due to the reduced voltage applied by the converter, this strategy allows the drive operation under faulty conditions.

In this work, only the two non-redundant fault-tolerant power converter topologies shown in Figure 6.1 are considered. This choice is justified by the fact that these reconfigurations require less supplementary and cheaper components, comparing to the redundant ones, making them very attractive. Furthermore, the non-redundant topologies are more interesting to exploit and analyze since due to their specific limitations, they require additional control modifications in order to optimize the drive performance.

6.1 Post-Fault Control Strategies

Beyond the hardware reconfiguration, the post-fault control strategies applied to the non-redundant power converters must include some specific changes/modifications in order to adapt them to the corresponding converter topology and to the implemented drive control and modulation schemes. In this way, it is possible to improve the PMSM global drive performance under post-fault operating conditions.

The remedial post-fault control strategies for the three considered control techniques (SVM vector control, HCC vector control and DTC) are presented and analyzed in the next subsections. All these control methods are evaluated for the previously described non-redundant fault-tolerant converter topologies. The first one is based on a motor phase to capacitors midpoint (PCM) connection, shown in Figure 6.1a, while the second one consists of the neutral to capacitors midpoint (NCM) reconfiguration, shown in Figure 6.1b.

6.1.1 SVM Vector Control

Considering a fault in the inverter phase a, under post-fault operating conditions the converter is reconfigured in order to isolate the faulty phase and connect the corresponding PMSM phase to the DC link capacitors midpoint, as illustrated in Figure 6.4.

Under these circumstances, the PMSM is no longer fed by a three-phase six-switch inverter topology, being supplied by a three-phase four-switch reconfigured power converter. Since the motor phase a is connected to the DC link capacitors midpoint, the generated voltage vectors will

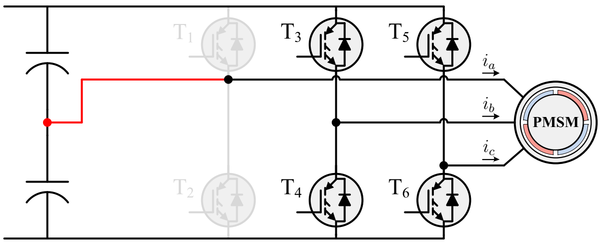

Figure 6.4: Fault-tolerant converter for a PCM reconfiguration with a fault in phase a.

be different when comparing to the healthy case. As a result, for this case the PMSM phase voltages are given by:

$$\begin{bmatrix} v_a \\ v_b \\ v_c \end{bmatrix} = \frac{V_{dc}}{3} \begin{bmatrix} 2 & -1 & -1 \\ -1 & 2 & -1 \\ -1 & -1 & 2 \end{bmatrix} \begin{bmatrix} 1/2 \\ S_b \\ S_c \end{bmatrix} \tag{6.1}$$

In order to calculate the generated voltage space vectors, equation (3.9) can be applied, which is equivalent to use the transformation from abc quantities to $\alpha\beta$ components in the stationary reference frame, defined by (3.10). Therefore, by substituting (6.1) in (3.10), the voltage space vector components are obtained:

$$\begin{cases} v_\alpha = \frac{1}{3} V_{dc} \left(1 - S_b - S_c\right) \\ v_\beta = \frac{1}{\sqrt{3}} V_{dc} \left(S_b - S_c\right) \end{cases} \tag{6.2}$$

As a result, for the PCM reconfiguration, there are only four active vectors available and no zero vectors, as shown in Figure 6.5.

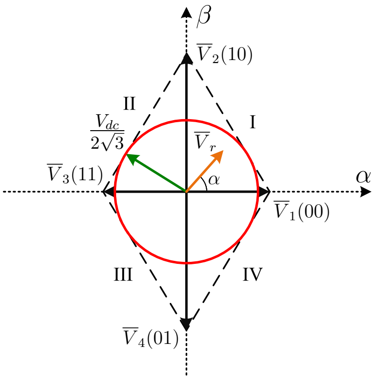

Figure 6.5: Representation of the basic voltage vectors in the complex plane for a PCM reconfiguration with a fault in phase a.

The same theory can be applied for the equivalent inverter hardware connections for the other two cases. Following this, the voltage space vector real and imaginary components for the connection of phase b and c to the DC bus capacitors, are respectively given by:

$$\begin{cases} v_\alpha = \frac{1}{3}V_{dc}\left(2S_a - S_c - \frac{1}{2}\right) \\ v_\beta = \frac{1}{\sqrt{3}}V_{dc}\left(\frac{1}{2} - S_c\right) \end{cases} \tag{6.3}$$

$$\begin{cases} v_\alpha = \frac{1}{3}V_{dc}\left(2S_a - S_b - \frac{1}{2}\right) \\ v_\beta = \frac{1}{\sqrt{3}}V_{dc}\left(S_b - \frac{1}{2}\right) \end{cases} \tag{6.4}$$

By using these equations, the four active vectors generated for each reconfiguration can be represented in the complex plane as shown in Figure 6.6.

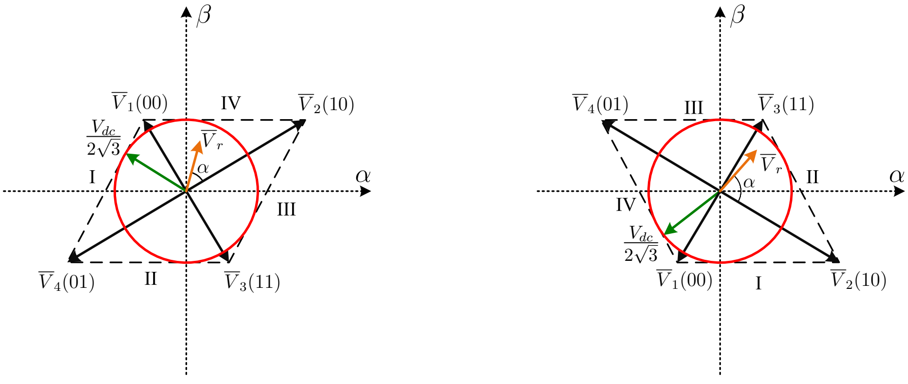

(a) (b)

Figure 6.6: Representation of the basic voltage vectors in the complex plane for a PCM reconfiguration with a fault: (a) in phase b and (b) in phase c.

Considering all this, it is clear that some software changes are mandatory in order to adapt and optimize the modulation strategy to the new inverter topology. In a similar way, the reference voltage vector $\overline{V}_r$, defined by the reference voltage components (v_α^*, v_β^*) calculated by the vector control, can be generated through an average relationship between the available active vectors. Assuming that $\overline{V}_r$ is on sector I (Figure 6.5), the voltage vectors $\overline{V}_1$ and $\overline{V}_2$ are used to synthetize it through the expression:

$$T_s\overline{V}_r = t_x\overline{V}_1 + t_y\overline{V}_2 + t_0\overline{V}_0 \tag{6.5}$$

The switching time duration of each vector t_x and t_y and the equivalent zero vector t_0 are given by:

$$\begin{cases} t_x = \left|\overline{V}_r\right| T_s \cos(\alpha) \,/\, \left|\overline{V}_1\right| = \dfrac{3\left|\overline{V}_r\right|}{V_{dc}} T_s \cos(\alpha) \\ t_y = \left|\overline{V}_r\right| T_s \sin(\alpha) \,/\, \left|\overline{V}_2\right| = \dfrac{\sqrt{3}\left|\overline{V}_r\right|}{V_{dc}} T_s \sin(\alpha) \\ t_0 = T_s - t_x - t_y \end{cases} \tag{6.6}$$

Since there are no zero vectors, the remaining time can be compensated by using two vectors with opposite direction, applied in a flyback mode for the same amount of time. Consequently, the flux linkage vector trajectory travels back and forward for the same period of time t_0, resulting in a virtual zero vector. With the available two pairs of opposite vectors ($\overline{V}_1$&$\overline{V}_3$ and $\overline{V}_2$&$\overline{V}_4$), the time t_0 can be distributed in different ways. Nevertheless, only three vectors are required to accurately define the required voltage vector $\overline{V}_r$. Considering this, two different approaches can be used: selecting two short vectors and one long or two long vectors and one short. The first approach is preferable since the use of long voltage vectors leads to larger voltage drop on inductive loads, generating larger ripple. The implemented approach takes this into account and is arranged in such a way that three different vectors are used in each sampling period which results in two main vectors used for both synthesizing the desired reference vector and compensating the remaining time, and another one used just to compensate the remaining time. The selection of the vectors is performed in five steps per switching period. The implemented vector sequence and timing plan is represented in Table 6.1.

Table 6.1: SVM voltage vectors sequence and timing plan for a phase a PCM reconfiguration

Sector	Voltage Vector Sequence	Voltage Vector Timing
I	$\overline{V}_1\to\overline{V}_2\to\overline{V}_3\to\overline{V}_2\to\overline{V}_1$	$(t_x+t_0/2)\to(t_y)\to(t_0)\to(t_y)\to(t_x+t_0/2)$
II	$\overline{V}_3\to\overline{V}_2\to\overline{V}_1\to\overline{V}_2\to\overline{V}_3$	$(t_y+t_0/2)\to(t_x)\to(t_0)\to(t_x)\to(t_y+t_0/2)$
III	$\overline{V}_3\to\overline{V}_4\to\overline{V}_1\to\overline{V}_4\to\overline{V}_3$	$(t_x+t_0/2)\to(t_y)\to(t_0)\to(t_y)\to(t_x+t_0/2)$
IV	$\overline{V}_1\to\overline{V}_4\to\overline{V}_3\to\overline{V}_4\to\overline{V}_1$	$(t_y+t_0/2)\to(t_x)\to(t_0)\to(t_x)\to(t_y+t_0/2)$

This table can also be used for PCM reconfiguration with a fault in the inverter phase c. However, for the situation where the PMSM phase b is connected to the DC capacitors midpoint, some additional considerations must be taken into account. As shown in Figure 6.6, the voltage vectors distribution in a counterclockwise sequence for a phase b PCM reconfiguration ($\overline{V}_1$, $\overline{V}_4$, $\overline{V}_3$ and $\overline{V}_2$) is different from the one observed for the other two cases ($\overline{V}_1$, $\overline{V}_2$, $\overline{V}_3$ and $\overline{V}_4$). Therefore, assuming the considered sector numeration, Table 6.1 can also be used by changing the selection of $\overline{V}_2$ by $\overline{V}_4$ and vice-versa. For all the three cases, the sector localization conditions (represented by the angle α) of the reference voltage vector must be considered.

Further than this modification on the modulation strategy, it is also verified that with a PCM reconfiguration, the maximum voltage space vector amplitude that can be applied to the machine in the linerar modulation range ($V_{dc}/2\sqrt{3}$) is reduced by one-half, when comparing with the healthy situation. This fact is illustrated by comparing the schemes presented in Figure 3.5 and Figure 6.5 (Figure 6.6). As a consequence, in order to allow rated load torque operation with minimum electromagnetic torque pulsation, the PMSM maximum operating speed must be limited to one-half of its rated value.

Regarding the NCM reconfiguration, Figure 6.7 illustrates the power converter post-fault operating condition for a fault in the inverter phase a, where after its isolation, the PMSM neutral point is connected to the DC link capacitors midpoint.

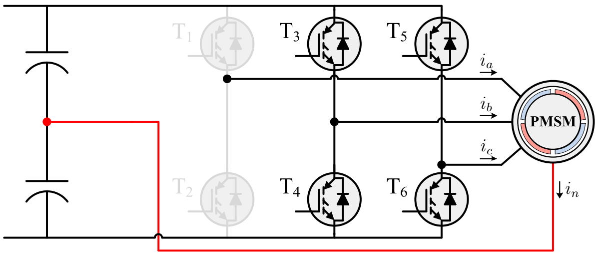

Figure 6.7: Fault-tolerant converter for a NCM reconfiguration with a fault in phase a.

In this topology, one of the motor phases is in open-circuit and as a result, its phase voltage is floating. In this case, the inverter generates voltage vectors with no well-defined amplitude and phase. Nevertheless, the average voltage space vector amplitude applied to the motor is also limited when comparing with the normal case, requiring therefore the mechanical speed limitation under post-fault conditions. Furthermore, this topology also does not allow the generation of zero vectors and therefore, the previously described modulation strategy is also used, optimizing this way the system performance. This leads to the increasing of the motor currents in the healthy phases by a factor of $\sqrt{3}$ and with a phase shift of 60° in order to maintain the same torque level. This will be described in a more detailed way in the next subsection.

6.1.2 HCC Vector Control

For a vector controlled PMSM drive using HCCs, the analysis is very similar to the previous one. Consequently, for a PCM reconfiguration, the voltage vector amplitude is reduced to one-half, leading also to the need of limiting the motor speed to one-half of its rated value, in order to maintain the capability of rated torque operation.

However, as in this case the PMSM phase currents are directly controlled using hysteresis comparators, by controlling the two healthy phases, the third one is also automatically imposed. As the machine neutral point is not connected, assuming a fault in phase a as depicted in Figure 6.4, the PMSM phase a current is imposed by the currents in phases b and c since $i_a = -i_b - i_c$. Consequently, there is no need for additional changes at the modulation strategy level, making this control strategy very simple to implement for a PCM converter topology.

Regarding the NCM reconfiguration, beyond the speed limitation, this topology requires special modifications when a HCC vector control strategy is used. Considering that N_{ef} is the effective number of stator turns per phase, the generated magnetomotive force $\overline{F}_s$ is calculated by:

$$\overline{F}_s = N_{ef}\left(i_a + a i_b + a^2 i_c\right) \tag{6.7}$$

Assuming that under normal operating conditions the PMSM is supplied by a three-phase balanced direct current system given by:

$$i_n = \begin{cases} i_a = I_m \cos\left(\omega t + \phi\right) \\ i_b = I_m \cos\left(\omega t - \frac{2\pi}{3} + \phi\right) \\ i_c = I_m \cos\left(\omega t + \frac{2\pi}{3} + \phi\right) \end{cases} \tag{6.8}$$

The obtained magnetomotive force under these circumstances is:

$$\overline{F}_s = \frac{3}{2} N_{ef} I_m e^{j\omega t + \phi} \tag{6.9}$$

For the NCM reconfiguration, the machine is fed by the inverter two healthy phases and its neutral is connected to the DC link capacitors midpoint. Assuming a fault in the inverter phase a, after the hardware isolation and reconfiguration the corresponding motor phase current becomes zero. In this case, the generated magnetomotive force is only given by the contribution of phase b and phase c currents:

$$\overline{F}_{s_f} = N_{ef}\left(a i_b + a^2 i_c\right) \tag{6.10}$$

With the objective to keep a magnetomotive force value under a NCM reconfiguration equal to the one generated under normal operating conditions, (6.10) must be equal to (6.9):

$$\frac{3}{2} N_{ef} I_m e^{j\omega t + \phi} = N_{ef}\left[\left(-\frac{1}{2} + j\frac{\sqrt{3}}{2}\right) i_b + \left(-\frac{1}{2} - j\frac{\sqrt{3}}{2}\right) i_c\right] \tag{6.11}$$

By solving the previous equation, the two reference motor phase currents of the inverter healthy phases can be obtained:

$$\begin{cases} i_{b_f} = \sqrt{3} I_m \left[-\frac{\sqrt{3}}{2}\cos\left(\omega t + \phi\right) + \frac{1}{2}\sin\left(\omega t + \phi\right)\right] \\ i_{c_f} = \sqrt{3} I_m \left[-\frac{\sqrt{3}}{2}\cos\left(\omega t + \phi\right) - \frac{1}{2}\sin\left(\omega t + \phi\right)\right] \end{cases} \tag{6.12}$$

These equations can also be rewritten in the form:

$$\begin{cases} i_{b_f} = \sqrt{3} I_m \cos\left(\omega t - \frac{2\pi}{3} + \phi - \frac{\pi}{6}\right) \\ i_{c_f} = \sqrt{3} I_m \cos\left(\omega t + \frac{2\pi}{3} + \phi + \frac{\pi}{6}\right) \end{cases} \tag{6.13}$$

From (6.13) it can be proven that the PMSM drive can operate under a NCM reconfiguration with a fault in phase a if the remaining healthy inverter phases are controlled in such a way that a phase shift of 60º between them is imposed, together with an amplitude increase by a factor of $\sqrt{3}$. This means that, the new phase b reference current is regulated to be retarded 30º in relation to the original one, and phase c current to be in advance by 30º (Figure 6.8).

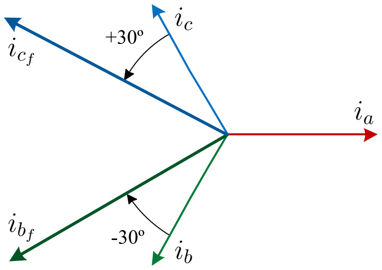

Figure 6.8: PMSM phase currents modification for a NCM reconfiguration with a fault in phase a.

In practice, these new reference currents are obtained by acting in the dq to abc transformation used for the HCC vector control. As a result, the new phase b and phase c reference currents are calculated as:

$$\begin{cases} i_b^* = \sqrt{3}i_d^* \cos\left(\theta - \frac{2\pi}{3} - \frac{\pi}{6}\right) - \sqrt{3}i_q^* \sin\left(\theta - \frac{2\pi}{3} - \frac{\pi}{6}\right) \\ i_c^* = \sqrt{3}i_d^* \cos\left(\theta + \frac{2\pi}{3} + \frac{\pi}{6}\right) - \sqrt{3}i_q^* \sin\left(\theta + \frac{2\pi}{3} + \frac{\pi}{6}\right) \end{cases} \tag{6.14}$$

Basically, a simple change is introduced in the transformation in order to add the phase shift of ±30º and to increase the amplitude by a factor of $\sqrt{3}$. By doing this, the same magnetomotive force generated under normal operating conditions is achieved, meaning that the same load torque operation is possible with minimum electromagnetic torque oscillation.

The same analysis can be applied for the cases where a NCM topology is considered with an inverter fault in phase b or phase c. Therefore, the reference currents that must be imposed to the inverter are:

$$\begin{cases} i_{a_f} = \sqrt{3}I_m \cos\left(\omega t + \phi + \frac{\pi}{6}\right) \\ i_{c_f} = \sqrt{3}I_m \cos\left(\omega t + \frac{2\pi}{3} + \phi - \frac{\pi}{6}\right) \end{cases} \tag{6.15}$$

$$\begin{cases} i_{a_f} = \sqrt{3}I_m \cos\left(\omega t + \phi - \frac{\pi}{6}\right) \\ i_{b_f} = \sqrt{3}I_m \cos\left(\omega t - \frac{2\pi}{3} + \phi + \frac{\pi}{6}\right) \end{cases} \tag{6.16}$$

The required modifications in the dq to abc transformation used in the HCC vector control strategy that allow to impose the necessary conditions are:

$$\begin{cases} i_a^* = \sqrt{3}i_d^* \cos\left(\theta + \frac{\pi}{6}\right) - \sqrt{3}i_q^* \sin\left(\theta + \frac{\pi}{6}\right) \\ i_c^* = \sqrt{3}i_d^* \cos\left(\theta + \frac{2\pi}{3} - \frac{\pi}{6}\right) - \sqrt{3}i_q^* \sin\left(\theta + \frac{2\pi}{3} - \frac{\pi}{6}\right) \end{cases} \tag{6.17}$$

$$\begin{cases} i_a^* = \sqrt{3}i_d^* \cos\left(\theta - \frac{\pi}{6}\right) - \sqrt{3}i_q^* \sin\left(\theta - \frac{\pi}{6}\right) \\ i_b^* = \sqrt{3}i_d^* \cos\left(\theta - \frac{2\pi}{3} + \frac{\pi}{6}\right) - \sqrt{3}i_q^* \sin\left(\theta - \frac{2\pi}{3} + \frac{\pi}{6}\right) \end{cases} \tag{6.18}$$

The diagrams showing the difference between the phasor relationships under normal and post-fault operating conditions are depicted in Figure 6.9.

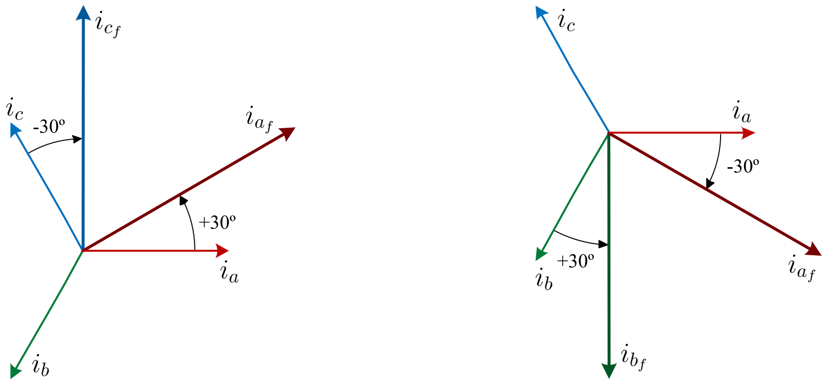

(a) (b)

Figure 6.9: PMSM phase currents modification for a NCM reconfiguration with a fault in: (a) in phase b and (b) in phase c.

Regarding the neutral current, it is determined by the sum of the two healthy currents. Therefore, for a fault in phase a ($i_a = 0$), the neutral current will be given by:

$$i_n = i_{b_f} + i_{c_f} \tag{6.19}$$

By substituting (6.13) in (6.19), the neutral current is obtained:

$$i_n = 3I_m \cos\left(\omega t + \phi + \pi\right) \tag{6.20}$$

From this equation it can be demonstrated that the current flow through the neutral conductor will be three times larger than the original line current value obtained for the normal case. The same conclusion is observed for a NCM reconfiguration with a fault in phase b or phase c, respectively:

$$i_n = 3I_m \cos\left(\omega t + \phi + \frac{\pi}{3}\right) \tag{6.21}$$

$$i_n = 3I_m \cos\left(\omega t + \phi - \frac{\pi}{3}\right) \tag{6.22}$$

Hence, special attention must be given to the proper design of the DC link capacitors since they must be able to withstand large current values, avoiding overheating problems and keeping simultaneously an acceptable DC link voltage ripple value.

6.1.3 Direct Torque Control

Under normal operating conditions, six active voltage vectors and two zero vectors are available to control the PMSM. However, for a PCM reconfiguration, it was already demonstrated that only four active voltage vectors can be applied to the machine. These can be calculated using the DC link voltage and the inverter switching states for the three PCM reconfigurations, using equations (6.2), (6.3) and (6.4). The voltage vectors distribution in the complex plane are represented in Figure 6.5 and Figure 6.6. As a result, the average amplitude of the rotating voltage space vector is also limited to one-half of the value under normal operating conditions, imposing the need to limit the PMSM mechanical speed after the converter reconfiguration.

In addition, due to the different vectors distribution generated by the PCM topology, the DTC optimum switching table derived for normal operation must be modified in order to take into account the correct selection of the new voltage vectors.

Assuming a PCM reconfiguration with a fault in phase a and considering that the stator flux vector is located in Sector I, the voltage vectors selection is illustrated in Figure 6.10.

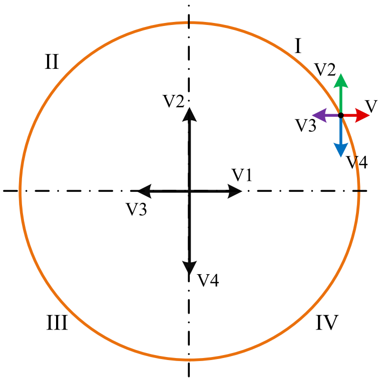

Figure 6.10: Voltage vectors selection for DTC.

If it is required to increase the torque in order to achieve a counter-clockwise rotation, $\overline{V}_2$ should be used to increase the stator flux linkage amplitude and, otherwise, $\overline{V}_3$ to decrease its amplitude. On the contrary, if the stator flux is moving in a clockwise direction (negative torque) also in the same region, $\overline{V}_1$ should be used to increase the amplitude and $\overline{V}_4$ to decrease it.

For the PCM converter topology, zero vectors cannot be generated. As explained in Section 3.3, under normal operating conditions, typically zero vectors are not used in the DTC of PMSMs. Therefore, no extra control modifications are required, namely at the level of the electromagnetic torque and flux hysteresis controllers, which means that only the switching table and the sector location conditions must be changed.

Considering all this, the new optimum switching table for the DTC under a phase a PCM reconfiguration is presented in Table 6.2.

The same theory can also be extended to the other two remaining cases of the PCM reconfiguration. Therefore, by analyzing the voltage vectors distribution shown in Figure 6.5 and Figure 6.6, it can be verified that the same optimum switching table shown in Table 6.2 can be directly applied for a fault occurrence in the inverter phase c. For the case of a phase b PCM reconfiguration, Figure 6.6 shows that the voltage vectors distribution in a counter-clockwise sequence ($\overline{V}_1$, $\overline{V}_4$, $\overline{V}_3$ and

Table 6.2: DTC voltage vectors switching table for a phase a PCM reconfiguration.

Flux	Torque	Section			
		I	II	III	IV
F⁻	T⁻	$\overline{V}_4$	$\overline{V}_1$	$\overline{V}_2$	$\overline{V}_3$
	T⁺	$\overline{V}_3$	$\overline{V}_4$	$\overline{V}_1$	$\overline{V}_2$
F⁺	T⁻	$\overline{V}_1$	$\overline{V}_2$	$\overline{V}_3$	$\overline{V}_4$
	T⁺	$\overline{V}_2$	$\overline{V}_3$	$\overline{V}_4$	$\overline{V}_1$

$\overline{V}_2$) is different from the one for the other two cases ($\overline{V}_1$, $\overline{V}_2$, $\overline{V}_3$ and $\overline{V}_4$). As a consequence and considering the sector numbering, the same DTC switching table can also be used by changing the selection of $\overline{V}_2$ by $\overline{V}_4$ and vice-versa. For all the three cases, the sector localization conditions of the stator flux vector must be considered.

For a NCM reconfiguration, the inverter applies to the PMSM voltage vectors with no well-defined amplitude and phase due to the floating voltage of the affected motor phase. Nonetheless, comparing with the healthy case, the average voltage space vector amplitude applied to the motor is also limited, leading to the need of limiting the post-fault mechanical speed. Additionally, no zero voltage vectors can also be generated by this inverter topology, which means that the same DTC switching tables derived for the PCM reconfiguration can be used to optimize the global drive performance.

In a similar way to the previous cases, in order to maintain the same torque level, the motor currents in the healthy phases must increase by a factor of $\sqrt{3}$ with a phase shift between them of 60º. This also leads to a neutral current value three times higher than the one obtained for the phase currents under normal operating conditions. Therefore, special attention must be given to the DC bus capacitors dimensioning.

6.2 Fault-Tolerant Control System

With the aim to develop a fully integrated fault-tolerant PMSM drive, the control system must be designed in such a way to be able to perform some critical tasks. Figures 6.11 to 6.13 present the block diagram schematic representation of the fault-tolerant control system for the three considered PMSM control strategies.

The most important feature is the fault-tolerant control system capability to accomplish four critical steps: fault diagnosis, inverter faulty leg isolation, hardware reconfiguration and post-fault control modification.

Regarding the first step, the control system must integrate an algorithm that allows the real-time fault detection and localization of inverter power switch open-circuit faults. As a consequence, this algorithm must present some important features such as reliability, operating conditions independence, the requirement of no extra sensors and must have low hardware requirements in order

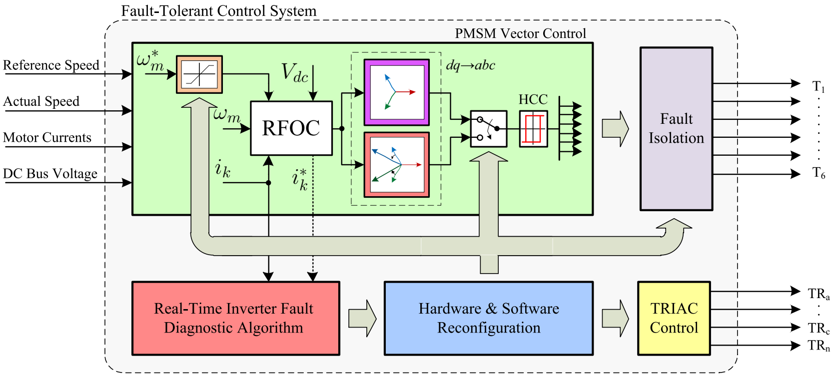

Figure 6.11: Fault-tolerant control system block diagram for the HCC vector control strategy.

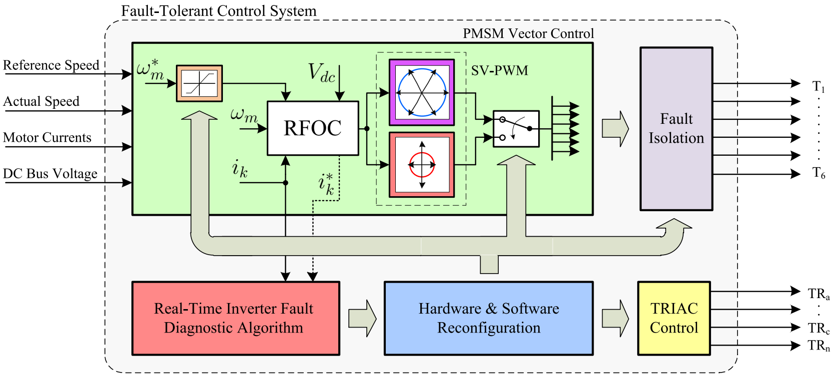

Figure 6.12: Fault-tolerant control system block diagram for the SVM vector control strategy.

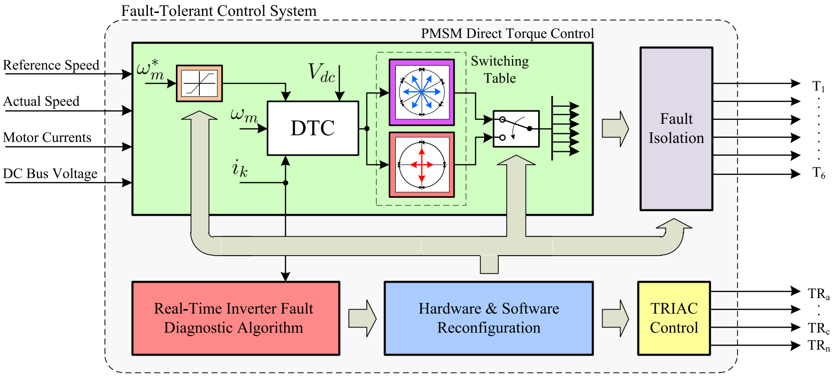

Figure 6.13: Fault-tolerant control system block diagram for the DTC control strategy.

to avoid as much as possible the additional computational burden on the drive controller. Indeed, the two developed real-time algorithms discussed in Chapter 5 allow to completely fulfill these requirements.

For the second stage, the information provided by the fault diagnostic algorithm regarding the faulty phase is then used to remove the two IGBT gate command signals of the affected phase in order isolate the corresponding PMSM phase.

The next step is to perform the hardware reconfiguration by triggering the triac that changes the inverter topology according to the desired one. Therefore, for a PCM hardware reconfiguration, the corresponding triac (TR_a, TR_b or TR_c) is turned on in order to connect the isolated motor phase to the DC bus capacitors midpoint. On the other hand, for the case of a NCM reconfiguration, the triac TR_n is activated, connecting the PMSM neutral point to the DC link capacitors midpoint.

Finally, and as described in the previous section, some software modifications are required in order to adapt the post-fault control strategy to the new converter topology, optimizing the drive overall performance. Accordingly, for a SVM vector control strategy, the modulation process is changed taking into account that only four active space vectors are available. For the HCC vector control strategy with a NCM reconfiguration, the dq to abc transformation must be changed according to the faulty phase and imposing an amplitude increase of $\sqrt{3}$ and a phase shift of 60º. For the PCM reconfiguration there is no need to act at this level. Regarding the DTC, the optimum switching table must be changed according to the different four voltage space vectors. Moreover, for all the control strategies, the PMSM operating speed must be limited according to the post-fault converter topology in order to minimize the electromagnetic torque pulsation.

In general, after the fault occurrence, the execution of all these four steps can be accomplished in a relatively fast time interval (less than one fundamental period), depending on the time taken by the fault diagnostic algorithm to detect and localize the fault. Indeed, the transition between the last three steps can be performed in a few miliseconds, or even microseconds, while the first step duration is strongly dependent on the diagnostic algorithm performance.

6.3 Simulation Results

The developed fully integrated fault-tolerant PMSM drive was simulated using the models implemented in the Matlab/Simulink software. The same conditions and parameters defined for the normal and faulty operation analysis were also used. The three fault-tolerant control systems presented and discussed in the previous section were also implemented into the existing mathematical models.

Simulation results are presented showing the drive transient behavior during all the reconfiguration process and for the final steady state waveforms. In the first case, a step-by-step examination is performed by analyzing each of the four reconfiguration stages that take place immediately after the fault occurrence. In order to accomplish this, a time delay equal to 200 ms was imposed between each reconfiguration stage. For the final steady state analysis, the PMSM drive behavior under the post-fault operating strategies already discussed is investigated. In this case, and in order to allow a good comparison to the drive healthy and faulty behavior, the same load conditions of 750 rpm and 7 Nm are also assumed for all situations.

All the results taken for both PCM and NCM reconfigurations were obtained assuming an inverter open-circuit fault in IGBT T1 (top power switch in phase a).

6.3.1 PCM Reconfiguration

6.3.1.1 HCC Vector Control

Considering first the drive transient analysis during all the reconfiguration process, Figure 6.14 presents the simulation results regarding the step-by-step drive behavior for a HCC vector control strategy under a motor reference speed of 900 rpm and a load torque equivalent to 35%.

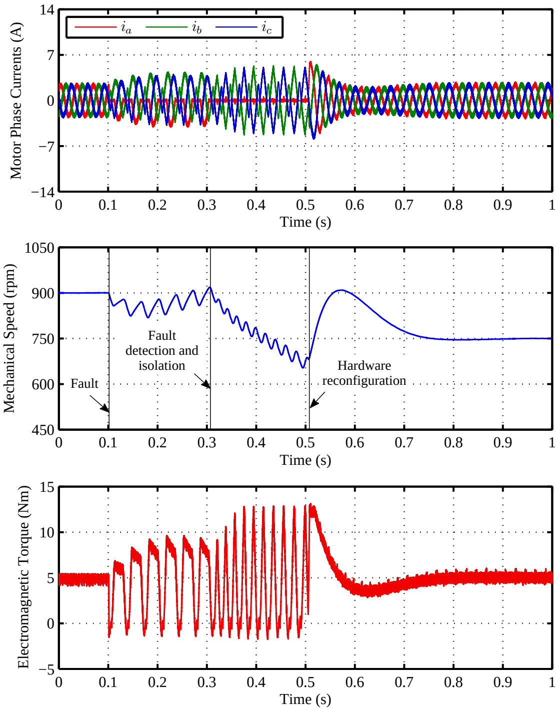

Figure 6.14: Simulation results regarding the reconfiguration process for a HCC vector control strategy under a phase a PCM reconfiguration.

During the first instants the PMSM is supplied by a balanced three-phase current system, working at a constant mechanical speed of 900 rpm and with a smooth electromagnetic torque equivalent to the imposed load torque level.

At the instant $t = 0.1\ s$, a fault in the inverter IGBT T1 is introduced. Under these faulty operating conditions, there is no current flowing in phase a during the positive half-cycle due to the damaged power switch. As a result, the three motor phase currents become highly distorted, leading to a pulsating electromagnetic torque waveform and the arising of mechanical speed oscillations.

Then, at the instant $t = 0.3109\ s$, the real-time fault diagnostic algorithm effectively diagnose the faulty IGBT and the corresponding inverter phase. This information is then used by the fault-tolerant control system that immediately proceeds to the fault isolation by inhibiting the gate command signals for the two inverter power switches. Consequently, during this stage, there is no current flowing through the PMSM phase a, being the machine supplied by the only two healthy phases. This results in an even larger electromagnetic torque pulsation at twice the frequency of the motor phase currents, leading to the decrease of the motor mechanical speed.

Finally, 200 ms after, the power converter topology is reconfigured by triggering on the triac TR_a, connecting the PMSM phase a to the DC bus midpoint capacitors. At this stage, the fault-tolerant control also proceeds to the limitation of the motor operating speed to one-half of its rated value.

Regarding the steady-state analysis, Figure 6.15 presents the time-domain waveforms of the PMSM phase currents for a HCC vector control strategy under a PCM reconfiguration.

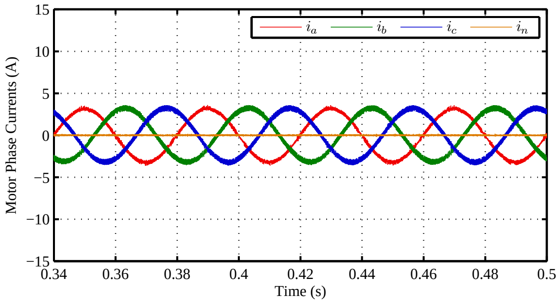

Figure 6.15: Simulation results of the time-domain waveforms of the PMSM phase currents for a HCC vector control strategy under a phase a PCM reconfiguration.

The results allow to verify that under post-fault operating conditions the PMSM is supplied by a balanced three-phase current system, very similar to the healthy case. Nevertheless, by comparing with the healthy phases or with the equivalent simulation results obtained for normal operating conditions shown in Figure 3.8, it is possible to see that the phase a current presents less ripple. This is justified by the connection of this phase to the DC bus midpoint, leading to a lower voltage rms value and therefore, a small decrease of the current harmonic distortion.

This fact is illustrated by the time-domain waveforms of the phase a and phase b voltages, depicted in Figure 6.16.

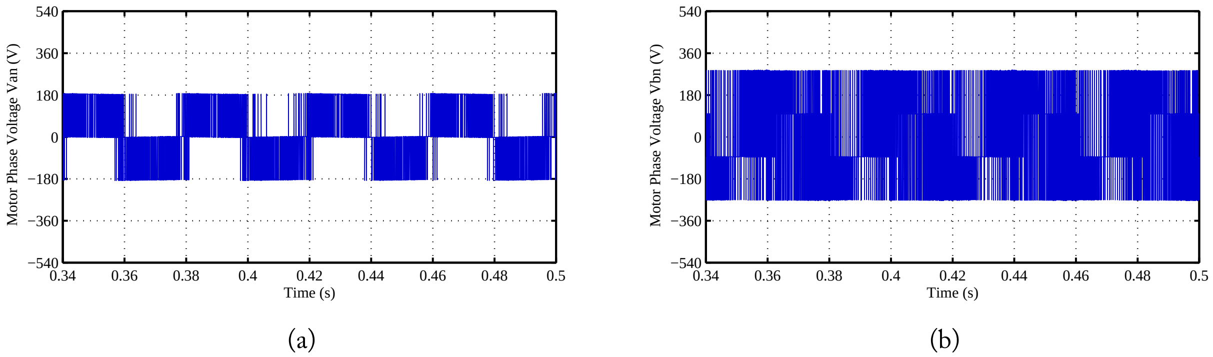

(a) (b)

Figure 6.16: Simulation results of the time-domain waveforms of the PMSM phase voltages for a HCC vector control strategy under a phase a PCM reconfiguration: (a) phase a; (b) phase b.

Comparing both, it is clear that the connection of phase a to the DC link midpoint limits the amplitude of the PMSM phase a voltage, and its corresponding rms value. A more detailed analysis allows to conclude that with this inverter reconfiguration, the phase a voltage amplitude maximum value oscillates between $\pm 1/3$ of the DC link voltage.

With respect to the phase b voltage, this new inverter topology also changes its voltage levels when comparing to the healthy case. Therefore, it can be noticed that in this case the voltage oscilates within the range of $\pm 1/6$ and $\pm 1/2$ of the DC bus voltage. Due to the similar conditions, phase c voltage is very similar to the one of phase b. As a result, for the sake of simplicity, its waveform is not present since the same analysis is applied.

6.3.1.2 SVM Vector Control

Figure 6.17 presents the time domain waveforms of the motor phase currents, its mechanical speed and electromagnetic torque for all the reconfiguration process under a motor reference speed of 900 rpm and a load torque equivalent to 35%.

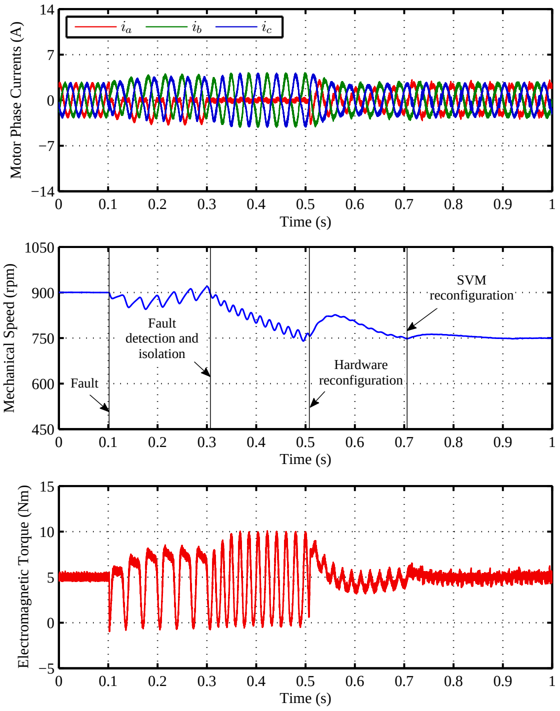

Figure 6.17: Simulation results regarding the reconfiguration process for a SVM vector control strategy under a phase a PCM reconfiguration.

At the instant $t = 0.1\ s$ a fault in IGBT T1 is introduced, being then effectively detected and localized by the integrated real-time algorithm at the instant $t = 0.3092\ s$. Immediately, the fault-tolerant control system acts in order to isolate this fault by removing the gate command signals to both inverter phase a power switches. As a consequence, it is observed that there is no current flow through the PMSM phase a, and the machine is only fed by the two healthy inverter phases. This leads to the generation of a very pulsating electromagnetic torque, with a low average value, resulting in the decrease of the motor speed. 200 ms after, the power converter hardware reconfiguration takes place by the connection of the motor phase a to the DC link capacitors midpoint. Therefore, it can be seen that after this moment, there is current flowing again in phase a, leading to a noticeable decreasing of the electromagnetic torque oscillation. Simultaneously, the fault-tolerant control system also acts in order to limit the motor mechanical speed to one-half of its rated value (750 rpm).

Finally, at the instant $t = 0.7092\,s$, the last step is performed by changing the post-fault modulation strategy, where the SVM is optimized for the new inverter reconfiguration. This has a direct impact on the electromagnetic torque, reducing even more its pulsating component for a more optimized operation.

Figure 6.18 presents the time-domain waveforms of the PMSM phase currents for a SVM vector control strategy under a PCM reconfiguration and for a mechanical speed of 750 rpm and 7 Nm of load torque.

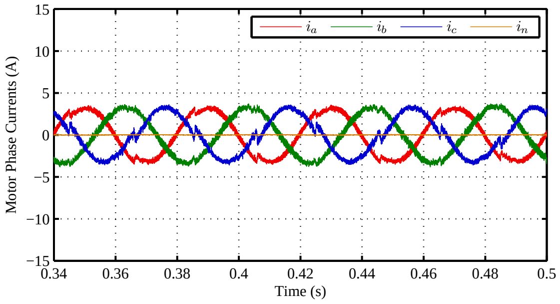

Figure 6.18: Simulation results of the time-domain waveforms of the PMSM phase currents for a SVM vector control strategy under a phase a PCM reconfiguration.

The results allow to verify that under post-fault operating conditions the PMSM is supplied by a three-phase current system with larger harmonic distortion. This increased harmonic distortion is justified by the fact that phase a is not directly supplied by active power switches. Taking into account that SVM is strongly dependent on the number of healthy power switches that supply the motor, and that the currents are indirectly controlled through voltage modulation, all this leads to the increasing of the machine phase currents distortion.

Figure 6.19 presents the time-domain waveforms of the PMSM phase a and phase b voltages for the same conditions.

In a similar way to the previous case, it is clear that the voltage phase a amplitude is lower than the one of phase b, oscillating within a voltage range comprised between ±1/3 of the DC link voltage. Regarding the phase b and c voltages, their switching waveforms oscillate within the levels corresponding to ±1/6 and ±1/2 of the DC bus voltage.

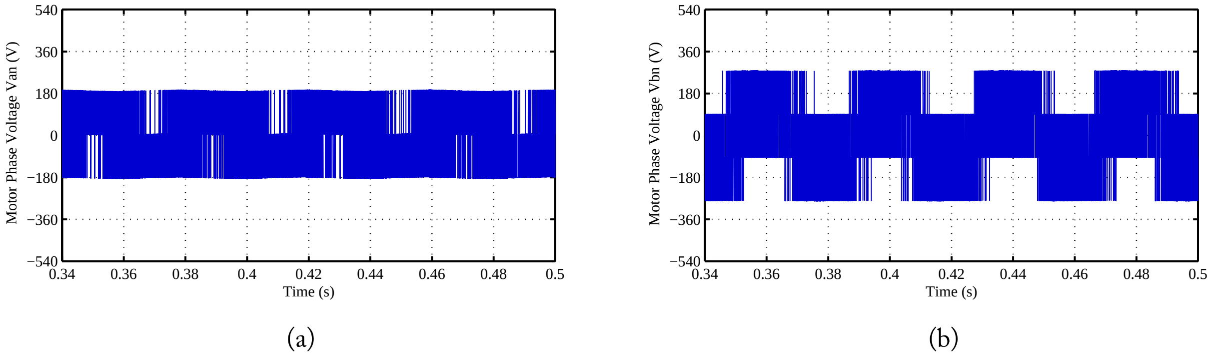

Figure 6.19: Simulation results of the time-domain waveforms of the PMSM phase voltages for a SVM vector control strategy under a phase a PCM reconfiguration: (a) phase a; (b) phase b.

6.3.1.3 Direct Torque Control

The simulation results regarding the drive transient analysis during the reconfiguration process for the DTC control strategy are depicted in Figure 6.20.

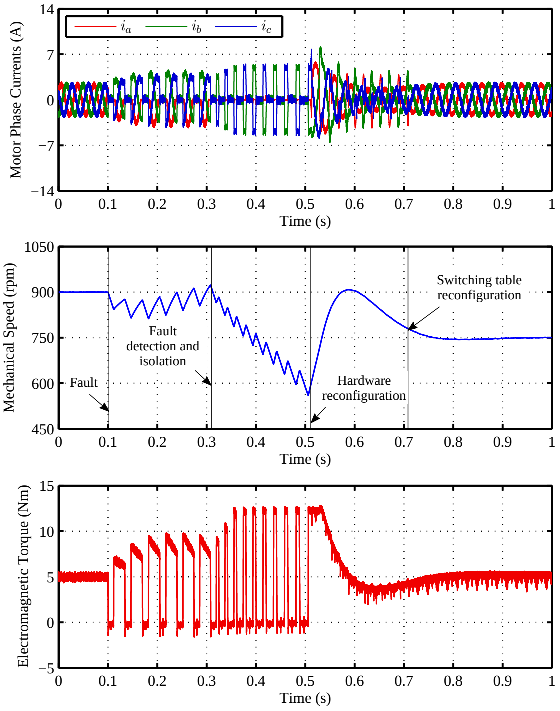

Figure 6.20: Simulation results regarding the reconfiguration process for a DTC control strategy under a phase a PCM reconfiguration.

These results are very similar to the ones obtained for the two vector control strategies and therefore, the same analysis is also valid. For this specific case, it is worth noting that after the converter hardware reconfiguration, the motor phase currents become distorted due to the presence of high-current spikes. This is then compensated by the reconfiguration of the DTC optimum switching table, resulting in much less distorted current waveforms.

Under steady state operation, the time-domain waveforms of the PMSM phase currents shows that the machine is also fed by a balanced three-phase current system, as illustrated in Figure 6.21.

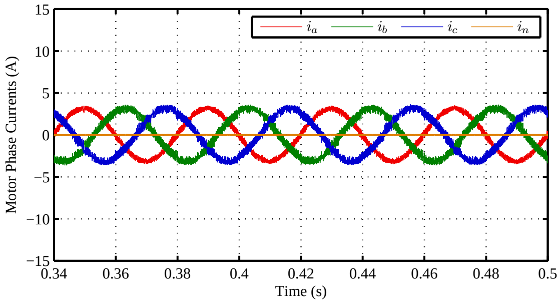

Figure 6.21: Simulation results of the time-domain waveforms of the PMSM phase currents for a DTC control strategy under a phase a PCM reconfiguration.

It can be also noticed that, comparing with the equivalent results regarding the drive normal operation (Figure 3.10), the currents ripple/distortion decreases a little bit, special for the phase a current, due to the lower voltages amplitude values generated by this inverter PCM reconfiguration.

Finally, Figure 6.22 presents the time-domain waveforms of the PMSM phase a and phase b voltages for a PCM reconfiguration.

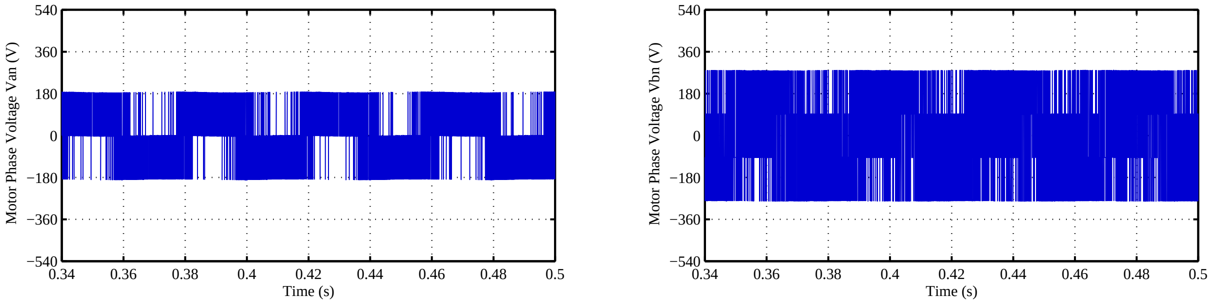

(a) (b)

Figure 6.22: Simulation results of the time-domain waveforms of the PMSM phase voltages for a DTC control strategy under a phase a PCM reconfiguration: (a) phase a; (b) phase b.

These results are very similar to the ones obtained for the HCC vector control and therefore, the same analysis can be also applied.

6.3.2 NCM Reconfiguration

6.3.2.1 HCC Vector Control

Considering first the drive transient analysis during all the reconfiguration process, Figure 6.23 presents the simulation results regarding the step-by-step drive behavior for a HCC vector control strategy under a motor reference speed of 900 rpm and a load torque equivalent to 35%.

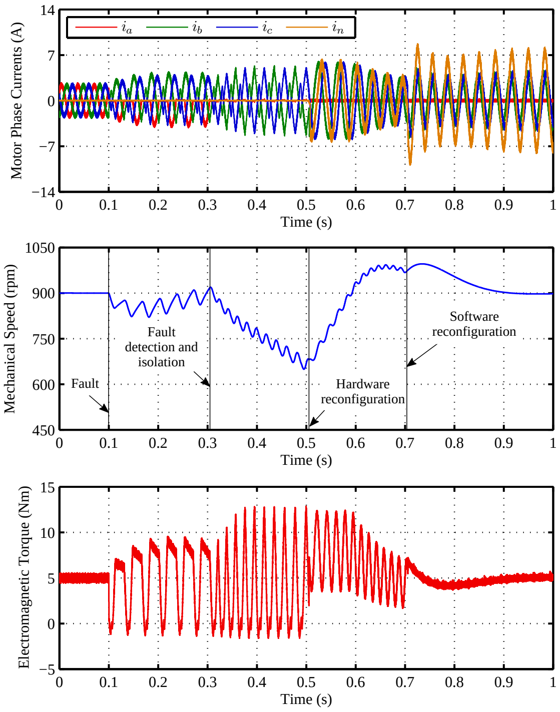

Figure 6.23: Simulation results regarding the reconfiguration process for a HCC vector control strategy under a phase a NCM reconfiguration.

The obtained results for the first two reconfiguration stages are virtually equal to ones obtained for the PCM reconfiguration process, and therefore, the previous analysis is also valid. The main differences are observed when the hardware reconfiguration is performed. In this case, the PMSM stator winding neutral point is connected to the DC bus capacitors midpoint, resulting in current flow through the neutral conductor. After this moment, the developed electromagnetic torque pulsation is reduced, and the PMSM mechanical speed increases. Finally, when the fault-tolerant control system performs the software reconfiguration by imposing a new phase-shift and amplitude to the currents, the electromagnetic torque ripple becomes similar to the one seen under normal operating conditions, and the machine operating speed converges to the initial value of 900 rpm.

Considering now the PMSM drive steady state analysis for a NCM reconfiguration, Figure 6.24 presents the time-domain waveforms of the motor phase currents and phase b voltage for a HCC vector control strategy.

Since the PMSM phase a is isolated from its corresponding inverter faulty leg, under post-fault operating conditions it is in open-circuit and as a consequence, there is no current flow. On the other hand, in order to maintain the same magnetomotive force generated under normal operating conditions, it can be clearly seen that the currents in the healthy phases increase by a factor of $\sqrt{3}$ with a phase shift of 60º. Regarding the neutral current, its value is three times higher than the value of the motor phase currents under normal operating conditions. It can be also noticed that due to the direct control of the PMSM phase currents through the hysteresis controllers, their

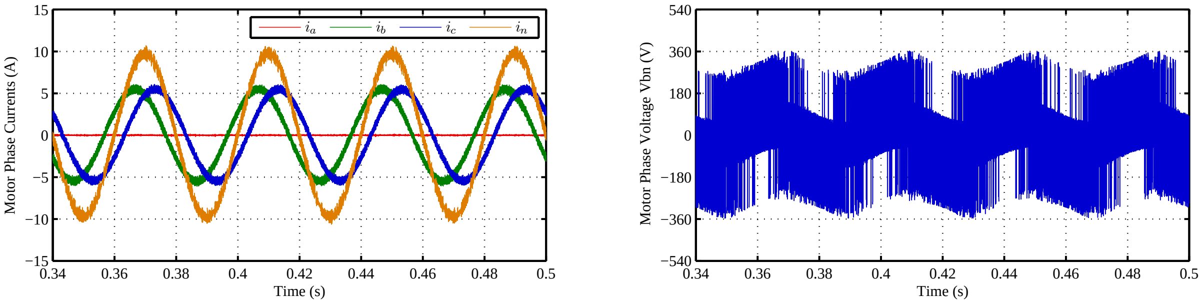

(a)

(b)

Figure 6.24: Simulation results of the time-domain waveforms for a HCC vector control strategy under a phase a NCM reconfiguration: (a) motor phase currents; (b) phase b voltage.

waveform distortion is relatively low.

As far as the PMSM phase voltages is concerned, the results shown in Figure 6.24b show that the phase b voltage waveform presents some similarities to the one obtained for the PCM reconfiguration. The major difference is that the voltages stages are not well defined since the neutral current flow directly influences the PMSM winding neutral point potential, leading to its oscillation, also seen in the phase b voltage.

The motor phase c is also supplied by analogous conditions, presenting therefore a similar waveform. As a result, the same analysis can be extended to it. On the other side, as phase a is disconnected from the power converter, its contribution is not relevant for this analysis, being therefore disregarded.

6.3.2.2 SVM Vector Control

Figure 6.25 presents the simulation results for all the SVM vector control NCM reconfiguration process under a motor reference speed of 900 rpm and a load torque equivalent to 35%.

In analogy to the previous case, the obtained results are equivalent to ones obtained for the PCM reconfiguration with the exception for the hardware reconfiguration. When this step is performed by the fault-tolerant control system, it is possible to observe the current flow through the neutral conductor. This immediately leads to a noticeable decrease of the PMSM electromagnetic torque pulsation and an increasing of the motor speed. Finally, after the SVM reconfiguration, although the electromagnetic torque ripple increases a little bit, this allows to reduce the currents distortion.

Regarding the steady-state analysis, Figure 6.26 presents the time-domain waveforms of the PMSM phase currents and phase b voltage for a SVM vector control strategy under a NCM converter reconfiguration.

The most evident aspect shown by the motor phase currents is that for this inverter configuration there is no current flow through the faulty phase (phase a) since it is in open-circuit. Instead, due to the neutral point connection to the DC bus capacitors midpoint, it can be observed a large

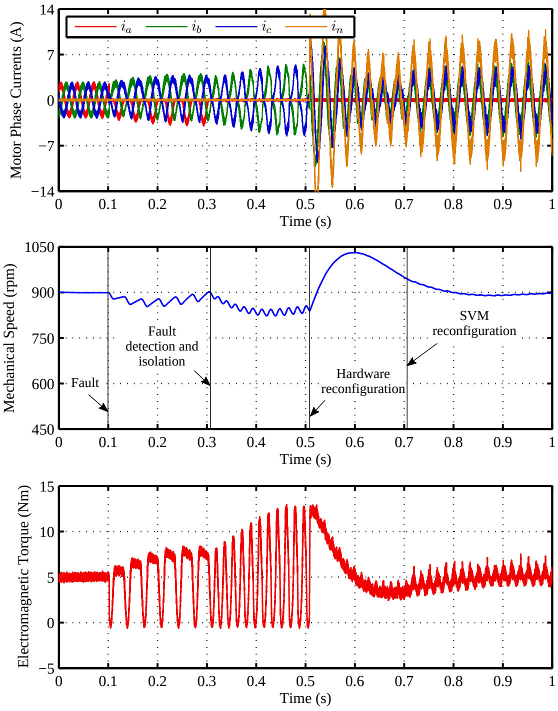

Figure 6.25: Simulation results regarding the reconfiguration process for a SVM vector control strategy under a phase a NCM reconfiguration.

current flow in the neutral conductor. Moreover, and as predicted by the theoretical analysis, comparing with the normal situation, the healthy motor phase currents amplitude increases by a factor of approximately $\sqrt{3}$, with a phase shift of 60°, in order to maintain the same magnetomotive force. However, it can be also verified that all the three currents present a noticeable distortion. As explained before, this is justified by the combination of the machine neutral connection to a non-active supply point, together with the indirect current control through voltage modulation, which leads to the generation of higher current harmonic distortion.

With respect to the PMSM phase b voltage, though it also presents some similarities to the equivalent results obtained for the PCM reconfiguration, their amplitude appears modulated due to the voltage oscillation imposed by the current flow through the neutral conductor connected to the DC bus capacitors midpoint.

6.3.2.3 Direct Torque Control

The simulation results regarding the drive transient analysis during the reconfiguration process for the DTC control strategy are depicted in Figure 6.27.

Once more, it can be verified a similar behavior to the PCM reconfiguration process. When the machine windings neutral point is connected to the DC bus capacitors midpoint, the electromagnetic torque oscillation is strongly attenuated and the PMSM speed increases. Finally, the drive performance is optimized by the reconfiguration of the DTC voltage vectors switching table.

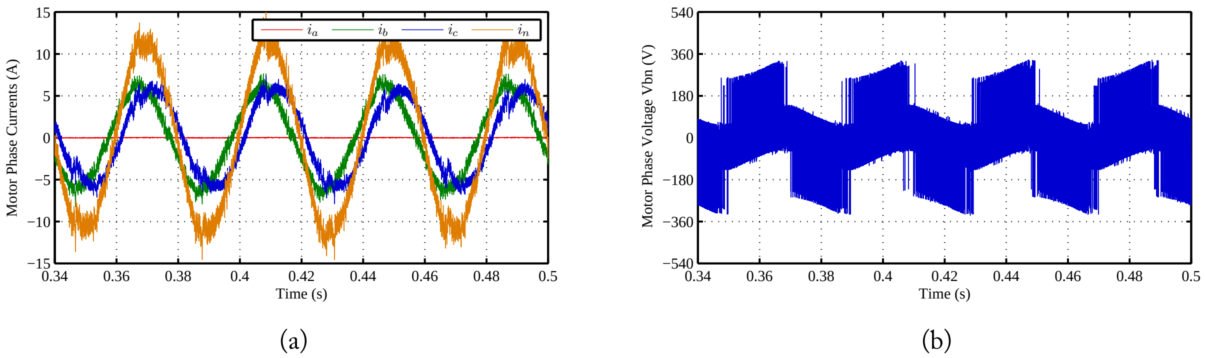

(a)

(b)

Figure 6.26: Simulation results of the time-domain waveforms for a SVM vector control strategy under a phase a NCM reconfiguration: (a) motor phase currents; (b) phase b voltage.

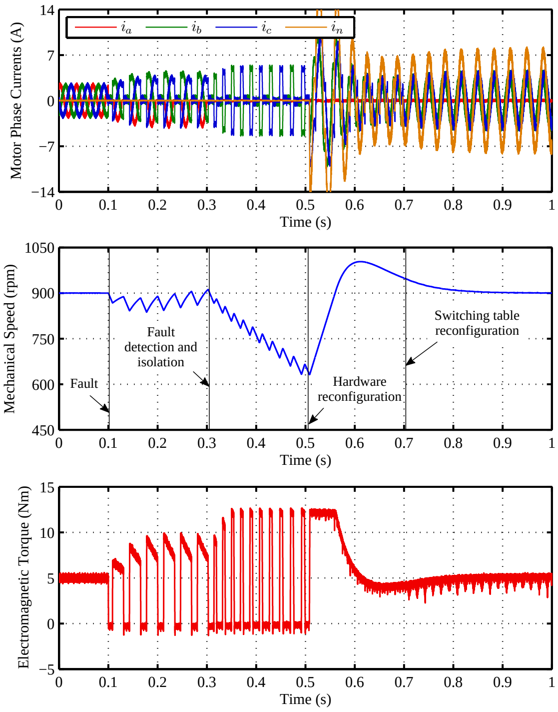

Figure 6.27: Simulation results regarding the reconfiguration process for a DTC control strategy under a phase a NCM reconfiguration.

Figure 6.28 presents the time-domain waveforms of the PMSM phase currents and phase b voltage for a DTC control strategy under a NCM converter reconfiguration.

Comparing to the previous case, despite the more noticeable current ripple, the motor phase currents obtained for a DTC control strategy are very similar. Regarding the PMSM voltages, the same conclusions are verified and therefore, the analysis is the same to the previously analyzed situation.

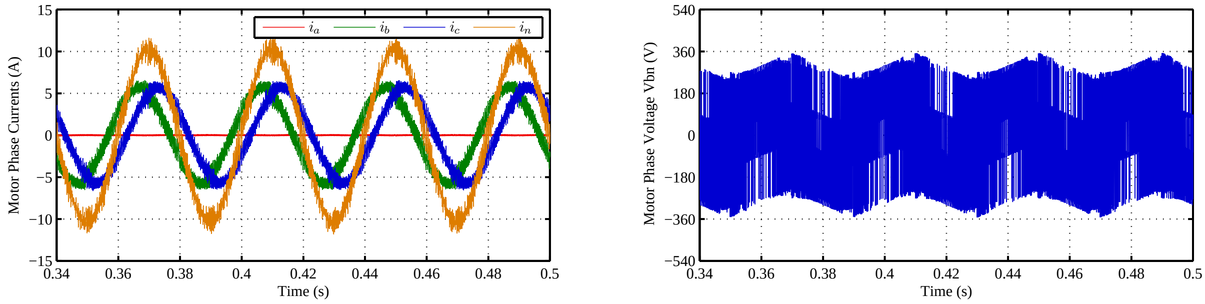

(a)

(b)

Figure 6.28: Simulation results of the time-domain waveforms for a DTC control strategy under a phase a NCM reconfiguration: (a) motor phase currents; (b) phase b voltage.

6.4 Experimental Results

A laboratory prototype was built in order to test and validate the developed fully integrated fault-tolerant PMSM drive. The same equipment previously reported in Section 3.5 was used. More detailed information regarding the laboratory setup can be found in Appendix B.

In order to enable a correct comparison, the same conditions and parameters defined for the normal and faulty operation analysis were also used for the experimental tests. The three developed fault-tolerant control systems explain in Section 6.2 were also implemented into the dSPACE DS1103 controller using a sampling time of 25 µs.

Figure 6.29 presents a block diagram of the experimental setup used to implement the fully integrated fault-tolerant PMSM drive.

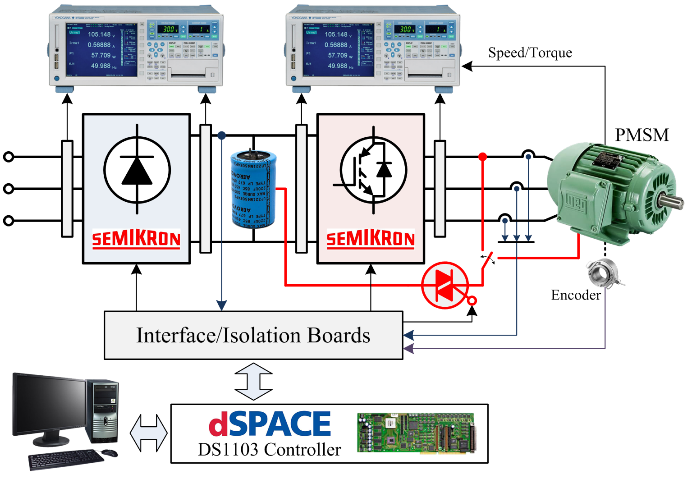

Figure 6.29: Block diagram with the main components of the experimental setup.

In a similar way to the simulation results, only inverter open-circuit faults in the top IGBT of phase a (T1) are considered for all experimental tests. As a result, only one triac is used to perform the connection between the motor phase a or its neutral point and the DC link capacitors midpoint, required for the PCM and NCM converter reconfigurations. The triac is also driven by an interface/isolation board, also connected and commanded by the DS1103 controller.

Experimental results are presented taking into account the transient analysis during all the reconfiguration process, showing the step-by-step drive behavior during all the four stages that occur when the fault is introduced. The final behavior analysis is also presented, where the imposed delay time between each step is reduced to a minimum value equal to 100 μs. As the simulation results, a PMSM reference speed of 900 rpm and a load torque equivalent to 35% of the motor rated value were assumed.

Finally, the PMSM drive steady state analysis is also evaluated under post-fault operating conditions assuming the same mechanical speed of 750 rpm and a load torque of 7 Nm.

6.4.1 PCM Reconfiguration

6.4.1.1 HCC Vector Control

Considering first the drive transient analysis during all the reconfiguration process, Figure 6.30 presents the experimental results for a HCC vector control strategy under a motor reference speed of 900 rpm and a load torque equivalent to 35%.

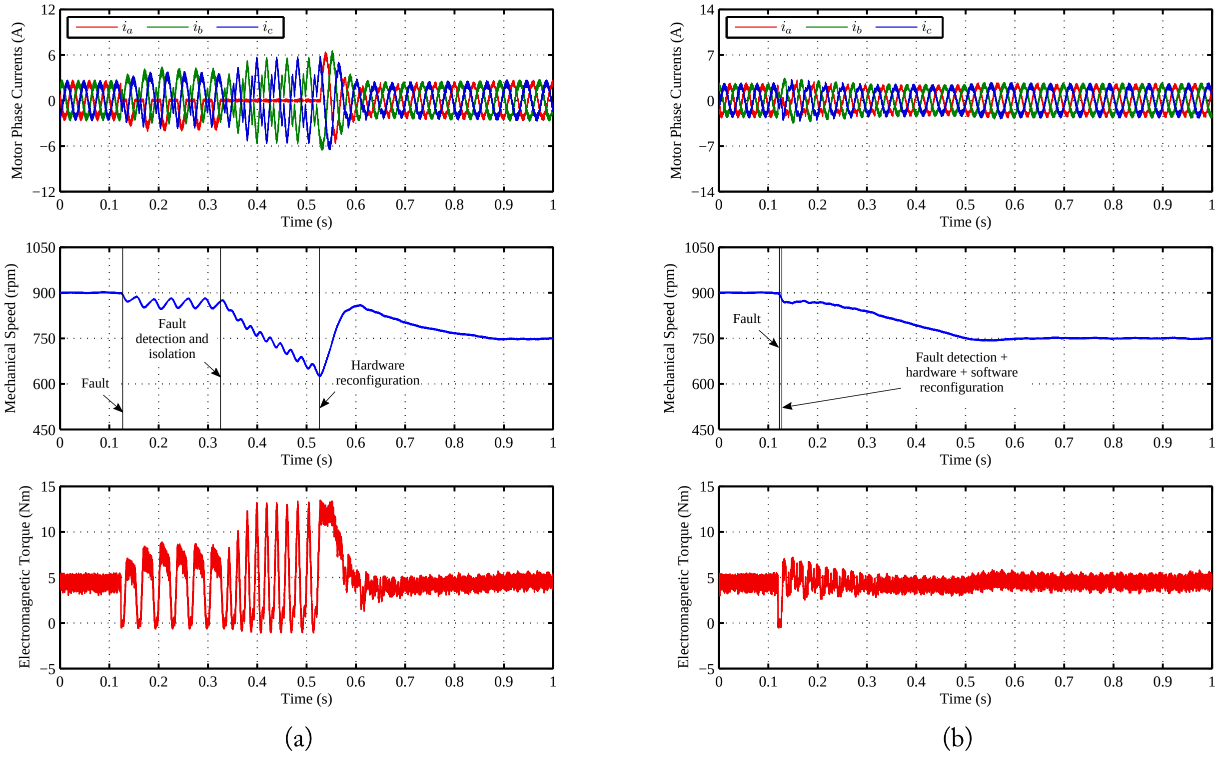

Figure 6.30: Experimental results regarding the reconfiguration process for a HCC vector control strategy under a phase a PCM reconfiguration: (a) step-by-step behavior; (b) final reconfiguration behavior.

Comparing with the equivalent simulation waveforms shown in Figure 6.14, it can verified that the experimental ones (Figure 6.30a) are very similar, demonstrating an excellent agreement between the theoretical and experimental results. Therefore, the analysis already done for the simulation results is also valid for this case.

Regarding the final reconfiguration behavior (Figure 6.30b), when the fault occurs, all the process is performed in a small time fraction. Immediately after the reconfiguration is finished, the PMSM still operates at a speed value near the initial one. As it can be seen, this leads to the arising of a larger torque ripple that then decreases proportionally to the machine speed. This justifies the need to limit the PMSM mechanical speed to one-half of its rated value under a PCM reconfiguration. As far as the reconfiguration process speed is concerned, it is concluded that the fault-tolerant control system can suppress the inverter fault in a very short time interval. Basically, as the time delay between each reconfiguration step is relatively small, the reconfiguration speed is limited by the diagnostic algorithm performance.

Figure 6.31 presents the experimental results regarding the time-domain waveforms of the PMSM phase currents for a HCC vector control strategy under a PCM reconfiguration.

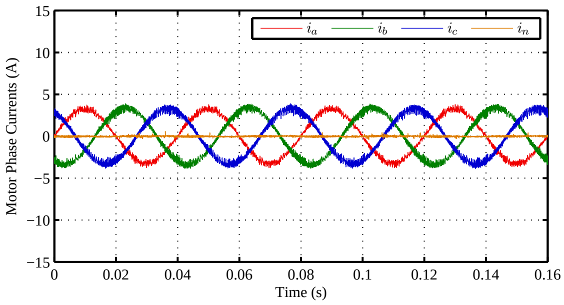

Figure 6.31: Experimental results of the time-domain waveforms of the PMSM phase currents for a HCC vector control strategy under a phase a PCM reconfiguration.

By comparing with the equivalent simulation waveforms shown in Figure 6.15, it can be confirmed a very good agreement between the simulation and experimental results. The PMSM is supplied by a balanced three-phase current system with low harmonic distortion, similar to the healthy case. It can be also noticed a small decrease of the phase a current ripple due to the lower rms value of the corresponding motor phase voltage.

Regarding the PMSM phase voltages, Figure 6.32 presents the time-domain waveforms of the phase a and phase b voltages.

The obtained results are also very similar to the ones obtained from the computational simulations. It is also clearly observed that the phase a amplitude is lower than the one of phase b, oscillating within a voltage range comprised between ±1/3 of the DC bus voltage. On the other hand, it is also confirmed that the phase b and phase c voltages oscillate within the values comprised between ±1/6 and ±1/2 of the DC link voltage.

Considering now the PMSM electromagnetic torque analysis, Figure 6.33 presents its time-

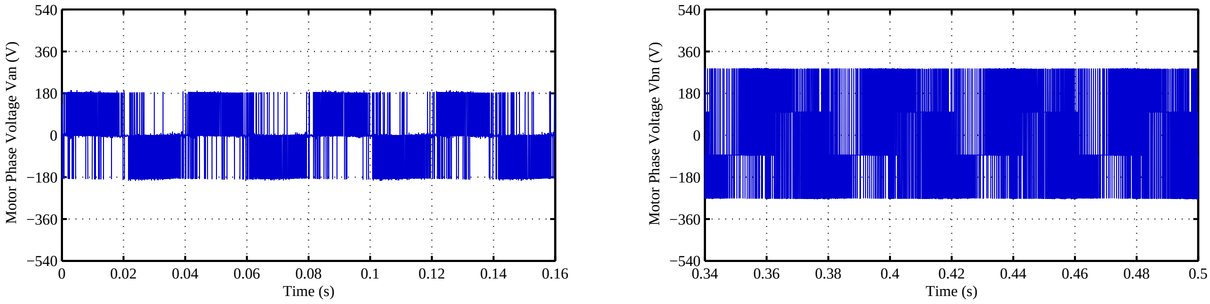

(a) (b)

Figure 6.32: Experimental results of the time-domain waveforms of the PMSM phase voltages for a HCC vector control strategy under a phase a PCM reconfiguration: (a) phase a; (b) phase b.

domain waveform for a HCC vector control strategy under a PCM reconfiguration.

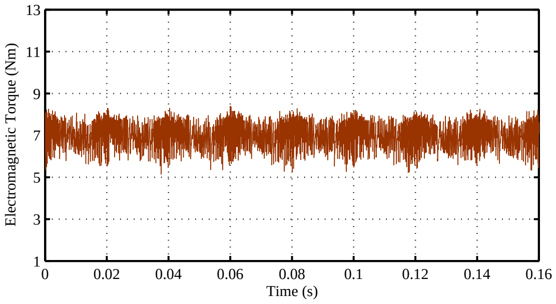

Figure 6.33: Experimental results of the time-domain waveforms of the PMSM electromagnetic torque for a HCC vector control strategy under a phase a PCM reconfiguration.

It can be seen that, comparing with the electromagnetic torque waveform obtained for the healthy case (Figure 3.13), the results are very similar. In fact, the small decrease of the current phase a waveform distortion has a positive impact on the PMSM electromagnetic torque, represented by the decreasing of the TWO factor from 8.66% to 7.76%.

Finally, the PMSM phase voltages complex representation in the $\alpha\beta$ plane can be also evaluated, as shown in Figure 6.34.

The four well-defined active voltage vectors are clearly visible, with same coordinates predicted by the theoretical analysis, illustrated in Figure 6.5. As a result, it can be confirmed that in order to avoid overmodulation and assuming that the drive mains supply conditions are maintained (DC link voltage approximately the same), the PMSM mechanical speed must be limited to one-half of its rated value under post-fault operating conditions.

6.4.1.2 SVM Vector Control

The experimental results regarding the drive transient analysis during the PCM reconfiguration process for the SVM control strategy are depicted in Figure 6.35.

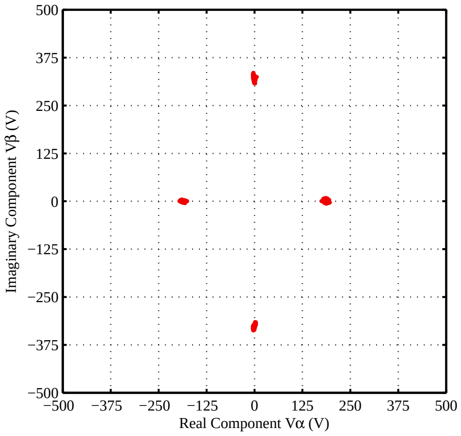

Figure 6.34: Experimental results of the PMSM phase voltages representation in the complex plane for a HCC vector control strategy under a phase a PCM reconfiguration.

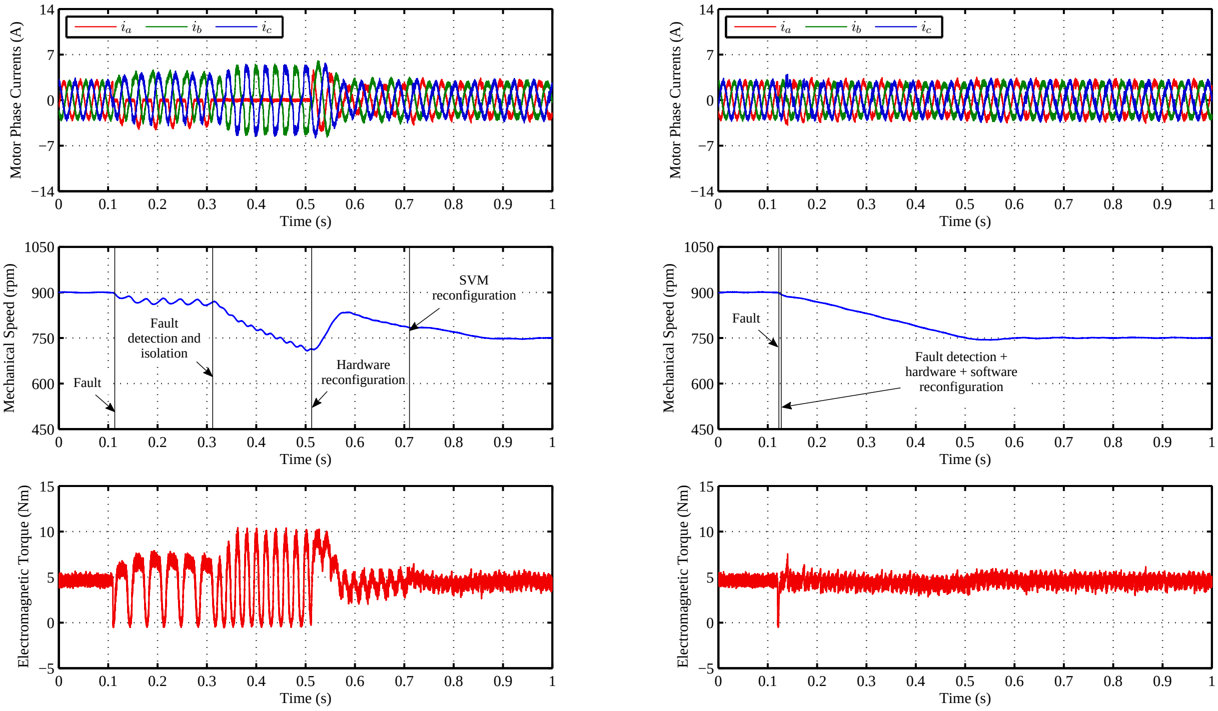

(a)

(b)

Figure 6.35: Experimental results regarding the reconfiguration process for a SVM vector control strategy under a phase a PCM reconfiguration: (a) step-by-step behavior; (b) final reconfiguration behavior.

Once more, it is observed a good agreement between these experimental results (Figure 6.35a) and the equivalent simulation ones (Figure 6.17). Regarding the results shown in Figure 6.35b, they are also very similar to the ones obtained for the HCC vector control strategy, being therefore applied the same analysis.

Figure 6.36 presents the time-domain waveforms of the PMSM phase currents for a SVM vector control strategy under a PCM reconfiguration.

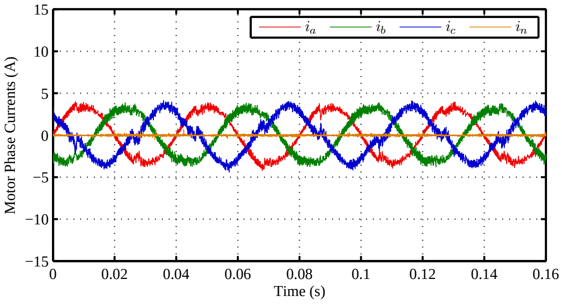

Figure 6.36: Experimental results of the time-domain waveforms of the PMSM phase currents for a SVM vector control strategy under a phase a PCM reconfiguration.

Comparing with the simulation results shown in Figure 6.18, it can be also seen that the obtained experimental ones are very similar. Under post-fault operating conditions the PMSM is supplied by a three-phase current system with a relatively low harmonic distortion. Nevertheless, the HCC vector control allows to generate better current waveforms since for the SVM vector control, there is no direct control of the motor currents, being accomplished by an indirect control through voltage modulation.

As far as the motor phase voltages is concerned, Figure 6.37 presents the time-domain waveforms of the phase a and phase b voltages.

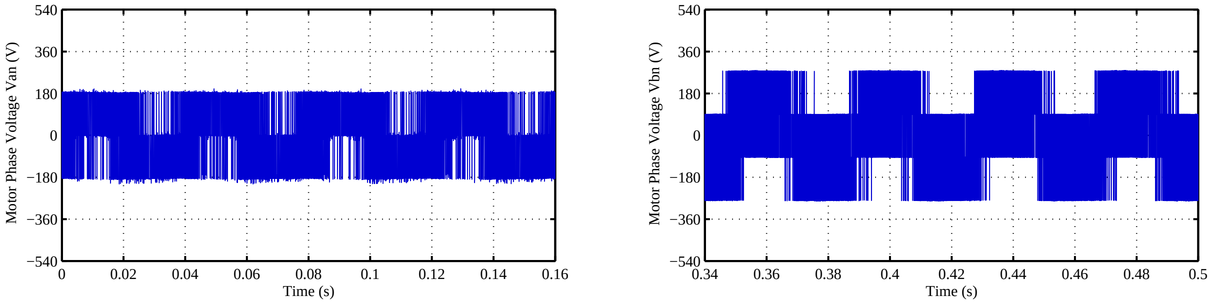

(a) (b)

Figure 6.37: Experimental results of the time-domain waveforms of the PMSM phase voltages for a SVM vector control strategy under a phase a PCM reconfiguration: (a) phase a; (b) phase b.

Once more, the obtained experimental results are very similar to the time-domain waveforms obtained from the computational simulations. The PMSM phase a voltage has a lower amplitude value, oscillating within the voltage levels comprised between ±1/3 of the DC link voltage while the phase b voltage oscillates between ±1/6 and ±1/2 of the DC link voltage.

Regarding the PMSM electromagnetic torque analysis, Figure 6.38 presents its time-domain waveform for a SVM vector control strategy under a phase a PCM reconfiguration.

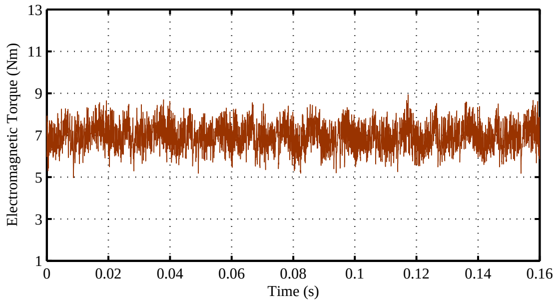

Figure 6.38: Experimental results of the time-domain waveforms of the PMSM electromagnetic torque for a SVM vector control strategy under a phase a PCM reconfiguration.

It is shown that the waveform is quite smooth, in a similar way to the time-domain waveform obtained for the healthy case. However, the small increase of the motor phase currents distortion leads to a more oscillating electromagnetic torque waveform. Consequently, comparing with the TWO value of 6.84% obtained for the healthy situation, under post-fault operating conditions the TWO increases to 8.78%.

With respect to the complex representation of the PMSM voltage vectors, the obtained experimental results are depicted in Figure 6.39.

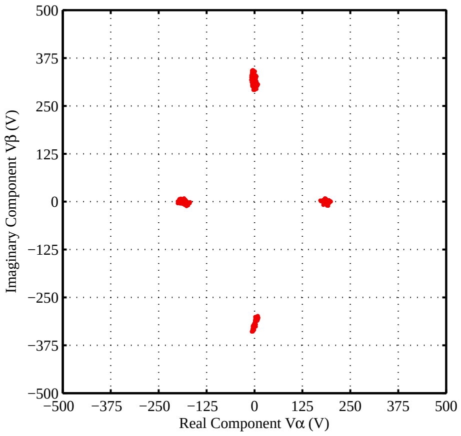

Figure 6.39: Experimental results of the PMSM phase voltages representation in the complex plane for a SVM vector control strategy under a phase a PCM reconfiguration.

The obtained results also allow to confirm the very good agreement between the theoretical analysis and the experimental tests. Despite of some vectors surrounding the main coordinates due to the voltage spikes, the four active voltage vectors are also clearly defined, with an amplitude equal to the theoretical values equivalent to $1/3$ and $1/\sqrt{3}$ of the DC bus voltage. As a result, the boundary between linear modulation and overmodulation occurs when $\left|\overline{V}_r\right|$ reaches a value equivalent to $0.289V_{dc}$, which corresponds to one-half of the value obtained for the healthy case. Hence, the post-fault mechanical speed must be limited to one-half of the PMSM rated value in order to avoid electromagnetic torque pulsation.

6.4.1.3 Direct Torque Control

Figure 6.40 presents the experimental results regarding the reconfiguration process for the DTC control strategy under a PCM reconfiguration under a motor reference speed of 900 rpm and a load torque equivalent to 35%.

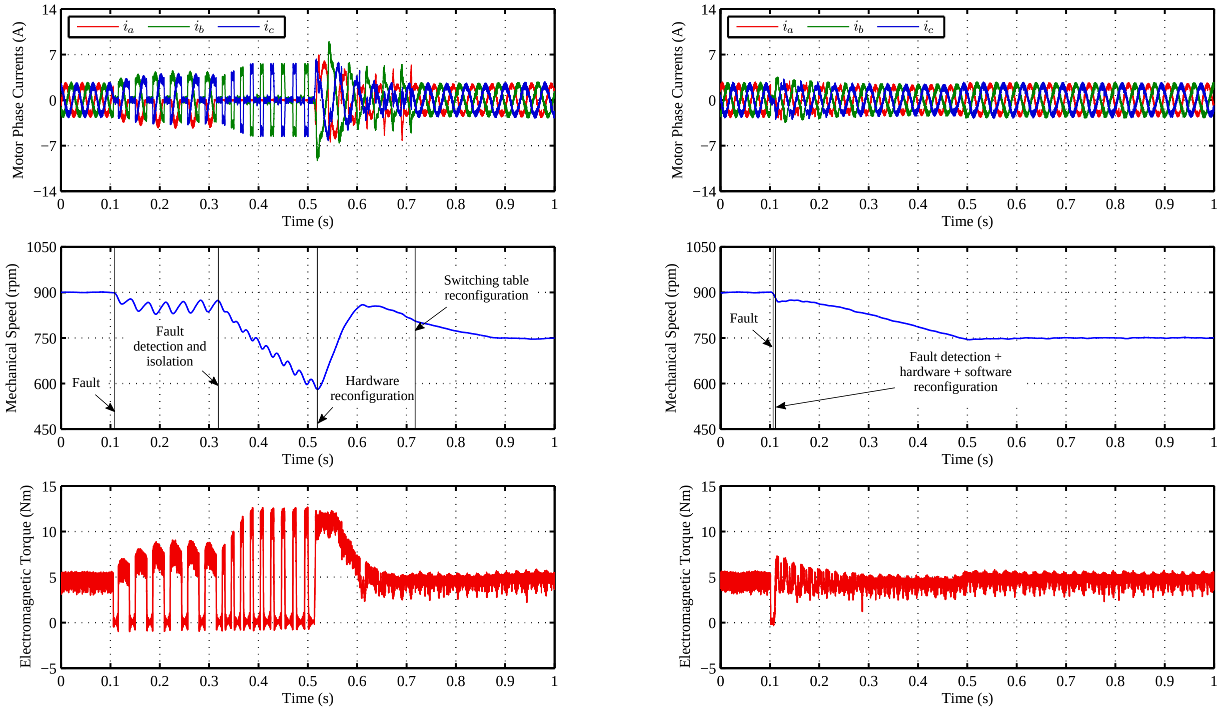

(a)

(b)

Figure 6.40: Experimental results regarding the reconfiguration process for a DTC control strategy under a phase a PCM reconfiguration: (a) step-by-step behavior; (b) final reconfiguration behavior.

Due to the equivalent similarities obtained for this case, the same analysis already done for the previous cases can also be extended to this specific control strategy.

Figure 6.41 presents the time-domain waveforms of the PMSM phase currents for a DTC control strategy under a PCM reconfiguration.

In a similar way to previous cases, a very good match between the simulation and experimental results is also obtained for this control technique. This converter reconfiguration allows the PMSM to be fed by a balanced and low distortion three-phase current system. Furthermore, it is also noticed that the phase a current presents a little bit less ripple than the others, as verified for the simulation results.

Regarding the PMSM phase voltages, the results shown in Figure 6.42 are also similar to equivalent simulation ones. The same analysis done for the two previous cases can also be extended for

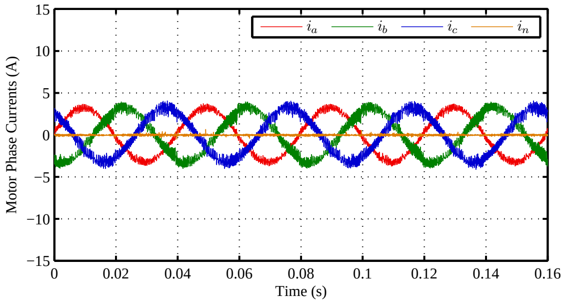

Figure 6.41: Experimental results of the time-domain waveforms of the PMSM phase currents for a DTC control strategy under a phase a PCM reconfiguration.

this specific case.

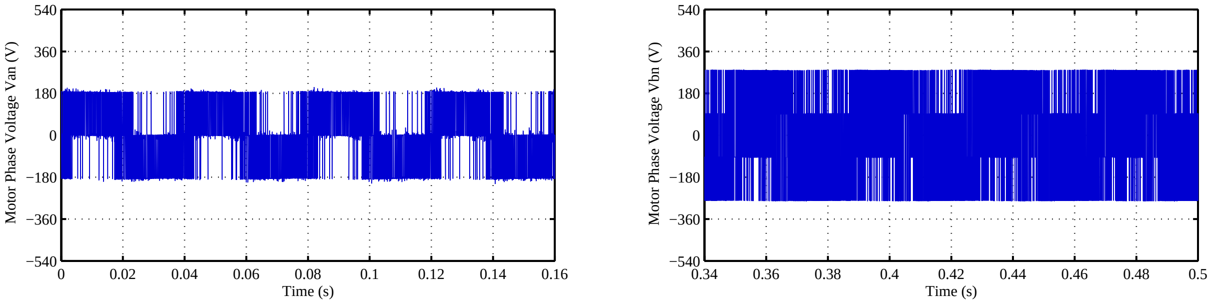

(a) (b)

Figure 6.42: Experimental results of the time-domain waveforms of the PMSM phase voltages for a DTC control strategy under a phase a PCM reconfiguration: (a) phase a; (b) phase b.

With respect to the PMSM electromagnetic torque analysis, Figure 6.43 presents its time-domain waveform for a DTC control strategy under an inverter PCM reconfiguration.

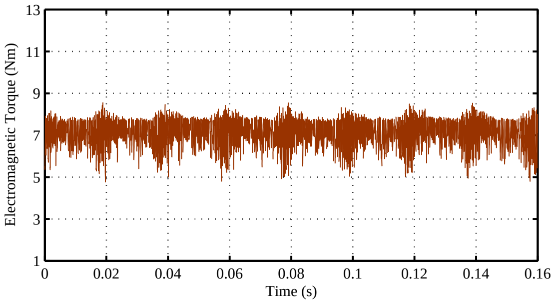

Figure 6.43: Experimental results of the time-domain waveforms of the PMSM electromagnetic torque for a DTC control strategy under a phase a PCM reconfiguration.

The obtained electromagnetic torque waveform is also very smooth as the one obtained under normal operating conditions. It also benefits from the lower phase a current distortion, leading to the small decrease of the TWO from 10.89%, obtained for the healthy case, to 9.06%.

Finally, Figure 6.44 presents the complex representation of the PMSM phase voltages in the complex $\alpha\beta$ plane.

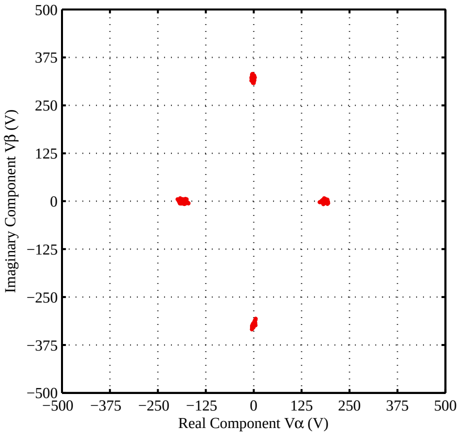

Figure 6.44: Experimental results of the PMSM phase voltages representation in the complex plane for a DTC control strategy under a phase a PCM reconfiguration.

The results are in accordance to the ones presented for the two previous control strategies and therefore, the same analysis is also applied.

6.4.2 NCM Reconfiguration

6.4.2.1 HCC Vector Control

Considering now the NCM reconfiguration, Figure 6.45 presents the experimental results regarding the reconfiguration process for the HCC control strategy under a PCM reconfiguration.

In analogy to the previous cases, these waveforms are very similar to the ones obtained by the simulations, demonstrating once more the good agreement between the theoretical and experimental results. Accordingly, the analysis already performed for the simulations results is also extended to this case.

Regarding the final reconfiguration process shown in Figure 6.45b, it can be seen that the inverter fault is suppressed very quickly by the developed fault-tolerant control system. All the reconfiguration process is accomplished in a very short time interval, which minimizes the impact on the drive performance.

Figure 6.46 presents the time-domain waveforms of the PMSM phase currents and phase b voltage for a HCC vector control strategy under a NCM reconfiguration.

Once more, comparing with the corresponding simulation results shown in Figure 6.24, it is evident the great agreement between the computational simulations and the experimental results. Under post-fault operating conditions, the PMSM phase a is isolated from the VSI, becoming in open-circuit. As a result, there is no current flow in the corresponding PMSM phase. On

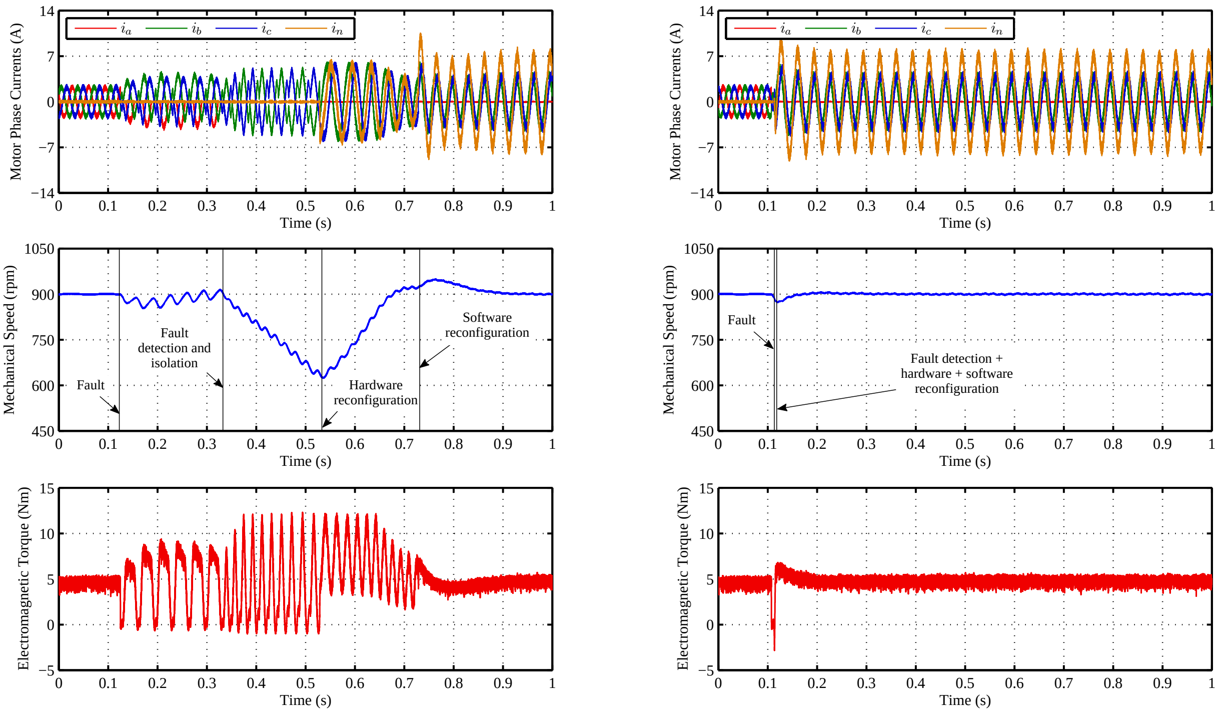

(a)

(b)

Figure 6.45: Experimental results regarding the reconfiguration process for a HCC vector control strategy under a phase a NCM reconfiguration: (a) step-by-step behavior; (b) final reconfiguration behavior.

the other hand, because of the connection of the PMSM winding neutral point to the DC bus capacitors midpoint, a large current flow through the neutral conductor is observed. As predicted by the theoretical analysis, its value is three times higher than the value of the motor phase currents under normal operating conditions. Furthermore, it is also seen that the motor phase currents amplitude in the two healthy phases increase by a factor of $\sqrt{3}$ with a phase shift of 60° in order to maintain the same magnetomotive force obtained for the drive normal situation.

Regarding the PMSM phase voltages, the phase b voltage waveform also presents some similarities to the one for the PCM reconfiguration. However, due to the neutral current flow, the neutral potential also oscillates, being this effect also visible in the motor phase voltages. The same analysis is also extended for the phase c voltage, being disregarded the one for phase a since it is not supplied by the inverter.

As far as the PMSM electromagnetic torque is concerned, Figure 6.47 presents its time-domain waveform for a HCC vector control strategy.

In analogy with the obtained waveform for the normal case, under these post-fault operating conditions the electromagnetic torque is also very smooth, presenting a TWO value equal to approximately 7.41%.

With respect to the complex representation of the PMSM voltage vectors, the obtained experimental results are depicted in Figure 6.48.

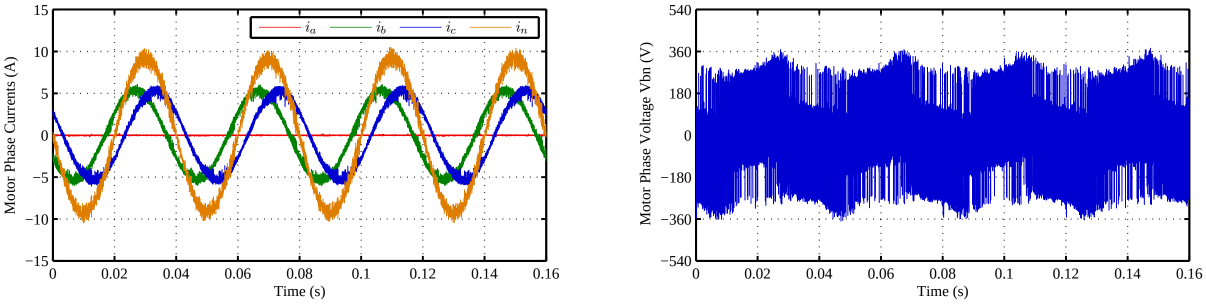

(a) (b)

Figure 6.46: Experimental results of the time-domain waveforms for a HCC vector control strategy under a phase a NCM reconfiguration: (a) motor phase currents; (b) phase b voltage.

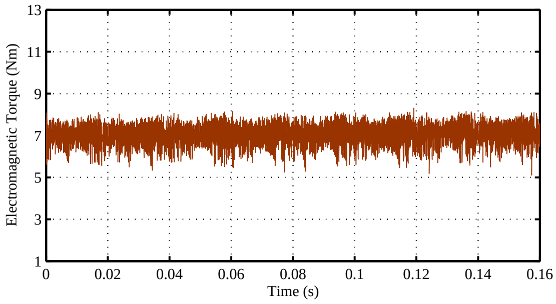

Figure 6.47: Experimental results of the time-domain waveforms of the PMSM electromagnetic torque for a HCC vector control strategy under a phase a NCM reconfiguration.

Despite of noticeable differences, comparing with the experimental results obtained for the PCM reconfiguration, it can be seen that only four active vectors are generated. However, since the motor phase voltages do not assume values between well-defined voltage levels, the introduced oscillations by this converter topology leads to a great dispersion of voltage vectors in a more complicated way, being required a different approach to analyze how this affects the drive post-fault performance.

An important aspect that is clearly seen is that for this NCM reconfiguration with a fault in phase a, the voltage vectors dispersion occurs in a horizontal direction. In fact, this direction is defined by the orientation of the two smaller voltage vectors[1]. As a result, for a NCM reconfiguration with a fault in phase b or phase c, the results are similar but suffer a rotation of +120º and -120º, respectively.

In order to calculate the linear range/overmodulation limits, the process is not so straightforward. Therefore, taking into account the obtained complex representation of the PMSM phase voltages, the scheme presented in Figure 6.49 illustrates how this can be accomplished.

A hexagon can be defined in order to limit the generated voltage space vectors. The horizontal

---

[1] This analysis is based on the voltage vectors representation shown in Figure 6.5 and Figure 6.6.

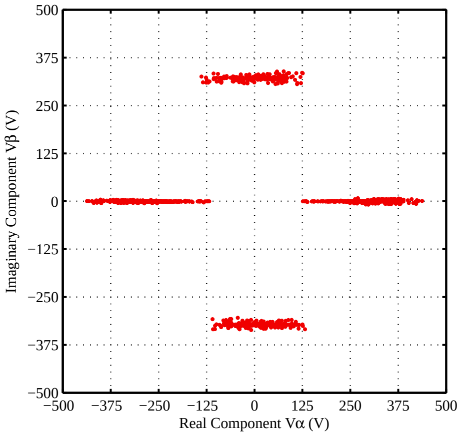

Figure 6.48: Experimental results of the PMSM phase voltages representation in the complex plane for a HCC vector control strategy under a phase a NCM reconfiguration.

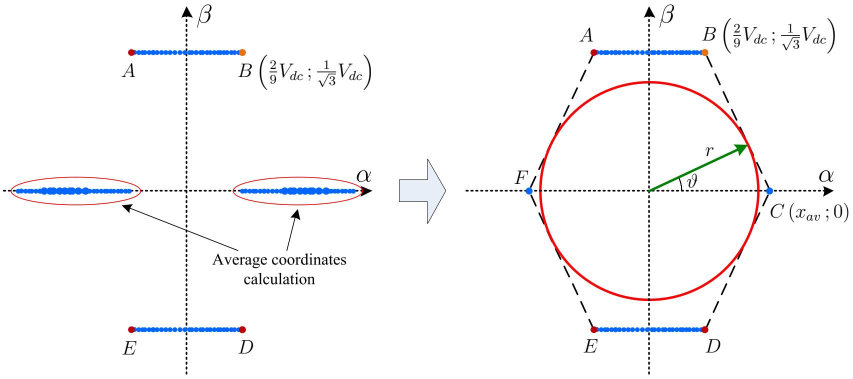

Figure 6.49: Linear modulation range calculation for a phase a NCM reconfiguration.

vectors distribution seen at the top and bottom of Figure 6.48 and delimited by $\overline{AB}$ and $\overline{DE}$ in the previous scheme, is approximately even and well defined. The coordinates of these points can be directly related to the DC link voltage, as illustrated for the point B. Hence, two sides of the hexagon are defined by $\overline{AB}$ and $\overline{DE}$.

On the contrary, the voltage vectors distribution along the real axis is uneven. Consequently, the calculation of the average coordinates of these two distributions can be performed in order to calculate the hexagon remaining two points. Considering this, an hexagon defined by the points $[ABCDEF]$ is obtained, which can now be used to calculate the radius r of the circle that limits the linear/overmodulation range.

Assuming that r is perpendicular to the line segment defined by $\overline{BC}$, the angle ϑ can be calculated using the expression:

$$\vartheta = \frac{\pi}{2} - \arctan\left(\frac{\frac{1}{\sqrt{3}}V_{dc}}{x_{av} - \frac{2}{9}V_{dc}}\right) \tag{6.23}$$

where x_{av} is the average absolute value of the x-coordinate of the vectors distribution along the real axis. Finally, it can be demonstrated that the value of r can be calculated using the expression:

$$r = x_{av} \cos\vartheta \tag{6.24}$$

For this specific case, the value of x_{av} is approximately equal to 279. Therefore, applying the previous equation, the radius of the circle that limits the linear/overmodulation range becomes equal to 252, which corresponds to about 77% of the experimental value obtained for normal operating conditions (approximately equal to 325).

6.4.2.2 SVM Vector Control

Figure 6.50 presents the time domain waveforms of the motor phase currents, its mechanical speed and electromagnetic torque for all the reconfiguration process under a SVM vector control strategy.

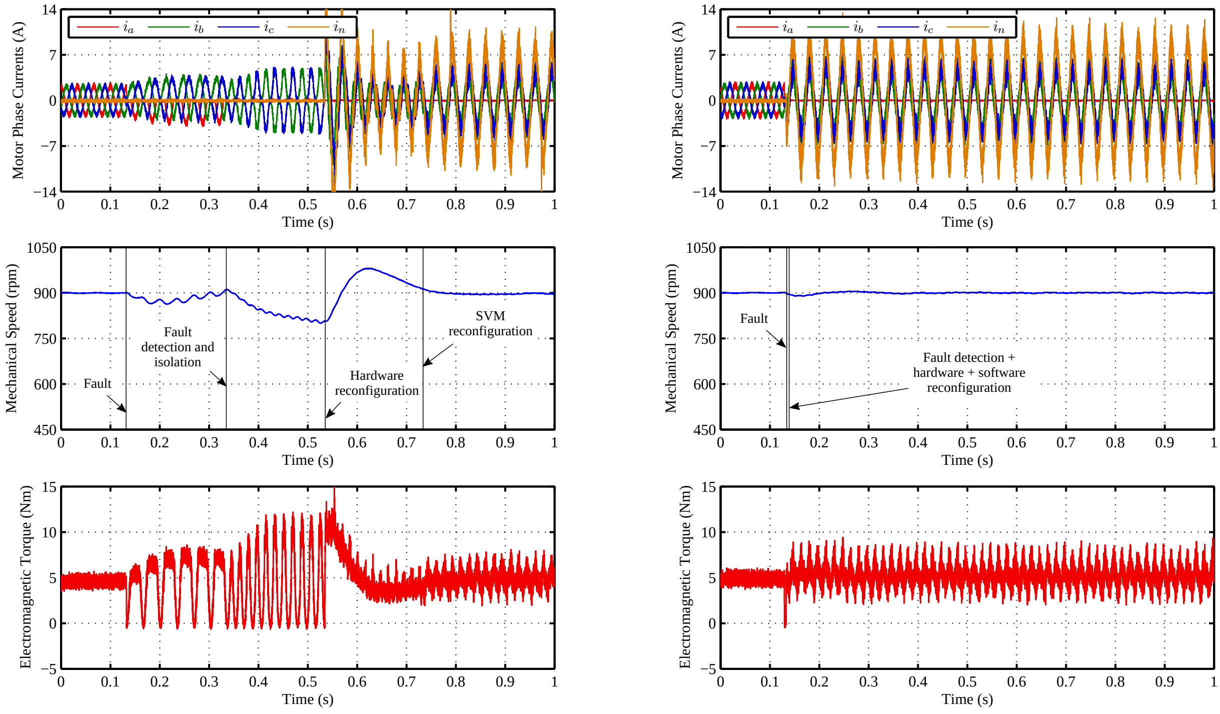

(a) (b)

Figure 6.50: Experimental results regarding the reconfiguration process for a SVM vector control strategy under a phase a NCM reconfiguration: (a) step-by-step behavior; (b) final reconfiguration behavior.

A great agreement between the results shown in Figure 6.50a and the simulation ones depicted in Figure 6.25 is also verified. For the final reconfiguration process shown in Figure 6.50b, it is again observed that the fault-tolerant control system acts relatively fast in order to compensate for the inverter abnormal operation.

Figure 6.51 presents the time-domain waveforms of the PMSM phase currents and phase b voltage for a SVM vector control strategy under a NCM reconfiguration.

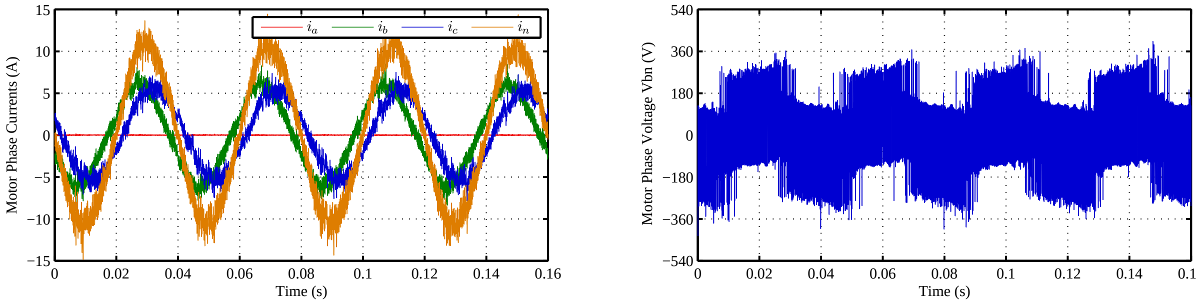

(a) (b)

Figure 6.51: Experimental results of the time-domain waveforms for a SVM vector control strategy under a phase a NCM reconfiguration: (a) motor phase currents; (b) phase b voltage.

The obtained results are also in agreement with the simulation results presented in Figure 6.26. During the reconfiguration process performed by the fault-tolerant control system, the PMSM phase a is isolated from the corresponding inverter leg, becoming in open-circuit. Accordingly, no current flow in the motor phase a is observed. On the other hand, due to the connection of the PMSM winding neutral point to the DC link capacitors midpoint, a large current can be seen, approximately equal to three times the value of the motor phase currents under normal operating conditions. In addition, the currents in the healthy phases also increase by factor of about $\sqrt{3}$, as predicted by the theoretical analysis and in order to generate a magnetomotive force value equivalent to the one obtained for the normal case. It must be noticed that, comparing with the previous case, there is a more noticeable waveform distortion in the motor currents, justified by the combination of the machine neutral connection to a non active supply point, together with the indirect current control through voltage modulation.

As far as the motor phase voltages is concerned, the results present in Figure 6.51b also allow to show that the neutral current flow leads to the arising of a modulation effect on the PMSM healthy phase voltages.

Regarding the PMSM electromagnetic torque analysis, Figure 6.52 presents its time-domain waveform for a SVM vector control strategy.

Comparing with results obtained under normal operating conditions and shown in Figure 3.16, it can be seen that with this converter reconfiguration, the electromagnetic torque waveform presents a more noticeable ripple, represented by a small oscillation at the same frequency of the motor phase currents. Therefore, this leads to a reasonable increase of the TWO from 6.84% under healthy operation to 19.03% under post-fault operation.

Considering now the PMSM phase voltages complex representation, the obtained results are depicted in Figure 6.53.

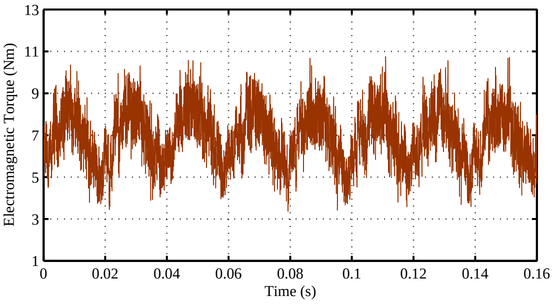

Figure 6.52: Experimental results of the time-domain waveforms of the PMSM electromagnetic torque for a SVM vector control strategy under a phase a NCM reconfiguration.

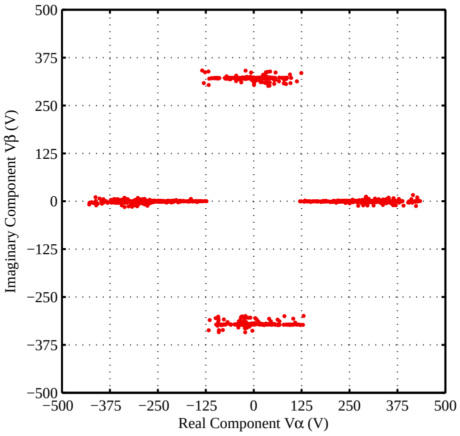

Figure 6.53: Experimental results of the PMSM phase voltages representation in the complex plane for a SVM vector control strategy under a phase a NCM reconfiguration.

In analogy with the obtained results for the HCC vector control, it can be verified that they are very similar. No null vectors are generated and the four active voltage vectors are also horizontally dispersed around the coordinates of the main vectors. Applying the analysis previously done, it is also possible to determine the linear range/overmodulation limits for this specific case. Therefore, a value of 273 is obtained for x_{av}, which means that the boundary between the linear modulation and over modulation occurs when the amplitude of the reference vector reaches a value equivalent to $0.441V_{dc}$, which corresponds to approximately ¾ of the value obtained for the healthy case. Hence, the post-fault mechanical speed must be limited by an equivalent factor in order to avoid electromagnetic torque pulsation.

6.4.2.3 Direct Torque Control

With respect to the reconfiguration transient analysis, equivalent results are also obtained for a DTC control strategy under a NCM reconfiguration (Figure 6.54). Therefore, the same is also applied to this specific case.

Figure 6.55 presents the time-domain waveforms of the PMSM phase currents and phase b

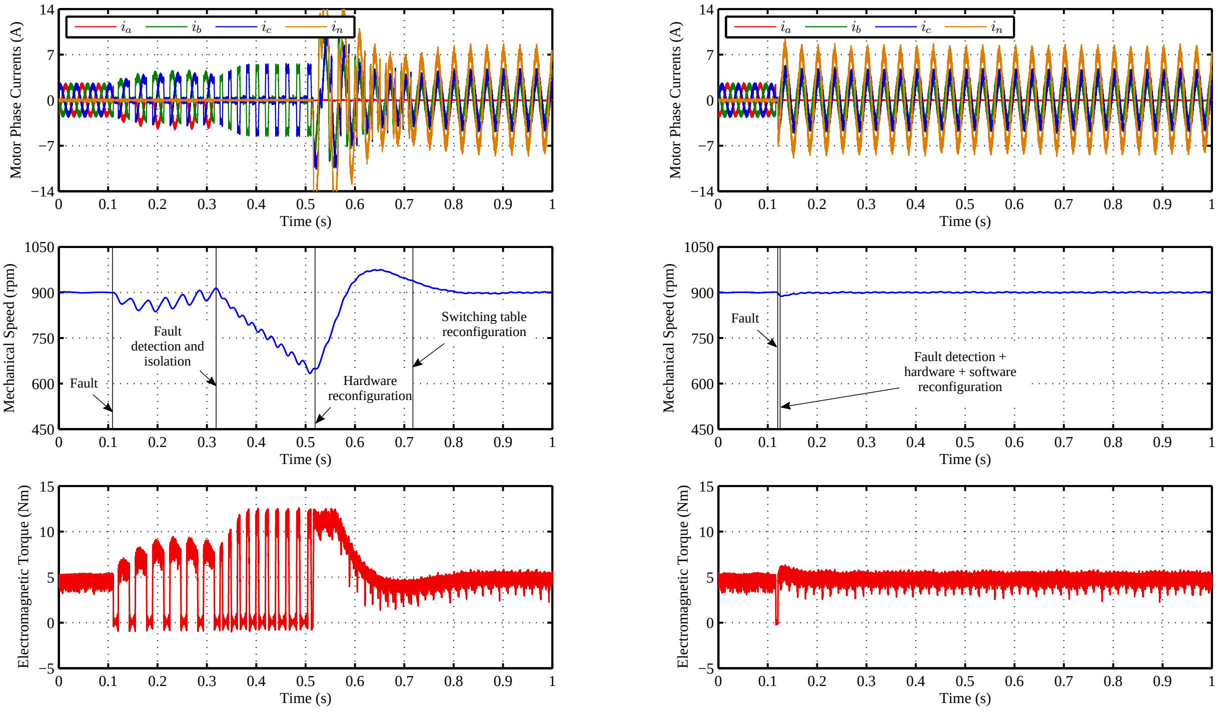

(a)

(b)

Figure 6.54: Experimental results regarding the reconfiguration process for a DTC control strategy under a phase a NCM reconfiguration: (a) step-by-step behavior; (b) final reconfiguration behavior.

voltage for a DTC control strategy under a NCM reconfiguration.

In comparison to the equivalent simulation results, it can be seen that the experimental results are also very similar, demonstrating once more the excellent agreement between the theoretical and laboratory results. Considering that these results are also very similar to the ones obtained for the two previously analyzed cases, the analysis is basically the same.

Regarding the electromagnetic torque, its time-domain waveform for a DTC control strategy and for a phase a NCM reconfiguration is presented in Figure 6.56.

These results show that under post-fault operating conditions, the PMSM electromagnetic torque waveform is very similar to the one obtained for the healthy case. This is also proved by the TWO results, where a value of 10.74% is obtained for this situation, which is very similiar to the value of 10.89% obtained under normal operating conditions.

Finally, with respect to the PMSM phase voltages complex representation, the obtained results are presented in Figure 6.57.

The pattern defined by the voltage vectors coordinates is also very similar to the two previous cases. Applying the same analysis, a value of 278 is obtained for x_{av}. Using then equation (6.24), the radius that limit the linear modulation range becomes equal to 251, which means that it also corresponds to approximately ¾ of the obtained value for the healthy case.

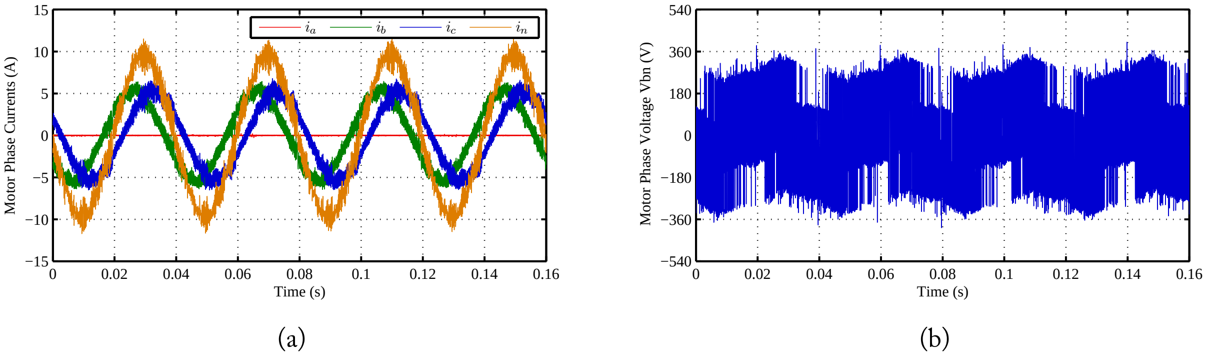

Figure 6.55: Experimental results of the time-domain waveforms for a DTC control strategy under a phase a NCM reconfiguration: (a) motor phase currents; (b) phase b voltage.

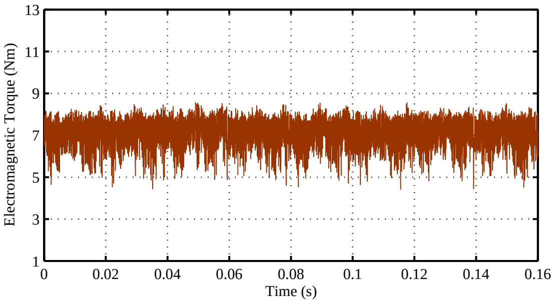

Figure 6.56: Experimental results of the time-domain waveforms of the PMSM electromagnetic torque for a DTC control strategy under a phase a NCM reconfiguration.

6.5 Final Remarks

Taking into account the three control strategies for PMSM drives under study in this work, the post-fault control modifications were derived and discussed for the drive fault-tolerant operating mode under a PCM and NCM converter reconfigurations. The three final fault-tolerant control systems were presented, which are capable to automatically act when an inverter fault occurs by performing four important steps, namely fault diagnosis, inverter faulty leg isolation, converter topology reconfiguration and post-fault control optimization.

Several simulation and experimental results were presented regarding the drive system analysis under a PCM and NCM reconfiguration and for the three considered control techniques. The obtained results allow to demonstrate an excellent agreement between the theoretical results obtained from the computational simulations and the experimental ones, obtained from the developed laboratory setup. Despite of only a phase a reconfiguration was considered, additional simulation and experimental results have demonstrated that an equivalent behavior is also observed for the other two cases, being therefore applied the same analysis.

The developed fault-tolerant control system allows to effectively compensate for an inverter malfunction by rapidly performing these four important steps. All this fully automated reconfigu-

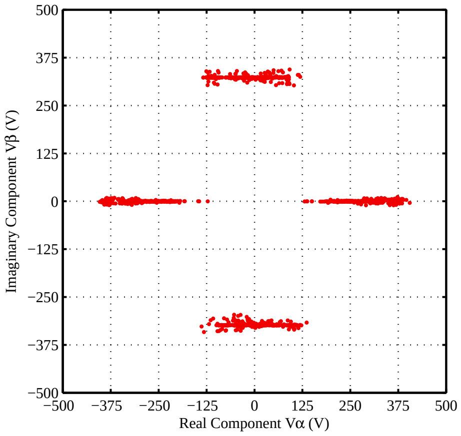

Figure 6.57: Experimental results of the PMSM phase voltages representation in the complex plane for a DTC control strategy under a phase a NCM reconfiguration.

ration process can be accomplished in a relatively short time which allows to minimize the impact of the inverter fault in the drive performance.

Finally, it has been proved that for a PCM reconfiguration the machine can operate at full torque but its mechanical speed must be limited to one-half of its rated value in order to optimize the overall performance. As far as the NCM reconfiguration is concerned, the motor phase currents increasing lead to the need to limit the load torque to $1/\sqrt{3}$ of the rated value while the PMSM mechanical speed must be limited to approximately ¾ of its rated value.

Chapter 7

Performance Analysis

This chapter is entirely dedicated to the performance evaluation of the developed fault-tolerant PMSM drive prototype through an exhaustive analysis of experimental results. In order to accomplish this objective, three different type of analysis are considered: an electrical analysis, a thermal analysis and an acoustic analysis.

The first analysis type is the most important one since the components that comprise the system under study are electrical/electronic devices or are strongly dependent on electrical characteristics. Hence, special attention was given to this subject by performing a very detailed evaluation of several parameters such as voltage and currents rms and distortion values, motor power factor and efficiency values.

Regarding the thermal analysis, the main objective is to evaluate the drive temperature profile for three distinct operating conditions, namely the healthy case, inverter fault operation and post-fault operating conditions (fault-tolerant mode). In this case, the inverter and PMSM temperatures are considered since these drive components are the most affected ones by the fault and reconfiguration modes.

Finally, an acoustical analysis is also performed in order to evaluate the noise characteristics emitted by the PMSM. This is accomplished by studying the noise spectrum and by the calculation of their rms values obtained for each considered fault-tolerant operating condition.

For this experimental analysis, the conditions and parameters already defined for the previously analyzed experimental results were also used.

7.1 Electrical Analysis

This electrical analysis takes into account the evaluation of several key parameters namely the PMSM voltage and currents rms and TWD values, its power factor and efficiency. The inverter efficiency is also addressed as well as the inverter+motor efficiency.

With the aim to perform a very detailed study, the majority of the results are presented in the form of three-dimensional maps. In this way, instead of analyzing the drive performance for some specific operating points, it is possible to characterize the drive performance in all its operating range, therefore allowing a more complete analysis.

All the previous parameters are evaluated for the three considered PMSM control strategies (HCC vector control, SVM vector control and DTC) and for three distinct operating conditions, namely the healthy case, the PCM reconfiguration and the NCM reconfiguration.

Under normal operating conditions, the drive can operate up to the PMSM rated speed and torque values. Consequently, all the presented results are taken assuming the rated values as limiting conditions (1500 rpm and 14 Nm).

For the PCM reconfiguration post-fault operating mode, it was already proved that the PMSM motor speed must be limited to one-half of the rated value. Therefore, the results were obtained for the full load torque range (14 Nm) but taking into account this speed limitation (750 rpm).

Regarding the NCM reconfiguration, due to the motor currents increase by a factor of $\sqrt{3}$, and in order to avoid the PMSM current overload, the load torque must be limited to $1/\sqrt{3}$ of the rated value (nearly 8 Nm). On the other hand, it was also demonstrated that under these conditions, the PMSM mechanical speed must be limited to approximately ¾ of its corresponding rated value (1125 rpm).

7.1.1 Voltage RMS Values

7.1.1.1 Normal Operating Conditions

Figure 7.1 presents the PMSM phase voltage rms values[1] obtained for the three considered control strategies under normal operating conditions.

The obtained results allow to conclude that the HCC vector control and the DTC control techniques supply the PMSM with larger voltage rms values than for the SVM vector control. The indirect current control trough voltage modulation that characterizes this last control strategy generates a voltage waveform with less harmonic distortion, imposing simultaneously to the inverter a fixed switching frequency. As a result, by reducing the voltage harmonics, lower rms values can be obtained for the SVM vector control.

This is clearly seen by the results shown in Figure 7.1d, of the minimum, maximum and average values obtained for each control strategy. For the HCC vector control and DTC, the voltage rms values do not vary significantly for all the considered operating points. Therefore, the minimum and maximum values are relatively close to each other. On the contrary, for the SVM vector control, there is a big difference between these values. In fact, Figure 7.1b shows that, the voltage rms values approximately vary in a proportional manner in relation to the PMSM mechanical speed. Despite the rms value of the voltage fundamental component varies proportionally to the mechanical speed

---

[1] All the voltage rms values presented in this section result from an arithmetic mean calculation considering the rms values of the motor phases that are supplied.

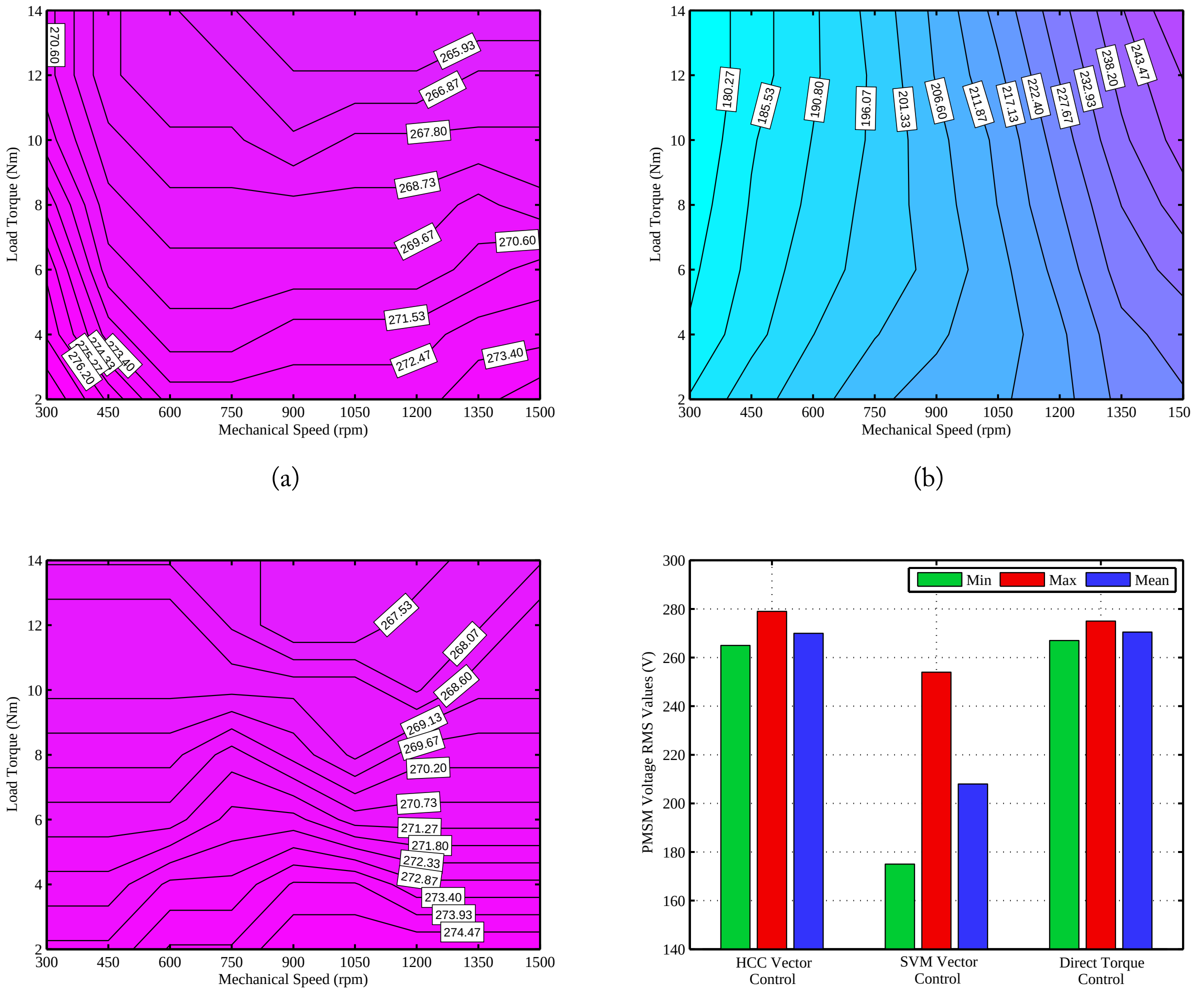

(a) (b)

(c) (d)

Figure 7.1: Experimental results of the PMSM phase voltage rms values under normal operating conditions: (a) HCC vector control; (b) SVM vector control; (c) DTC; (d) Global statistical results.

(frequency) for all the three considered control strategies, the additional voltage harmonic content generated by the HCC vector control and DTC contributes to the global rms values increasing.

7.1.1.2 PCM Reconfiguration

Figure 7.2 presents the PMSM phase voltage rms values obtained for the three considered control strategies under a phase a PCM reconfiguration.

As seen before, with an inverter PCM reconfiguration, the motor phase voltages decrease considerably, especially for the PMSM phase a. Therefore, and comparing to the healthy situation, the average values of all the three motor phase voltages rms values are noticeable lower. Nevertheless, it can be also verified that the SVM vector control still allows to fed the PMSM with lower rms voltage values, as compared to the two other techniques.

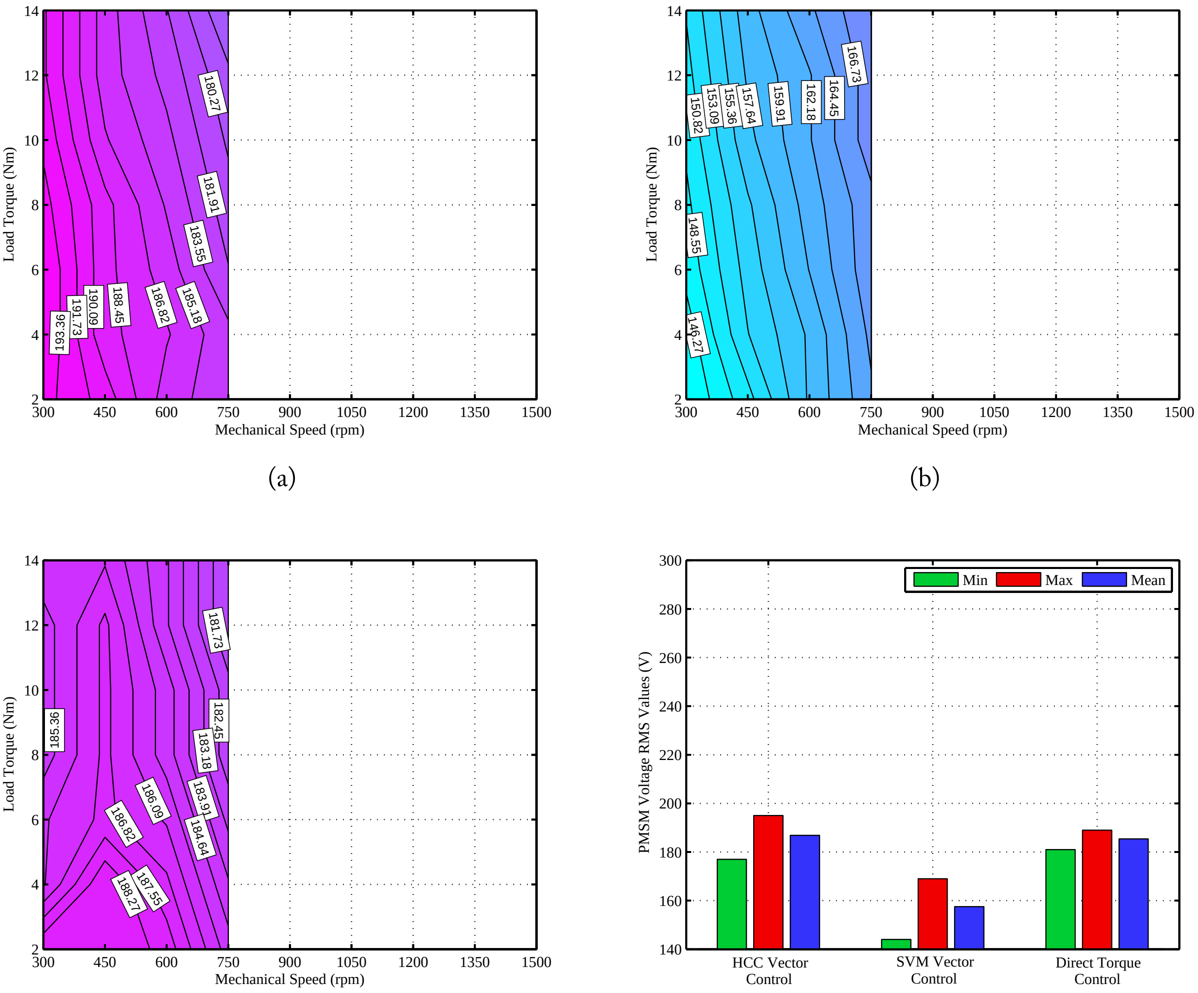

(a) (b)

(c) (d)

Figure 7.2: Experimental results of the PMSM phase voltage rms values for a phase a PCM reconfiguration: (a) HCC vector control; (b) SVM vector control; (c) DTC; (d) Global statistical results.

7.1.1.3 NCM Reconfiguration

Considering now the results obtained for a phase a NCM reconfiguration, Figure 7.3 presents the PMSM phase voltage rms values obtained for the three considered control strategies.

Analyzing the three voltage rms values maps, it is evident than in general, the rms values increase proportionally in relation to the PMSM mechanical speed. However, and in contrast to the previous cases, the results shown in Figure 7.3d allow to conclude that there are no significant differences between each control strategy, which means that the machine is fed by voltage waveforms with equivalent rms values.

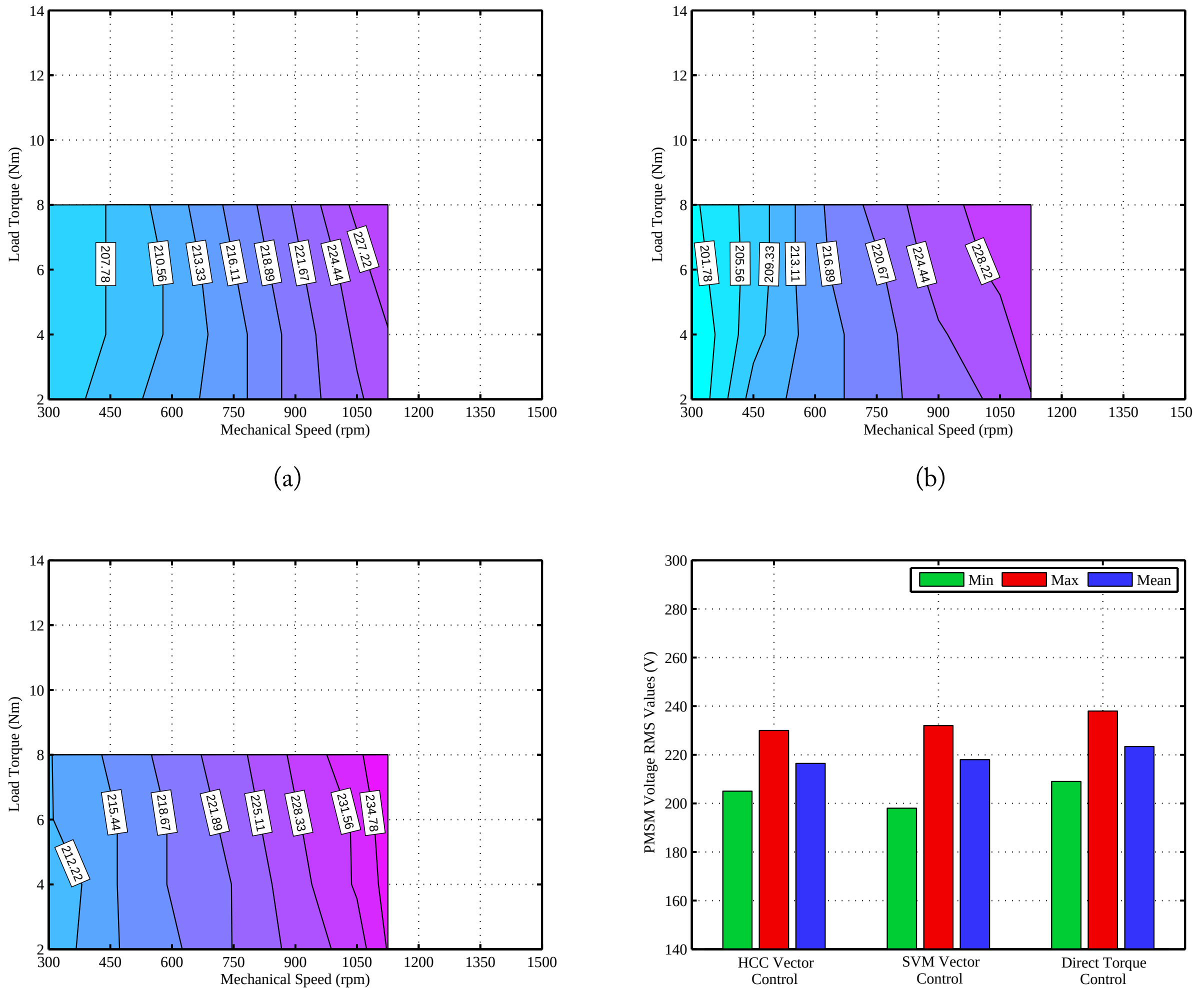

(a) (b)

(c) (d)

Figure 7.3: Experimental results of the PMSM phase voltage rms values for a phase a NCM reconfiguration: (a) HCC vector control; (b) SVM vector control; (c) DTC; (d) Global statistical results.

7.1.2 Voltage Waveform Distortion

7.1.2.1 Normal Operating Conditions

The voltage distortion was evaluated for the three considered control strategies by the calculation of the TWD values[2]. The obtained results are depicted in Figure 7.4.

Comparing the results for the three control strategies, it can be observed that similar TWD values are obtained for the HCC vector control and DTC. These control strategies present some similarities since the switching states are determined by hysteresis controllers that cannot impose a fixed switching frequency. Consequently, the generated voltage waveforms are also similar, presenting equivalent TWD values. On the other side, and as mentioned before, the results in Figure

---

[2] All the voltage TWD values presented in this section result from an arithmetic mean calculation considering the TWD values of the motor phases that are supplied.

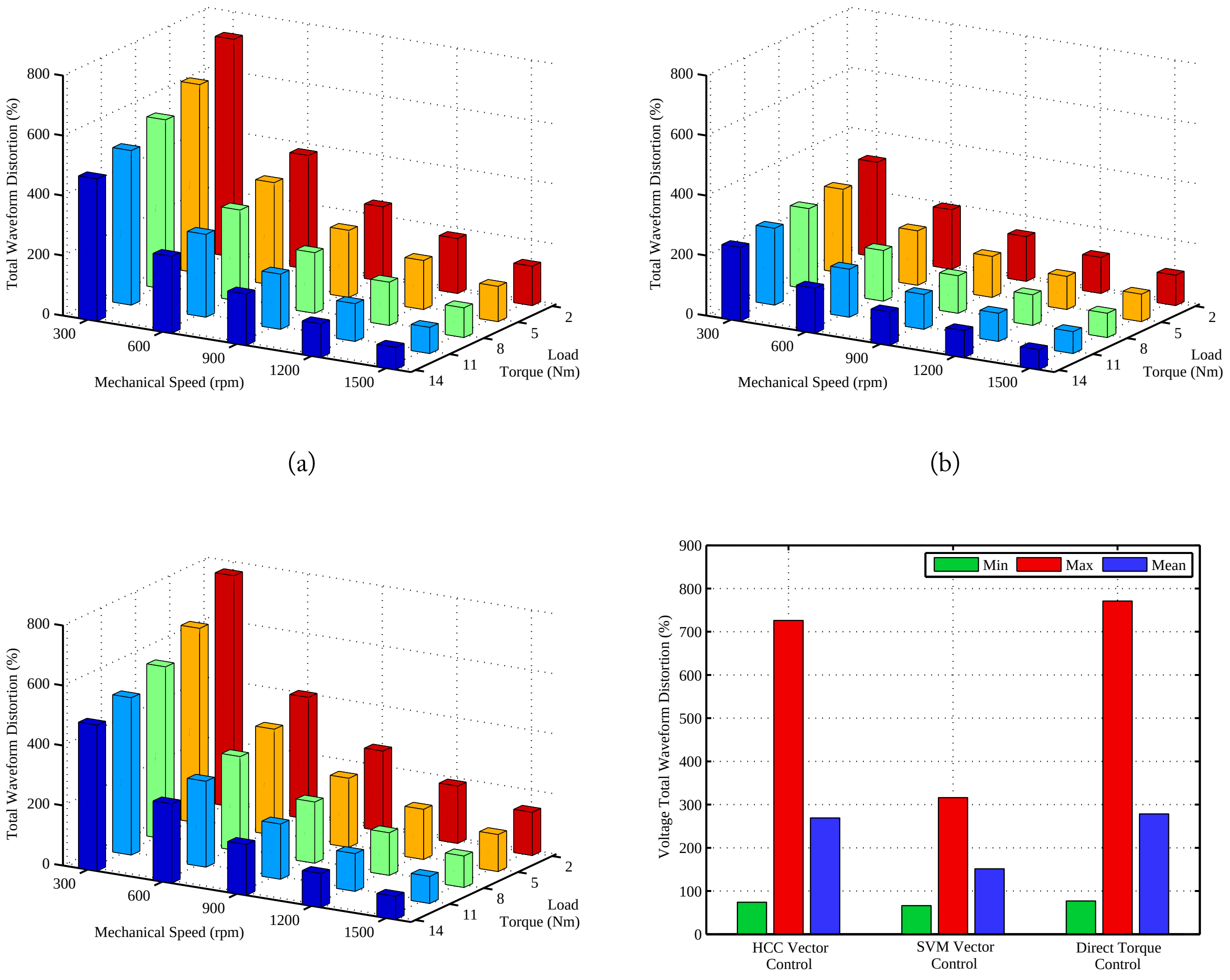

(a) (b)

(c) (d)

Figure 7.4: Experimental results of the PMSM phase voltage TWD values under normal operating conditions: (a) HCC vector control; (b) SVM vector control; (c) DTC; (d) Global statistical results.

7.4b clearly show that the SVM vector control supplies the PMSM with a much less distorted voltage waveform. Furthermore, it can be also seen that the TWD values decrease with the increasing of the load and mechanical speed values.

From the global statistical analysis presented in Figure 7.4d, the same conclusions can be taken. The maximum voltage TWD values obtained for the HCC vector control and DTC are more than twice the value obtained for the SVM vector control. Therefore, from a global point of view, the results show that this last technique allows to generate almost one-half of the voltage distortion, when comparing with the other two control strategies.

7.1.2.2 PCM Reconfiguration

Figure 7.5 presents the PMSM phase voltage TWD values obtained for the three considered control strategies under a phase a PCM reconfiguration.

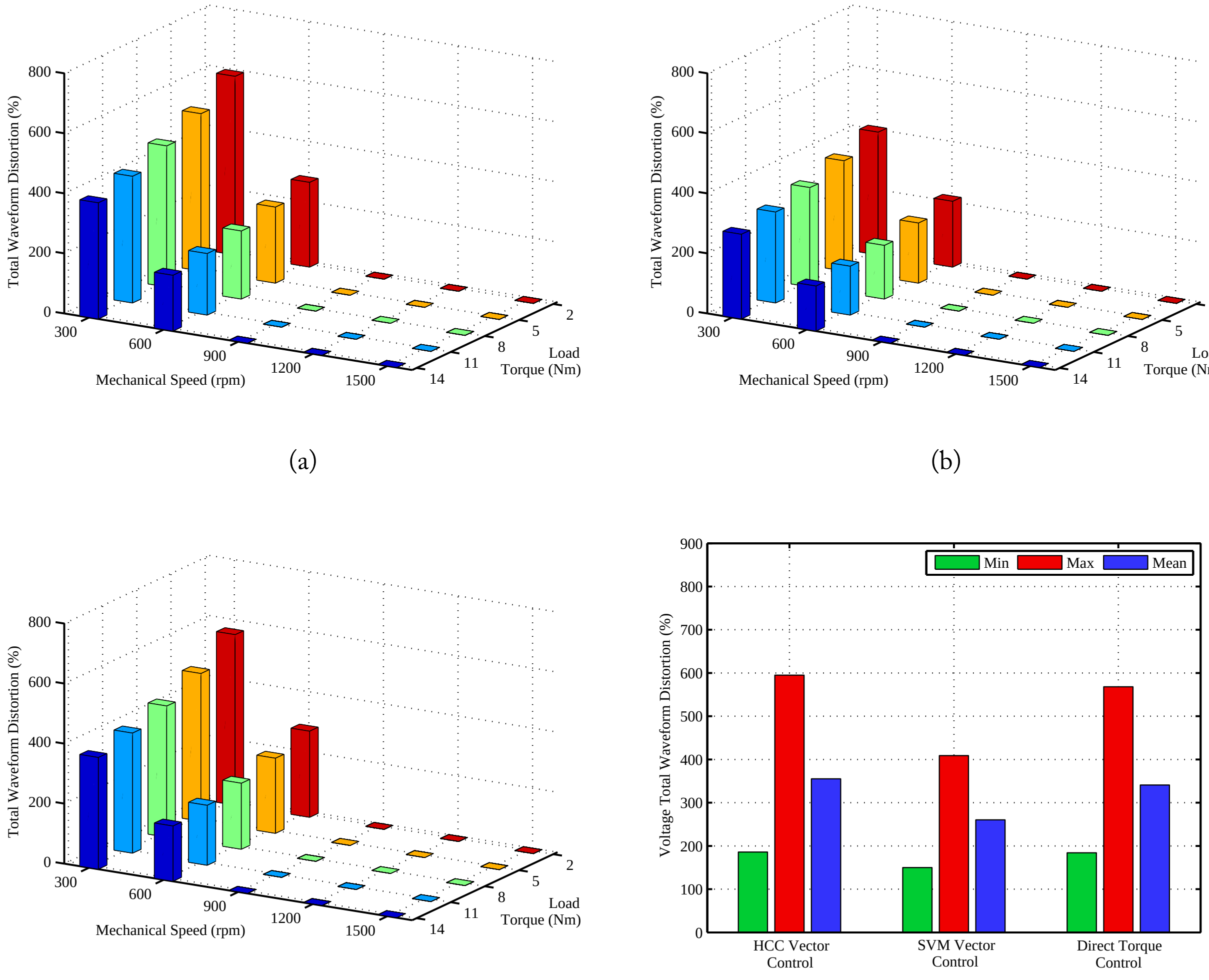

(a) (b)

(c) (d)

Figure 7.5: Experimental results of the PMSM phase voltage TWD values for a phase a PCM reconfiguration: (a) HCC vector control; (b) SVM vector control; (c) DTC; (d) Global statistical results.

Due to the PMSM phase connection to the DC link capacitors midpoint, the amplitude of the motor phase voltages are reduced. Therefore, comparing with the equivalent mechanical operating points for the healthy case, it can be seen that the voltage distortion is lower for all the three control strategies. Moreover, it can be also observed that HCC vector control and DTC have similar distortion values, while the SVM vector control strategy presents the best performance by generating the lowest distorted voltage waveforms.

7.1.2.3 NCM Reconfiguration

Considering now the drive post-fault operation under a phase a NCM reconfiguration, the corresponding phase voltage TWD results are presented in Figure 7.6.

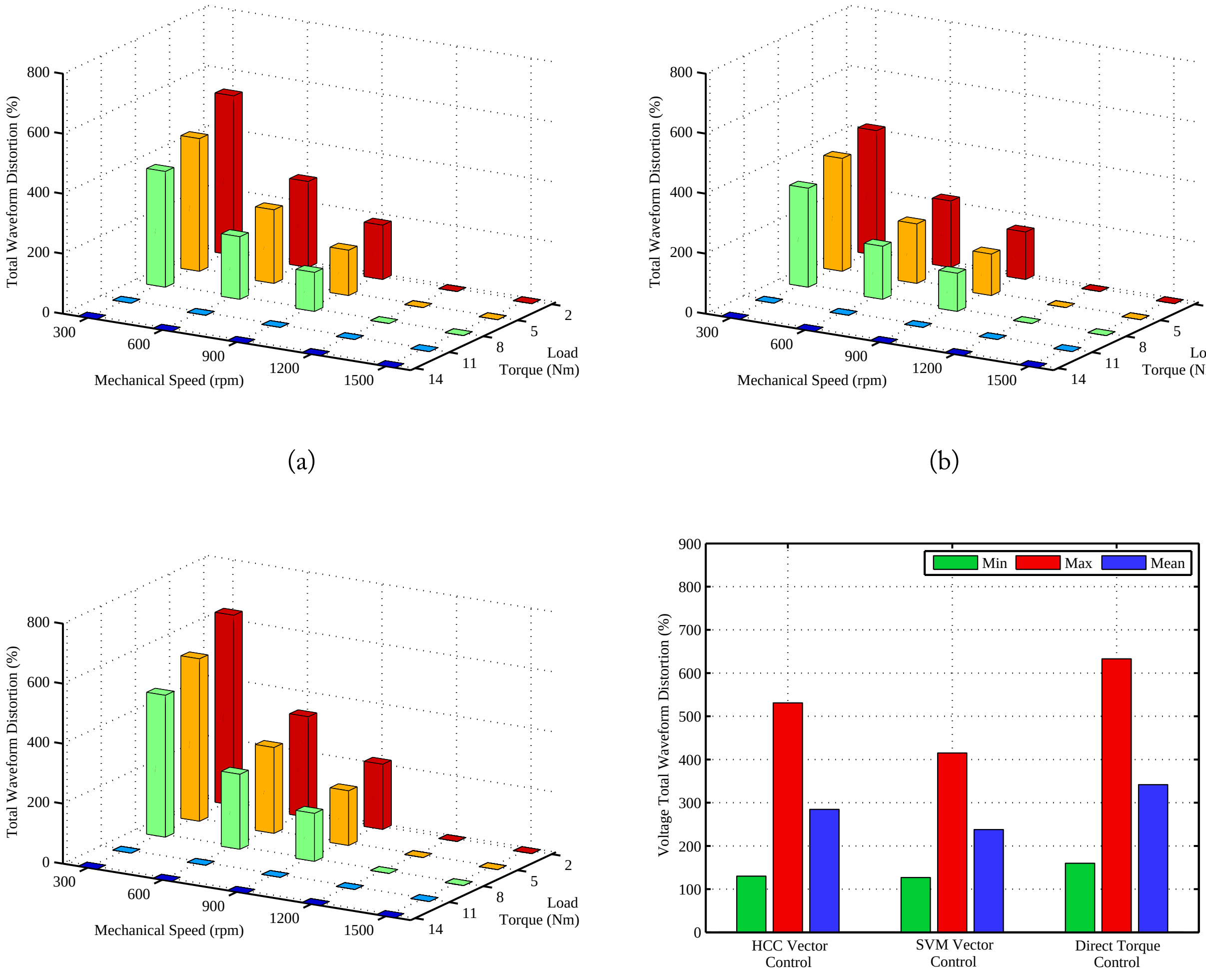

(a) (b)

(c) (d)

Figure 7.6: Experimental results of the PMSM phase voltage TWD values for a phase a NCM reconfiguration: (a) HCC vector control; (b) SVM vector control; (c) DTC; (d) Global statistical results.

Comparing with the normal situation, it can be verified that the voltage distortion values also decrease under these conditions for all control strategies. However, the presented results allow to conclude that the DTC generates more distorted voltage waveforms, followed by the HCC vector control, presenting the SVM vector control strategy the lowest TWD values.

7.1.3 Current RMS Values

7.1.3.1 Normal Operating Conditions

Figure 7.7 presents the PMSM phase currents rms values obtained for the three considered control strategies under normal operating conditions.

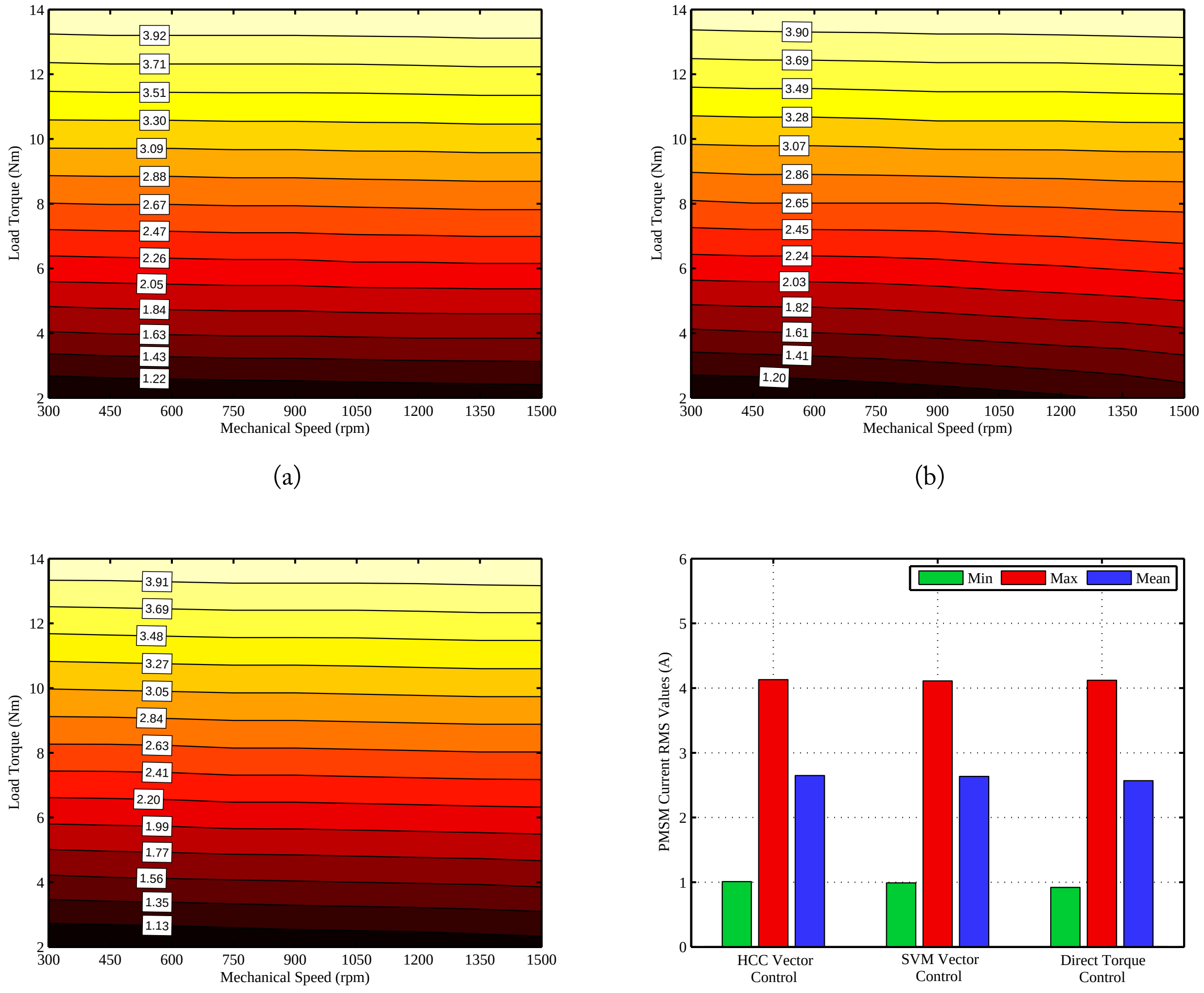

(a)

(b)

(c)

(d)

Figure 7.7: Experimental results of the PMSM phase current rms values under normal operating conditions: (a) HCC vector control; (b) SVM vector control; (c) DTC; (d) Global statistical results.

Analyzing the previous results, it is clearly observed that the current rms values are virtually the same for the three considered control strategies. In contrast to the voltage rms values that typically increase with the motor mechanical speed increasing, the current rms values are strongly dependent on the machine load torque. This is illustrated by the almost horizontal isometric lines, demonstrating the proportional relation between the current rms values and the load torque level.

The similarity of the obtained values is also patent on the global statistical results shown in

Figure 7.7d, where the minimum, maximum and average values are practically the same for the three control techniques.

7.1.3.2 PCM Reconfiguration

Figure 7.8 presents the PMSM phase currents rms values obtained for the three considered control strategies under a phase a PCM reconfiguration.

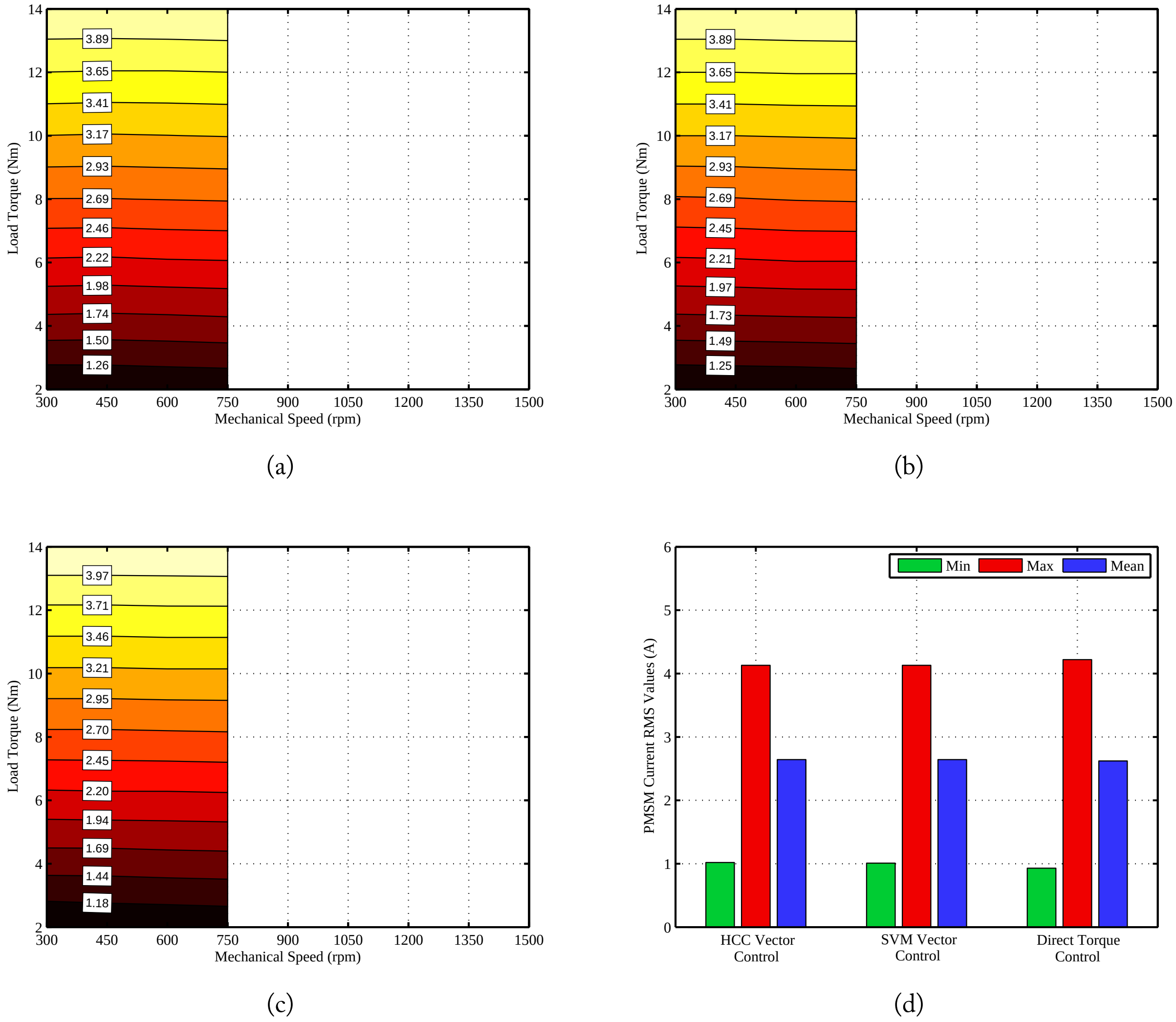

(a)

(b)

(c)

(d)

Figure 7.8: Experimental results of the PMSM phase current rms values for a phase a PCM reconfiguration: (a) HCC vector control; (b) SVM vector control; (c) DTC; (d) Global statistical results.

Despite the mechanical speed limitation that must be imposed for this post-fault reconfiguration, the machine is still capable to operate at full torque. Therefore, the current rms values are very similar to the ones obtained for the normal situation, showing also the direct relation between the load torque and the current rms values.

7.1.3.3 NCM Reconfiguration

Regarding the NCM inverter reconfiguration, Figure 7.9 presents the PMSM phase currents rms values obtained for the three considered control strategies.

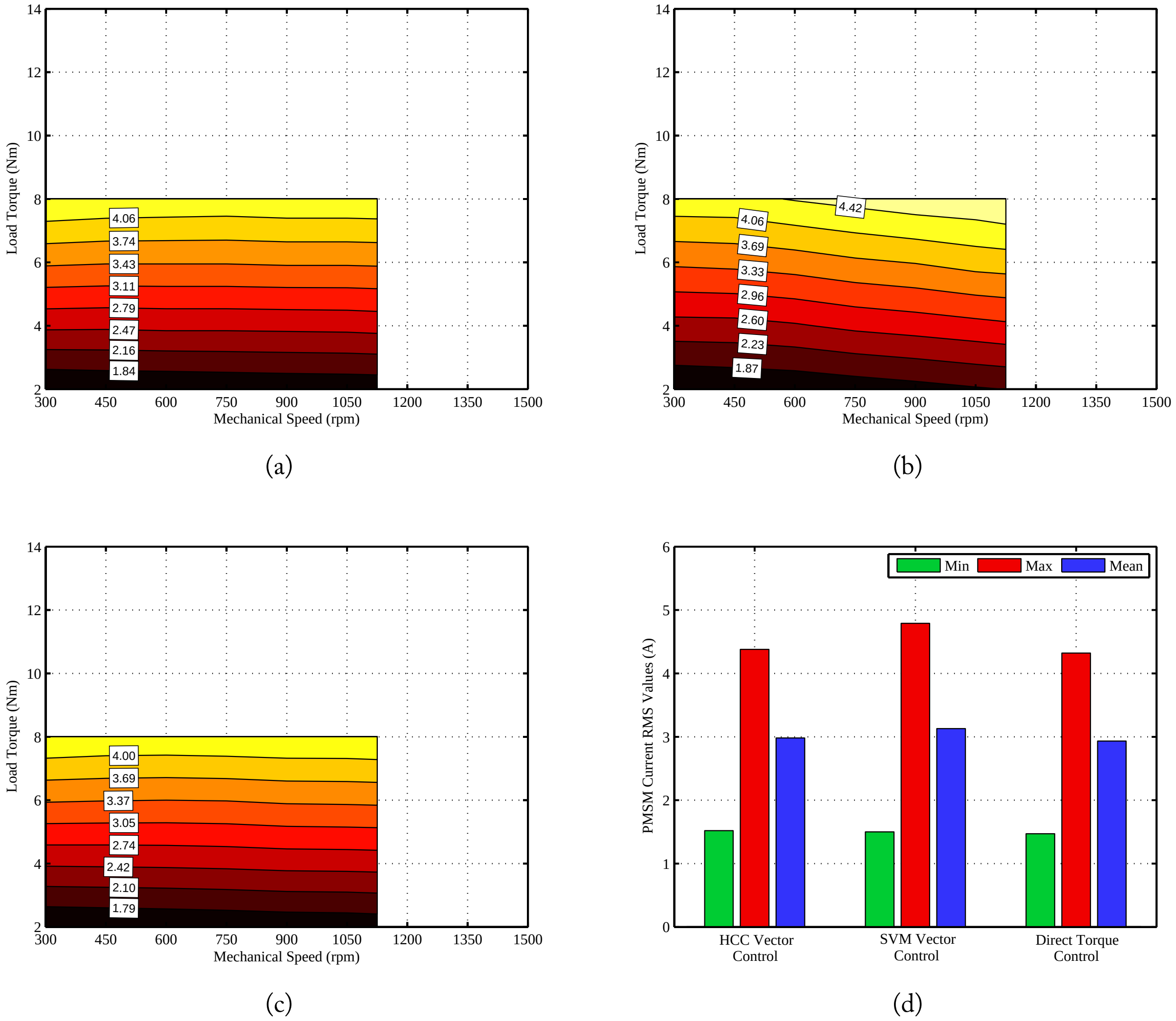

(a) (b)

(c) (d)

Figure 7.9: Experimental results of the PMSM phase current rms values for a phase a NCM reconfiguration: (a) HCC vector control; (b) SVM vector control; (c) DTC; (d) Global statistical results.

The proportional relation between the current rms values and the load torque level is also demonstrated by these results. Beyond this, it can be seen that in order to avoid overcurrent values, the PMSM load torque must be limited to $1/\sqrt{3}$ of the rated value. Furthermore, similar results are obtained for the HCC vector control and DTC, whereas the SVM vector control supplies the PMSM with a little bit larger current values due to the indirect current control through voltage modulation that characterizes this method.

7.1.4 Current Waveform Distortion

7.1.4.1 Normal Operating Conditions

Figure 7.10 presents the PMSM phase currents TWD results obtained for the three considered control strategies under normal operating conditions.

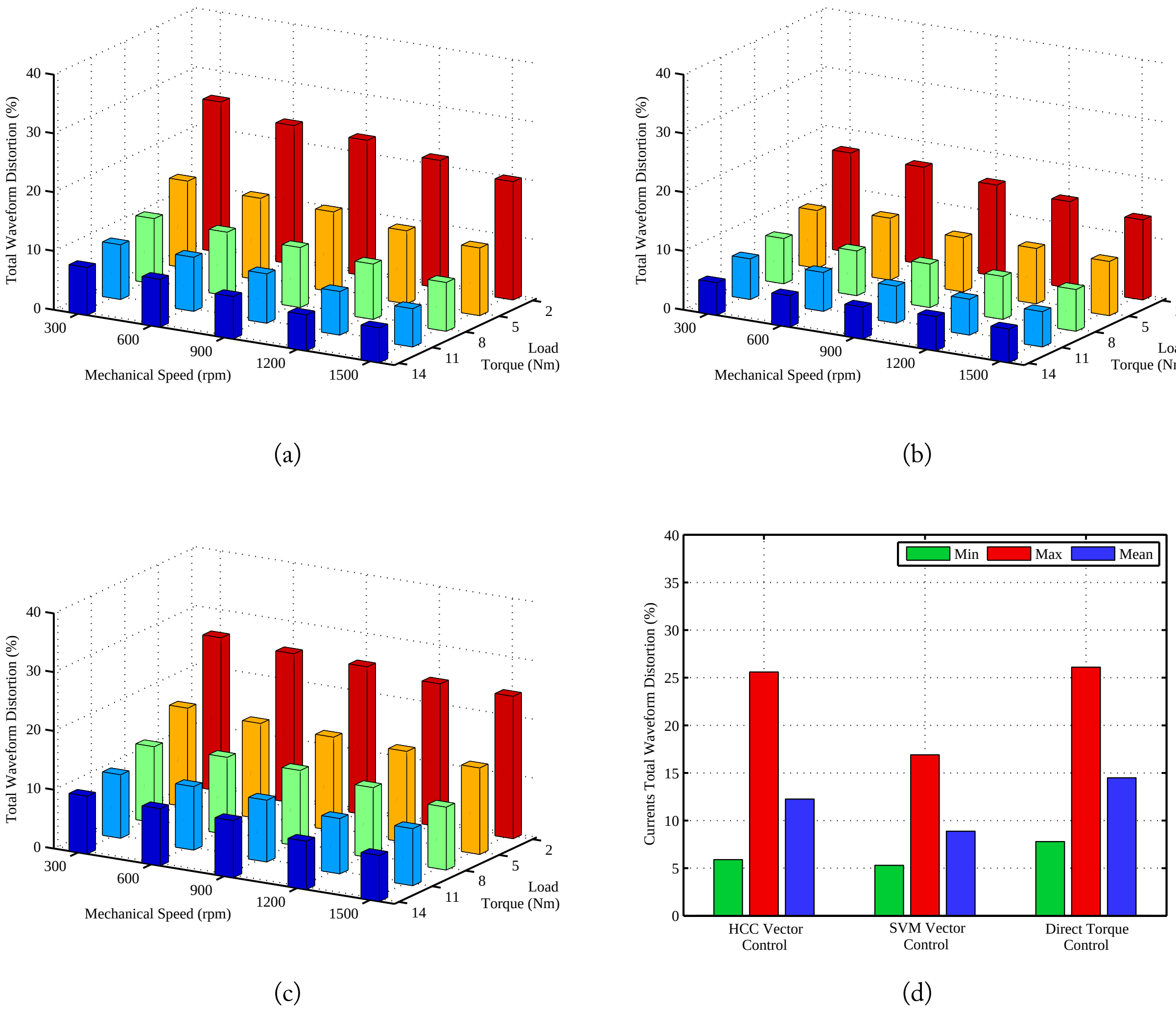

Figure 7.10: Experimental results of the PMSM phase current TWD values under normal operating conditions: (a) HCC vector control; (b) SVM vector control; (c) DTC; (d) Global statistical results.

In analogy with the voltage TWD values obtained for the drive healthy operation, it can be seen that the current TWD values decrease with the increasing of the load and mechanical speed values. Furthermore, it can be concluded that due to the torque ripple that characterizes the DTC, this control technique generates larger current distortion values when comparing with the other two. On the other hand, the low harmonic content of the PMSM voltage waveforms generated by the SVM vector control leads to less distorted current waveforms, allowing this control strategy to achieve a better performance.

7.1.4.2 PCM Reconfiguration

Regarding the PCM inverter reconfiguration, Figure 7.11 presents the PMSM phase currents TWD values obtained for the three considered control strategies.

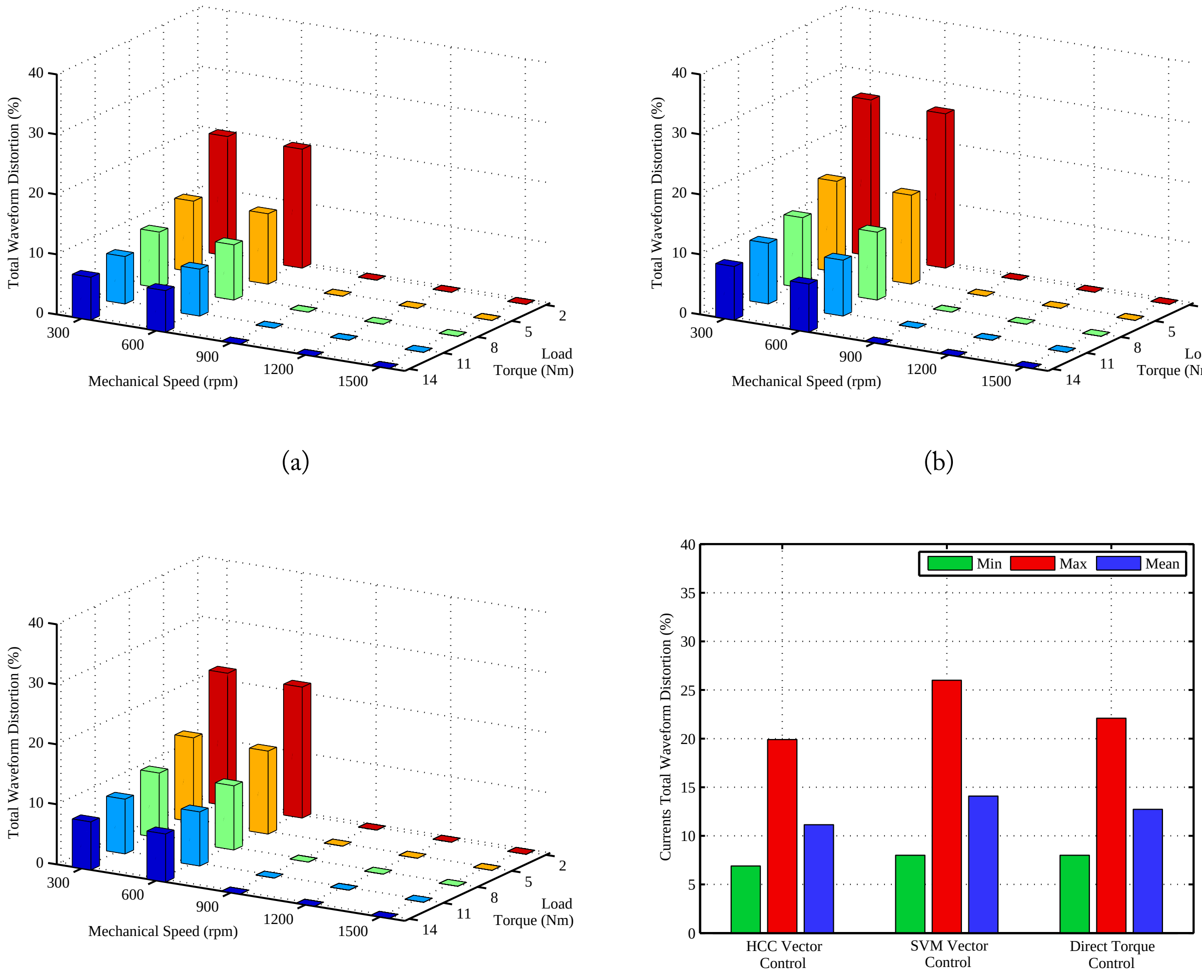

(a) (b)

(c) (d)

Figure 7.11: Experimental results of the PMSM phase current TWD values for a phase a PCM reconfiguration: (a) HCC vector control; (b) SVM vector control; (c) DTC; (d) Global statistical results.

Despite the lowest voltage TWD values obtained for the SVM vector control under this inverter reconfiguration, it can be seen that as far the motor currents TWD values is concerned, in comparison with the two other techniques, this control strategy leads to the generation of more distorted current waveforms. As discussed before, this is justified by the machine phase connection to a nonactive supply point, together with the indirect current control through voltage modulation, which leads to the generation of higher current harmonic distortion.

For the HCC vector control and DTC, the average current TWD decreases when comparing to the healthy case, in accordance with the similar behavior that is observed for the PMSM phase voltage TWD values.

7.1.4.3 NCM Reconfiguration

With respect to the NCM inverter reconfiguration, Figure 7.12 presents the PMSM phase currents TWD values obtained for the three considered control strategies.

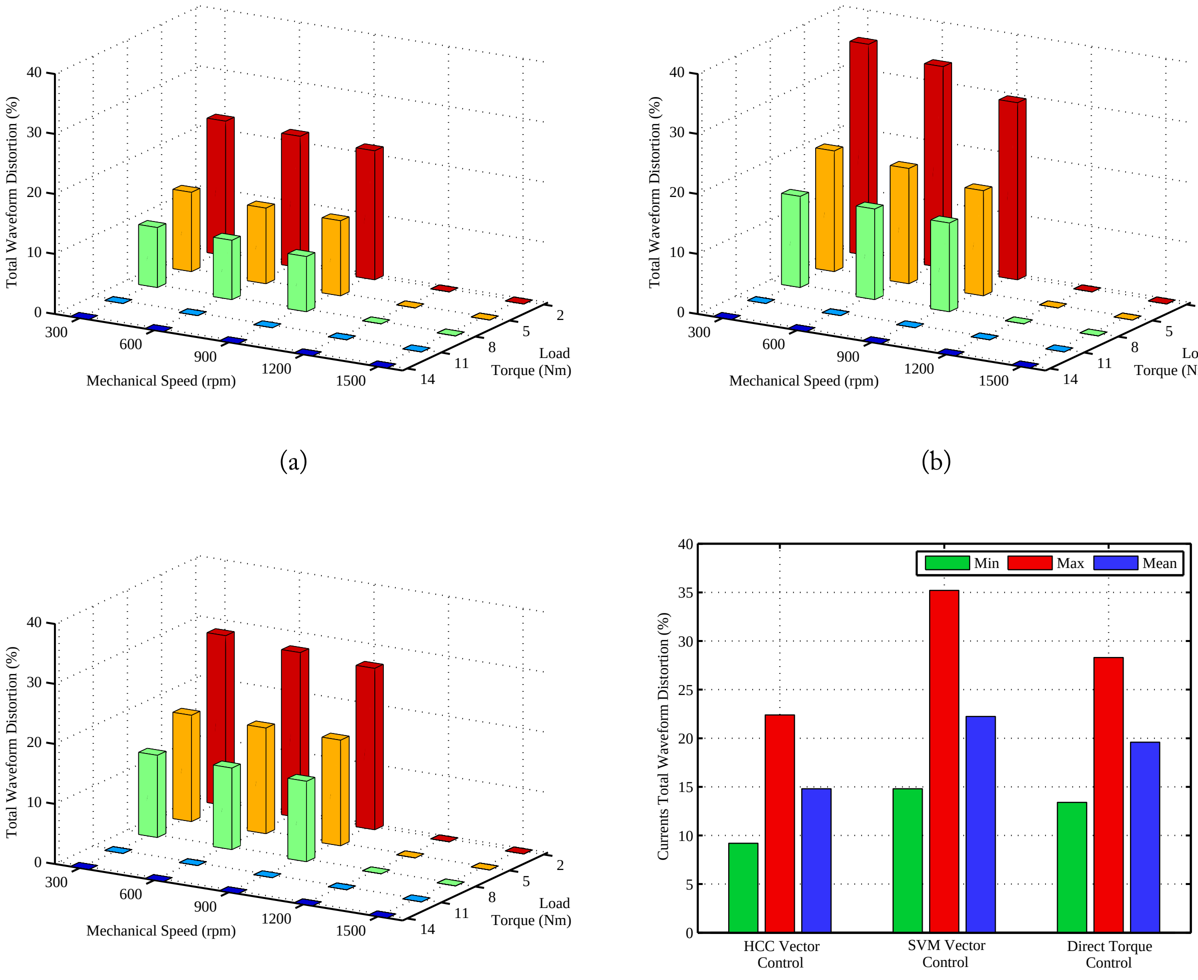

(a) (b)

(c) (d)

Figure 7.12: Experimental results of the PMSM phase current TWD values for a phase a NCM reconfiguration: (a) HCC vector control; (b) SVM vector control; (c) DTC; (d) Global statistical results.

Comparing now these TWD results with the ones obtained for the drive normal operation, it can be verified that in general, all values are higher for this post-fault reconfiguration. This is also confirmed by the statistical analysis depicted in Figure 7.12d, where it is possible to conclude that all TWD mean values are larger than the ones obtained for the healthy situation.

It is worth noticing the great difference observed for the SVM vector control results, where the TWD values are more than two times larger than the ones obtained for the normal case. This is justified by the machine neutral connection to a nonactive supply point, together with the indirect current control, leading to a less effective current control and therefore, to a larger current waveform distortion.

7.1.5 Power Factor

7.1.5.1 Normal Operating Conditions

Figure 7.13 presents the PMSM power factor values obtained for the three considered control strategies under normal operating conditions.

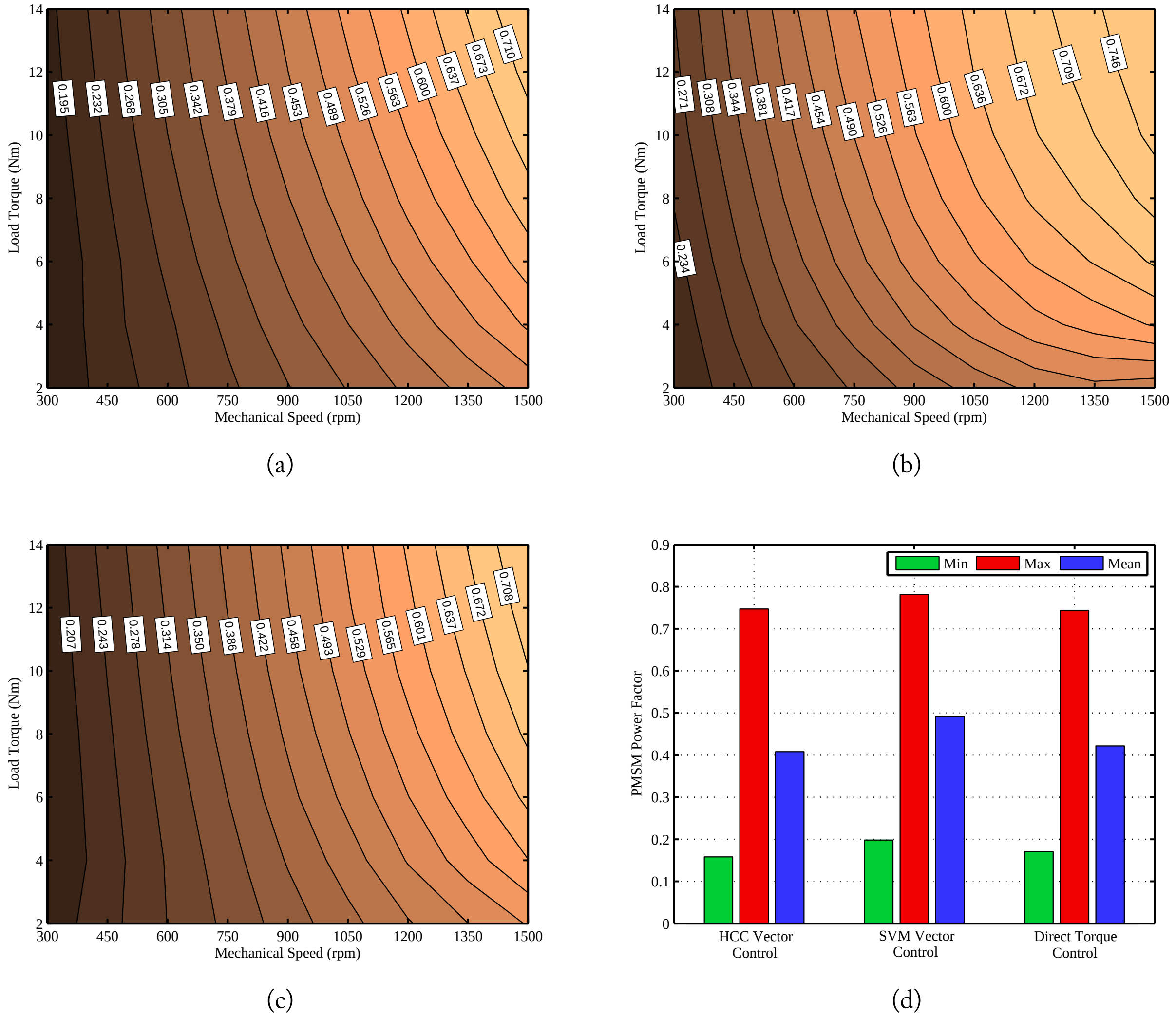

(a) (b)

(c) (d)

Figure 7.13: Experimental results of the PMSM power factor values under normal operating conditions: (a) HCC vector control; (b) SVM vector control; (c) DTC; (d) Global statistical results.

From these results it can be concluded that the higher power factor values are obtained when the load and mechanical speed increase. It is also observed that when a HCC vector control or DTC strategy is used to control the machine, similar power factor values are obtained. Additionally, the SVM vector control strategy allows to achieve the best performance levels, represented by the highest PMSM power factor values.

One of the most relevant factors that has an important impact on the PMSM power factor are the voltage rms values that supply the machine. Accordingly, it was already verified from the results in Figure 7.1 that larger voltage rms values are obtained for the HCC vector control and DTC. Consequently, and taking into account that the rms motor phase currents are virtually the same for the three control techniques, this leads to larger apparent power values and thus, lower power factor values obtained. On the contrary, the lower motor phase rms voltage values generated by the SVM technique, reduces the machine apparent power and leads to the subsequent increase of the motor power factor.

7.1.5.2 PCM Reconfiguration

Regarding the PCM reconfiguration, the PMSM power factor values obtained for the three considered control strategies are presented in Figure 7.14.

From a global point of view, it can be verified that the results obtained for the HCC vector control and DTC are also very similar to each other. On the other side, the SVM vector control still reveals the best results, presenting higher power factor values than the other two control strategies. Furthermore, comparing with the results obtained under normal operating conditions, the overall power factor values decrease for this post-fault converter reconfiguration.

7.1.5.3 NCM Reconfiguration

Considering now a phase a NCM reconfiguration, Figure 7.15 presents the PMSM power factor values obtained for the three considered control strategies.

Comparing with the healthy drive operation results, the previous figure shows that for this post-fault converter topology, the PMSM power factor values are negatively affected. One of the causes that contribute to this is related to the motor phase currents increasing by a factor of $\sqrt{3}$ in the two healthy phases that result in larger apparent power values.

It is also important to notice that as opposed to the two previously discussed situations, for this specific case the SVM vector control shows the worst overall power factor results. Despite the lower voltage rms values obtained for this technique under these conditions, due to the worse current control performance, larger current rms and TWD values are obtained, leading to larger apparent power values and lower power factor values.

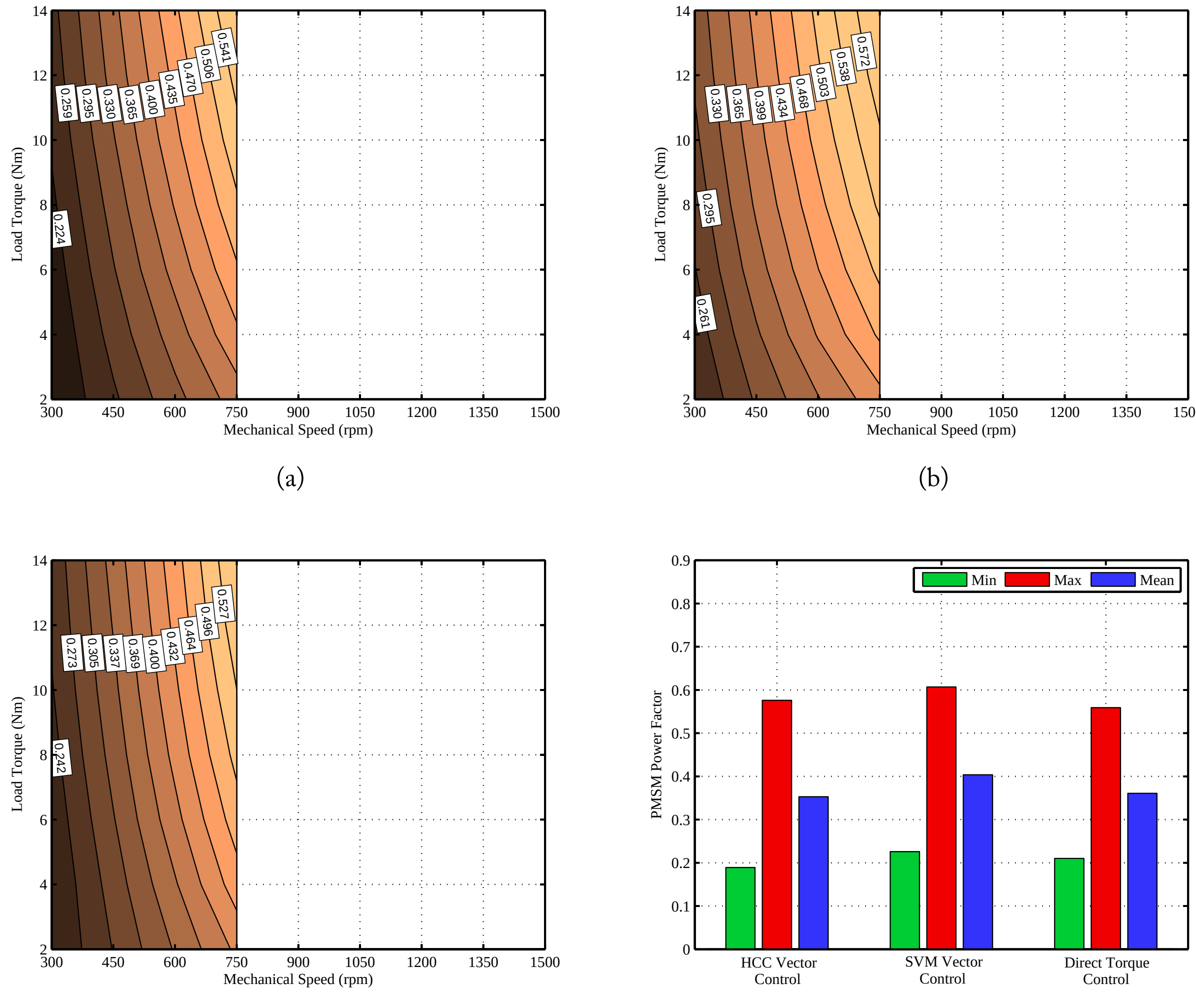

(a)

(b)

(c)

(d)

Figure 7.14: Experimental results of the PMSM power factor maps for a phase a PCM reconfiguration: (a) HCC vector control; (b) SVM vector control; (c) DTC; (d) Global statistical results.

7.1.6 PMSM Efficiency

7.1.6.1 Normal Operating Conditions

Figure 7.16 presents the PMSM efficiency maps obtained for the three considered control strategies under normal operating conditions.

By comparing these results, it can be verified that the maximum efficiency value for each control strategy is achieved for the rated operating conditions. It is also observed that similar results are obtained for the HCC vector control and the DTC techniques.

Higher efficiency values are achieved for the vector control employing a SVM strategy. This technique allows to supply the motor with less distorted waveforms that leads to the decrease of the voltages rms values, especially for low operating speeds, reducing the iron losses in the PMSM

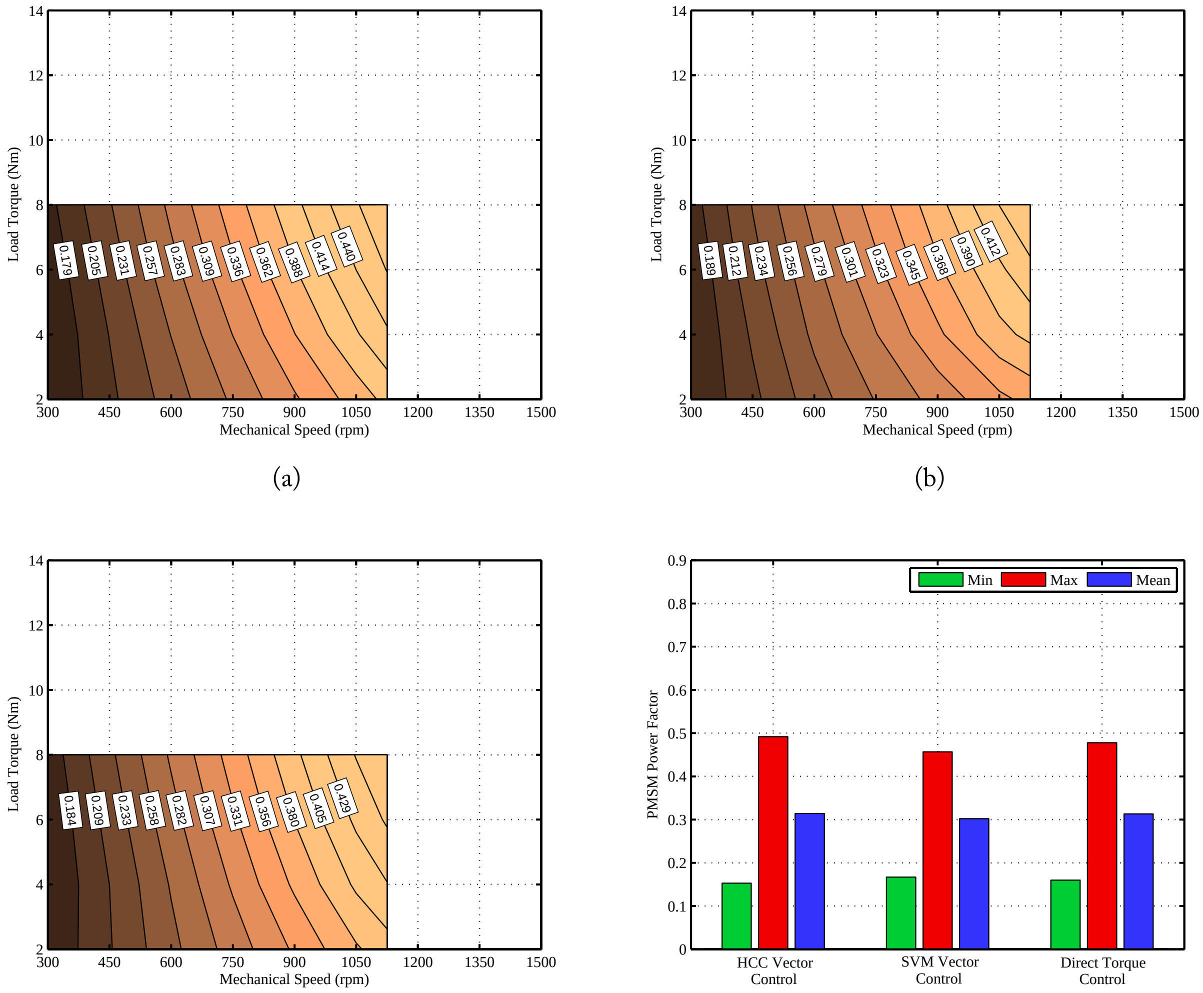

(a) (b)

(c) (d)

Figure 7.15: Experimental results of the PMSM power factor maps for a phase a NCM reconfiguration: (a) HCC vector control; (b) SVM vector control; (c) DTC; (d) Global statistical results.

stator stack. This is clearly seen in Figure 7.16d, where the minimum efficiency value obtained for the SVM vector control is much higher than the ones obtained for the two other control strategies.

7.1.6.2 PCM Reconfiguration

Considering now the phase a PCM reconfiguration, Figure 7.17 presents the PMSM efficiency maps obtained for the three considered control strategies.

In a similar way to the previous case, the maximum efficiency operating points are achieved for high load torque and speed values. On the other hand, the HCC vector control and DTC also present similar results.

Comparing with the efficiency values obtained under normal operating conditions, it can be seen that for low speed and torque values the motor efficiency is higher. However, the global

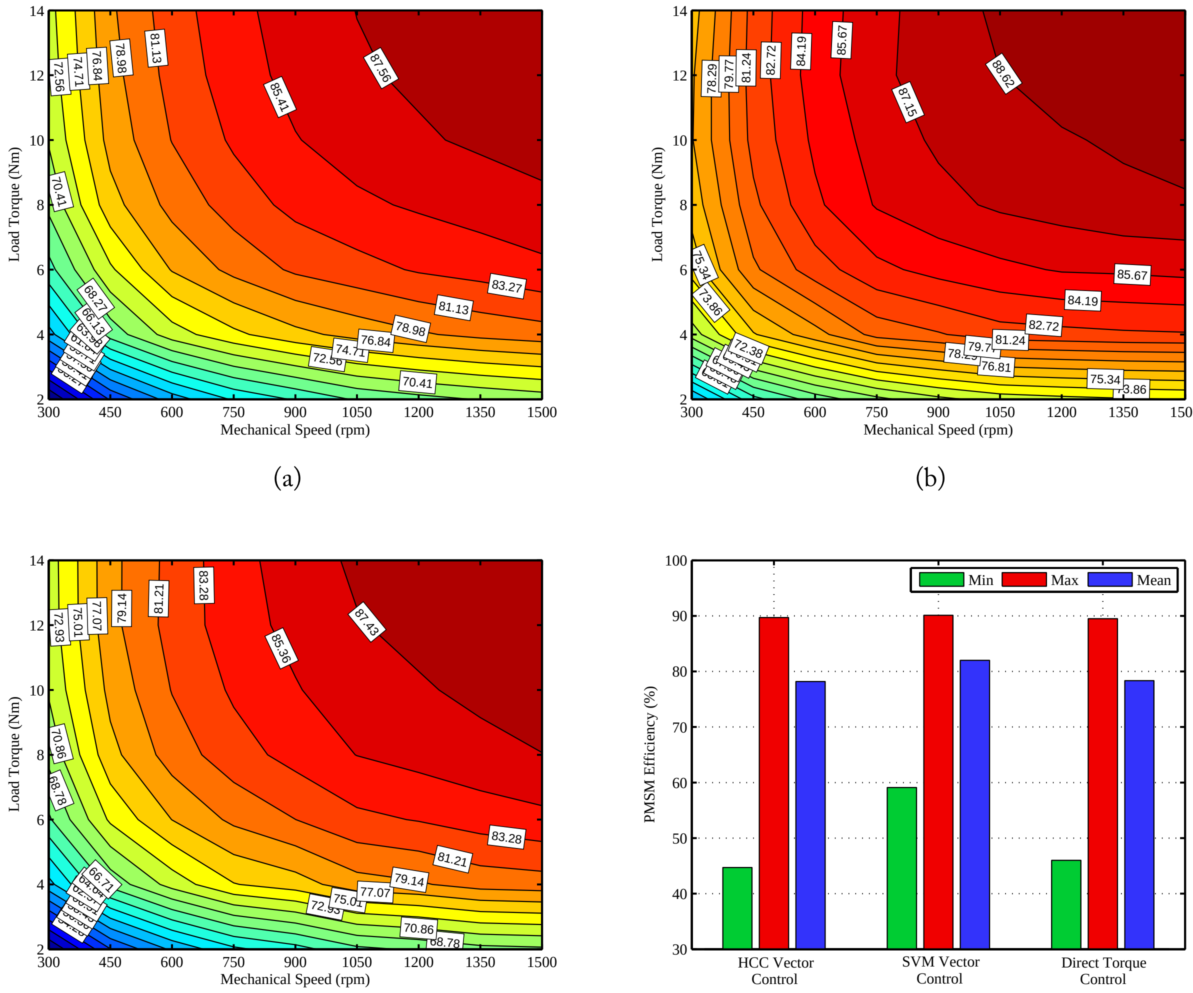

(a)

(b)

(c)

(d)

Figure 7.16: Experimental results of the PMSM efficiency maps under normal operating conditions: (a) HCC vector control; (b) SVM vector control; (c) DTC; (d) Global statistical results.

efficiency mean values decrease, especially for the SVM vector control, due to the increase of the current harmonic distortion. Nevertheless, this control strategy still allows to achieve a larger overall efficiency value than the one obtained for the HCC vector control or DTC.

7.1.6.3 NCM Reconfiguration

With respect to the NCM reconfiguration, the PMSM efficiency maps obtained for the three considered control strategies are presented in Figure 7.18.

In analogy with the previous cases, the maximum efficiency values are achieved for high speed and load torque values. Comparing with the healthy case, it is verified that the minimum efficiency values obtained for the HCC vector control and DTC increase for this converter reconfiguration, while the opposite occurs for the SVM vector control. Regarding the maximum and mean values,

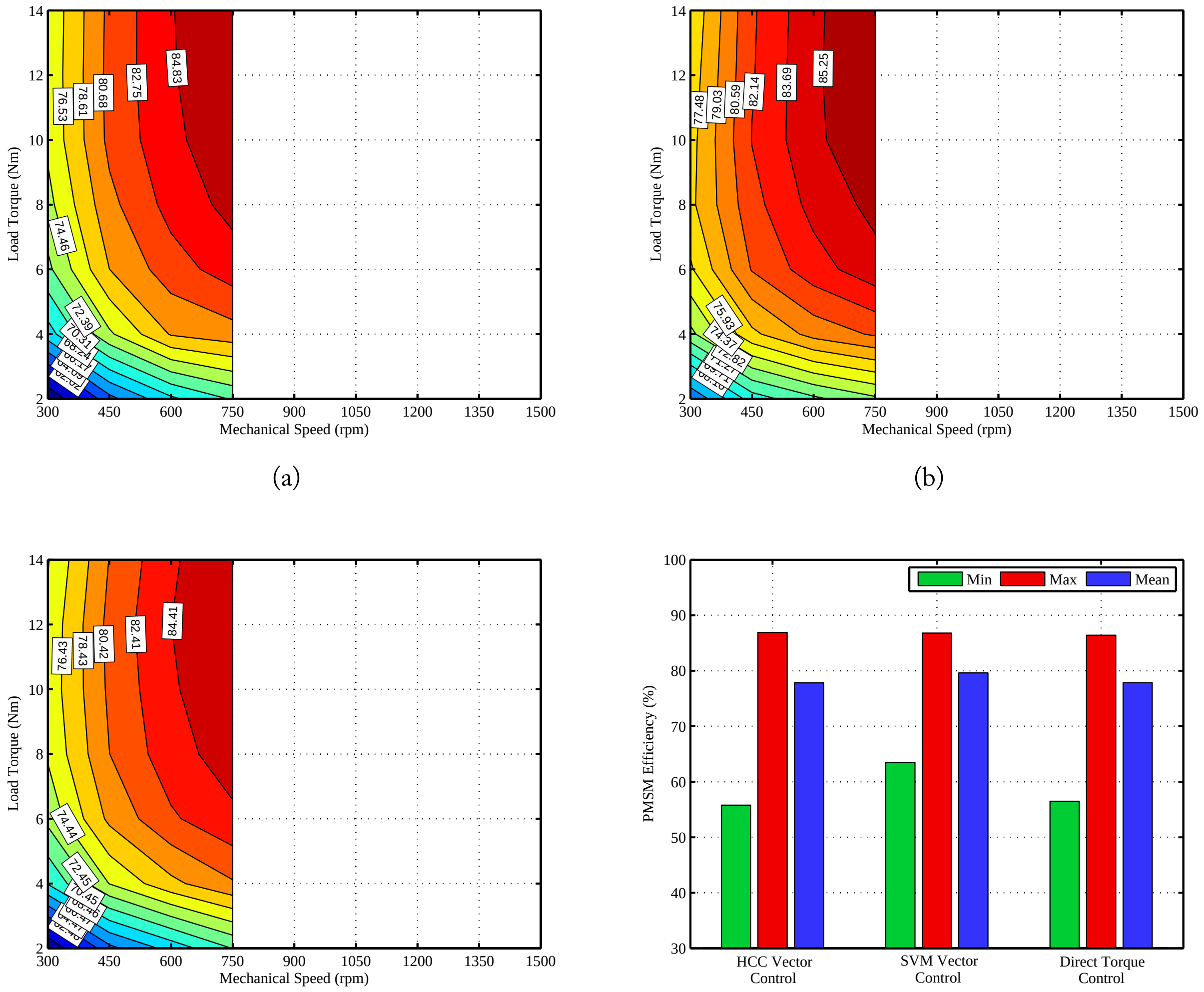

(a) (b)

(c) (d)

Figure 7.17: Experimental results of the PMSM efficiency maps for a phase a PCM reconfiguration: (a) HCC vector control; (b) SVM vector control; (c) DTC; (d) Global statistical results.

for this post-fault topology, all values decrease due to the required motor currents increase, resulting in extra Joule losses and the subsequent motor efficiency decrease.

7.1.7 Inverter Efficiency

7.1.7.1 Normal Operating Conditions

Figure 7.19 presents the inverter efficiency maps obtained for the three considered control strategies under normal operating conditions.

In analogy with the motor efficiency maps, it can be concluded that for the three control techniques, the inverter maximum efficiency values are obtained for high speed and load torque values. It is also shown that the HCC vector control and DTC present very similar results, presenting

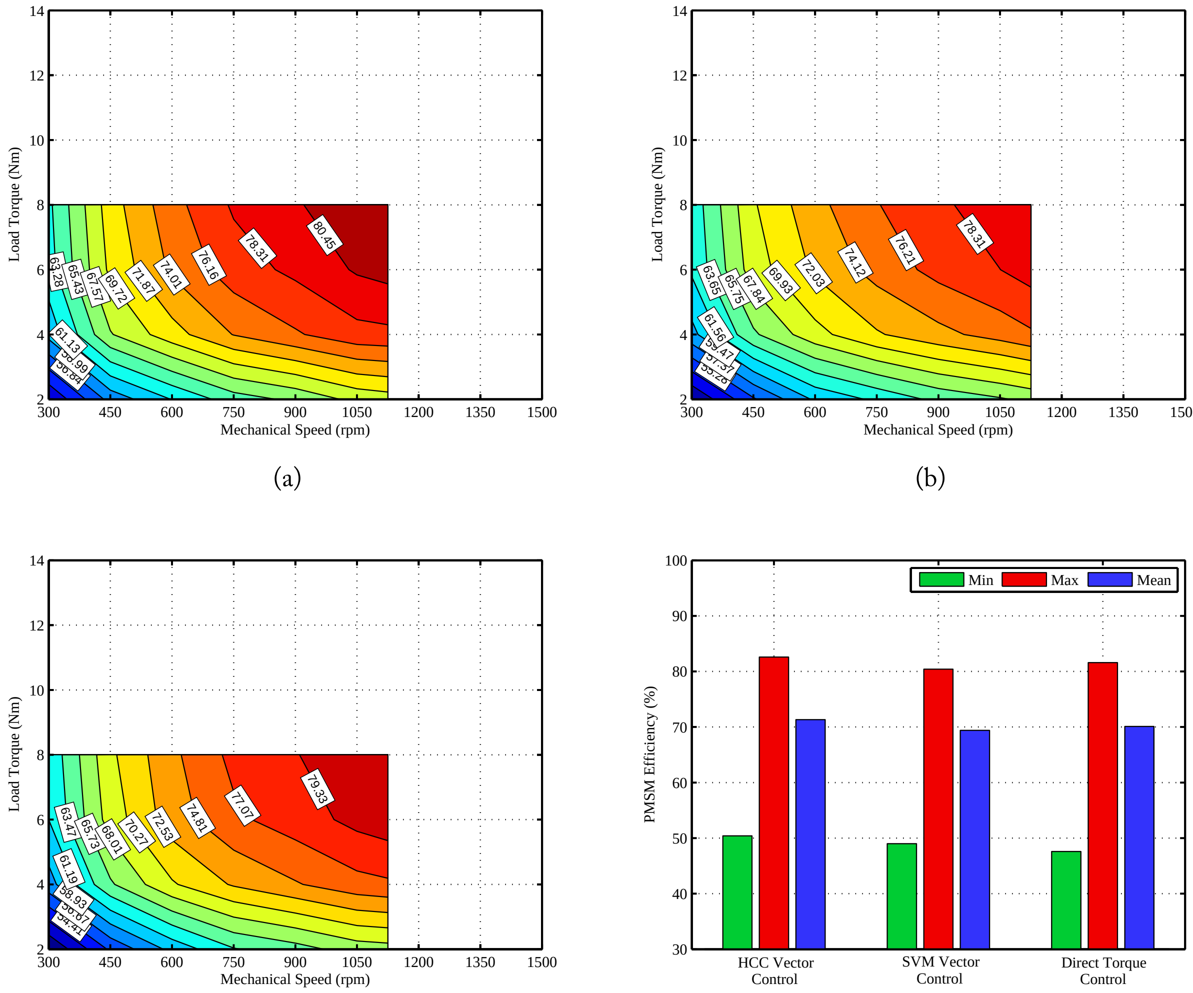

(a)

(b)

(c)

(d)

Figure 7.18: Experimental results of the PMSM efficiency maps for a phase a NCM reconfiguration: (a) HCC vector control; (b) SVM vector control; (c) DTC; (d) Global statistical results.

efficiency values very close to each other.

On the other hand, it is also visible that these two control strategies present higher efficiency values than the ones obtained for the SVM vector control. This means that this technique imposes to the inverter a large number of switching states per current period, leading to the increase of the inverter switching losses and the subsequent decrease of its efficiency.

7.1.7.2 PCM Reconfiguration

Regarding the inverter efficiency maps for the three considered control strategies under a phase a PCM reconfiguration, the obtained values are depicted in Figure 7.20.

Once more it can be seen that the inverter efficiency values distribution for the HCC vector control is very similar to the one for the DTC since these two techniques rely on hysteresis con-

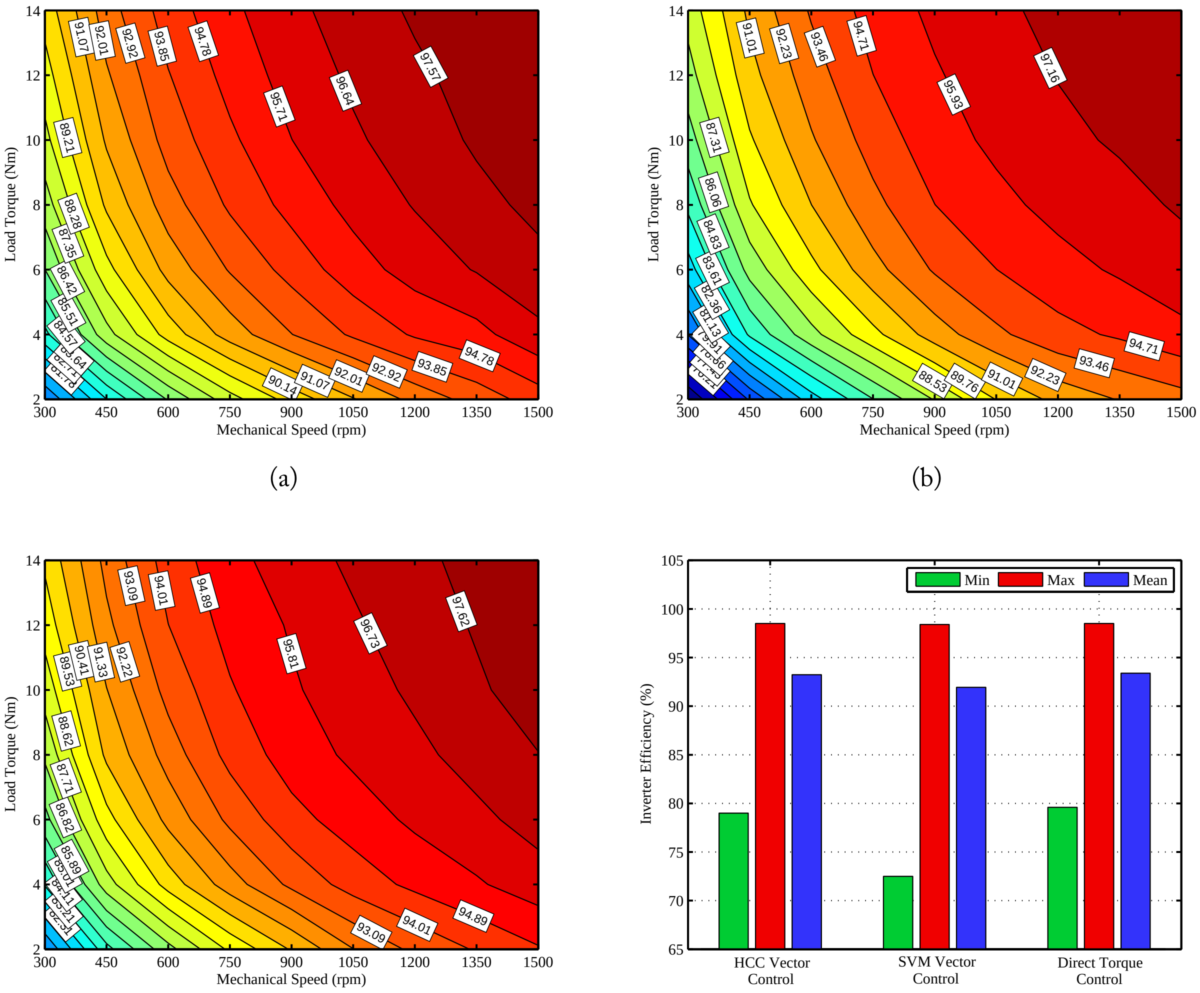

(a) (b)

(c) (d)

Figure 7.19: Experimental results of the inverter efficiency maps under normal operating conditions: (a) HCC vector control; (b) SVM vector control; (c) DTC; (d) Global statistical results.

trollers to control the VSI switching states. On the contrary, a different distribution is obtained for the SVM vector control since a completely distinct modulation technique is used.

Comparing with the results obtained under normal operating conditions, it is observed that all the minimum efficiency values increase for this post-fault converter topology while the maximum and mean values decrease. The exception is the DTC where all values slightly increase, achieving this way the highest inverter efficiency value.

7.1.7.3 NCM Reconfiguration

Regarding the NCM reconfiguration, Figure 7.21 presents the inverter efficiency maps obtained for the three considered control strategies.

Under these operating conditions, the inverter efficiency results distribution is distinct for the

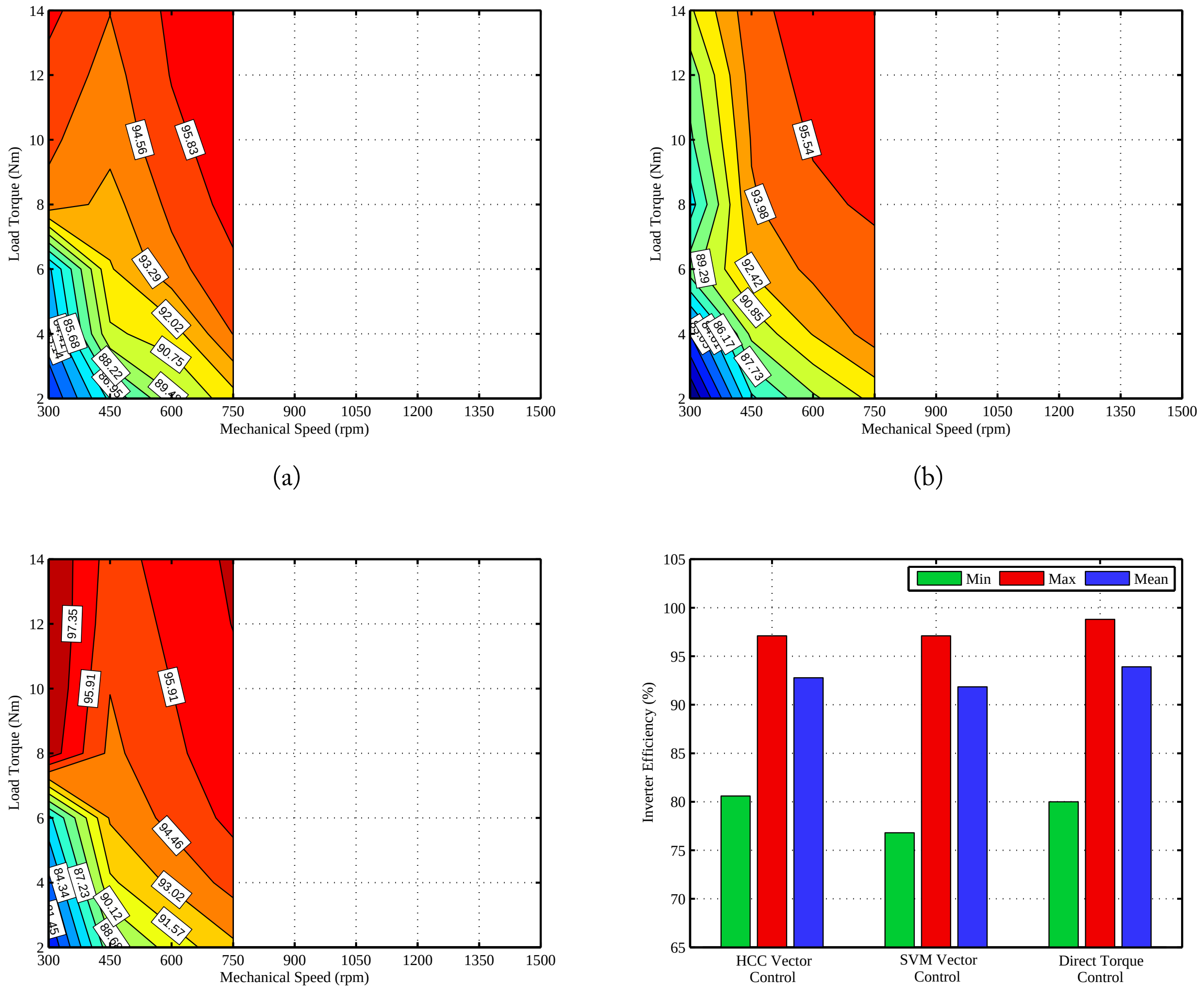

(a) (b)

(c) (d)

Figure 7.20: Experimental results of the inverter efficiency maps for a phase a PCM reconfiguration: (a) HCC vector control; (b) SVM vector control; (c) DTC; (d) Global statistical results.

three control techniques. Comparing with the obtained values for the healthy case, it is verified that the overall mean values decrease, especially for the HCC vector control that shows a great decrease of the minimum value, negatively affecting the global efficiency. As discussed before, the HCC vector control allows to achieve a better current control under a NCM reconfiguration. This is accomplished by increasing the switching frequency, resulting in larger switching losses.

7.1.8 PMSM+Inverter Efficiency

7.1.8.1 Normal Operating Conditions

Figure 7.22 presents the PMSM+inverter efficiency maps obtained for the three considered control strategies under normal operating conditions.

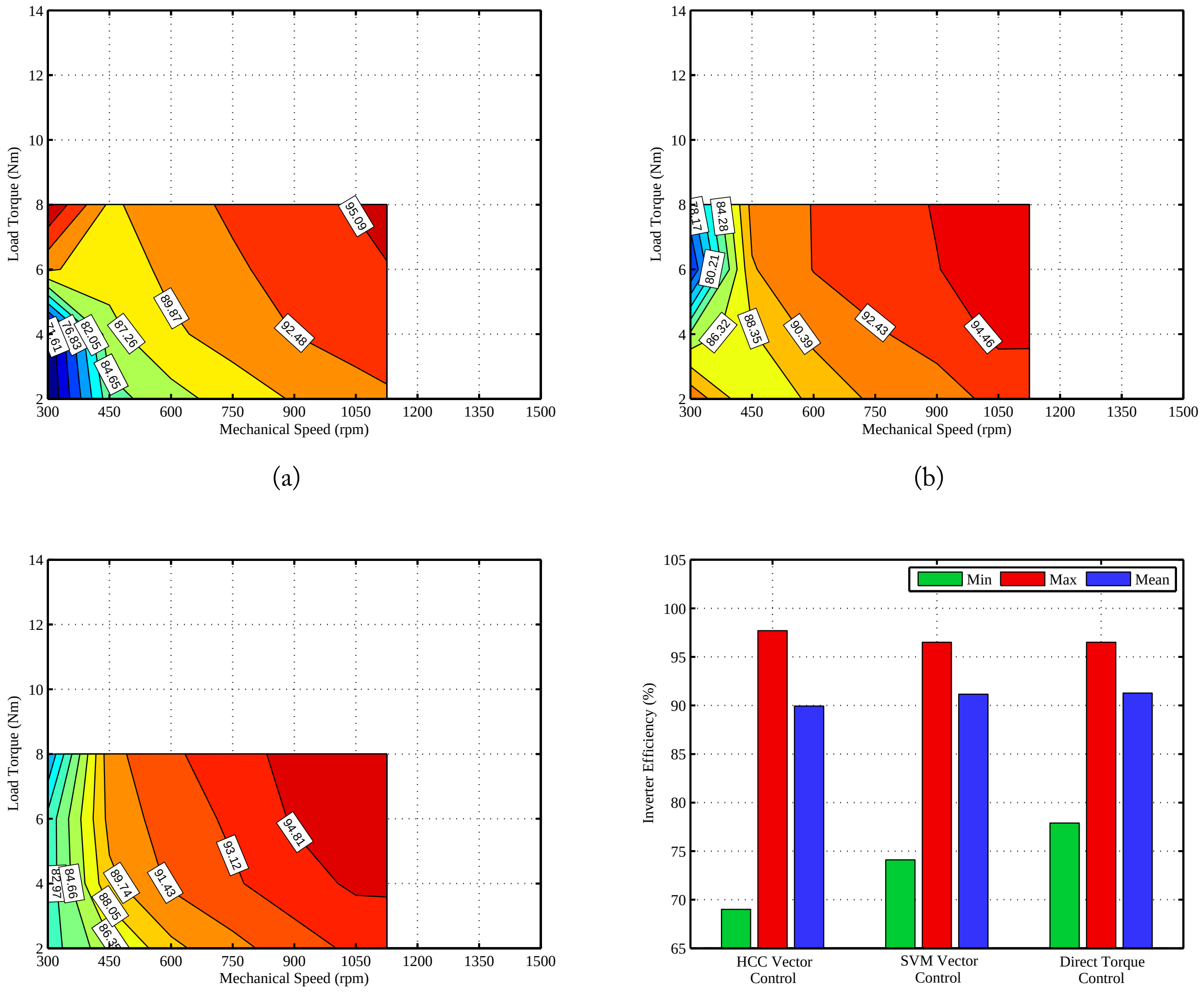

(a) (b)

(c) (d)

Figure 7.21: Experimental results of the inverter efficiency maps for a phase a NCM reconfiguration: (a) HCC vector control; (b) SVM vector control; (c) DTC; (d) Global statistical results.

By analyzing the three efficiency maps, it can be seen that similar values are also obtained for the HCC vector control and DTC. The global statistical results show that the maximum efficiency values of the system PMSM+inverter are practically equal for the three control techniques. Nevertheless, taking into account the minimum values, it is clear that the SVM vector control allows to achieve higher values, resulting in the highest overall performance.

7.1.8.2 PCM Reconfiguration

With respect to the PCM reconfiguration, the efficiency maps for the system PMSM+inverter obtained for the three considered control strategies are presented in Figure 7.23.

For this inverter fault-tolerant topology, all the minimum values are higher than the ones obtained for the healthy operating conditions. Nevertheless, the maximum values decrease, re-

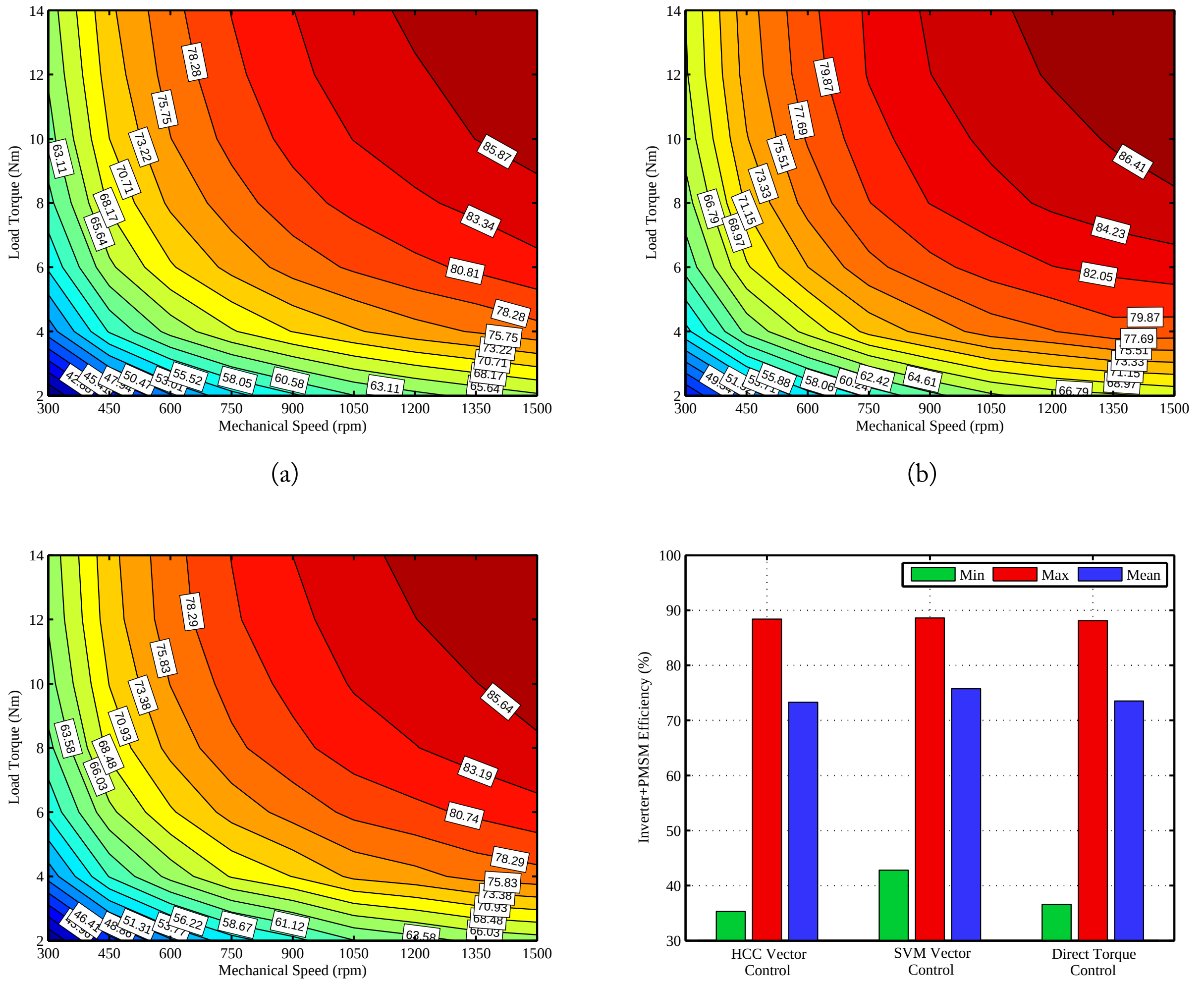

(a) (b)

(c) (d)

Figure 7.22: Experimental results of the PMSM+inverter efficiency maps under normal operating conditions: (a) HCC vector control; (b) SVM vector control; (c) DTC; (d) Global statistical results.

sulting in slightly lower overall mean values. From a global point of view and considering the PMSM+inverter efficiency, there are no noticeable differences between each considered control strategy.

7.1.8.3 NCM Reconfiguration

Finally, Figure 7.24 presents the PMSM+inverter efficiency maps obtained for the three considered control strategies under a phase a NCM reconfiguration.

Due to the superior performance of the SVM vector control for low speed and torque values, better efficiency values are achieved for these operating conditions. However, the inferior current control for higher load levels result in lower PMSM efficiency, negatively affecting the system comprised by the motor and the inverter.

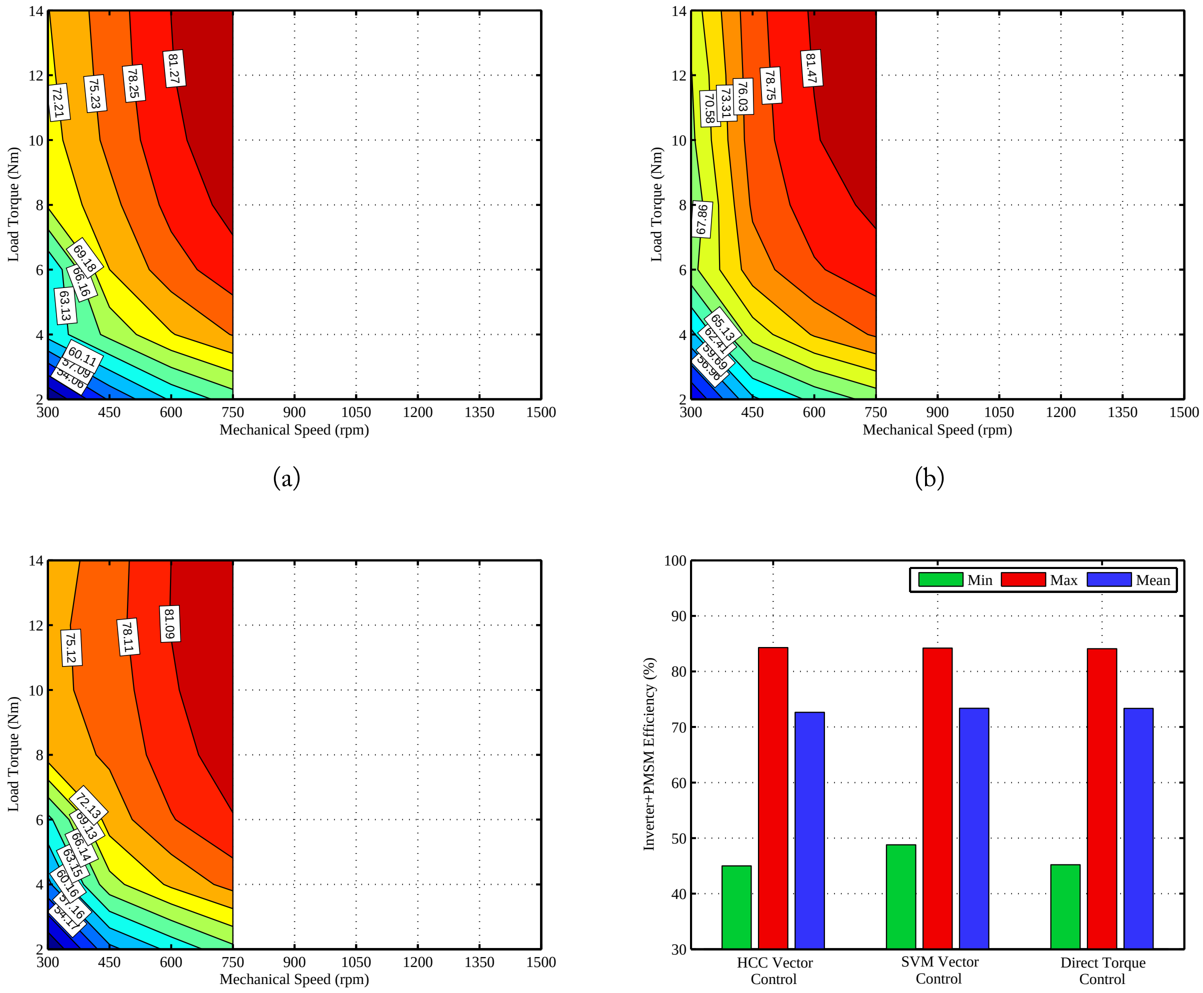

(a)

(b)

(c)

(d)

Figure 7.23: Experimental results of the PMSM+inverter efficiency maps for a phase a PCM reconfiguration: (a) HCC vector control; (b) SVM vector control; (c) DTC; (d) Global statistical results.

It is also seen that, comparing with the healthy situation, the overall efficiency mean values are severely affected under this fault-tolerant converter operation. This is justified by the imposed motor phase currents increasing by a factor of $\sqrt{3}$ that leads to a noticeable decrease of the PMSM efficiency.

Comparing the efficiency mean values, it can be observed that the obtained values are similar. Nevertheless, the HCC vector control and DTC control strategies can achieve slightly higher values than the SVM vector control.

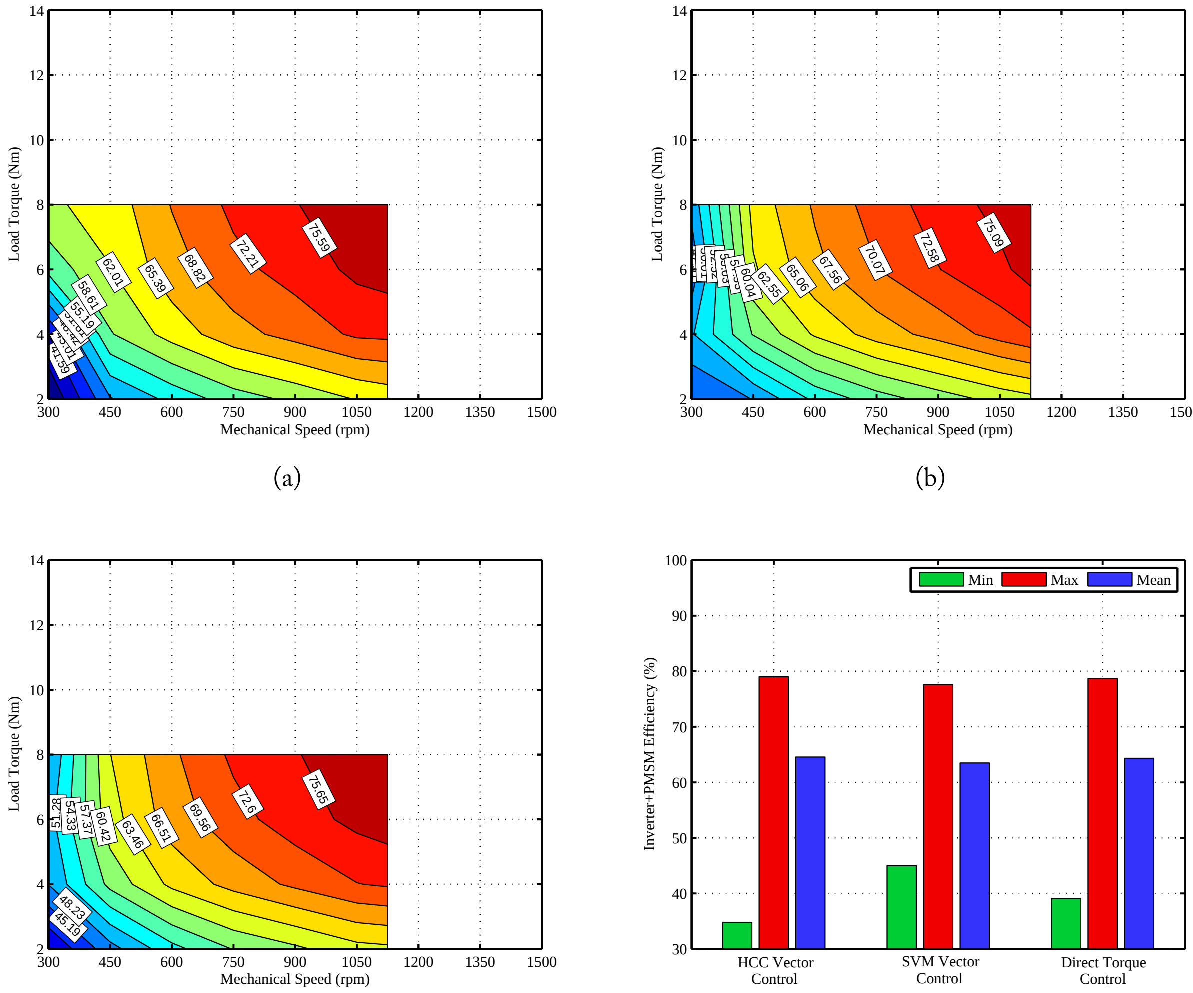

(a)

(b)

(c)

(d)

Figure 7.24: Experimental results of the PMSM+inverter efficiency maps for a phase a NCM reconfiguration: (a) HCC vector control; (b) SVM vector control; (c) DTC; (d) Global statistical results.

7.2 Thermal Analysis

For the thermal analysis, the temperature in some specific drive points was measured and evaluated for three consecutive operating modes during a total time of six hours (360 minutes). The first one is the healthy mode where the drive works normally with no fault or reconfiguration during the first 165 minutes. Then, in the second mode an open-circuit fault in the inverter IGBT T1 is introduced. The drive operates under these conditions for 45 minutes. Finally, it is introduced the converter and software reconfiguration, and the drive operates under the fault-tolerant mode during the last 150 minutes.

Considering these operating modes, the inverter and the motor are the drive components that are directly involved and the most affected ones by the fault and reconfiguration modes. As a result, it becomes obvious that their temperature variation is more significant, presenting therefore important information for the desired analysis.

Taking all this into account, six temperature readings were taken for this thermal study. Regarding the inverter, a temperature sensor was inserted inside its heat sink. As far as the PMSM is concerned, it was equipped with four temperature sensors. Three of them were put inside the PMSM, each one measuring the winding head temperature of each phase. The other one was inserted from the outside through a hole, reaching 5 mm in the machine stator in order to measure its temperature.

Additionally, another temperature sensor was used to measure the room temperature. This measurement is also important because by calculating the average temperature during each test, it is possible to normalize all the temperature readings by simply adjusting the offset values.

The used hardware to acquire the temperature values comprises a National Instruments NI cDAQ-9174 chassis together with two RTD modules NI 9217. The inverter and machine temperatures were measured using RTDs (PT100) in a 3-wire configuration while the room temperature uses a RTD in a 4-wire configuration. A dedicated program was built using the LabView programing environment that allowed to acquire all the six readings using a sampling time of one second.

All these temperature values are evaluated for the three considered PMSM control strategies (HCC vector control, SVM vector control and DTC) and for the two fault-tolerant modes (PCM and NCM reconfigurations).

Several temperature profiles were obtained according to all these control strategies and operating modes assuming a constant load level for all tests equivalent to a PMSM mechanical speed of 750 rpm and a load torque of 7 Nm.

7.2.1 HCC Vector Control

Figure 7.25 presents the temperature profile for a HCC vector control strategy and considering the PCM and NCM converter reconfigurations.

Considering first the behavior for the PCM reconfiguration shown in Figure 7.25a, it can be seen that under normal operating conditions, the initial temperature values of the three PMSM windings increase faster than the others, converging to a final value of about 38.4 ºC. As the motor is fed by a balanced supply current system, the temperature values of each motor phase winding are virtually the same.

The motor stator temperature has a similar behavior to the winding temperatures. However, as the machine stator has better cooling conditions mainly due the outside cooling fan, its temperature is lower, stabilizing in a value of approximately 35ºC.

Regarding the inverter heat sink temperature, it is clear that it presents a much larger thermal constant since the temperature variation rate is low. It can be seen that after the first 165 minutes,

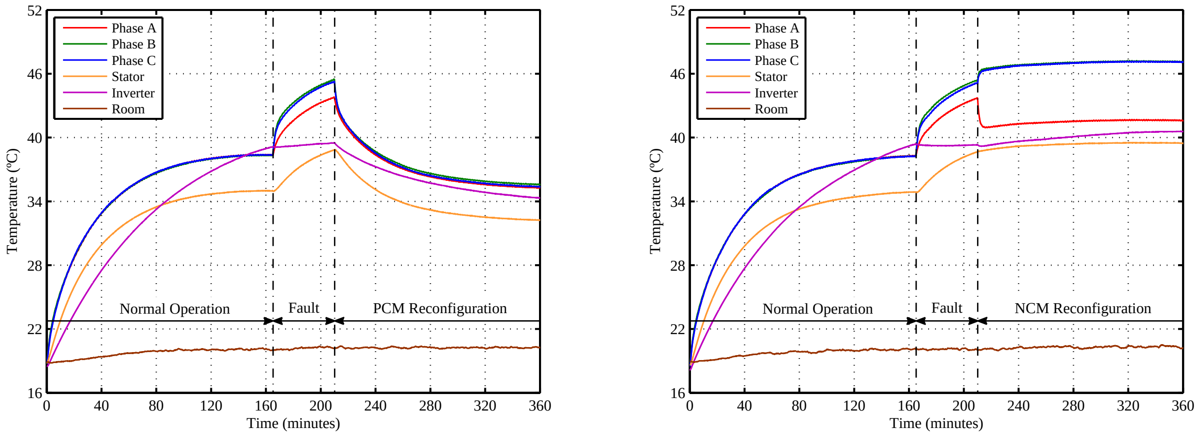

(a)

(b)

Figure 7.25: Experimental results of the temperatura profile for a HCC vector control strategy: (a) PCM reconfiguration; (b) NCM reconfiguration.

the temperature is higher than the motor windings temperature, reaching a value of 39.1 °C and with the tendency to increase even more. It is worth noting that no forced cooling is used in the inverter, which contributes to the tendency to reach higher temperature values.

When a fault in IGBT T1 is introduced, all the three currents become very distorted and the currents in the healthy phases increase. As a result, the winding temperatures in the healthy phases rapidly increase, presenting the phase a winding a lower value. This additional winding heating is also transferred to the machine stator, leading to its temperature increase. On the other side, due to the open-circuit fault, only one healthy IGBT is operating in the inverter faulty phase. As a consequence, the global switching losses are reduced, represented by the inverter heatsink lower temperature rate increasing.

After the PCM reconfiguration, all temperature values start to decrease, converging to values even lower than the ones obtained for the healthy situation. Considering the three winding temperatures, under these post-fault operating conditions the PMSM is supplied by a nearly balanced current system, and consequently, all values are close to each other, reaching a final vale of about 35.4 °C. This also has a positive impact on the stator temperature since colder windings mean a colder iron stack. After the six hour test, the stator temperature is 32.2 °C. The extra temperature decrease comparing with the normal case is justified by the lower iron losses. As seen before, with this topology the motor is fed by lower voltage rms values, and therefore, the flux linkage is reduced which also results in lower iron losses.

The inverter temperature also decreases and becomes lower (34.3 °C) than the value obtained at the beginning since under these circumstances only two phases are working and the current rms values are basically the same. Thus, the inverter power losses are reduced and the heat sink temperature decreases.

Considering now the obtained results for the NCM reconfiguration shown in Figure 7.25b, the obtained results for normal and faulty operating conditions are, as expected, very similar to the previous case since the conditions are the same. Therefore, the previous analysis is also valid in this case.

When the NCM reconfiguration is introduced, it can be observed a very different behavior. For this fault-tolerant topology, the healthy motor phase currents increase by a factor of $\sqrt{3}$. This is clearly seen by the high temperature values reached by the windings phase b and phase c (47.1 ºC), much higher than the normal operation. Since there is no current in phase a, the temperature value is much lower (41.6 ºC) than the ones of the healthy phases.

The larger winding temperatures also negatively affect the PMSM stator temperature since the generated heat is transferred for the iron stack, leading to its temperature increasing, reaching a final value of approximately 39.5 ºC.

As far as the inverter temperature is concerned, although only two inverter phases operate under these conditions, the noticeable increase of the motor phase currents imposes larger conduction and switching losses, which contribute the overall inverter losses and the heat sink temperature increases to a value of 40.6 ºC.

7.2.2 SVM Vector Control

Considering now the SVM vector control technique, Figure 7.26 presents the temperature profile for the PCM and NCM converter reconfigurations.

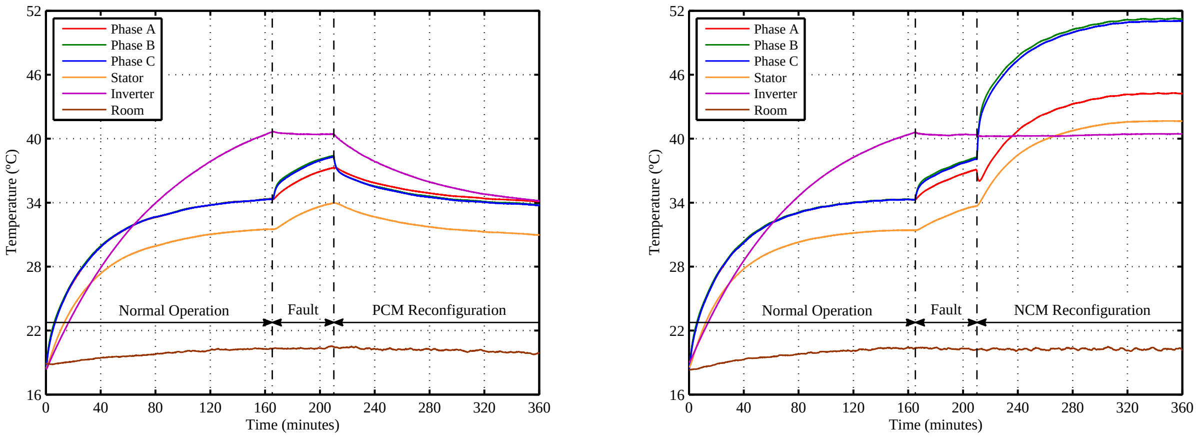

(a)

(b)

Figure 7.26: Experimental results of the temperatura profile for a SVM vector control strategy: (a) PCM reconfiguration; (b) NCM reconfiguration.

The obtained results are very similar to the previous ones and therefore, the same analysis can be also extended to this case. After the first 165 minutes the three winding temperatures reach a value of approximately 34.3 °C while the machine stator core presents a value of 31.5 °C. Comparing to the HCC vector control, it can be clearly seen that these temperature values are lower since the SVM technique generates less distorted voltage waveforms, strongly contributing to the decrease of the PMSM rms voltage values. As the stator iron losses are proportional to the air-gap flux level, low voltage rms values contribute to the reduction of the air-gap flux, decreasing therefore the iron losses and resulting in a lower stator temperature. Taking this into account and also considering that lower current distortion values are also obtained, the internal winding temperatures also decrease.

Regarding the inverter heat sink temperature, at the end of the first period a temperature of 40.6 °C was reached. This value is slightly higher than the one obtained for the previous case since as discussed before, the SVM vector control imposes larger inverter losses, which lead to the increasing of the heat sink temperature.

For the PCM reconfiguration, the three PMSM winding temperatures reach an average final value of approximately 33.9 °C while a value of 31 °C is obtained for the motor stator temperature. These values are also slightly lower than the ones acquired for the HCC vector control because of the same reasons already discussed. As far the inverter temperature is concerned, the behavior is very similar to the previous considered case.

Considering now the temperature profile shown in Figure 7.26b, it can be also seen that for a NCM reconfiguration, the winding temperatures of the healthy phases greatly increase, whereas the isolated phase present much lower values. In this specific case, phase b and phase c windings reach a final value of approximately 51.1 °C while a value of 44.2 °C is obtained for the motor phase a winding. These temperature levels are noticeable larger than the ones obtained for the HCC vector control under the same post-fault operating conditions since the worse current control performed by the SVM technique enables the generation of much distorted current waveforms. Consequently, slightly larger rms currents are obtained that also result in larger power losses and winding temperature increasing. This also has a negative influence on the PMSM stator temperature, which reaches a final value of 41.7 °C. Finally, the inverter heat sink temperature does not suffer a visible variation during this fault-tolerant operating mode, presenting a final value similar to the one for normal and faulty modes operation.

7.2.3 Direct Torque Control

Figure 7.27 presents the temperature profile for a DTC control strategy and considering the PCM and NCM converter reconfigurations.

The obtained results for the PCM reconfiguration are very similar to the equivalent ones obtained for the HCC vector control, reaching approximately the same temperature values at the end of the normal and fault-tolerant operating modes. At the end of the test it is verified that the inverter heat sink temperature is visibly lower since the global inverter power losses for the PCM reconfiguration under a DTC control technique are lower.

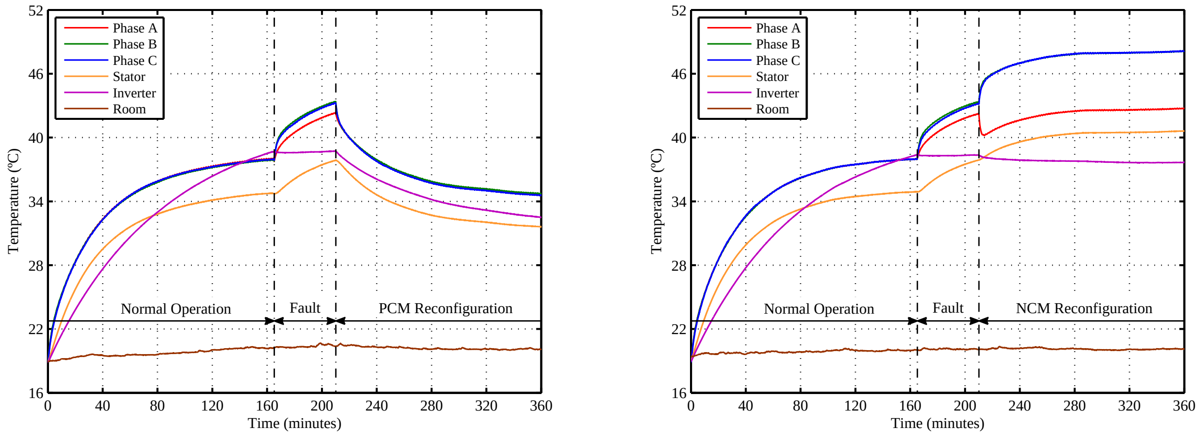

(a) (b)

Figure 7.27: Experimental results of the temperatura profile for a DTC control strategy: (a) PCM reconfiguration; (b) NCM reconfiguration.

Regarding the NCM reconfiguration, the obtained results are also very similar to the ones shown in Figure 7.25b, and subsequently, the same analysis is also valid. In this case the winding temperatures of the healthy phases reach a final value of approximately 48.1 ºC and the phase a winding presents a value of 42.8 ºC. The stator temperature reaches a final value of approximately 40.6 ºC.

The most visible difference is the inverter heat sink temperature that comparing with the HCC vector control, reaches a lower value of about 27.7 ºC due to the decrease of the power losses under these operating conditions.

7.3 Acoustic Analysis

The acoustic noise emitted by the PMSM varies according to the different operating conditions and control techniques. Therefore, an acoustic noise evaluation was also performed through the analysis of several noise spectra and by the calculation of the noise rms values.

The required sound samples were obtained using a microphone placed near the PMSM and using the WavePad Sound Editor software. This software incorporates several editing tools as well as more advanced analysis algorithms such FFT and temporal FFT, which are very useful for a preliminary study. The final results were processed using the Matlab in order to generate the spectra and for the calculation of the rms values.

It is worth noting that this is a very simple and preliminary analysis and therefore, the measurements were taken in an open environment (ideally, an anechoic chamber should be used) and without using specialized measurement equipment.

Several results are presented considering the PMSM drive operation under healthy conditions, PCM reconfiguration and NCM reconfiguration, taking also into account the three considered control strategies (HCC vector control, SVM vector control and DTC). For each case, it was assumed a constant load level equivalent to a PMSM mechanical speed of 750 rpm and a load torque of 7 Nm.

7.3.1 Normal Operating Conditions

Figure 7.28 presents the acoustic noise spectrograms and rms values obtained for the three considered control strategies under normal operating conditions.

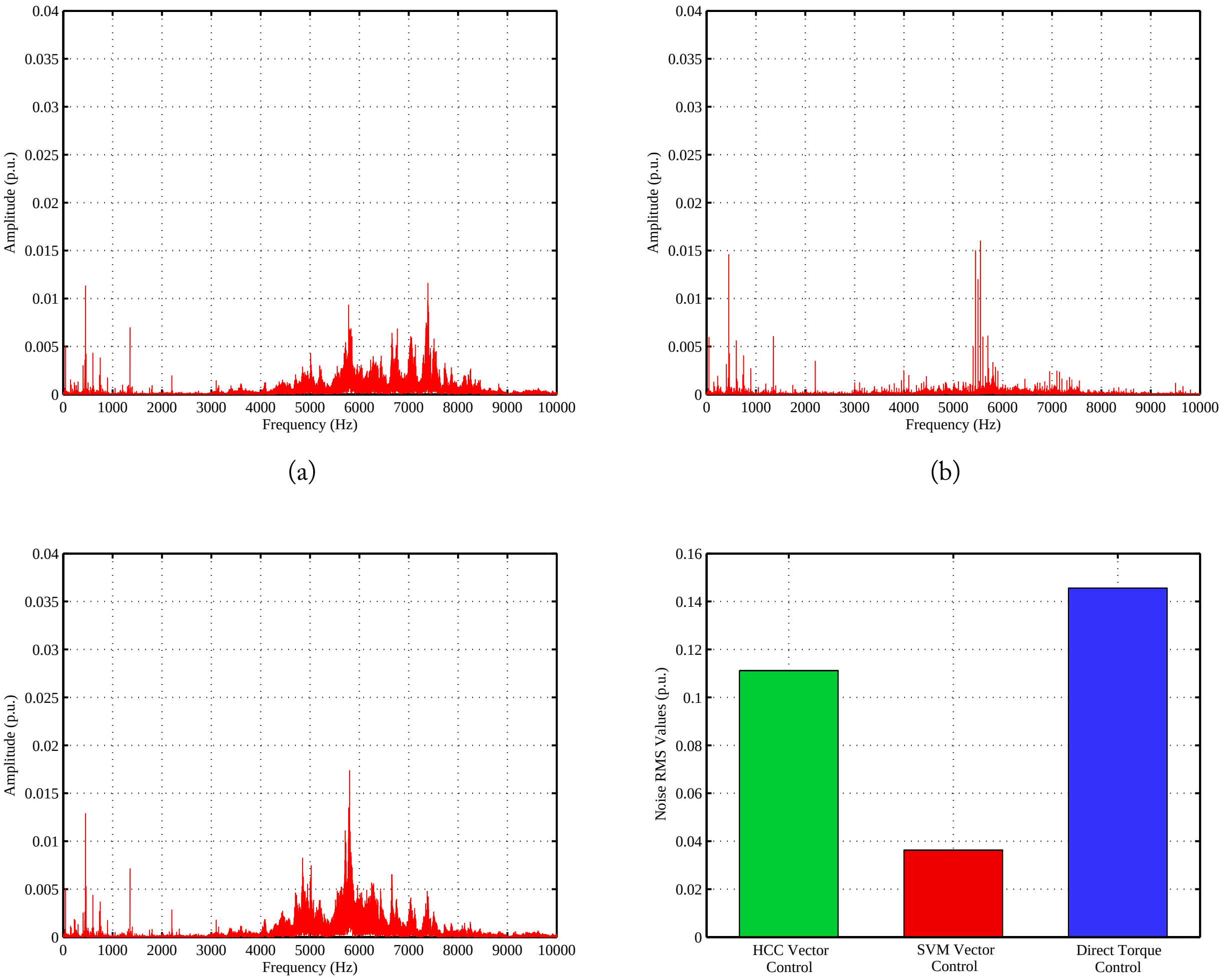

(a) (b)

(c) (d)

Figure 7.28: Experimental results regarding the PMSM acoustic noise under normal operating conditions: (a) HCC vector control spectrogram; (b) SVM vector control spectrogram; (c) DTC spectrogram; (d) Global rms values.

Comparing the three spectrograms it can be seen that approximately below the 3 kHz the generated frequency components are similar for all the control strategies. This range of frequency is directly related with the noise that has an aerodynamic origin, principally due to the PMSM fan operation, and mechanical origin, mainly due to bearings and their defects, shaft and rotor irregularities, rotor imbalance or shaft misalignment. Other noise components have an electromagnetic origin related to the interaction of the current harmonics with the machine physical/construction aspects.

Above 3 kHz, the sound has essentially an electromagnetic origin that results from the force waves produced by the interaction of the MMF and permeance space harmonics with the time harmonics due to converter operation. This effect is clearly seen for the SVM vector control where it can be concluded that the high-frequency sound harmonics are directly related with the imposed switching frequency. In this case, a fixed switching frequency of 5.5 kHz is used for the SVM technique, resulting in an audible noise with a characteristic high-pitch sound, illustrated in Figure 7.28b by the side bands placed around this frequency value. For the HCC vector control and DTC, there are no well-defined high-frequency sound harmonics since the use of hysteresis comparators cannot imposed a fixed inverter switching frequency. As a consequence, the voltage harmonics and the correspondent sound harmonics are spread around a relatively large frequency band. All this has a negative impact on the noise rms values, that become much higher for these two techniques than for the SVM vector control, allowing to conclude that fixed switching frequency modulation techniques generate less acoustic noise.

7.3.2 PCM Reconfiguration

With respect to the PCM reconfiguration, Figure 7.29 presents the spectrograms and rms values obtained for the three considered control strategies under a phase a fault.

In analogy with the previous case, for low frequency components, the spectra are similar to each other since the physical setup and conditions are always the same. The main differences are observed at high-frequencies for the SVM vector control where it is clearly observed an obvious increase of the harmonic components around the switching frequency. On the contrary, the HCC vector control and DTC spectra show an overall decrease of the high-frequency sound components. Hence, and comparing with the healthy behavior, the results in Figure 7.29d show that for this fault-tolerant mode, the noise generated by the SVM vector control doubles while for the DTC the noise rms value decreases by nearly 50%. Nevertheless, the rms noise levels obtained for these two control strategies are very similar to each other. Regarding the HCC vector control, the overall noise level also decreases to a level slightly higher than for the two other cases.

7.3.3 NCM Reconfiguration

Finally, Figure 7.30 presents the spectra and rms values obtained for the three considered control strategies under a phase a NCM reconfiguration.

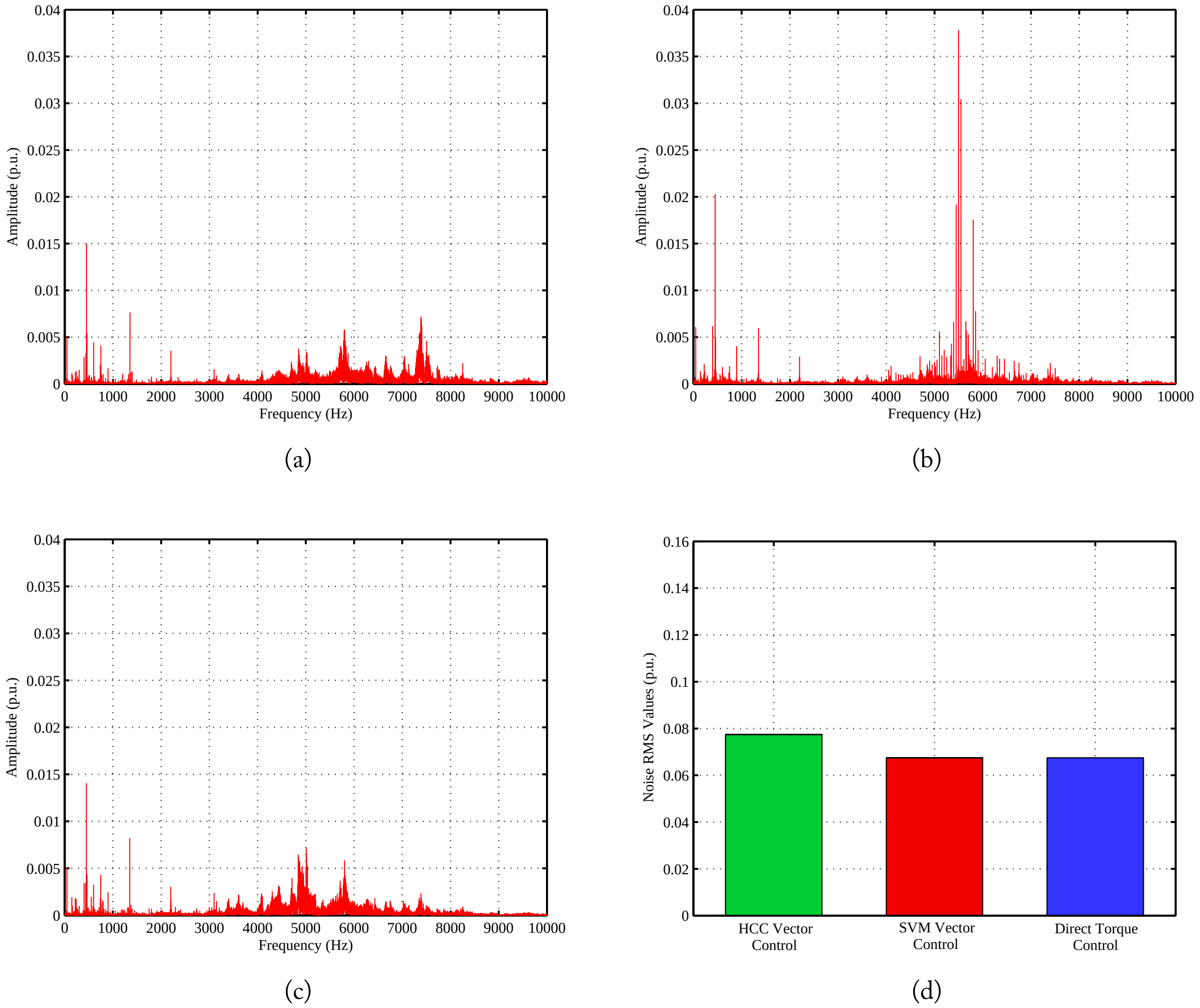

(a) (b) (c) (d)

Figure 7.29: Experimental results regarding the PMSM acoustic noise for a phase a PCM reconfiguration: (a) HCC vector control spectrogram; (b) SVM vector control spectrogram; (c) DTC spectrogram; (d) Global rms values.

Once more it is verified that for low frequency values, the harmonic components are similar in all spectrograms. Regarding the frequency values above 3 kHz, the spectra for the HCC vector control and DTC are analogous to the ones obtained for the drive healthy operation. In contrast, for this fault-tolerant topology under a SVM vector control technique, it is observed a noticeable increase of the harmonic components around the PWM switching frequency. Consequently, the results shown in Figure 7.30d allow to concluded that global noise level emitted with this control strategy almost triples, when comparing the drive normal operation. Despite this, the SVM vector control strategy still achieves the best behavior by generating the lowest noise level.

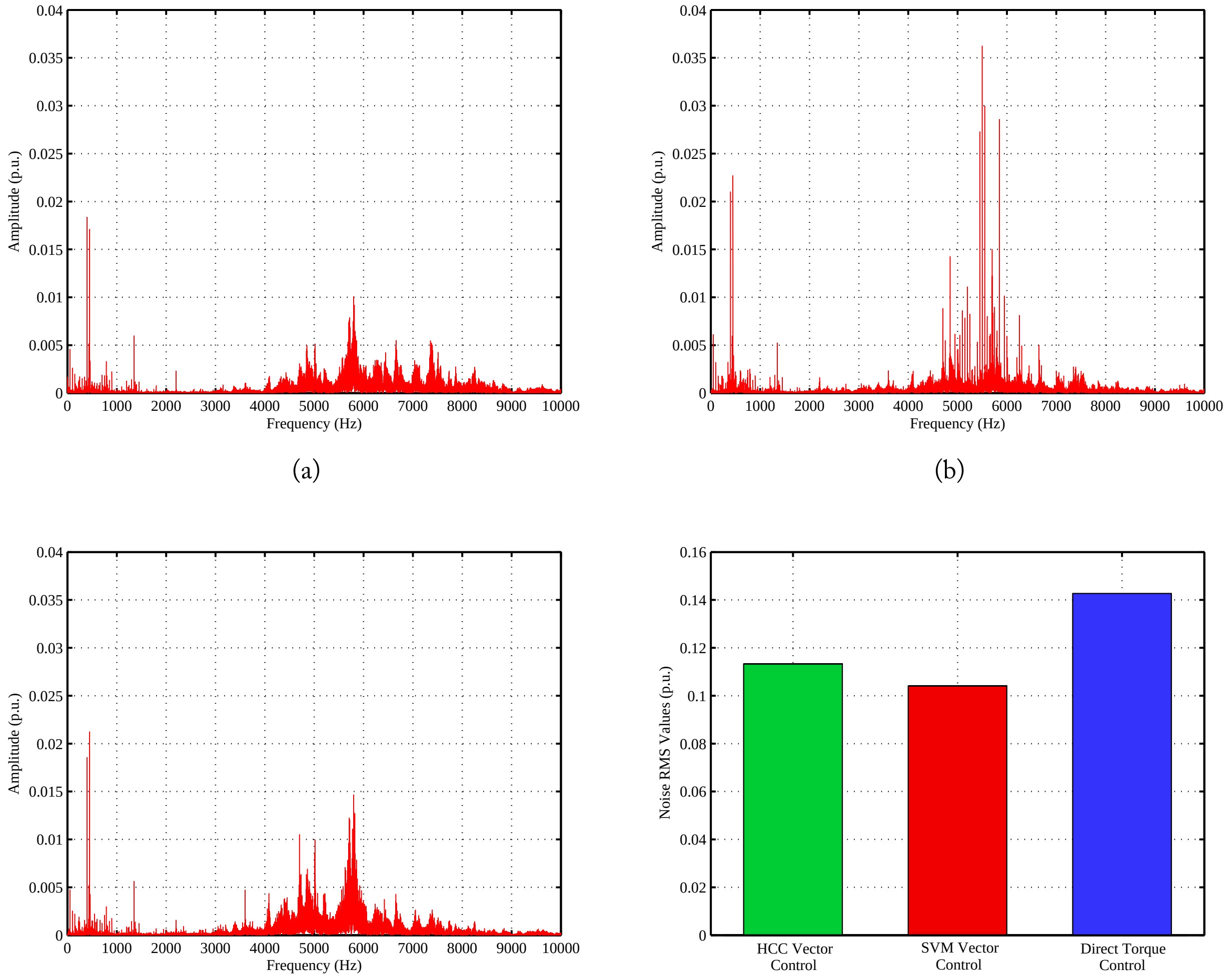

(a) (b)

(c) (d)

Figure 7.30: Experimental results regarding the PMSM acoustic noise for a phase a NCM reconfiguration: (a) HCC vector control spectrogram; (b) SVM vector control spectrogram; (c) DTC spectrogram; (d) Global rms values.

7.4 Final Remarks

A very detailed performance evaluation of the PMSM drive system was presented in this chapter. This was accomplished by analyzing several experimental results, divided into three main categories, namely electrical, thermal and acoustic analysis.

Regarding the first and most important one, several parameters were calculated and the majority of the results were presented in the form of three dimensional maps, allowing the drive characterization in all its operating range. From a global point of view, comparing the three control strategies, it was observed that the SVM vector control presents the best steady-state performance level under normal operating conditions. For the PCM reconfiguration, all the control techniques present equivalent global efficiency values, with a slightly advantage for SVM vector control and DTC.

Nevertheless, lower current distortion values can be obtained with the HCC vector control. With respect to the NCM reconfiguration, the SVM vector control reveals the worst performance level by showing low overall efficiency values as well as high current distortion levels. On the opposite side, the HCC vector control presents a high overall drive efficiency together with the lowest current harmonic distortion values.

As far as the thermal analysis is concerned, the SVM vector control presents the most desirable behavior by showing the lowest motor temperature values under normal operating conditions and for the PCM reconfiguration mode. For the converter NCM reconfiguration, the HCC vector control is the most advantageous control technique.

Finally, from the PMSM acoustic noise analysis it can be concluded that the SVM vector control generates the lowest noise level under healthy operation due to the fixed switching frequency used by the modulation technique. For a PCM reconfiguration, the emitted noise levels by the PMSM are practically the same for the three considered control strategies. Regarding the NCM reconfiguration, the two vector control strategies allow the generation of equivalent noise levels.

Chapter 8

Conclusions and Future Work

8.1 Conclusions

This work has presented a detailed investigation on variable speed PMSM fault-tolerant drives capable to operate under inverter faulty conditions, including a very detailed analysis of the PMSM performance when it is fed by a fault-tolerant VSI.

For the theoretical analysis, a PMSM dynamic model was used for this purpose. Typically, the most common PMSM mathematical models found in the literature are derived for normal/balanced operating conditions and do not take into consideration the stator iron losses. Therefore, there was the need to develop and implement a more complex PMSM model that beyond the inclusion of the iron losses for a more accurate modeling, full access to the motor terminals had to be considered in order to perform all the desired connections and reconfigurations.

With the aim to cover the majority of the control techniques used worldwide in variable speed PMSM drives, three main control strategies where considered in this work, namely the HCC vector control, the SVM vector control and the DTC. All these techniques were presented and described by explaining their mathematical fundamentals and addressing their corresponding technical and implementation principles. In order to validate them, several simulation and experimental results were taken for the drive normal operation. A simple analysis was primarily done through the evaluation of the time-domain waveforms of the motor phase currents, voltages and electromagnetic torque. In addition, the electromagnetic torque ripple was also addressed, as well as the complex representation of the PMSM phase voltages. The obtained results have allowed to demonstrate an excellent agreement between the theoretical results obtained from the computational simulations and the experimental ones, obtained from the laboratory tests.

Valuable information was obtained by the drive analysis under inverter faulty operating conditions. In order to develop a PMSM drive with inverter fault-tolerant capability, the study of the drive operation under inverter fault occurrences is very important for the correct design of fault diagnostic algorithms, the development of special hardware protection devices and to predict how the entire system will react under unexpected operating conditions. Therefore, several simulation and experimental results were obtained for the three considered control strategies in order to evaluate the PMSM drive performance under an inverter single-power switch open-circuit fault. These results allow to conclude that a well-defined pattern is generated by the three control strategies. Under a single IGBT open-circuit fault, the motor phase current corresponding to the inverter faulty leg will be severely affected, presenting a very distorted waveform with a large DC component. As one of the two power switches per phase is damage, the inverter cannot be used to control the current in the faulty phase during an entire fundamental period. As a result, the current will always be zero during one-half of the current period. Accordingly, if a fault occurs in the top IGBT of one inverter leg, current flow in that phase is only possible during the negative half-cycle. On the contrary, a fault in the bottom IGBT only allows current flow in that phase during the positive half-cycle. The fault also has a negative impact on the other two healthy phases, contributing to the increase of their waveform distortion.

Regarding the generated PMSM electromagnetic torque under faulty operating conditions, despite its average value is the same to the obtained one for the healthy case, it can be concluded that it presents a very pulsating nature. From the spectral analysis it was observed that a well-defined oscillating component is introduced at the same frequency of the motor phase currents, as well as other harmonics multiple of this fundamental component. This electromagnetic torque oscillation is undesirable because it imposes large mechanical stresses on the motor shaft and all moving parts, resulting in the increase of the vibration and acoustic noise levels.

The performance evaluation of the three considered control strategies under these abnormal conditions allowed to conclude that the DTC has the lowest performance since this technique presents the highest motor phase currents distortion and electromagnetic torque oscillation. On the contrary, the SVM vector control shows the best performance under inverter faulty operating conditions.

As far as the inverter fault diagnosis is concerned, two novel algorithms for real-time diagnostic of multiple power switches open-circuit faults in voltage-fed PWM motor drives have been developed in this work. They just use as inputs variables that are already available from the main control system. This means that comparing with other techniques, they avoid the use of extra sensors or electric devices and the subsequent increase of the system complexity and costs. The obtained results allow to conclude that in opposition to the majority of the existing techniques, the presented methods can handle with extreme and fast transients, without emitting false diagnostics. Furthermore, thanks to the use of normalized quantities, the algorithms behavior does not depend neither on the motor rated power, and its load level, nor on its mechanical speed. Accordingly, universal threshold values can be defined, independently of these issues.

The developed algorithms also present advantageous features regarding the detection speed. Comparing with similar diagnostic methods that usually need almost one fundamental period to detect the inverter faulty device, the proposed algorithms are much faster, allowing to perform a diagnostic in a time interval as short as 5% of the motor phase currents period.

The two diagnostic methods are also much more simple than the other similar ones since they just require a few and basic mathematical operations. Therefore, there is no need to use complex algorithms such the ones based on FFT or pattern recognition, making them not computationally demanding and therefore, very suitable to be easily integrated into the drive control system without great effort.

Considering the fault-tolerant strategies, an extensive literature survey has been presented where the fault-tolerant remedial strategies applied to two-level VSIs in variable speed PMSM drives were discussed. These can be broadly classified into redundant and non-redundant fault-tolerant topologies. Typically, for the redundant configurations, extra hardware components with the same characteristics are used as backup units, as an alternative to the faulty devices. On the contrary, the non-redundant configurations, in general only use supplementary and simpler devices that create a different path for load current flow without any additional redundant devices. Hence, these topologies are cheaper than the redundant configurations, and may be considered acceptable in some applications. The redundant topologies present the advantage of integrally saving the drive system operation but at a higher cost.

In this work, only the non-redundant topologies were considered. Accordingly, two inverter configurations were addressed, namely the PCM and NCM reconfigurations. The first one is based on the motor phase connection to the DC link capacitors midpoint while in the second, the machine neutral point is connected to the DC link capacitors midpoint. These topologies also require some modifications at the control software level in order to optimize the drive global performance. It has been demonstrated that for the PCM reconfiguration, the PMSM can operate at rated torque but at a limited mechanical speed, corresponding to one-half of the motor rated value. On the other hand, the NCM reconfiguration imposes a current increasing on the healthy phases, leading to the need to limit the load torque to a value equivalent to $1/\sqrt{3}$ of the rated value under steady state operation. Additionally, it was also concluded that the PMSM mechanical speed must be limited to a value equivalent to ¾ of the rated value.

Other specific modifications must be performed according to each control strategy. Therefore, for the HCC vector control, the reference motor phase currents calculation must be changed in order to impose a current increase in the healthy phases by a factor of $\sqrt{3}$ with a phase shift of 60°. For the PCM reconfiguration, no changes are required at this level.

As far as the SVM vector control is concerned, due to the different voltage vectors generated by these topologies, there is the need to optimize the SVM technique. The absence of null voltage vectors imposes a different vector selection in order to synthetize the desired reference voltage vector. In this case, the post-fault control strategy is the same for both PCM and NCM reconfigurations.

Due to the same reasons, the DTC control strategy must be changed in order to optimize the post-fault drive behavior. This is accomplished by acting on the voltage vector optimum switching table.

Considering all this, and with the aim to develop a fully-integrated fault-tolerant PMSM drive, the control system was designed in order to perform four critical steps: inverter fault diagnosis, faulty leg isolation, hardware reconfiguration and post-fault control optimization. Considering the first step, the developed real-time algorithms enable to effectively detect and localize inverter open-circuit faults. The information of the faulty device is then used by the control system to isolate the corresponding inverter phase. On the third stage, the fault-tolerant control system triggers the specific triac, changing the converter topology. At last, the control routines are modified according to each converter topology in order to optimize the post-fault drive performance.

Regarding the drive system analysis under a PCM and NCM reconfiguration, several simulation and experimental results were presented for the three considered control strategies. It was also verified an excellent agreement between the theoretical results obtained from the computational simulations and the experimental ones, obtained from the developed prototype.

The obtained voltage, current and electromagnetic torque waveforms allowed to conclude that the behavior for the three control techniques is very similar. Under a PCM reconfiguration, the PMSM phase currents are similar to the ones obtained for the drive healthy operation. With respect to the motor phase voltages, the one corresponding to the faulty phase clearly presents a lower RMS value than the other two since it is connected to the DC bus capacitors midpoint. The obtained electromagnetic torque waveforms are also very similar for the three cases, presenting equivalent ripple values.

For a NCM converter reconfiguration, it was verified that the motor phase currents in the healthy phases increase by a factor of $\sqrt{3}$, when comparing with the normal drive operation. Furthermore, in order to optimize the drive performance, a phase shift of 60° is imposed to the phase currents. This leads to a large current flow through the neutral conductor equivalent to three times the value of a phase current under healthy operating conditions. Regarding the PMSM phase voltages, it can be concluded that their amplitude oscillates due to the current flow through the neutral conductor, making the PMSM neutral potential oscillating. As far as the electromagnetic torque is concerned, it can be concluded that due to the connection to a non-active supply point and taking into account the indirect current control through voltage modulation, the SVM vector control strategy presents a more pulsating electromagnetic torque. On the contrary, the direct current control imposed by the HCC vector control allows to obtain less distorted currents, resulting in a smoother electromagnetic torque waveform.

Additionally, it was concluded that the results regarding the complex representation of the PMSM phase voltages are also very similar for the three control techniques. Furthermore, these results allowed to experimentally validate the mechanical speed limitations under post-fault operating conditions.

Finally, a very detailed drive performance analysis was performed, with special focus on the PMSM evaluation. This was accomplished by an exhaustive analysis of a great variety of experimental results, divided into three basic categories: electrical analysis, thermal analysis and acoustic analysis.

Considering the first and most important one, several key parameters were considered, namely the motor phase current and voltage rms and distortion values, PMSM power factor and its efficiency. Moreover, the inverter efficiency as well as the inverter+motor efficiency were also addressed. The majority of these results were present in the form of three dimensional maps since it is possible to fully characterize the entire operating range, enabling a very detailed study.

Under steady-state normal operating conditions and from a global point of view, it can be concluded that the SVM vector control presents the best performance levels. This control strategy allows to achieve lower rms and distortion values for the PMSM phase currents and voltages, higher power factor values and overall efficiency values.

Regarding the PCM inverter reconfiguration, comparing the three control strategies, it can be concluded that, in general, they present an equivalent performance level. Due to the connection to a non active supply point and due to the indirect current control, large current waveform distortion values are obtained for the SVM vector control. Nevertheless, the inverter+PMSM average efficiency results show that all the considered control strategies present similar values.

Under a NCM reconfiguration, it becomes clear that the SVM vector control performance is the most affected one. The indirect current control through voltage modulation leads to the generation of large current waveform distortion and slightly higher current rms values, resulting in lower machine efficiency. As a consequence, the lowest global drive average efficiency is obtained. On the contrary, it can be concluded that the direct current control provided by the HCC vector control allows to achieve the best PMSM efficiency results. Despite the lower inverter efficiency performance, the best global drive efficiency values are obtained for this control strategy.

The results obtained for the drive thermal analysis allow to conclude that under normal operating conditions, the HCC vector control and DTC present a very similar temperature behavior. Both control techniques rely on hysteresis controllers, which impose a non-fixed inverter switching frequency. Consequently, as the PMSM supply characteristics are directly related to its thermal behavior, the equivalent voltage and current waveforms generated by these two control strategies lead to a similar temperature profile.

As far as the thermal performance is concerned, the obtained experimental temperature measurements allow to demonstrate that, under normal operating conditions, the best results were clearly achieved by the SVM vector control. Despite the slightly higher inverter heat sink temperature, justified by the extra inverter power losses imposed by the SVM technique, the less distorted PMSM voltage waveforms significantly contribute to the decreasing of their rms values, and the subsequent decreasing of the stator iron losses. As a result, this has a positive impact on the reduction of the machine stator and winding temperatures, which means that, comparing with HCC vector control and DTC, the PMSM can operates under the same load conditions but at lower temperatures.

For a PCM reconfiguration, all the three considered control strategies present an equivalent thermal profile, and therefore, there is no clear advantage of a particular technique for this converter post-fault topology.

On the other side, considering the NCM inverter reconfiguration, the HCC vector control and DTC present once more an equivalent thermal performance level, despite the slightly lower temperature values obtained for the first one. The most noticeable difference is observed for the inverter heat sink temperature that is higher for the HCC vector control due to the larger inverter power losses. Regarding the SVM vector control technique, the inferior current control capability under these post-fault operating conditions generate more distorted current waveforms and with larger rms values, which directly contributes to the PMSM temperature increase, showing this way the worst thermal behavior.

At last, from the PMSM acoustic noise analysis, it can be concluded that under healthy operation, the lowest noise level is generated by the SVM vector control strategy. The fixed inverter switching frequency imposed by the SVM has a direct impact on the machine emitted noise, where it was possible to clearly identify specific sound components related to the PWM frequency. For the two other control strategies, the variable inverter switching frequency leads to a greater spectrum noise dispersion at high frequency values, contributing to higher noise levels, especially for the DTC.

With respect to the PCM reconfiguration, the obtained results allow to conclude that the noise levels emitted by the PMSM are very similar. In this case and comparing with the healthy case, it is worth noting the great noise level increasing obtained for the SVM vector control while the noise is reduced by one-half for the DTC.

For the NCM reconfiguration, the noise levels are very similar to the ones measured for the drive healthy operation, with the exception of the SVM vector control that shows an impressive increase of approximately three times. Despite this, the DTC technique still is the one that leads to the highest motor noise level generation, while the lowest levels are achieved for the SVM vector control strategy.

8.2 Future Work

Considering all the developed work presented in this thesis, some suggestions for future research can be made. One of the most important issues in PMSMs is the demagnetization of the rotor magnets due to high temperatures. As a result, a more exhaustive thermal analysis would allow to better evaluate the PMSM temperature behavior for different operating conditions, including post-fault operation. From the thermal analysis presented in this work, it is possible to verify that that the motor temperature is negatively affected by inverter faults. Therefore, beyond the temperature analysis for different post-fault converter topologies, it becomes clear that the thermal study of the drive operation under inverter faulty operating conditions is also very important.

With the continuous development and improvement of digital controllers, the tendency to integrate more advanced diagnostic techniques/algorithms into variable speed drives controllers will continue to increase. As a consequence, further work can be done in order to develop real-time diagnostic methods for other different components such as the PMSM itself (winding inter-turn short-circuit faults, demagnetization faults, etc…), DC bus capacitors and feedback sensors.

This work can also be extended to another important research field related to the application of permanent magnet synchronous generators to wind energy conversion systems. This type of machine is being more and more used by many manufacturers, together with back-to-back full-scale power converters in wind turbines. Basically, this converter type comprises two VSIs connected by the DC bus, resulting in a more complex converter topology. Consequently, the development of fault-tolerant strategies applied to these energy conversion systems represent a very important research topic.

Bibliography

[1] J. O. Estima, "Accionamentos electromecatrónicos baseados em motores síncronos de ímanes permanentes", BSc Thesis, *University of Coimbra*, 2007.

[2] R. R. Errabelli, "Inverter and controller for highly available permanent magnet synchronous drives", PhD Thesis, *Technische Universität Darmstadt*, 2012.

[3] F. Meinguet, "Fault-tolerant permanent-magnet synchronous machine drives: fault detection and isolation, control reconguration and design considerations", PhD Thesis, *Université Libre de Bruxelles*, 2012.

[4] B. K. Bose, "Power electronics and motor drives recent progress and perspective", *IEEE Transactions on Industrial Electronics*, vol. 56, no. 2, pp.581-588, February 2009.

[5] T. M. Jahns, G. B. Kliman and T. W. Neuman, "Interior PM synchronous motors for adjustable speed drives", *IEEE Transactions on Industry Applications*, vol. 22, no. 4, pp. 738-747, July 1986.

[6] P. Pillay and R. Krishnan, "Modeling of permanent magnet motor drives", *IEEE Transactions on Industrial Electronics*, vol. 35, no. 4, pp. 537-541, November 1988.

[7] P. Pillay and R. Krishnan, "Modeling, simulation, and analysis of permanent-magnet motor drives. I. The permanent-magnet synchronous motor drive," *IEEE Transactions on Industry Applications*, vol. 25, no. 2, pp. 265-273, March/April 1989.

[8] S. Sunter and H. Altun, "Control of a permanent magnet synchronous motor fed by a direct AC-AC converter", *Electrical Engineering Journal*, vol. 87, no. 2, February 2005.

[9] A. A. Hassan and M. Azzam, "Robust control of a speed sensorless permanent magnet synchronous motor drive", *5th International Conference on Technology and Automation*, Thessaloniki, Greece, 15-16 October 2005.

[10] W. Kaewjinda and M. Konghirun, "Vector control drive of permanent magnet synchronous motor using resolver sensor", *ECTI Transactions on Electrical Engineering, Electronics and Comunications*, vol. 5, no. 1, February 2007.

[11] H. Chaoui and P. Sicard, "Adaptive fuzzy logic control of permanent magnet synchronous machines with nonlinear friction", *IEEE Transactions on Industrial Electronics*, vol. 59, no. 2, pp. 123-1133, February 2012.

[12] S. Po-Ngam and S. Sangwongwanich, “Stability and dynamic performance improvement of adaptive full-order observers for sensorless PMSM drive”, *IEEE Transactions on Power Electronics*, vol. 27, no. 2, pp. 588-600, February 2012.

[13] T. Boileau, N. Leboeuf, B. Nahid-Mobarakeh and F. Meibody-Tabar, “Online identification of PMSM parameters: parameter identifiability and estimator comparative study”, *IEEE Transactions on Industry Applications*, vol. 47, no. 4, pp. 1944-1957, July/August 2011.

[14] C. Xia, Y. Yan, P. Song and T. Shi, “Voltage disturbance rejection for matrix converter-based PMSM drive system using internal model control”, *IEEE Transactions on Industrial Electronics*, vol. 59, no. 1, pp. 361-372, January 2012.

[15] H. Liu and S. Li, “Speed control for PMSM servo system using predictive functional control and extended state observer”, *IEEE Transactions on Industrial Electronics*, vol. 59, no. 2, pp. 1171-1183, February 2012.

[16] K.-H. Dempewolf and B. Ponick, “Modelling of permanent magnet synchronous machines for simulations of transient phenomena”, *European Conference on Power Electronics and Applications*, 10 pp., 2-5 September 2007.

[17] M. Zeki Bilgin and B. Çakir, “Neuro-PID position controller design for permanent magnet synchronous motor”, *Lecture Notes in Computer Science*, vol. 4221, 418-426, 2006.

[18] D. Wang, X. Wang, H. Chen and R. Zhang, “Matlab/Simulink-based simulation of line-start PMSM used in pump jacks”, *IEEE Conference on Industrial Electronics and Applications*, pp. 1179-1181, 23-25 May 2007.

[19] N. Urasaki, T. Senjyu and K. Uezato, “A novel calculation method for iron loss resistance suitable in modeling permanent-magnet synchronous motors”, *IEEE Transactions on Energy Conversion*, vol. 18, no. 1, pp. 41- 47, March 2003.

[20] J. Hur, “Characteristic analysis of interior permanent-magnet synchronous motor in electro-hydraulic power steering systems”, *IEEE Transactions on Industrial Electronics*, vol. 55, no. 6, pp. 2316-2323, June 2008.

[21] S. Bolognani, L. Peretti, M. Zigliotto and E. Bertotto, “Commissioning of electromechanical conversion models for high dynamic PMSM drives”, *IEEE Transactions on Industrial Electronics*, vol. 57, no. 3, pp. 986-993, March 2010.

[22] C. Cavallaro, A. O. DiTommaso, R. Miceli, A. Raciti, A. G. R. Galluzzo and M. Trapanese, “Efficiency enhancement of permanent-magnet synchronous motor drives by online loss minimization approaches”, *IEEE Transactions on Industrial Electronics*, vol. 52, no. 4, pp. 1153-1160, August 2005.

[23] S. Morimoto, Y. Tong, Y. Takeda and T. Hirasa, “Loss minimization control of permanent magnet synchronous motor drives”, *IEEE Transactions on Industrial Electronics*, vol. 41, no. 5, pp. 511-517, October 1994.

[24] C. Mademlis, I. Kioskeridis and N. Margaris, “Optimal efficiency control strategy for interior permanent-magnet synchronous motor drives”, *IEEE Transactions on Energy Conversion*, vol. 19, no. 4, pp. 715-723, December 2004.

[25] N. Urasaki, T. Senjyu and K. Uezato, “Relationship of parallel model and series model for permanent magnet synchronous motors taking iron loss into account”, *IEEE Transactions on Energy Conversion*, vol. 19, no. 2, pp. 265-270, June 2004.

[26] T. F. Chan, W. Wang and L. Lai, “Magnetic field in a transverse- and axial-flux permanent magnet synchronous generator from 3D FEA”, *IEEE Transactions on Magnetics*, vol. 48, no. 2, pp. 1055-1058, February 2012.

[27] J. Güemes, A. Iraolagoitia, J. Del Hoyo and P. Fernández, “Torque analysis in permanent-magnet synchronous motors: a comparative study”, *IEEE Transactions on Energy Conversion*, vol. 26, no. 1, pp. 55-63, March 2011.

[28] T. Sun, J. Kim, G. Lee, J. Hong and M. Choi, “Effect of pole and slot combination on noise and vibration in permanent magnet synchronous motor”, *IEEE Transactions on Magnetics*, vol. 47, no. 5, pp. 1038-1041, May 2011.

[29] G. Heins, M. Thiele and T. Brown, “Accurate torque ripple measurement for PMSM”, *IEEE Transactions on Instrumentation and Measurement*, vol. 60, no. 12, pp. 3868-3874, December 2011.

[30] M. Hsieh and Y. Hsu, “A generalized magnetic circuit modeling approach for design of surface permanent-magnet machines”, *IEEE Transactions on Industrial Electronics*, vol. 59, no. 2, pp. 779-792, February 2012.

[31] B. K. Bose, *Modern power electronics and AC drives*, Upper Saddle River, NJ 07458, Prentice-Hall, 2002.

[32] M. Cacciato, A. Consoli, G. Scarcella and G. Scelba, “A novel efficiency optimization scalar control technique for industrial IPMSM drives”, *IEEE International Symposium on Industrial Electronics*, pp. 1181-1186, 4-7 July 2010.

[33] W. Cuui, K.T.Chau, J. Z. Jiang, Y. Fan, Z. Wang, “Scalar control of a new phase-decoupling permanent magnet synchronous motor for servo application”, *IAS Annual Meeting Industry Applications Conference*, vol. 3, pp. 1762-1769, 2-6 October 2005.

[34] P. D. C. Perera, F. Blaabjerg, J. K. Pedersen, P. Thogersen, “A sensorless, stable V/f control method for permanent-magnet synchronous motor drives”, *IEEE Transactions on Industry Applications*, vol. 39, no. 3, pp. 783-791, May/June 2003.

[35] R. Ancuti, I. Boldea, and G.-D. Andreescu, “Sensorless V/f control of high-speed surface permanent magnet synchronous motor drives with two novel stabilising loops for fast dynamics and robustness”, *IET Electric Power Applications*, vol. 4, no. 3, pp. 149-157, March 2010.

[36] F. Blaschke, “A new method for the structural decoupling of A.C. induction machines,” *IFAC Conference Record*, Duesseldorf, Germany, pp. 1–15, October 1971.

[37] P. Vas, *Sensorless Vector and Direct Torque Control*, Oxford University Press, 1998, ISBN 0-19-856465-1.

[38] B. Nahid-Mobarakeh, F. Meibody-Tabar and F.-M. Sargos, "Mechanical sensorless control of PMSM with online estimation of stator resistance", *IEEE Transactions on Industry Applications*, vol. 40, no. 2, pp. 457-471, March/April 2004.

[39] J.-L. Shi, T.-H. Liu and Y.-C. Chang, "Position control of an interior permanent-magnet synchronous motor without using a shaft position sensor", *IEEE Transactions on Industrial Electronics*, vol. 54, no. 4, pp. 1989-2000, June 2007.

[40] L. Chretien and I. Husain, "Position sensorless control of non-salient PMSM from very low speed to high speed for low cost applications", *IEEE Industry Applications Society Annual Meting*, pp. 289-296, 23-27 September 2007.

[41] R. W. Hejny and R. D. Lorenz, "Evaluating the practical low-speed limits for back-EMF tracking-based sensorless speed control using drive stiffness as a key metric", *IEEE Transactions on Industry Applications*, vol. 47, no. 3, pp. 1337-1343, May/June 2011.

[42] H. Kim, J. Son and J. Lee, "A high-speed sliding-mode observer for the sensorless speed control of a PMSM", *IEEE Transactions on Industrial Electronics*, vol. 58, no. 9, pp. 4069-4077, September 2011.

[43] J. Jang, S.-K. Sul and Y.-C. Son, "Current measurement issues in sensorless control algorithm using high frequency signal injection method", *IEEE Industry Applications Society Annual Meting*, vol. 2, pp. 1134-1141, 12-16 October 2003.

[44] R. Raute, C. Caruana, J. Cilia, C. S. Staines and M. Sumner, "A zero speed operation sensorless PMSM drive without additional test signal injection", *European Conference on Power Electronics and Applications*, 10 pp., 2-5 September 2007.

[45] J.-H. Jang, J.-I. Ha, M. Ohto, K. Ide and S.-K. Sul, "Analysis of permanent-magnet machine for sensorless control based on high-frequency signal injection", *IEEE Transactions on Industry Applications*, vol. 40, no. 6, pp. 1595-1604, November/December 2004.

[46] Z. Wang, S. Niu, S. L. Ho, W. N. Fu and J. Zhu, "A position detection strategy for sensorless surface mounted permanent magnet motors at low speed using transient finite-element analysis", *IEEE Transactions on Magnetics*, vol. 48, no. 2, pp.1003-1006, February 2012.

[47] J.-H. Jang, S.-K. Sul, J.-I. Ha, K. Ide and M. Sawamura, "Sensorless drive of surface-mounted permanent-magnet motor by high-frequency signal injection based on magnetic saliency", *IEEE Transactions on Industry Applications*, vol. 39, no. 4, pp. 1031-1039, July/August 2003.

[48] M. J. Corley, R. D. Lorenz, "Rotor position and velocity estimation for a salient-pole permanent magnet synchronous machine at standstill and high speeds", *IEEE Transactions on Industry Applications*, vol. 34, no. 4, pp. 784-789, July/August 1998.

[49] A. Consoli, G. Scarcella and A. Testa, "Industry application of zero-speed sensorless control techniques for PM synchronous motors", *IEEE Transactions on Industry Applications*, vol. 37, no. 2, pp. 513-521, March/April 2001.

[50] O. Wallmark and L. Harnefors, "Sensorless control of salient PMSM drives in the transition region", *IEEE Transactions on Industrial Electronics*, vol. 53, no. 4, pp. 1179-1187, June 2006.

[51] S. Morimoto, M. Sanada and Y. Takeda, "Mechanical sensorless drives of IPMSM with online parameter identification", *IEEE Transactions on Industry Applications*, vol. 42, no. 5, pp. 1241-1248, September/October 2006.

[52] B. Gumus, M. S. Ozerdem and M. Ozdemir, "Permanent magnet synchronous motor's sensorless vector control with artificial neural network observer", *International Aegean Conference on Electrical Machines and Power Electronics*, pp. 643-648, 10-12 September 2007.

[53] S. Unal and M. Ozdemir, "Sensorless control of the permanent magnet synchronous motor using neural networks", *International Aegean Conference on Electrical Machines and Power Electronics*, pp. 638-642, 10-12 September 2007.

[54] T. Pajchrowski and K. Zawirski, "Robust speed and position control based on neural and fuzzy techniques", *European Conference on Power Electronics and Applications*, 10 pp., 2-5 September 2007.

[55] T. D. Batzel and K. Y. Lee, "An approach to sensorless operation of the permanent-magnet synchronous motor using diagonally recurrent neural networks", *IEEE Transactions on Energy Conversion*, vol. 18, no. 1, pp. 100-106, March 2003.

[56] A. Accetta, M. Cirrincione, M. Pucci and G. Vitale, "Sensorless control of PMSM fractional horsepower drives by signal injection and neural adaptive-band filtering", *IEEE Transactions on Industrial Electronics*, vol. 59, no. 3, pp. 1355-1366, March 2012.

[57] M. Rashed, P. MacConnell, A. Stroncach and P. Acarnley, "Sensorless indirect rotor field orientation speed control of permanent magnet synchronous motor using adaptive rotor flux estimator", *IEEE Conference on Decision and Control*, pp. 647- 652, 12-15 December 2005.

[58] M. Elbuluk and L. Changsheng, "Sliding mode observer for wide-speed sensorless control of PMSM drives", *IEEE Industry Applications Society Annual Meting*, vol. 1, pp. 480-485, 12-16 October 2003.

[59] S. Po-ngam and S. Sangwongwanich, "Stability and dynamic performance improvement of adaptive full-order observers for sensorless PMSM drive", *IEEE Transactions on Power Electronics*, vol. 27, no. 2, pp. 588-600, February 2012.

[60] G. Zhu, A. Kaddouri, L. A. Dessaint and O. Akhrif, "A nonlinear state observer for the sensorless control of a permanent-magnet AC machine", *IEEE Transactions on Industrial Electronics*, vol. 48, no. 6, pp. 1098-1108, December 2001.

[61] S. Bolognani, R. Oboe and M. Zigliotto, "Sensorless full-digital PMSM drive with EKF estimation of speed and rotor position", *IEEE Transactions on Industrial Electronics*, vol. 46, no. 1, pp. 184-191, February 1999.

[62] S. Bolognani, M. Zigliotto and M. Zordan, "Extended-range PMSM sensorless speed drive based on stochastic filtering", *IEEE Transactions on Power Electronics*, vol. 16, no. 1, pp. 110-117, January 2001.

[63] S. Bolognani, M. Zigliotto and M. Zordan, "Extended Kalman filter tuning in sensorless PMSM drives", *IEEE Transactions on Industry Applications*, vol. 39, no. 6, pp. 1741-1747, November/December 2003.

[64] M. Boussak, “Implementation and experimental investigation of sensorless speed control with initial rotor position estimation for interior permanent magnet synchronous motor drive”, *IEEE Transactions on Power Electronics*, vol. 20, no. 6, pp. 1413-1422, November 2005.

[65] *A1000 Inverter Series - High performance vector control*, Literature No. YEU INV A1000 EN v3 1110, Yaskawa Electric Europe GmbH, November 2010.

[66] *Frequency Inverter CFW-11 V3.1X*, Programing Manual, Document No. 0899.5664/05, WEG Equipamentos Elétricos S.A., December 2011.

[67] M. Kazmierkovski, R. Krishnan and F. Blaabjerg, *Control in Power Electronics: Selected Problems*, Academic Press 2002, ISBN 0-12-402772-5.

[68] J. Holtz, “Pulsewidth modulation-a survey”, *IEEE Transactions on Industrial Electronics*, vol. 39, no. 5, pp. 410-420, October 1992.

[69] M. Kazmierkowski and L. Malesani, “Current control techniques for three-phase voltage-source PWM converters: a survey”, *IEEE Transactions on Industrial Electronics*, vol. 45, no. 5, pp. 691-703, October 1998.

[70] M. A. Rahman, T. S. Radwan, A. M. Osheiba and A. E. Lashine, “Analysis of current controllers for voltage-source inverter”, *IEEE Transactions on Industrial Electronics*, vol. 44, no. 4, pp. 477-485, August 1997.

[71] K. Zhou and D. Wang, “Relationship between space-vector modulation and three-phase carrier-based PWM: a comprehensive analysis”, *IEEE Transactions on Industrial Electronics*, vol. 49, no. 1, pp. 186-196, February 2002.

[72] A. M. Hava, R. J. Kerkman and T. A. Lipo, “Simple analytical and graphical methods for carrier-based PWM-VSI drives”, *IEEE Transactions on Power Electronics*, vol. 14, no. 1, pp. 49-61, January 1999.

[73] B. K. Bose, *Power Electronics and Motor Drives—Advances and Trends*, Burlington, MA: Academic, 2006.

[74] M. P. Kazmierkowski, L. G. Franquelo, J. Rodriguez, M. A. Perez and J. I. Leon, “High-performance motor drives”, *IEEE Industrial Electronics Magazine*, vol. 5, no. 3, pp. 6-26, September 2011.

[75] I. Takahashi and T. Noguchi, “A new quick response and high efficiency control strategy of an induction motor”, *IEEE Industry Applications Society Annual Meting*, pp. 496-502, 1985.

[76] M. Depenbrock, “Direct self-control (DSC) of inverter-fed induction machine”, *IEEE Transaction on Power Electronics*, vol. PE-3, No. 4, pp. 420-429, October 1988.

[77] L. Zhong, M. F. Rahman, W. Y. Hu and K. W. Lim, “Analysis of direct torque control in permanent magnet synchronous motor drives”, *IEEE Transactions on Power Electronics*, vol. 12, no. 3, pp. 528-536, May 1997.

[78] M. F. Rahman, L. Zhong and K. W. Lim, "A direct torque-controlled interior permanent magnet synchronous motor drive incorporating field weakening", *IEEE Transactions on Industry Applications*, vol. 34, no. 6, pp. 1246-1253, November/Decemeber 1998.

[79] D. Sun, F. Weizhong and H. Yikang, "Study on the direct torque control of permanent magnet synchronous motor drives", *International Conference on Electrical Machines and Systems*, vol. 1, pp. 571-574, 2001.

[80] L. Zhong, M. F. Rahman, W. Y. Hu, K. W. Lim and M. A. Rahman, "A direct torque controller for permanent magnet synchronous motor drives", *IEEE Transactions on Energy Conversion*, vol. 14, no. 3, pp. 637-642, Sepember 1999.

[81] Z. Lu, H. Sheng, H. L. Hess and K. M. Buck, "The modeling and simulation of a permanent magnet synchronous motor with direct torque control based on Matlab/Simulink", *IEEE International Conference on Electric Machines and Drives*, 7 pp., May 2005.

[82] L. Bao-hua, L. Wei-guo, Z. Xi-wei and L. Rong, "Research on direct torque control of permanent magnet synchronous motor based on optimized state selector", *IEEE International Symposium on Industrial Electronics*, vol. 3, pp. 2105-2109, 9-13 July 2006.

[83] *Direct torque control - the world's most advanced AC drive technology*, Techinal Guide No. 1, ABB Drives, 2011.

[84] D. Telford, M. W. Dunnigan and B. W. Williams, "A comparison of vector control and direct torque control of an induction machine", *IEEE Power Electronics Specialists Conference*, vol. 1, pp. 421-426, 2000.

[85] M. S. Merzoug, and F. Naceri, "Comparison of field-oriented control and direct torque control for permanent magnet synchronous motor (PMSM)", *Proceedings of World Academy of Science, Engineering and Technology*, vol. 45, pp. 299-304, 2008.

[86] D. Casadei, F. Profumo, G. Serra and A. Tani, "FOC and DTC: two viable schemes for induction motors torque control", *IEEE Transactions on Power Electronics*, vol. 17, no. 5, pp. 779-787, September 2002.

[87] V. Comnac, F. Moldoveanu and M. Cernat, "Sensorless speed and direct torque control of surface permanent magnet synchronous machines using stochastic filtering techniques", *Convention of Electrical and Electronics Engineers in Israel*, pp. 39- 40, 1 December 2002.

[88] M. F. Rahman, L. Zhong, M. E. Haque and M. A. Rahman, "A direct torque-controlled interior permanent-magnet synchronous motor drive without a speed sensor", *IEEE Transactions on Energy Conversion*, vol. 18, no. 1, pp. 17-22, March 2003.

[89] V. Comnac, M. Cernat, F. Moldoveanu, and I. Draghici, "Sensorless speed and direct torque control of surface permanent magnet synchronous machines using an extended kalman filter", *Mediterranean Conference on Control and Automation*, 6 pp., 27-29 June 2001.

[90] G. H. Foo and M. F. Rahman, "Direct torque control of an IPM-synchronous motor drive at very low speed using a sliding-mode stator flux observer", *IEEE Transactions on Power Electronics*, vol. 25, no. 4, pp. 933-942, April 2010.

[91] G. H. Foo, S. Sayeef, M. F. Rahman, "Low-speed and standstill operation of a sensorless direct torque and flux controlled IPM synchronous motor drive", *IEEE Transactions on Energy Conversion*, vol. 25, no. 1, pp. 25-33, March 2010.

[92] G. H. Foo and M. F. Rahman, "Sensorless direct torque and flux-controlled IPM synchronous motor drive at very low speed without signal injection", *IEEE Transactions on Industrial Electronics*, vol. 57, no. 1, pp. 395-403, January 2010.

[93] J. Habibi and S. Vaez-Zadeh, "Efficiency-optimizing direct torque control of permanent magnet synchronous machines", *IEEE Power Electronics Specialists Conference*, pp. 759-764, June 2005.

[94] J. Siahbalaee, S. Vaez-Zadeh and F. Tahami, "A new loss minimization approach with flux and torque ripples reduction of Direct torque controlled permanent magnet synchronous motors", *European Conference on Power Electronics and Applications*, 8 pp., 8-10 September 2009.

[95] S. Vaez-Zadeh and M. Khayamy, "Efficiency-optimizing direct torque control of interior permanent magnet synchronous machines with fastest start up", *IET Conference on Power Electronics, Machines and Drives*, pp. 218-224, 2-4 April 2008.

[96] J. Faiz and S. H. Mohseni-Zonoozi, "A novel technique for estimation and control of stator flux of a salient-pole PMSM in DTC method based on MTPF", *IEEE Transactions on Industrial Electronics*, vol. 50, no. 2, pp. 262-271, April 2003.

[97] M. Meyer, T. Grote and J. Bocker, "Direct torque control for interior permanent magnet synchronous motors with respect to optimal efficiency", *European Conference on Power Electronics and Applications*, 9 pp., 2-5 September 2007.

[98] A. Daghigh, M. B. Sharifian and M. Farasat, "A modified direct torque control of IPM synchronous machine drive with constant switching frequency and low ripple in torque", *Iranian Conference on Electrical Engineering*, pp. 778-783, 11-13 May 2010.

[99] J. Zhang, M. F. Rahman and C. Grantham, "A new scheme to direct torque control of interior permanent magnet synchronous machine drives for constant inverter switching frequency and low torque ripple", *CES/IEEE International Power Electronics and Motion Control Conference*, vol. 3, 5 pp., 14-16 August 2006.

[100] C. Lascu and A. M. Trzynadlowski, "Combining the principles of sliding mode, direct torque control, and space-vector modulation in a high-performance sensorless AC drive", *IEEE Transactions on Industry Applications*, vol. 40, no. 1, pp. 170-177, January/February 2004.

[101] L. Tang, L. Zhong, M. F. Rahman and Y. Hu, "A novel direct torque controlled interior permanent magnet synchronous machine drive with low ripple in flux and torque and fixed switching frequency", *IEEE Transactions on Power Electronics*, vol. 19, no. 2, pp. 346-354, March 2004.

[102] D. Sun, J. G. Zhu and Y. K. He, "A space vector modulation direct torque control for permanent magnet synchronous motor drive systems", *International Conference on Power Electronics and Drive Systems*, vol. 1, pp. 692-697, 17-20 November 2003.

[103] G. S. Buja and M. P. Kazmierkowski, “Direct torque control of PWM inverter-fed AC motors - a survey”, *IEEE Transactions on Industrial Electronics*, vol. 51, no. 4, pp. 744-757, August 2004.

[104] Z. Xu and M. F. Rahman, “Direct torque and flux regulation of an IPM synchronous motor drive using variable structure control approach”, *IEEE Transactions on Power Electronics*, vol. 22, no. 6, pp. 2487-2498, November 2007.

[105] A. Jidin, N. R. Idris, A. H. Yatim, A. Z. Jidin and T. Sutikno, “Torque ripple minimization in DTC induction motor drive using constant frequency torque controller”, *International Conference on Electrical Machines and Systems*, pp. 919-924, 10-13 October 2010.

[106] N. R. Idris, A. H. Yatim, “Direct torque control of induction machines with constant switching frequency and reduced torque ripple”, *IEEE Transactions on Industrial Electronics*, vol. 51, no. 4, pp. 758-767, August 2004.

[107] Y. Zhang, J. Zhu, W. Xu and Y. Guo, “A simple method to reduce torque ripple in direct torque-controlled permanent-magnet synchronous motor by using vectors with variable amplitude and angle”, *IEEE Transactions on Industrial Electronics*, vol. 58, no. 7, pp. 2848-2859, July 2011.

[108] Y. Zhang and J. Zhu, “A novel duty cycle control strategy to reduce both torque and flux ripples for DTC of permanent magnet synchronous motor drives with switching frequency reduction”, *IEEE Transactions on Power Electronics*, vol. 26, no. 10, pp. 3055-3067, October 2011.

[109] M. F. Rahman, M. E. Haque, L. Tang and L. Zhong, “Problems associated with the direct torque control of an interior permanent-magnet synchronous motor drive and their remedies”, *IEEE Transactions on Industrial Electronics*, vol. 51, no. 4, pp. 799-809, August 2004.

[110] M. Kadjoudj, N. Goléa and M. E. Benbouzid, “Problems of stator flux estimation in DTC of PMSM drives”, *Journal of Electrical Engineering & Technology*, vol. 2, no. 4, pp. 468-477, 2007.

[111] J. Hu and B. Wu, “New integration algorithms for estimating motor flux over a wide speed range”, *IEEE Transactions on Power Electronics*, vol. 13, no. 5, pp. 969-977, Semptember 1998.

[112] M. Niemel and J. Pyrhonen, “Drift correction methods of the stator flux linkage in DTC synchronous motor drives”, *European Conference on Power Electronics and Applications*, 10 pp., 2009.

[113] M. E. Haque, L. Zhong and M. F. Rahman, “The effect of offset error and its compensation for a direct torque controlled interior permanent magnet synchronous motor drive”, *International Electric Machines and Drives Conference*, 17-21 June 2001.

[114] Z. Xu and M. F. Rahman, “An improved stator flux estimation for a variable structure direct torque controlled IPM synchronous motor drive using a sliding observer”, *IEEE Industry Applications Society Annual Meting*, pp. 2484-2490, 2-6 October 2005.

[115] G.-D. Andreescu, C. I. Pitic, F. Blaabjerg and I. Boldea, "Combined flux observer with signal injection enhancement for wide speed range sensorless direct torque control of IPMSM drives", *IEEE Transactions on Energy Conversion*, vol. 23, no. 2, pp. 393-402, June 2008.

[116] T. Vyncke, R. Boel and Jan Melkebeek, "A comparison of stator flux linkage estimators for a direct torque controlled PMSM drive", *Annual conference of IEEE Industrial Electronics Society*, pp. 967-974, 3-5 November 2009.

[117] M. E. Haque and M. F. Rahman, "Influence of stator resistance variation on direct torque controlled interior permanent magnet synchronous motor drive performance and its compensation", *IAS Annual Meeting Industry Applications Conference*, vol. 4, pp. 2563-2569, 30 Sepember-4 October 2001.

[118] L. Tang and M. F. Rahman, "A direct torque controlled interior permanent magnet synchronous machine drive with a new stator resistance estimator", *IAS Annual Meeting Industry Applications Conference*, vol. 1, pp. 632-639, 12-16 October 2003.

[119] M. E. Haque, L. Zhong and M. F. Rahman, "A sensorless initial rotor position estimation scheme for a direct torque controlled interior permanent magnet synchronous motor drive", *IEEE Transactions on Power Electronics*, vol. 18, no. 6, pp. 1376-1383, November 2003.

[120] Y. Yan, J. G. Zhu and Y. G. Guo, "Initial rotor position estimation and sensorless direct torque control of surface-mounted permanent magnet synchronous motors considering saturation saliency", *IET Electric Power Applications*, vol. 2, no. 1, pp. 42-48, January 2008.

[121] Y. Yan and J. G. Zhu, "A survey of sensorless initial rotor position estimation schemes for permanent magnet synchronous motors", *Australasian Universities Power Engineering Conference*, 6 pp., 26-29 September 2004.

[122] Y. Yang and H. Gao, "Initial rotor position estimation for low saliency interior permanent-magnet synchronous motor drives", *IEEE Applied Power Electronics Conference and Exposition*, pp.1022-1027, 6-11 March 2011.

[123] N. Bianchi, S. Bolognani and M. Zigliotto, "Analysis of PM synchronous motor drive failures during flux weakening operation", *27th Annual IEEE Power Electronics Specialists Conference*, Baveno, Italy, vol. 2, pp. 1542-1548, 23-27 June 1996.

[124] B. A. Welchko, T. M. Jahns and S. Hiti, "IPM synchronous machine drive response to a single-phase open circuit fault", *IEEE Transactions on Power Electronics*, vol. 17, no. 5, pp. 764-771, September, 2002.

[125] A. Gaeta, G. Scelba and A. Consoli, "Modeling and control of three-phase PMSMs under open-phase fault", *IEEE Energy Conversion Congress and Exposition*, pp. 1684-1691, 17-22 September 2011.

[126] B. A. Welchko, T. M. Jahns, W. L. Soong and J. M. Nagashima, "IPM synchronous machine drive response to symmetrical and asymmetrical short circuit faults", *IEEE Transactions on Energy Conversion*, vol. 18, no. 2, pp. 291-298, June 2003.

[127] M. Dai, A. Keyhani and T. Sebastian, “Fault analysis of a PM brushless DC Motor using finite element method”, *IEEE Transactions on Energy Conversion*, vol. 20, no. 1, pp. 1-6, March, 2005.

[128] T. Sun, S. H. Lee and J. P. Hong, “Faults analysis and simulation for interior permanent magnet synchronous motor using Simulink@MATLAB”, *International Conference on Electrical Machines and Systems*, Seul, South Korea, pp. 900-905, 8-11 October 2007.

[129] B. Vaseghi, B. Nahid-Mobarakeh, N. Takorabet and F. Meibody-Tabar, “Experimentally validated dynamic fault model for PMSM with stator winding inter-turn fault”, *IEEE Industry Applications Society Annual Meeting*, pp. 1-5, 5-9 October 2008.

[130] K.-H. Kim, D.-U. Choi, B.-G. Gu and I.-S. Jung, “Fault model and performance evaluation of an inverter-fed permanent magnet synchronous motor under winding shorted turn and inverter switch open”, *IET Electric Power Applications*, vol. 4, no. 4, pp. 214-225, April 2010.

[131] J. O. Estima and A. J. M. Cardoso, “Performance evaluation of permanent magnet synchronous motor drives under inverter fault conditions”, *XVIII International Conference on Electrical Machines*, Vilamoura, Portugal, CD-ROM, 6 pp., 6-9 September 2008.

[132] J. O. Estima and A. J. M. Cardoso, “Performance evaluation of DTC-SVM permanent magnet synchronous motor drives under inverter fault conditions”, *IEEE Industrial Electronics Conference*, Porto, Portugal, pp. 1228-1233, 3-5 November 2009.

[133] M. Harakawa, C. Dufour, S. Nishimura and T. Nagano, “Real-time simulation of a PMSM drive in faulty modes with validation against an actual drive system”, *13th European Conference on Power Electronics and Applications*, 9 pp., 8-10 September 2009.

[134] J. O. Estima and A. J. M. Cardoso, “Impact of inverter faults in the overall performance of permanent magnet synchronous motor drives”, *IEEE International Electric Machines and Drives Conference*, Miami, FL, USA, pp. 1319-1325, 3-6 May 2009.

[135] J. O. Estima and A. J. M. Cardoso, “The occurrence of faults in permanent magnet synchronous motor drives and its effects on the power supply quality”, *International Conference on Renewable Energies and Power Quality*, Santander, Spain, CD-ROM, 6 pp., 12-14 March 2008.

[136] H. Yu, Z. Liu and S. Cui, “Research on fault analysis and diagnosis of PMSM in HEV”, *International Conference on Electrical Machines and Systems*, 4 pp., 20-23 August 2011.

[137] V. Smet, F. Forest, J. Huselstein, F. Richardeau, Z. Khatir, S. Lefebvre and M. Berkani, “Ageing and failure modes of IGBT modules in high-temperature power cycling”, *IEEE Transactions on Industrial Electronics*, vol. 58, no. 10, pp. 4931-4941, October 2011.

[138] H. B. A. Sethom and M. A. Ghedamsi, “Intermittent misfiring default detection and localisation on a PWM inverter using wavelet decomposition”, *Journal of Electrical Systems*, vol. 4, no. 2, pp. 222-234, 2008.

[139] S. Yang, A. Bryant, P. Mawby, D. Xiang, L. Ran and P. Tavner, “An industry-based survey of reliability in power electronic converters”, *IEEE Transaction on Industry Applications*, vol. 47, no. 3, pp. 1441-1451, May/June 2011.

[140] S. Yang, A. Bryant, P. Mawby, D. Xiang, L. Ran and P. Tavner, "An industry-based survey of reliability in power electronic converters", *IEEE Energy Conversion Congress and Exposition*, pp. 3151-3157, 20-24 September 2009.

[141] S. Yang, D. Xiang, A. Bryant, P. Mawby, L. Ran, and P. Tavner, "Condition monitoring for device reliability in power electronic converters - a review", *IEEE Transactions on Power Electronics*, vol. 25, no. 11, November 2010.

[142] F. W. Fuchs, "Some diagnosis methods for voltage source inverters in variable speed drives with induction machines - a survey", *29th Annual Conference of the IEEE Industrial Electronics Society*, vol. 2, pp. 1378-1385, 2-6 November, 2003.

[143] A. M. S. Mendes, A. J. M. Cardoso and E. S. Saraiva, "Voltage source inverter fault diagnosis in variable speed AC drives, by Park's vector approach", *Seventh International Conference on Power Electronics and Variable Speed Drives*, Conf. Publ. No. 456, pp. 538-543, 1998.

[144] C. Kral and K. Kafka, "Power electronics monitoring for a controlled voltage source inverter drive with induction machines", *IEEE 31st Annual Power Electronics Specialists Conference*, vol. 1, pp. 213-217, 2000.

[145] P. Gilreath and B. N. Singh, "A new centroid based fault detection method for 3-phase inverter-fed induction motors", *IEEE Power Electronics Specialists Conference*, pp. 2664-2669, June 2005.

[146] D. Diallo, M. E. H. Benbouzid, D. Hamad, and X. Pierre, "Fault detection and diagnosis in an induction machine drive: a pattern recognition approach based on concordia stator mean current vector", *IEEE Transactions on Energy Conversion*, vol. 20, no. 3, pp. 512-519, September 2005.

[147] F. Zidani, D. Diallo and M. Benbouzid and R. Nait-Said, "A fuzzy-based approach for the diagnosis of fault modes in a voltage-fed PWM inverter induction motor drive", *IEEE Transactions on Industrial Electronics*, vol. 55, no. 2, pp. 586-593, February, 2008.

[148] L. Mihet-Popa, O. Prostean, I. Filip, I. Szeidert and C. Vasar, "Fault detection methods for frequency converters fed induction machines", *IEEE Conference on Emerging Technologies and Factory Automation*, pp. 161-168, 25-28 September 2007.

[149] D. Foito, J. F. Martins, V. F. Pires and J. Maia, "An eigenvalue/eigenvector 3D current reference method for detection and fault diagnosis in a voltage source inverter", *Annual Conference of IEEE Industrial Electronics*, pp. 190-194, 3-5 November 2009.

[150] R. Peuget, S. Courtine and J. P. Rognon, "Fault detection and isolation on a PWM inverter by knowledge-based model", *IEEE Transactions on Industry Applications*, vol. 34, no. 6, pp. 1318–1326, Nov./Dec., 1998.

[151] M. Trabelsi, M. Boussak and M. Gossa, "Multiple IGBTs open circuit faults diagnosis in voltage source inverter fed induction motor using modified slope method", *XIX International Conference on Electrical Machines*, 6 pp., 6-8 September 2010.

[152] A. M. S. Mendes and A. J. M. Cardoso, “Voltage source inverter fault diagnosis in variable speed AC drives, by the average current Park’s Vector approach”, *IEEE International Electric Machines and Drives Conference*, Seatle, Washington, USA, pp. 704-706, May 9-12, 1999.

[153] J. A. A. Caseiro, A. M. S. Mendes and A. J. M. Cardoso, “Fault diagnosis on a PWM rectifier AC drive system with fault tolerance using the average current Park’s Vector approach”, *IEEE International Electric Machines and Drives Conference*, Miami, FL, USA, pp. 695-701, 3-6 May, 2009.

[154] J. A. A. Caseiro, A. M. S. Mendes and A. J. M. Cardoso, “The usage of a PWM rectifier to improve three-phase induction motor drive performance under fault conditions”, *European Conference on Power Electronics and Applications*, Barcelona, Spain, 10 pp., 8-10 September, 2009.

[155] R. L. A. Ribeiro, C. B. Jacobina, E. R. C. Silva and A. M. N. Lima, “Fault detection in voltage-fed PWM motor drive systems”, *IEEE Annual Power Electronics Specialists Conference*, vol. 1, pp. 242-247, 2000.

[156] R. L. A. Ribeiro, C. B. Jacobina, E. R. C. Silva and A. M. N. Lima, “Fault detection of open-switch damage in voltage-fed PWM motor drive systems,” *IEEE Transactions on Power Electronics*, vol. 18, no. 2, pp. 587–593, March, 2003.

[157] M. Shahbazi, M.-R. Zolghadri, P. Poure ans S. Saadate, “Fast detection of open-switch faults with reduced sensor count for a fault-tolerant three-phase converter”, *Power Electronics, Drive Systems and Technologies Conference*, pp. 546-550, 16-17 February 2011.

[158] M. Trabelsi, M. Boussak and M. Gossa, “PWM-Switching pattern-based diagnosis scheme for single and multiple open-switch damages in VSI-fed induction motor drives”, *ISA Transactions*, vol. 51, no. 2, pp. 333–344, March 2012.

[159] Q. T. An, L. Z. Sun, K. Zhao and T. M. Jahns, “Low-cost diagnostic method for open-switch faults in inverters”, *Electronics Letters*, vol. 46, no.14, pp.1021-1022, July 2010.

[160] Q. T. An, L. Z. Sun, K. Zhao and L. Sun, “Switching function model based fast-diagnostic method of open-switch faults in inverters without sensors”, *IEEE Transactions on Power Electronics*, vol. 26, no. 1, pp. 119-126, January 2011.

[161] M. Trabelsi, M. Boussak, P. Mestre and M. Gossa, “Pole voltage based-approach for IGBTs open-circuit fault detection and diagnosis in PWM-VSI-Fed induction motor drives”, *International Conference on Power Engineering, Energy and Electrical Drives*, 6 pp., 11-13 May 2011.

[162] M. Trabelsi, M. Boussak, P. Mestre and M. Gossa, “An improved diagnosis technique for IGBTs open-circuit fault in PWM-VSI-fed induction motor drive”, *IEEE International Symposium on Industrial Electronics*, pp. 2111-2117, 27-30 June 2011.

[163] S.-M. Jung, J.-S. Park, H.-S. Kim, H.-W. Kim and M.-J. Youn, “Simple switch open fault detection method of voltage source inverter”, *IEEE Energy Conversion Congress and Exposition*, pp. 3175-3181, 20-24 September 2009.

[164] N. M. A. Freire, J. O. Estima and A. J. M. Cardoso, "A voltage-based approach for open-circuit fault diagnosis in voltage-fed SVM motor drives without extra hardware", *International Conference on Electrical Machines*, Marseille, France, 2-5 September 2012.

[165] S. Abramik, W. Sleszynski, J. Niezaniski and H. Piquet, "A diagnostic method for on-line fault detection and localization in VSI-fed AC drives", *European Conference on Power Electronics and Applications*, 8 pp., 2-4 September 2003.

[166] W. Sleszynski and J. Nieznanski, "Open-transistor fault diagnostics in voltage-source inverters by analyzing the load current", *IEEE International Symposium on Diagnostics for Electric Machines, Power Electronics and Drives*, pp. 70-73, 6-8 September 2007.

[167] W. Sleszynski, J. Nieznanski and A. Cichowski, "Open-transistor fault diagnostics in voltage-source inverters by analyzing the load currents", *IEEE Transactions on Industrial Electronics*, vol. 56, no. 11, pp. 4681-4688, November 2009.

[168] K. Rothenhagen and F. W. Fuchs, "Performance of diagnosis methods for IGBT open circuit faults in three phase voltage source inverters for ac variable speed drives", *European Conference on Power Electronics and Applications*, 10 pp., 2005.

[169] B. Lu and S. K. Sharma, "A survey of IGBT fault diagnostic methods for three-phase power inverters", *International Conference on Condition Monitoring and Diagnosis*, pp. 756-763, 21-24 April 2008.

[170] B. Lu and S. K. Sharma, "A Literature review of IGBT fault diagnostic and protection methods for power inverters", *IAS Annual Meeting Industry Applications Conference*, 8 pp., 5-9 October 2008.

[171] B. Lu and S. K. Sharma, "A literature review of IGBT fault diagnostic and protection methods for power inverters", *IEEE Transactions on Industry Applications*, vol. 45, no. 5, pp. 1770-1777, September/October 2009.

[172] J. O. Estima and A. J. M. Cardoso, "A novel diagnostic method for single power switch open-circuit faults in voltage-fed PWM motor drives", *International Symposium on Power Electronics, Electrical Drives, Automation and Motion*, Pisa, Italy, 6 pp., 14-16 June, 2010.

[173] J. O. Estima and A. J. M. Cardoso, "A new approach for real-time multiple open-circuit fault diagnosis in voltage source inverters", *IEEE Energy Conversion Congress and Exposition*, Atlanta, GA, USA, pp. 4328-4335, 12-16 September 2010.

[174] J. O. Estima and A. J. M. Cardoso, "A new approach for real-time multiple open-circuit fault diagnosis in voltage source inverters", *IEEE Transactions on Industry Applications*, vol. 47, no. 6, 8 pp., November/December 2011.

[175] N. M. A. Freire, J. O. Estima and A. J. M. Cardoso, "A new approach for current sensor fault diagnosis in PMSG drives for wind energy conversion systems", *IEEE Energy Conversion Congress and Exposition*, Raleigh, USA, 8 pp., 15-20 September 2012.

[176] D. U. Campos-Delgado and D. R. Espinoza-Trejo, "An observer-based diagnosis scheme for single and simultaneous open-switch faults in induction motor drives", *IEEE Transactions on Industrial Electronics*, vol. 58, no. 2, pp. 671-679, February 2011.

[177] B.-G. Park, T.-S. Kim, J.-S. Ryu and D.-S. Hyun, "Fault tolerant strategies for BLDC motor drives under switch faults", *IAS Annual Meeting Industry Applications Conference*, vol. 4, pp. 1637-1641, 8-12 October 2006.

[178] B.-G. Park, K.-J. Lee, T.-S. Kim, J.-S. Ryu and D.-S. Hyun, "Low-cost fault diagnosis algorithm for switch open-damage in BLDC motor drives", *Journal of Power Electronics*, vol. 10, no. 6, November 2010.

[179] B.-G. Park, K.-J. Lee, R.-Y. Kim, T.-S. Kim, J.-S. Ryu and D.-S. Hyun, "Simple fault diagnosis based on operating characteristic of brushless direct-current motor drives", *IEEE Transactions on Industrial Electronics*, vol. 58, no. 5, pp. 1586-1593, May 2011.

[180] M. A. Rodríguez-Blanco, A. Claudio-Sánchez, D. Theilliol, L. G. Vela-Valdés, P. Sibaja-Terán, L. Hernández-González, J. Aguayo-Alquicira, "A failure-detection strategy for IGBT based on gate-voltage behavior applied to a motor drive system", *IEEE Transactions on Industrial Electronics*, vol. 58, no. 5, pp. 1625-1633, May 2011.

[181] D.-E. Kim and D.-C. Lee, "Fault diagnosis of three-phase PWM inverters using wavelet and SVM", *IEEE International Symposium on Industrial Electronics*, pp. 329-334, June 30-July 2 2008.

[182] F. Charfi, S. Lesecq and F. Sellami, "Fault diagnosis using SWT and Neyman Pearson detection tests", *IEEE International Symposium on Diagnostics for Electric Machines, Power Electronics and Drives*, pp.1-6, 2009.

[183] K.-H. Kim, B.-G. Gu and I.-S. Jung, "Online fault-detecting scheme of an inverter-fed permanent magnet synchronous motor under stator winding shorted turn and inverter switch open", *IET Electric Power Applications*, vol. 5, no. 6, pp. 529-539, July 2011.

[184] M. Aktas and V. Turkmenoglu, "Wavelet-based switching faults detection in direct torque control induction motor drives", *IET Science, Measurement & Technology*, vol. 4, no. 6, pp. 303-310, November 2010.

[185] F. Meinguet and J. Gyselinck, "Sensor and open-phase fault detection and isolation for three-phase AC drives", *IET International Conference on Power Electronics, Machines and Drives*, 6 pp., 19-21 April 2010.

[186] D. Sun, J. Meng and Z. He, "Diagnosis of inverter faults in PMSM DTC drive using time-series data mining technique", *Advanced Data Mining and Applications*, vol. 4093/2006, pp. 741-748, 2006.

[187] M. Masrur, Z. Chen and Y. Murphey, "Intelligent diagnosis of open and short circuit faults in electric drive inverters for real-time applications", *IET Power Electronics*, vol. 3, no. 2, pp. 279-291, March 2010.

[188] F. Bo and N. Jiangchuang, "Three-phase SPWM inverter fault diagnosis based on optimized neural networks", *IEEE Power Engineering and Automation Conference*, vol. 3, pp. 331-335, 8-9 September 2011.

[189] N. M. A. Freire, J. O. Estima and A. J. M. Cardoso, "Converters fault-diagnosis in PMSG drives for wind turbine applications", *36th Annual Conference of the IEEE Industrial Electronics Society*, Phoenix, AZ, USA, pp. 403-408, 7-10 November 2010.

[190] N. M. A. Freire, J. O. Estima and A. J. M. Cardoso, "Open-circuit fault diagnosis in PMSG drives for wind turbine applications", *IEEE Transactions on Industrial Electronics*, 2012 (Early Acess).

[191] N. M. A. Freire, J. O. Estima and A. J. M. Cardoso, "Multiple open-circuit fault diagnosis in voltage-fed PWM motor drives using the current Park's Vector phase and the currents polarity", *8th IEEE International Symposium on Diagnostics for Electrical Machines, Power Electronics and Drives*, Bologna, Italy, pp. 397-404, 5-8 September 2011.

[192] A. Gaeta, G. Scarcella, G. Scelba, S. De Caro and A. Testa, "Inverter fault-identification for VSI motor drives", *8th IEEE International Symposium on Diagnostics for Electrical Machines, Power Electronics and Drives*, Bologna, Italy, pp. 413-419, 5-8 September 2011.

[193] J. O. Estima and A. J. M. Cardoso, "Single power switch open-circuit fault diagnosis in voltage-fed PWM motor drives by the reference current errors", *8th IEEE International Symposium on Diagnostics for Electrical Machines, Power Electronics and Drives*, Bologna, Italy, pp. 364-371, 5-8 September, 2011.

[194] J. O. Estima and A. J. M. Cardoso, "A new algorithm for real-time multiple open-circuit fault diagnosis in voltage-fed PWM motor drives by the reference current errors", *IEEE Transactions on Industrial Electronics*, 2012 (Early Acess).

[195] V. D. Broeck, W. Heinz, V. Wyk and D. Jacobus, "A comparative investigation of a three-phase induction machine drive with a component minimized voltage-fed inverter under different control options", *IEEE Transactions on Industry Applications*, vol. IA-20, no. 2, pp. 309-320, March 1984.

[196] J.-R. Fu and T. A. Lipo, "A strategy to isolate the switching device fault of a current regulated motor drive", *IAS Annual Meeting Industry Applications Conference*, vol. 2, pp. 1015-1020, 2-8 October 1993.

[197] H. Lin, H. Li, Y. Wang, M. Li, P. Wen and C. Zhang, "On inverter fault-tolerant operation vector control of a PMSM drive", *IEEE International Conference on Intelligent Computing and Intelligent Systems*, vol. 2, pp. 522-526, 20-22 November 2009.

[198] F. Genduso and R. Miceli, "A general mathematical model for non-redundant fault-tolerant inverters", *IEEE International Electric Machines & Drives Conference*, pp. 705-710, 15-18 May 2011.

[199] J. O. Estima and A. J. M. Cardoso, "A fault-tolerant permanent magnet synchronous motor drive with integrated voltage source inverter open-circuit faults diagnosis", *European Conference on Power Electronics and Applications*, Birmingham, UK, 10 pp., Aug./Sep. 2011.

[200] J. O. Estima and A. J. M. Cardoso, "Fast fault detection, isolation and reconfiguration in fault-tolerant permanent magnet synchronous motor drives", *IEEE Energy Conversion Congress and Exposition*, Raleigh, USA, 15-20 September 2012.

[201] B. A. Welchko, T. A. Lipo, T. M. Jahns and , S. E. Schulz, "Fault tolerant three-phase AC motor drive topologies; a comparison of features, cost, and limitations", *IEEE Transactions on Power Electronics*, vol. 19, no. 4, pp. 1108- 1116, July 2004.

[202] A. M. S. Mendes, "Análise do desempenho do motor de indução trifásico quando alimentado através de um inversor de fonte de tensão com tolerância a falhas", PhD Thesis, *University of Coimbra*, 2005.

[203] A. M. S. Mendes and A. J. M. Cardoso, "Fault-tolerant operating strategies applied to three-phase induction-motor drives", *IEEE Transactions on Industrial Electronics*, vol. 53, no. 6, pp. 1807-1817, December 2006.

[204] D. U. C. Delgado, D. R E. Trejo and E. Palacios, "Fault-tolerant control in variable speed drives: a survey", *IET Electric Power Applications*, vol. 2, no. 2, pp. 121-134, March 2008.

[205] K. D Hoang, Z. Q. Zhu, M. P. Foster and D. A. Stone, "Comparative study of current vector control performance of alternate fault tolerant inverter topologies for three-phase PM brushless ac machine with one phase open-circuit fault", *5th IET International Conference on Power Electronics, Machines and Drives*, 6 pp., 19-21 April 2010.

[206] J. O. Estima and A. J. M. Cardoso, "Efficiency evaluation of fault-tolerant operating strategies applied to three-phase permanent magnet synchronous motor drives", *International Conference on Electrical Machines*, Marseille, France, 7 pp., 2-5 September 2012.

[207] C. B. Jacobina, E. R. C. Silva, A. M. N. Lima and R. L. A. Ribeiro, "Vector and scalar control of a four switch three phase inverter", *IEEE Industry Applications Society Annual Meeting*, vol. 3, pp. 2422-2429, 8-12 October 1995.

[208] F. Blaabjerg, S. Freysson, H.-H. Hansen and S. Hansen, "A new optimized space-vector modulation strategy for a component-minimized voltage source inverter", *IEEE Transactions on Power Electronics*, vol. 12, no. 4, pp. 704-714, July 1997.

[209] J. Klima, "Analytical investigation of an induction motor fed from four-switch VSI with a new space vector modulation strategy", *IEEE Transactions on Energy Conversion*, vol. 21, no. 4, pp. 832-838, December 2006.

[210] M. B. R. Correa, C. B. Jacobina, E. R. C. Silva and A. M. N. Lima, "A general PWM strategy for four-switch three-phase inverters", *IEEE Transactions on Power Electronics*, vol. 21, no. 6, pp. 1618-1627, November 2006.

[211] J. Klima, "Analytical investigation of an induction motor drive under inverter fault mode operations", *IEE Electric Power Applications*, vol. 150, no. 3, pp. 255-262, May 2003.

[212] J. Klima, "Analytical investigation of an induction motor fed from four-switch VSI with a new space vector modulation strategy", *IEEE Transactions on Energy Conversion*, vol. 21, no. 4, pp. 832-838, December 2006.

[213] H. S. Alavije and M. Akhbari, "Investigation of induction motor drive behavior in low-cost fault tolerant control for electric vehicles", *International Power Engineering and Optimization Conference*, pp. 176-181, 6-7 June 2011.

[214] P. Q. Dzung, L. M. Phuong, P. Q. Vinh, N. M. Hoang and T. C. Binh, "New space vector control approach for four switch three phase inverter (FSTPI)", *International Conference on Power Electronics and Drive Systems*, pp. 1002-1008, 27-30 November 2007.

[215] Q.-T. An, L. Sun, K. Zhao and L.-Z. Sun, "Novel remedial control strategies for fault-tolerant pwm inverters", *International Journal of Applied Electromagnetics and Mechanics*, vol. 33, no. 3-4, pp. 1635-1642, 2010.

[216] A. Guermazi, M. Sahbi, A. Masmoudi and A. Elantably, "On the analysis and control of four-switch three-phase inverter fed brushless motor drives", *International Journal for Computation and Mathematics in Electrical and Electronic Engineering*, vol. 26, no. 5, pp. 1247-1261, 2007.

[217] B. El Badsi, A. Guermazi and A. Masmoudi, "On the comparison between different space vector PWM strategies implemented in FSTPI-fed induction motor drives", *International Journal for Computation and Mathematics in Electrical and Electronic Engineering*, vol. 26, no. 1, pp. 127-147, 2007.

[218] A. Guermazi, B. El Badsi, M. Masmoudi and A. Masmoudi, "RFOC implementation in four-switch three phase inverter-fed induction motor drive", *International Journal for Computation and Mathematics in Electrical and Electronic Engineering*, vol. 26, no. 1, pp. 167-182, 2007.

[219] Q.-T. An, L. Sun, K. Zhao and T. M. Jahns, "Scalar PWM algorithms for four-switch three-phase inverters", *Electronics Letters*, vol. 46, no. 13, pp. 900-902, June 2010.

[220] C. B. Jacobina, E. R. C. Silva, A. M. N. Lima and R. L. A. Ribeiro, "Vector and scalar control of a four switch three phase inverter", *IEEE Industry Applications Society Annual Meeting*, vol. 3, pp. 2422-2429, 8-12 October 1995.

[221] S. Bhattacharya, P. Deb, S. K. Biswas and S. K. Chowdhury, "A comprehensive study of modulation strategies for three phase low cost PWM converter", *International Journal of Engineering Science and Technology*, vol. 3, no. 7, pp. 5772-5777, 2011.

[222] M. Monfared, H. Rastegar, H. M. Kojabadi, "Overview of modulation techniques for the four-switch converter topology", *IEEE International Power and Energy Conference*, pp. 803-807, 1-3 December 2008.

[223] F. Blaabjerg, D. O. Neacsu and J. K. Pedersen, "Adaptive SVM to compensate DC-link voltage ripple for four-switch three-phase voltage-source inverters", *IEEE Transactions on Power Electronics*, vol. 14, no. 4, pp. 743-752, July 1999.

[224] S. Kazemlou and M. R. Zolghadri, "Direct torque control of four-switch three phase inverter fed induction motor using a modified SVM to compensate dc-link voltage imbalance", *International Conference on Electric Power and Energy Conversion Systems*, pp. 1-6, 10-12 November 2009.

[225] D. Sun, X. Liu; L. Shang and Y. B. Ivonne, "Four-switch three-phase inverter fed DTC system considering DC-link voltage imbalance", *International Conference on Electrical Machines and Systems*, pp. 1068-1072, 17-20 October 2008.

[226] H.-H. Lee, P. Q. Dzung, L. D. Khoa and L. M. Phuong, “The development of space vector PWM for four switch three phase inverter fed induction motor with DC - link voltage imbalance”, *IEEE International Conference on Industrial Technology*, pp. 1-6, 10-13 February 2009.

[227] H.-H. Lee, P. Q. Dzung, L. D. Khoa and L. M. Phuong, “The optimized adaptive space vector pulse width modulation for four switch three phase inverter under DC - link voltage ripple condition”, *IEEE Region 10 Conference*, pp.1-6, 23-26 January 2009.

[228] D. Sun and Y. He, “A modified direct torque control for PMSM under inverter fault”, *International Conference on Electrical Machines and Systems*, vol. 3, pp. 2569-2473, September 2005.

[229] S. B. Ozturk, W. C. Alexander and H. A. Toliyat, “Direct torque control of four-switch brushless DC motor with non-sinusoidal back EMF”, *IEEE Transactions on Power Electronics*, vol. 25, no. 2, pp. 263-271, February 2010.

[230] B. Wang, Y. He and Y. B. Ivonne, “Four switch three phase inverter fed PMSM DTC system with nonlinear perpendicular flux observer and sliding mode control”, *International Conference on Electrical Machines and Systems*, pp. 3206-3211, 17-20 October 2008.

[231] D. Sun, Z. He, Y. He and Y. Guan, “Four-switch inverter fed PMSM DTC with SVM approach for fault tolerant operation”, *IEEE International Electric Machines & Drives Conference*, vol. 1, pp. 295-299, 3-5 May 2007.

[232] K. D. Hoang, Z. Q. Zhu and M. P. Foster, “Influence and compensation of inverter voltage drop in direct torque-controlled four-switch three-phase PM brushless AC drives”, *IEEE Transactions on Power Electronics*, vol. 26, no. 8, pp. 2343-2357, August 2011.

[233] D. Sun and J. Meng, “Research on fault tolerant inverter based permanent magnet synchronous motor direct torque control drives”, *IEEE Conference on Industrial Electronics and Applications*, 5 pp., 24-26 May 2006.

[234] Y. B. Ivonne, D. Sun, Y.-K. He, “Study on inverter fault-tolerant operation of PMSM DTC”, *Journal of Zhejiang University SCIENCE A*, Vol. 9, No. 2, pp. 156-164, 2008.

[235] T. H. Liu, J. R. Fu and T. A. Lipo, “A strategy for improving reliability of field-oriented controlled induction motor drives”, *IEEE Transactions on Industry Applications*, vol. 29, no. 5, pp. 910-918, September/October 1993.

[236] Z. Q. Zhu, K. Utaikaifa, K. Hoang, Y. Liu and D. Howe, “Direct torque control of three-phase PM brushless AC motor with one phase open-circuit fault”, *IEEE International Electric Machines and Drives Conference*, pp. 1180-1187, 3-6 May 2009.

[237] B. R. Correa, C. B. Jacobina, E. R. C. Silva and A. M. N. Lima, “An induction motor drive system with improved fault tolerance”, *IEEE Transactions on Industry Applications*, vol. 37, no. 3, pp. 873-879, May/Jun 2001.

[238] O. Wallmark, L. Harnefors and O. Carlson, “Post-fault operation of fault-tolerant inverters for PMSM drives”, *European Conference on Power Electronics and Applications*, 10 pp., 2005.

[239] C. J. Gajanayake, B. Bhangu, S. Nadarajan and G. Jayasinghe, "Fault tolerant control method to improve the torque and speed response in PMSM drive with winding faults", *IEEE International Conference on Power Electronics and Drive Systems*, pp. 956-961, 5-8 December 2011.

[240] R. R. Errabelli and P. Mutschler, "A fault tolerant control and power electronic for a permanent magnet synchronous motor drive", *European Conference on Power Electronics and Applications*, 10 pp., Aug./Sep. 2011.

[241] R. L. A. Ribeiro, C. B. Jacobina, E. R. C. Silva and A. M. N. Lima, "A fault tolerant induction motor drive system by using a compensation strategy on the PWM-VSI topology", *IEEE 32nd Annual Power Electronics Specialists Conference*, vol. 2, pp. 1191-1196, 2001.

[242] M. A. Rodriguez, A. Claudio, D. Theilliol, L. G. Vela and L. Hernandez, "A novel strategy to replace the damaged element for fault-tolerant induction motor drive", *IEEE International Power Electronics Congress*, pp. 123-127, 24-27 August 2008.

[243] A. Cordeiro, J. Palma, J. Maia and M. Resende, "Combining mechanical commutators and semiconductors in fast changing redundant inverter topologies", *IEEE International Conference on Computer as a Tool*, pp.1-4, 27-29 April 2011.

[244] R. Errabelli and P. Mutschler, "Fault tolerant voltage source inverter for permanent magnet drives", *IEEE Transactions on Power Electronics*, vol. 27, no. 2, February 2012.

[245] R. L. A. Ribeiro, C. B. Jacobina, E. R. C. Silva and A. M. N. Lima, "Fault-tolerant voltage-fed PWM inverter AC motor drive systems", *IEEE Transactions on Industrial Electronics*, vol. 51, no. 2, pp. 439- 446, April 2004.

[246] R. L. A. Ribeiro, C. B. Jacobina, A. M. N. Lima and E. R. C. Silva, "A strategy for improving reliability of motor drive systems using a four-leg three-phase converter", *IEEE Applied Power Electronics Conference and Exposition*, vol. 1, pp. 385-391, 2001.

[247] O. Wallmark, L. Harnefors and O. Carlson, "Control algorithms for a fault-tolerant PMSM drive", *IEEE Transactions on Industrial Electronics*, vol. 54, no. 4, pp. 1973-1980, August 2007.

[248] O. Jasim, M. Sumner, C. Gerada and J. Arellano-Padilla, "Development of a new fault-tolerant induction motor control strategy using an enhanced equivalent circuit model", *IET Electric Power Applications*, vol. 5, no. 8, pp. 618-627, September 2011.

[249] L. Lillo, L. Empringham, P. Wheeler, S. Khwan and C. Gerada, "Emulation of faults and remedial control strategies in a multiphase power converter drive used to analyse fault tolerant drive systems for aerospace applications", *European Conference on Power Electronics and Applications*, 6 pp., 8-10 September 2009.

[250] S. Bolognani, M. Zordan and M. Zigliotto, "Experimental fault-tolerant control of a PMSM drive", *IEEE Transactions on Industrial Electronics*, vol. 47, no. 5, pp. 1134-1141, October 2000.

[251] F. Meinguet, X. Kestelynx, E. Semailx and J. Gyselinck, “Fault detection, isolation and control reconfiguration of three-phase PMSM drives”, *IEEE International Symposium on Industrial Electronics*, pp. 2091-2096, 27-30 June 2011.

[252] B. A. Welchko, T. M. Jahns and T. A. Lipo, “Fault interrupting methods and topologies for interior PM machine drives”, *IEEE Power Electronics Letters*, vol. 2, no. 4, pp. 139-143, December 2004.

[253] S. Khwan, L. Lillo, L. Empringham, P. Wheeler, C. Gerada, N. M. Othman, O. Jasim and J. Clare, “Fault tolerant power converter topologies for PMSM drives in aerospace applications”, *European Conference on Power Electronics and Applications*, pp. 1-9, 8-10 September 2009.

[254] F. Richardeau, J. Mavier, H. Piquet and G. Gateau, “Fault-tolerant inverter for on-board aircraft EHA”, *European Conference on Power Electronics and Applications*, pp.1-9, 2-5 September 2007.

[255] N. Bianchi, S. Bolognani, M. Zigliotto, M. Zordan, “Innovative remedial strategies for inverter faults in IPM synchronous motor drives”, *IEEE Transactions on Energy Conversion*, vol. 18, no. 2, pp. 306- 314, June 2003.

[256] M.-A. Shamsi-Nejad, B. Nahid-Mobarakeh, S. Pierfederici and F. Meibody-Tabar, “Control strategies for fault tolerant PM drives using series architecture”, *IEEE Vehicle Power and Propulsion Conference*, pp.1-6, 1-3 September 2010.

[257] M.-A. Shamsi-Nejad, B. Nahid-Mobarakeh, S. Pierfederici and F. Meibody-Tabar, “Series architecture for fault tolerant PM drives: Operating modes with one or two DC voltage source(s)”, *IEEE International Conference on Industrial Technology*, pp. 1525-1530, 14-17 March 2010.

[258] J. A. Restrepo, A. Berzoy, A. E. Ginart, J. M. Aller, R. G. Harley and T. G. Habetler, “Switching strategies for fault tolerant operation of single DC-link dual converters”, *IEEE Transactions on Power Electronics*, vol. 27, no. 2, pp. 509-518, February 2012.

Appendix A

Computational Simulation Details

This appendix presents some pictures regarding the implementation of the drive model using the software Matlab/Simulink. In addition, the parameters of the drive main components are also listed.

A.1 Drive Model Pictures

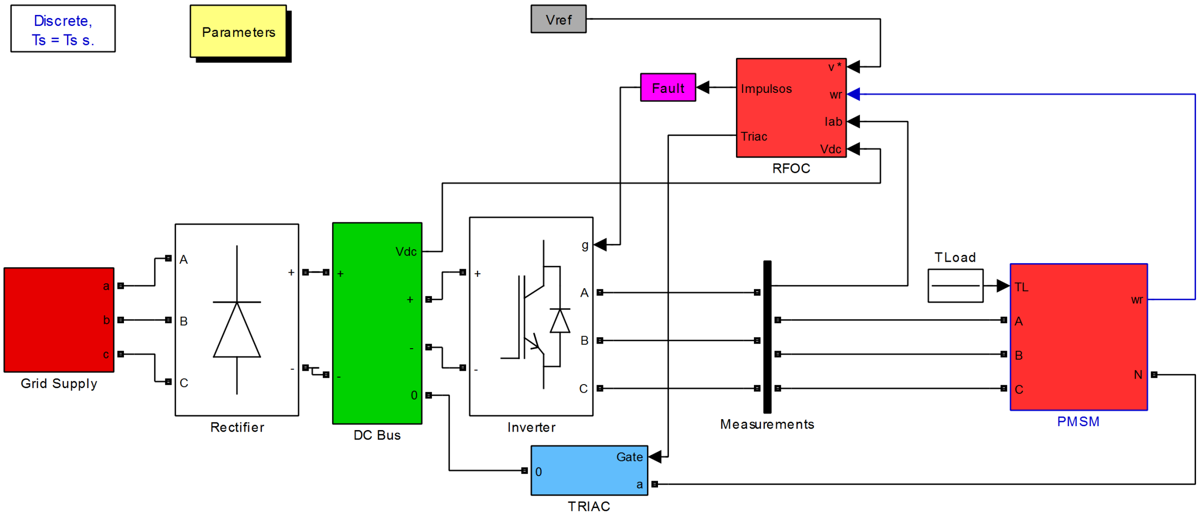

Figure A.1: General view of the drive main components implemented in Matlab/Simulink.

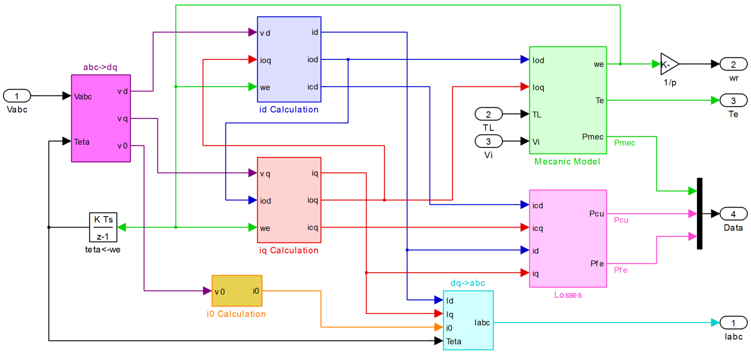

Figure A.2: Global view of the PMSM dynamic model implemented in Matlab/Simulink.

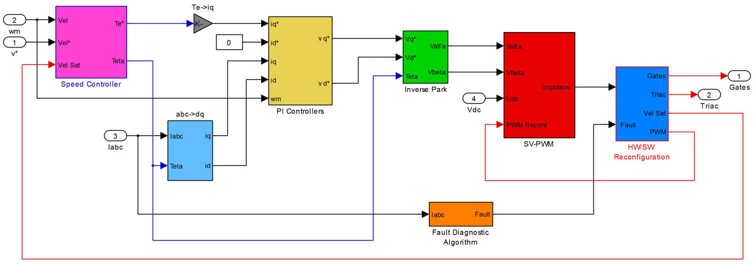

Figure A.3: Global view of the PMSM RFOC strategy implemented in Matlab/Simulink.

A.2 Main Simulation Parameters

Table A.1: Three-phase grid supply block parameters.

Parameters	Values
Phase-to-phase rms voltage	400 V
Phase angle of phase A	0°
Frequency	50 Hz
Internal Connection	Yg
Source Resistence	0.5 Ω
Source Inductance	1 mH

Table A.2: Three-phase diode bridge rectifier block parameters.

Parameters	Values
Snubber Resistence	100 kΩ
Snubber Capacitence	20 nF
R_{on}	1 kΩ
L_{on}	0 H
Forward Voltage	0.7 V

Table A.3: DC bus individual capacitor values.

Parameters	**Values**
Capacitance	4700 μF
Initial Voltage	282 V

Table A.4: Three-phase voltage source inverter block parameters.

Parameters	**Values**
Snubber Resistance	5000 Ω
Snubber Capacitance	1 μF
R_{on}	11.5 mΩ
Forward Voltages	1.3 V, 1.0 V
Tf(s), Tt(s)	1 μs, 2 μs

Table A.5: PMSM dynamic model parameters.

Parameters	**Values**
R_s	1.85 Ω
L_d	69.3 mH
L_q	98.1 mH
ψ_{PM}	0.743 Wb
J	0.02 Kgm^2
B	0.002 Nms/rad
p	2

Appendix B

Experimental Setup Details

This appendix presents the details of the equipment used to build the experimental prototype. Some pictures of the main components are shown, together with their principal specifications.

Additionally, various dedicated printed circuit boards were also designed and built in order to perform important tasks such as voltage and current measurements and for the interface and isolation between the power electronic components and the controller. Therefore, their schematics and pictures are also presented.

B.1 Experimental Setup Pictures

B.1.1 Autotransformer

An autotransformer was used to supply the drive with the standard three-phase supply of 400 V/50 Hz (Figure B.1). The possibility to adjust continuously the supply voltage allows to perform the tests in a safer way.

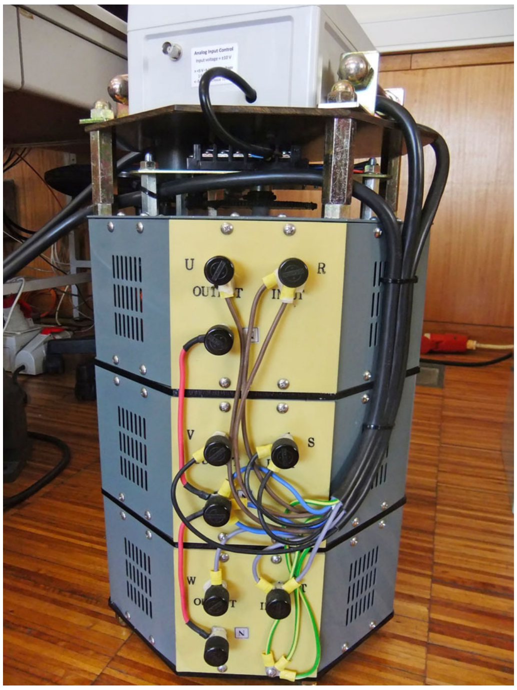

Figure B.1: Autotransformer used to supply the developed PMSM drive.

B.1.2 Power Converter

The power converter built in the laboratory uses various components, as it can be seen in Figure B.2. Both the three-phase diode bridge rectifier and inverter consist of two Semikron SKiiP 132GD120-3DUL power modules. Special measurement modules were built to measure the DC bus voltage and the PMSM voltages and currents. Some protection components such as fuses and circuit breakers were also included in order to avoid possible overload conditions.

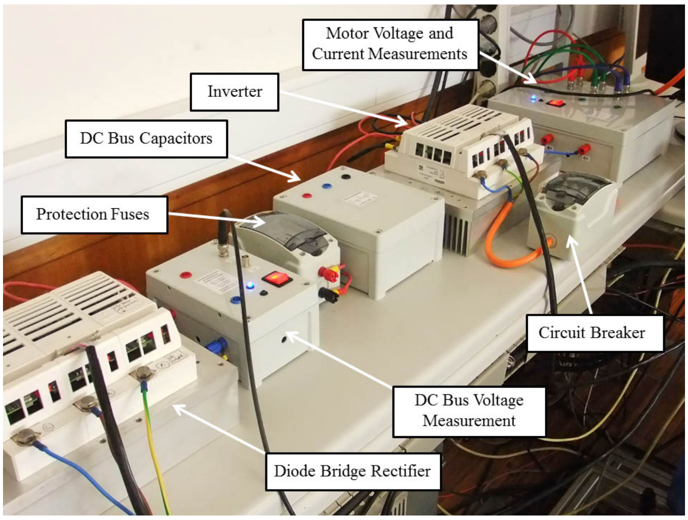

Figure B.2: General view of the built power converter.

B.1.2.1 DC Bus Capacitors

The used DC bus capacitors are shown in Figure B.3. A special module was built with two similar capacitors connected in series, making available the three required connectors, namely the positive, negative and midpoint terminais.

Figure B.3: DC bus capacitors power module with two Epcos 400 V 4700 μF capacitors.

B.1.2.2 Inverter

A detailed picture of the inverter is shown in Figure B.4. As said before, it consists of a Semikron SKiiP 132GD120-3DUL power module with NPT IGBTs. It can be also seen the RTD temperature sensor that measures the inverter heat sink temperature.

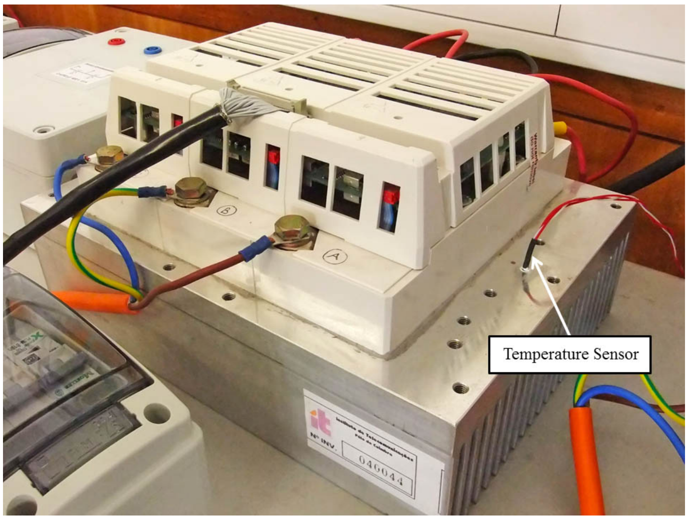

Figure B.4: Detail of the used voltage source inverter.

B.1.3 Electric Motor Test Bench

Figure B.5 presents the general view of the used PMSM coupled to an AC machine that is used as load. This machine is connected to a Yaskawa A1000 power converter that operates in torque control mode, allowing to easily adjusting the required load torque level. The precise torque value is measured using a torque sensor from Torqsense, model RWT321. The PMSM mechanical speed/position is measured using an incremental encoder from Hengstler, model RI 76TD, with 1024 pulses per revolution.

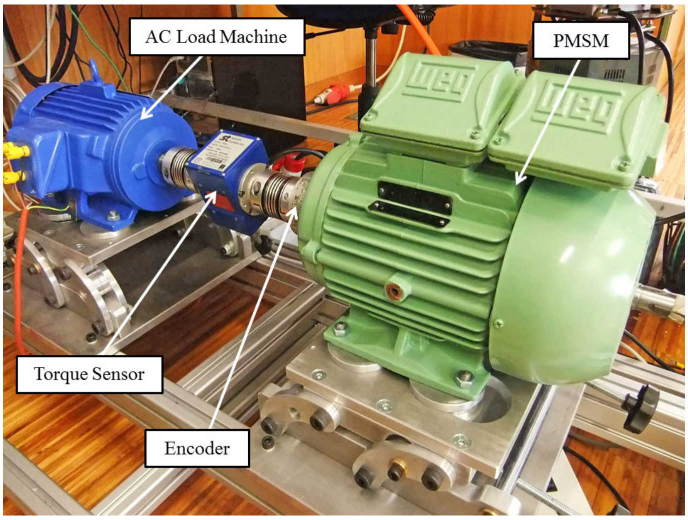

Figure B.5: Detail of the electric motor test bench.

B.1.4 PMSM Details

B.1.4.1 Connections

The used PMSM, a WQuattro motor from WEG, is equipped with two terminal boxes, one for the power connections corresponding to the motor supply, and another regarding the connection of the pt100 RTDs (Figure B.6). For the stator temperature measurement, a RTD was inserted through a hole in the outside of the PMSM, as it can be seen in Figure B.7.

B.1.4.2 Nameplate Parameters

The nameplate main parameters of the used PMSM are shown in Table B.1.

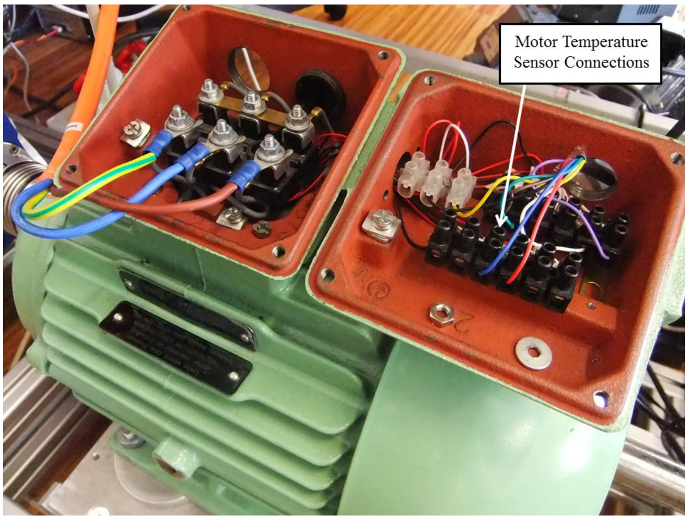

Figure B.6: Detail of the used PMSM connections.

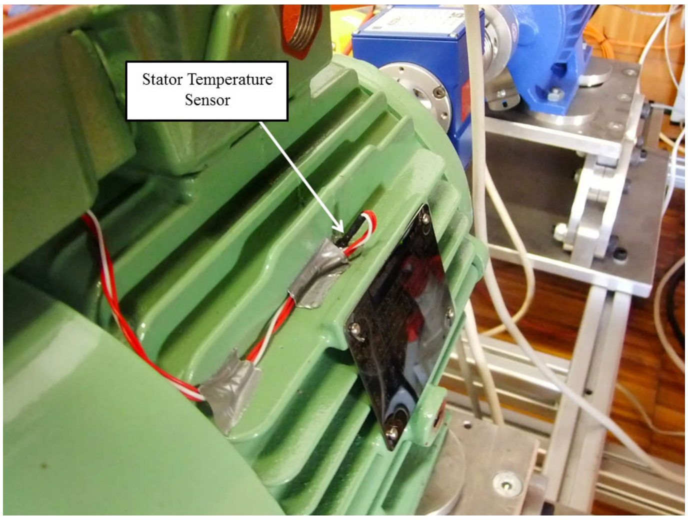

Figure B.7: Detail of the stator temperature sensor.

Table B.1: PMSM nameplate main parameters.

Parameters	**Values**
Power	2.2 kW
Frequency	50 Hz
Speed	1500 rpm
Voltage	400 V
Current	4.05 A

B.2 Built Printed Circuit Boards

In this section the circuit and board schematics of the design and built printed circuit boards are presented. Additionally, pictures of the final modules are also shown.

B.2.1 Single Phase Voltage and Current Measurements

This printed circuit board was designed with the aim to measure the voltage and current in a single-phase system. In this case, this board was used to measure the DC bus voltage. It uses two LEM sensors, a LA-55P and a LV-25P.

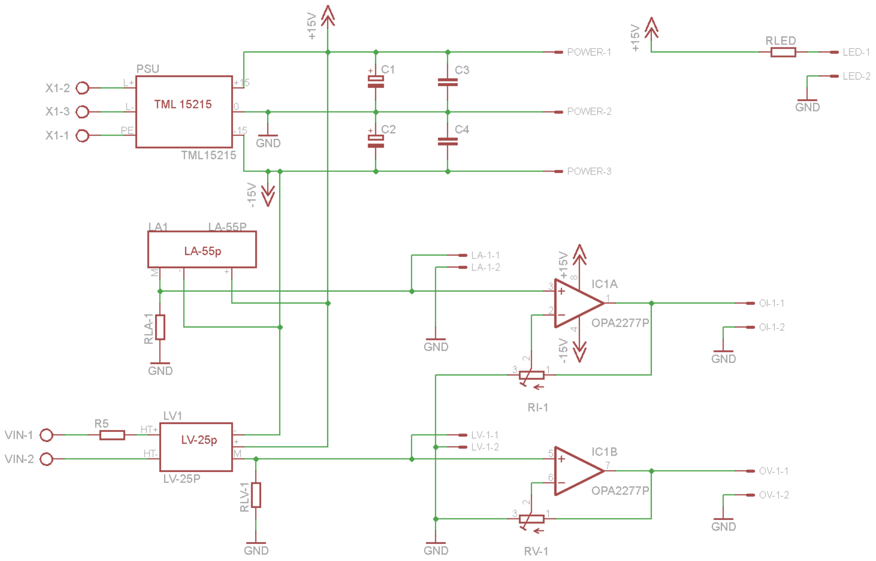

Figure B.8: Schematic circuit diagram of the single-phase voltage and current measurement board.

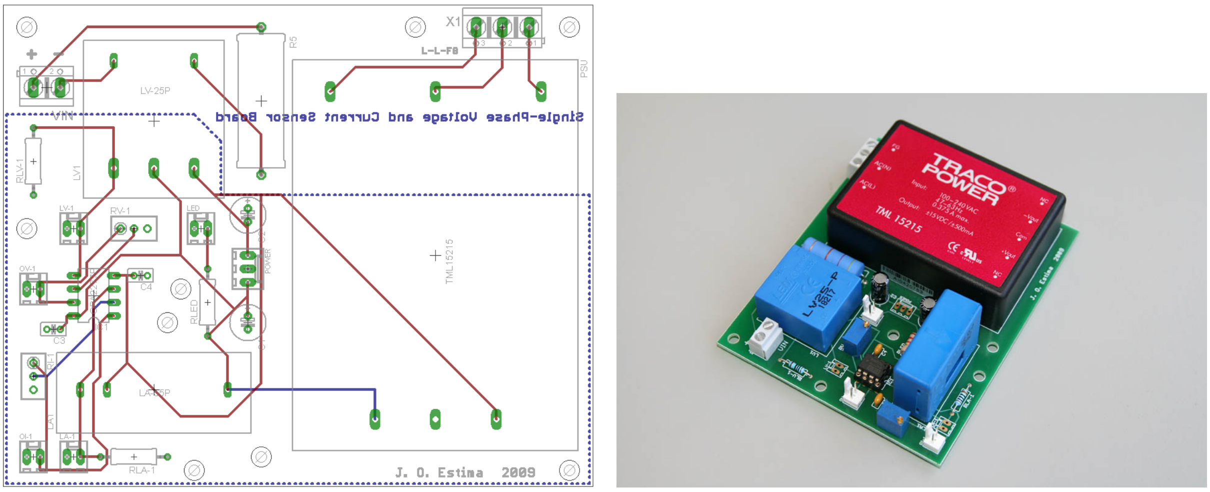

(a)

(b)

Figure B.9: Printed circuit board: (a) printed circuit diagram; (b) final design.

B.2.2 Three-Phase Voltage and Current Measurements

The motor supplying currents and voltages were measured using this board. The measurement module uses three LEM sensors LA-55P and an equal number of LEM CV3-1000 voltage sensors.

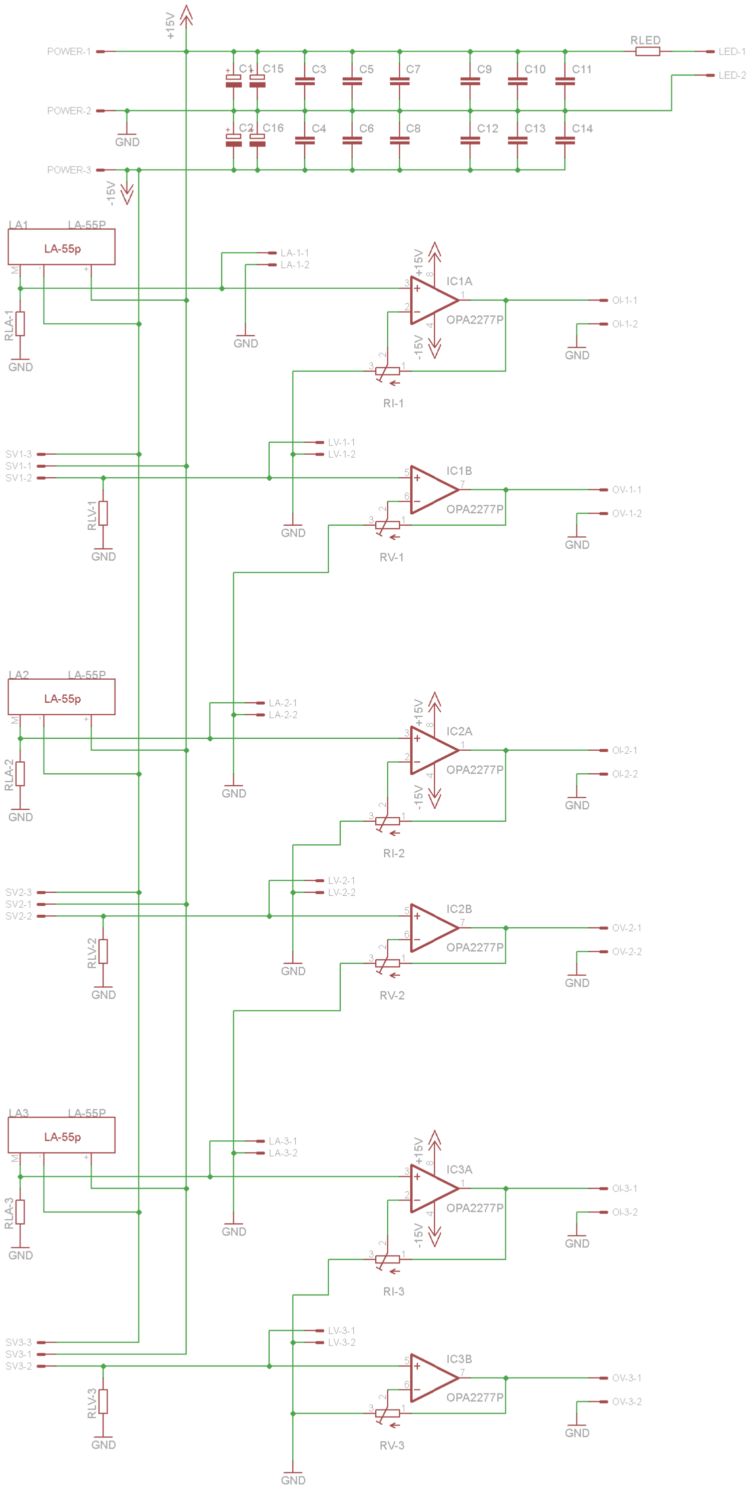

Figure B.10: Schematic circuit diagram of the three-phase voltage and current measurement board.

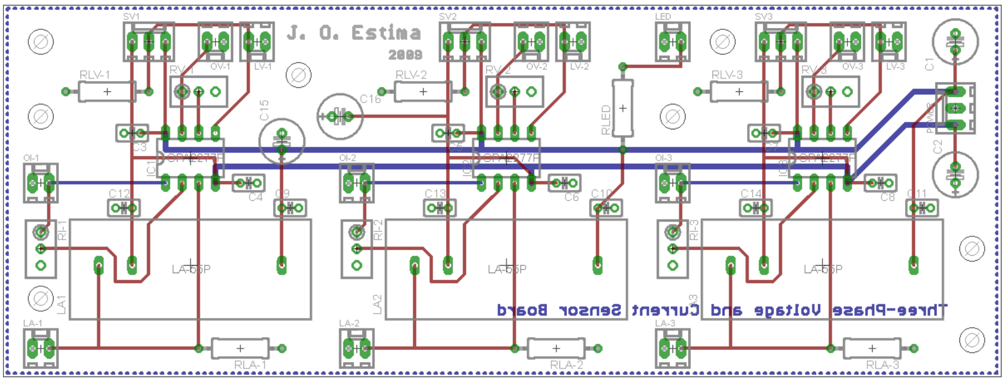

Figure B.11: Printed circuit diagram of the three-phase voltage and current measurement board.

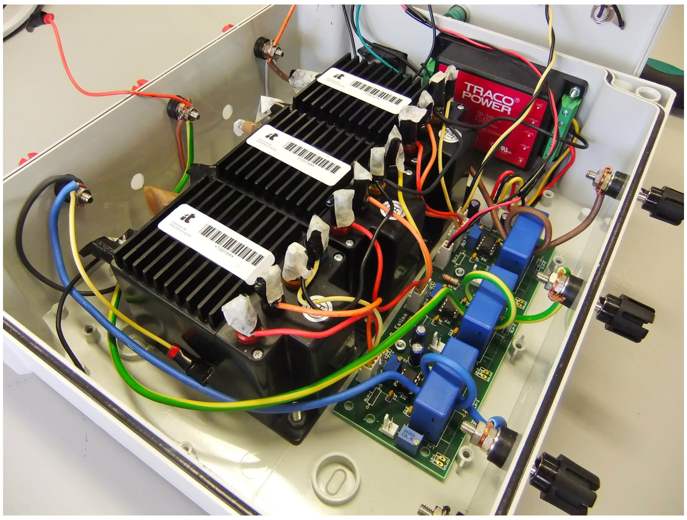

Figure B.12: Final design of the three-phase voltage and current measurement board.

Figure B.13: Final module of the three-phase voltage and current measurement board.

B.2.3 Inverter Interface Board

This board was designed and built with the aim to enable the interface between the dSPACE controller and two Semikron SKiiP 132GD120-3DUL power modules.

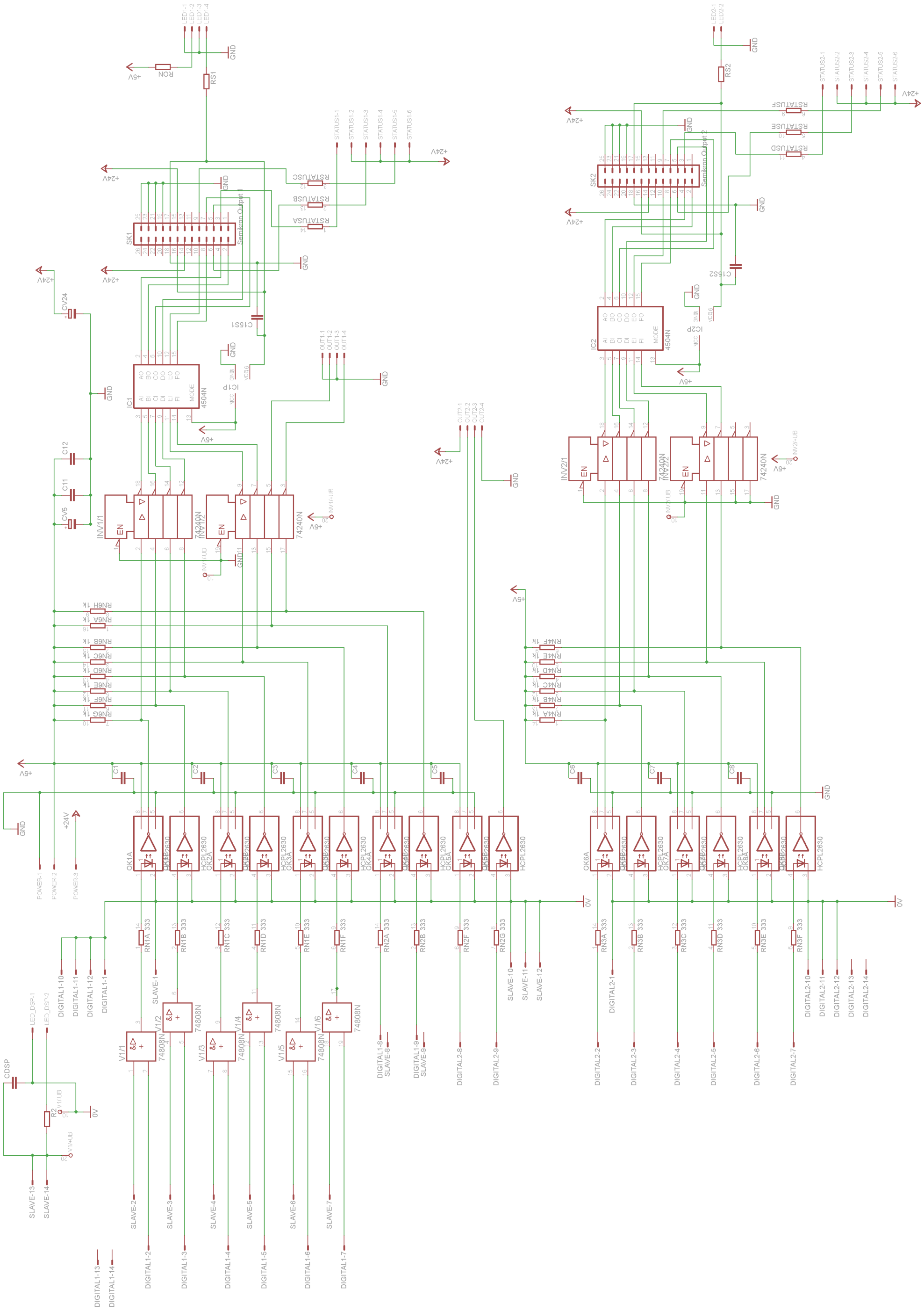

Figure B.14: Schematic circuit diagram of the inverter interface board.

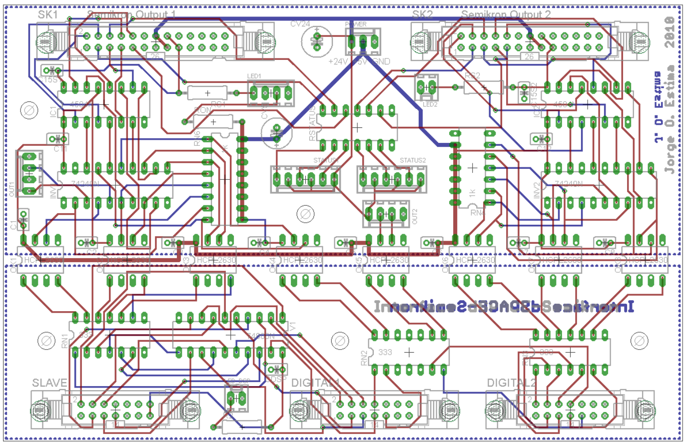

Figure B.15: Printed circuit diagram of the inverter interface board.

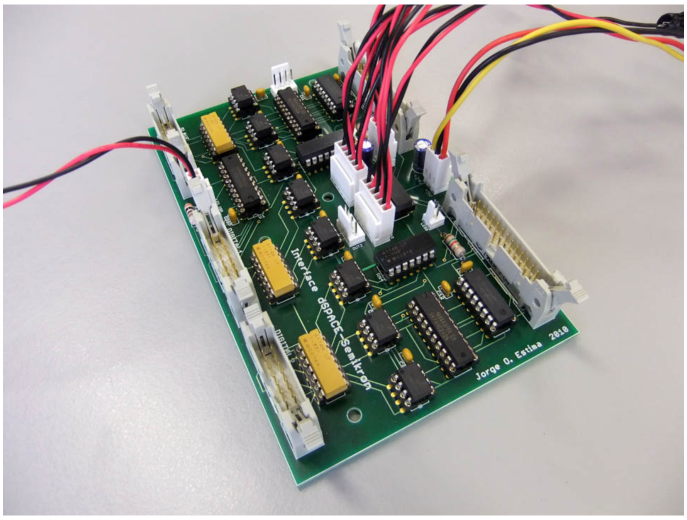

Figure B.16: Printed circuit board final design.

Figure B.17: Inverter interface final module.

B.2.4 Triac Interface Board

An additional auxiliary control board was built in order to make the interface between the controller and the triac. This board also has other features such as the control of an electromechanical relay and the possibility to control a SKiiP 132GD120-3DUL phase.

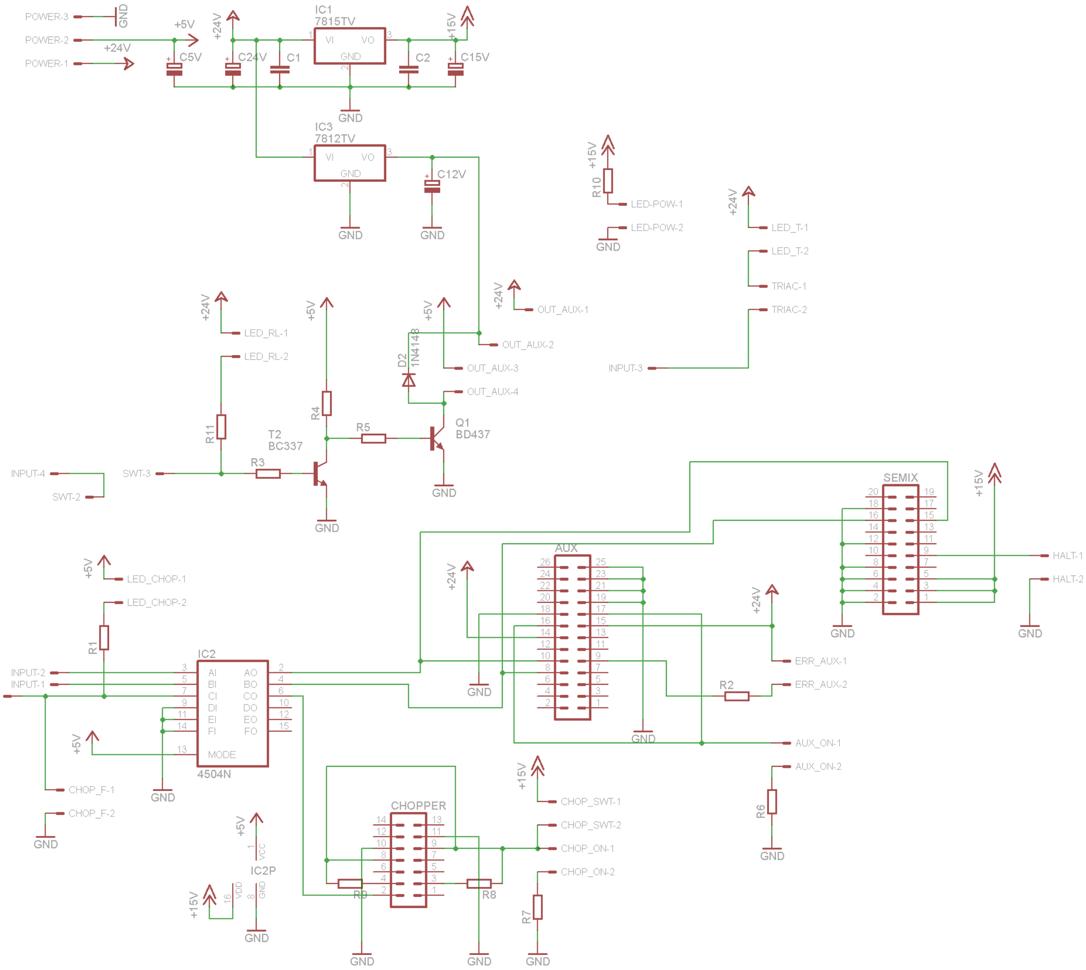

Figure B.18: Schematic circuit diagram of the triac interface board.

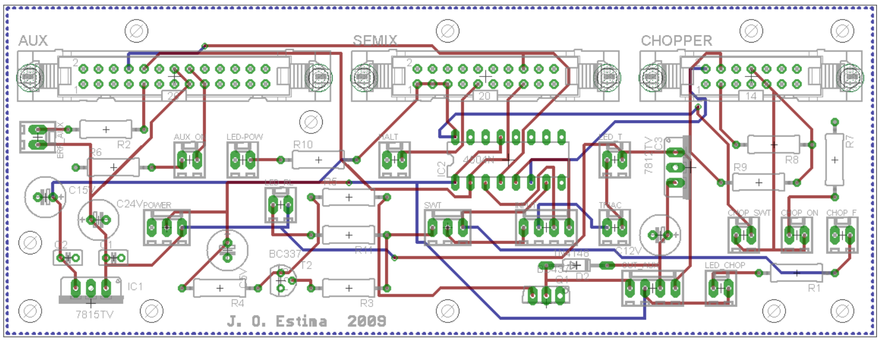

Figure B.19: Printed circuit diagram of the triac interface board.

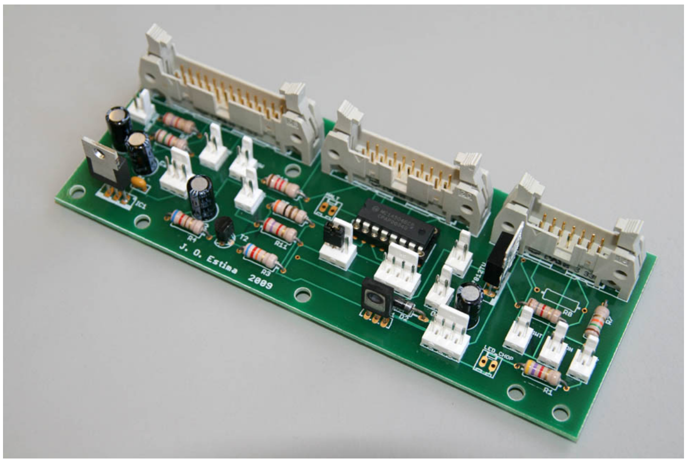

Figure B.20: Triac interface board final design.

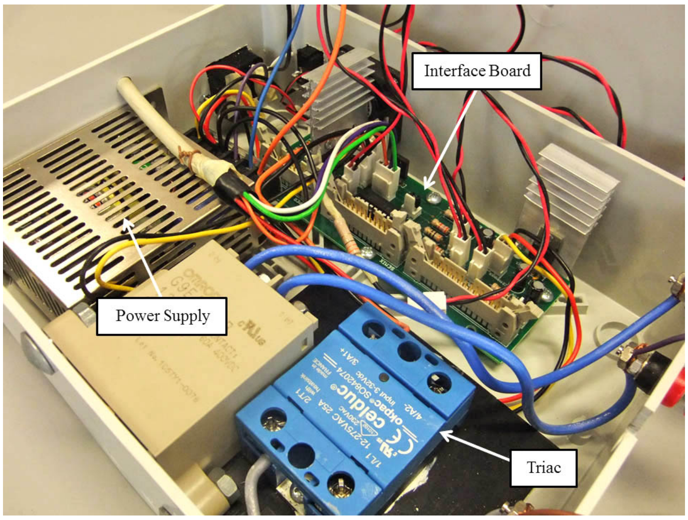

Figure B.21: Triac interface final module.

• U C •